

# Solid Oxide Fuel Cell Stack Diagnostics

**Mosbæk, Rasmus Rode**

*Publication date:*
2014

*Document Version*
Publisher's PDF, also known as Version of record

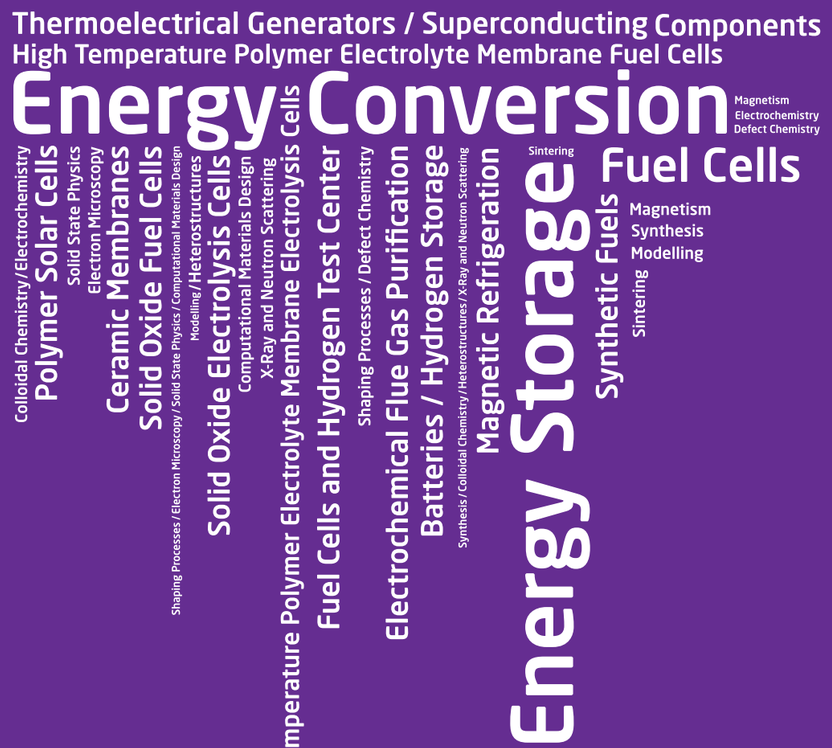


Department of Energy Conversion and Storage
Technical University of Denmark
Risø Campus
Frederiksborgvej 399
4000 Roskilde
Denmark
www.ecs.dtu.dk

ISBN 978-87-92986-20-7

Solid Oxide Fuel Cell Stack Diagnostics

Rasmus Rode Mosbæk

October 2014

Technical University of Denmark

DTU

# Solid Oxide Fuel Cell Stack Diagnostics

Rasmus Rode Mosbæk
Department of Energy Conversion and Storage
Ph.D. Thesis, October 2014






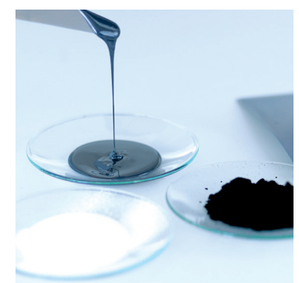

DTU Energy Conversion
Department of Energy Conversion and Storage

# Solid Oxide Fuel Cell Stack Diagnostics

## Author

**Rasmus Rode Mosbæk**
Applied Electrochemistry
Department of Energy Conversion and Storage
Technical University of Denmark
E-mail: rasmo@dtu.dk

## Supervisors

**Johan Hjelm**
Senior Scientist, Applied Electrochemistry
Department of Energy Conversion and Storage
Technical University of Denmark
E-mail: johh@dtu.dk

**Peter Vang Hendriksen**
Professor, Head of Section Mixed Conductors
Department of Energy Conversion and Storage
Technical University of Denmark
E-mail: pvhe@dtu.dk

**Rasmus Gottrup Barfod**
Technology Scout, Cell & Materials Group
Topsoe Fuel Cell A/S
E-mail: raba@topsoe.dk

## Technical University of Denmark

Section for Applied Electrochemistry
Department of Energy Conversion and Storage
Technical University of Denmark
Frederiksborgvej 399
DK-4000 Roskilde
Denmark
www.ecs.dtu.dk
Tel: +45 46 77 58 00
E-mail: info@ecs.dtu.dk

**Release date:** 7th October 2014
**Comment:** This report is part of the requirements to achieve the degree of Doctor of Philosophy (PhD) at the Department of Energy Conversion and Storage, Technical University of Denmark

# Abstract

As SOFC technology is moving closer to a commercial break through, methods to measure the "state-of-health" of operating stacks are becoming of increasing interest. This requires application of advanced methods for detailed electrical and electrochemical characterization during operation. An operating stack is subject to compositional gradients in the gaseous reactant streams, and temperature gradients across each cell and across the stack, which complicates detailed analysis. Several experimental stacks from Topsoe Fuel Cell A/S were characterized using Electrochemical Impedance Spectroscopy (EIS).

The stack measurement geometry was optimized for EIS by careful selection of the placement of current feeds and voltage probes in order to minimize measurement errors. It was demonstrated that with the improved placement of current feeds and voltage probes it is possible to separate the loss contributions in an ohmic and a polarization part and that the low frequency response is useful in detecting mass transfer limitations.

A sequential and a parallel measurement setup was developed for acquisition of impedance measurements. From the sequential to the parallel measurement setup the acquisition time was cut down significantly and it was demonstrated parallel acquisition of 16 repeating units (cells) and the total stack impedance could be made fully automated.

The performance and degradation of a 13-cell cross-flow stack was monitored for more than $2500$ hours at steady operating conditions using the sequential impedance measurement setup. Impedance measurements was used to examine the long-term behavior and monitor the evolution of the series and polarization resistances for four out of the 13 repeating units during the first $1400$ hours of operation. The losses for the four selected repeating units are reported and discussed.

The performance and degradation of a 14-cell co-flow stack was monitored for more than $667$ hours at steady operating conditions using the sequential impedance measurement setup. The stack was tested galvanostatically (at constant current) with $50\%$ steam in the hydrogen fuel gas supplied to the stack. EIS was used to examine the long-term behavior and monitor the evolution of the impedance of each of the repeating units and the whole stack. The observed impedance was analyzed in detail for one of the repeating units and the whole stack and the losses reported and discussed in the following.

Parallel acquisition using electrochemical impedance spectroscopy can be used to detect possible minor differences in the supply of gas to the individual cells, which is important when going to high fuel utilizations. The fuel flow distribution was determined and provides important information about the operating limits of the stack when high electrical efficiency is required. Furthermore, the measured gas concentration impedance was in between the impedances predicted by two different gas concentration impedance models.

Total harmonic distortion, THD, experiments were carried out on an experimental 14-cell SOFC stack at varying frequencies and fuel utilizations. The results illustrated that THD can be used to detect increasing non-linearities in the current-voltage characteristics of the stack when the stack suffers from fuel starvation by monitoring the stack sum voltage only.

# Resumé (Danish Abstract)

Da fastoxid-brændselscelle (SOFC) teknologien er på vej mod kommercielt gennembrud, er der kommet en øget interesse i metoder til at måle "sundhedstilstanden" brændselscellestakke under drift. Dette kræver anvendelse af avancerede metoder til detaljeret elektrisk of elektrokemisk karakterisering under drift. En brændselscellestak under drift er underlagt kompositionsgradienter i de reaktive gasstrømme, samt temperaturgradienter over hver celle og over stakken, hvilket komplicerer detaljeret analyse. Adskillige eksperimentelle stakke med lav ohmsk modstand fra Topsoe Fuel Cell A/S var karakteriseret ved brug af elektrokemisk impedans spektroskopi (EIS).

Stak målegeometrien var optimeret til EIS ved nøje udvalgt placering strømtilførsel og spændingsprober for at minimere målefejl. Det var demonstreret at ved at forbedre placeringen strømtilførsler og spændingsprober var det muligt at separere tabsbidrag i en ohmsk og polarisations del og det lavfrekvente respons var brugbart til at detektere massetransportbegrænsninger.

Både en sekventiel og parallel måleopstilling var udviklet for optagelse af impedans målinger. Fra den sekventielle til den parallelle måleopstilling var optagelsestiden minimeret betragteligt og det var demonstreret at parallel optagelse af $16$ gentagende enheder (celler) og den totale stak impedans kan gøres fuldt automatiseret og integreret i programmeret testsekvenser i en staktestopstilling.

Præstation og degradering af en $13$-cellers kryds-strømnings-stak var monitoreret for mere end $2.500$ timer ved konstante betingelser ved brug af en sekventiel impedans måleopstilling. Impedansmålinger var brugt til at undersøge langtids adfærd og monitorerer udviklingen af serie og polarisations modstanden for fire ud af $13$ gentagende enheder i løbet af de første $1.400$ timers drift. Tab for de fire udvalgte gentagende enheder er rapporteret og diskuteret.

Præstation og degradering af en $14$-cellers fælles-strømnings-stak var monitoreret i $667$ timer under konstante betingelser ved brug af en parallel impedans måleopstilling. Stakken var testet galvanostisk (ved konstant strøm) ved $50\%$ damp i brint brændselsgassen forsynet til stakken. EIS var brugt til at undersøge langtids effekterne og monitorerer udviklingen af serie og polarisations modstanden for alle gentagende enheder samtidig med hele stakken. Den observerede impedans var analyseret i detaljer og tabene var rapporteret og diskuteret.

Parallel optagelse ved brug af elektrokemisk impedans spektroskopi kan bruges til at detektere mulige mindre ændringer i forsyningen af gas til de individuelle celler, dette er vigtigt under høj brændsels udnyttelse. Fordelingen af brændselsstrømmen var afledt af målingerne af gaskoncentrations-modstanden for alle celler i stakken og leverede vigtige informationer omkring driftsbegrænsninger af stakken når høj elektrisk effektivitet er ønsket. Endvidere, var den observerede gas-koncentrations-modstand mellem modstanden forudset af gas koncentrations modeller baseret på stempelstrømning og kontinuerlig-omrørt-beholder-reaktor tilfælde.

Total harmonisk forvrængnings eksperimenter var udført på en $14$-cellers eksperimentel stak ved varierende frekvenser og brændselsforbrug. Dette resultat illustrerede at total harmonisk forvrængning kan bruges til at detektere stigende ulineariteter i strøm-spændings karakteristikken af stakken når stakken oplever mangel på brændsel kun ved at monitorerer den samlede stakspænding.

# Preface

This thesis is submitted to the Technical University of Denmark in partial fulfillment of the requirements of the PhD degree. The work presented in this thesis is a product of three years of work with solid oxide fuel cell (SOFC) stacks and has mainly been carried out at the Technical University of Denmark, Department of Energy Conversion and Storage. The PhD study involved close collaboration with Topsoe Fuel Cell A/S, including development and assembly of experimental SOFC stacks optimized for electrochemical impedance spectroscopy, and a two month external research stay at the Fuel Cell Engineering department at AVL List GmbH, Graz, Austria, which contributed with input and aided the setting up of a SOFC stack test for Total Harmonic Distortion Analysis.

The project was financed by Copenhagen Cleantech Cluster, the Danish Energy Authority's (Energi Styrelsen) Energy Technology Development and Demonstration Program, EUDP (Energiteknologisk Udvikling og Demonstrations Program), under the projects ENS-64010-0052 and ENS-64012-0225, and the Energinet.dk ForskEL program under the project number 2012-1-10747. Topsoe Fuel Cell A/S supplied materials and expertise in the production of experimental stacks needed for the PhD project.

Rasmus Rode Mosbæk
Roskilde, Denmark, 7th October 2014

# Acknowledgements

I would like to express my gratitude to my supervisors: Johan Hjelm for being a extraordinary main supervisor who not only guided and supported me well through the project but who also taught me to be a constantly investigating and curious researcher as well as helped me improve my computer skills in Linux operating systems and the programming language Python. Peter Vang Hendriksen for his pearls of wisdom and for always thinking outside the box. Rasmus Gottrup Barfod for bringing industrial knowhow and a bird's eye view to the project.

I would also like to thank the following people: Jens Høgh for sharing his expertise in fuel cell stack testing, for many fruitful discussions, and for proof reading of the "Improving the stack impedance response". Martin Nørby Nielsen for the development of software and electronic circuits for the project. Anders Petersen for technical assistance when mounting SOFC stacks. Søren Koch for software development and fruitful discussions regarding impedance spectroscopy. Christopher R. Graves for developing the RAVDAV software. If it was not for his software I would still be doing data analysis. Søren Højgaard Jensen for technical input on impedance spectroscopy, gas conversion impedance discussions and proof reading of the "Detection of Fuel Gradients" chapter. Jean-Claude Njodzefon for assisting me several times in rescuing the stack test after alarm 3 trips, and for proof reading the Time Dependent Degradation chapter. Anne Hauch for fruitful discussions on impedance analysis. Anke Hagen for making this project possible. Heidi Adler Berggren for keeping things organized and solving every practical problem with a smile. Kristian Bastholm Knudsen, Karl Thyden and Jonathan Hallinder for all the high fives on the corridors.

The people at Topsoe Fuel Cell A/S for their interest in my thesis. Thomas Heiredal-Clausen for fruitful discussions on test plans and experimental SOFC stack designs. Jette Mylner for stack assembly of custom experimental SOFC stacks. Bjarke Dalslet for assistance with data analysis. Stine Fie Brømsø for making sure that the experimental stack components got the right treatments. Niels Christiansen and Søren Primdahl for IPR approvements when needed. Thanks to Jürgen Rechberger and the rest of the Fuel Cell Engineering department at AVL List GmbH for making my stay most enjoyable.

Thanks to my robot vacuum cleaner for cleaning my home while I was in the test laboratory. My family and friends for their patience and support. Especially my wife Charlotte and my daughter Cecilie for their endless love and support, and for listening to stories, reflections, and for cheering up when needed. I could not have finished the thesis without you.

# Contents

CHAPTER 1

# Introduction

A fuel cell is an electrochemical device that can convert chemical energy directly into electrical energy (and heat) continuously as long as fuel is supplied. The fuel cell is much like a battery though it does need a continuous supply of fuel. In the simplest form, one can think of a fuel cell as a "black box" that takes fuel as input and produces electricity as output (See Figure 1.1) [1]. Both batteries and fuel cells rely on electrochemistry. A fuel cell will continue to produce electricity as long as fuel (chemical energy) is supplied, while a battery has a finite amount of chemical energy stored in its electrode. This is the key difference between a fuel cell and a battery.

As the conversion of chemical to electrical energy in a fuel cell does not include thermal and mechanical steps, the efficiency is not limited by Carnot efficiency, which is the case for mechanical devices such as a gas turbine. Fuel cells and batteries can thereby deliver higher electrical efficiencies compared to traditional technologies such as coal-fired power plants and electrical generators based on internal combustion engines [2]. A schematic comparison of the energy conversion steps between fuel cells, batteries and combustion engines is shown in Figure 1.2.

This chapter consist of seven parts. The first part introduces the solid oxide fuel cell. The second part gives a explanation of the losses inside the fuel cell. The third part explains the components and flow configurations in solid oxide fuel cell stacks. The fourth part gives a brief description of the theory of electrochemical impedance spectroscopy and some analysis tools for analyzing the impedance data. The firth part gives the goal of the thesis, the sixth part gives the outline of the thesis and the seventh part a list of included publications are given.

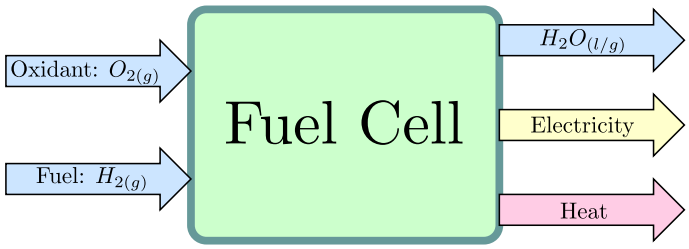


Figure 1.1: General concept of a hydrogen-oxygen $(H_2 - O_2)$ fuel cell. Adapted from Ref. [1].

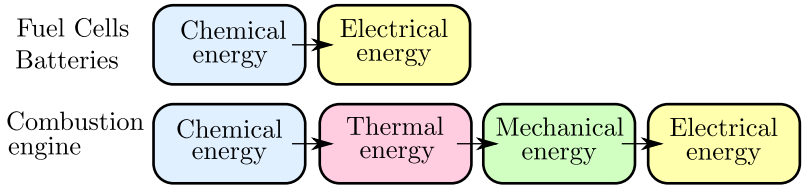


Figure 1.2: Schematic comparison of fuel cells, batteries and combustion engines. Adapted from Ref. [1].

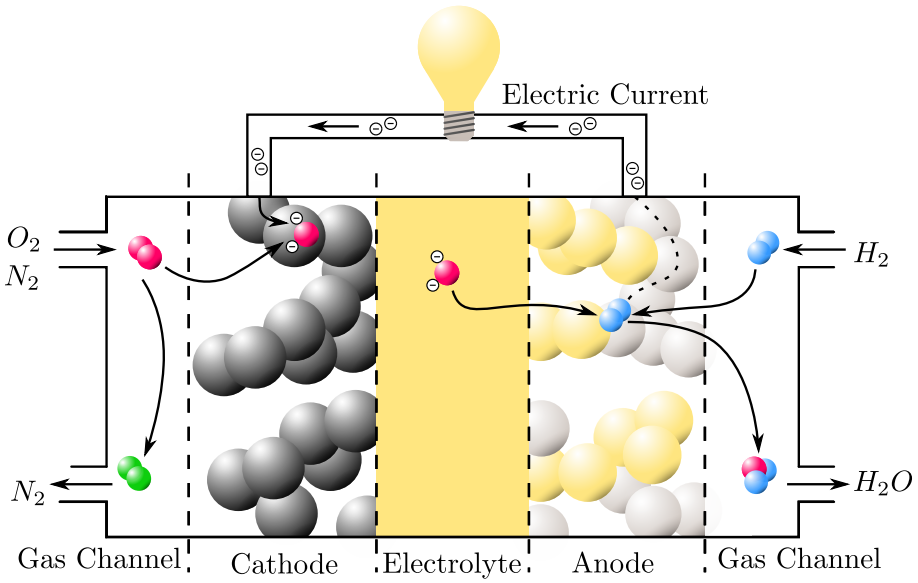


Figure 1.3: Working principle of the solid oxide fuel cell. Adapted from Ref. [3].

## 1.1 Solid Oxide Fuel Cells

### 1.1.1 Working principle

The solid oxide fuel cell (SOFC) consist of two electrodes, an anode and a cathode, which are separated by an electrolyte. Neither the electrodes nor the electrolyte are consumed by the operation of the cell. In a conventional combustion engine, fuel is burned which releases heat. Consider the simplest example, the combustion of hydrogen given in Equation 1.1.

$$\mathrm{H_2} + \frac{1}{2}\mathrm{O_2} \rightleftharpoons \mathrm{H_2O} \tag{1.1}$$

During combustion hydrogen molecules are oxidized, producing water and releases heat. In a fuel cell, hydrogen molecules are not combusted but instead the process is split into two electrochemical half reactions. The working principle of a solid oxide fuel cell is illustrated in Figure 1.3. Spatial separation of the two electrochemical half reactions are accomplished by an electrolyte. At high operating temperatures (above $500°C$) the solid oxide membrane becomes conducting for $\mathrm{O}^{2-}$ ions, thus acting as an electrolyte. At the cathode (oxygen electrode), oxygen from the gas phase disassociates, accepts two electrons and is incorporated into the electrolyte phase as given by Equation 1.2. Due to the potential drop between the fuel and oxidant sides of the electrolyte, the $\mathrm{O}^{2-}$ ions are transported through the electrolyte towards the anode (fuel electrode) where the $\mathrm{O}^{2-}$ ions reacts with hydrogen, $\mathrm{H_{2(g)}}$, to form steam, $\mathrm{H_2O_{(g)}}$, and releases two electrons (See Equation 1.3). The two electrons moves trough an external electric circuit.

$$\frac{1}{2}\mathrm{O_{2(g)}} + 2\,\mathrm{e}^- \rightleftharpoons \mathrm{O^{2-}_{(el)}} \tag{1.2}$$

$$\mathrm{O^{2-}_{(el)}} + \mathrm{H_{2(g)}} \rightleftharpoons \mathrm{H_2O_{(g)}} + 2\mathrm{e}^- \tag{1.3}$$

### 1.1.2 Electrolyte Materials

The SOFC electrolyte is exposed to both oxidizing (oxidant side) and reducing species (fuel side) at high temperatures. For successful long term operation the electrolyte must have a sufficient ionic conductivity, a dense structure (gas tight) and be chemically stable. The most common

electrolyte for SOFCs is Yttrium-stabilized $\mathrm{ZrO_2}$ (YSZ). For lower operating temperatures doped $\mathrm{CeO_2}$ can be used which have showed higher ionic conductivity, but on the other hand doped $\mathrm{CeO_2}$ has shown electronic conduction in reducing conditions at operating temperatures above $650°C$ [2].

### 1.1.3 Cathode Materials

The oxygen electrode material should possess a high electronic and ionic conductivity, and fast oxygen surface exchange in order to perform well as an SOFC cathode (Equation 1.2). The coefficient of thermal expansion should ideally match that of other cell components well, and show a minimum reactivity with the electrolyte and the interconnect. Finally, the cathode must have a stable and porous microstructure so the oxygen ions can easily diffuse to the cathode/electrolyte interface. Conducting perovskites are the preferred cathode materials. A widely used material is Sr- doped $\mathrm{LaMnO_3}$ (LSM) which has a relatively low oxide ion conductivity [2].

For SOFCs operating at lower temperatures new cathode materials have been developed since LSM is not the ideal candidate due to its low ionic conductivity and slow surface oxygen exchange kinetics. These cathodes are Mixed Ionic Electronic Conductors (MIEC). The $(La, Sr)\,(Co, Fe)\,O_3$ perovskite materials, LSCF, has received attention due to its high oxide ion diffusion rates and faster oxygen reduction kinetics [2]. However, LSCF materials are also more reactive than LSM and reacts to form insulating secondary phases (zirconates) with zirconia electrolytes, necessitating use of a protective inter diffusion barrier layer to avoid this problem. Such barrier layers are made from Gd-doped ceria [4, 5].

### 1.1.4 Anode Materials

The anode must be an excellent catalyst for the oxidation of the fuel (Equation 1.3), and must be stable in the reducing environment, have good electronic conductivity and a sufficient porosity. The anode must also have a good tolerance towards sulfur poisoning [6] and carbon deposition [7] when hydrocarbons are used as fuel. Nickel-zirconia (Ni-YSZ) anodes have been dominant for some fifty years even though Nickel has significant thermal expansion mismatch with stabilized zirconia, and at high temperatures Nickel aggregates by grain growth [8]. Alternative ceria-based anodes have been investigated which has shown larger resistance to carbon deposition [8] and alternative Ni-ScYSZ anodes exhibit higher sulfur tolerance compared to Ni-YSZ anodes [9].

### 1.1.5 Some relevant Equations

This section describes some of the equations relevant when operating SOFC. This includes the thermodynamically reversible voltage, the Nernst equation and the Faraday law which are all used in this work. Other relevant equations can be found in the following literature Ref. [1, 10].

#### 1.1.5.1 Thermodynamically reversible voltage

If the fuel cell is reversible (no losses) a voltage can be measured between anode and cathode when the reversible electrode reactions (Equation 1.2 and 1.3) reaches chemical equilibria. Then all the Gibbs free energy is converted into electrical energy. The reversible open circuit voltage (electromotive force, EMF) of a hydrogen fuel cell is given by Equation 1.4. $-\Delta G\ \left[\frac{J}{mol}\right]$ is the negative Gibbs free energy difference which is the maximum electrical work that a system can perform in a constant temperature and constant pressure process. $F\ \left[\frac{C}{mol}\right]$ is the Faraday constant (the charge of one mole electrons) and $n\ [-]$ is the number of moles of electrons transfered [1, 10].

$$U_{th} = E^0 = -\frac{\Delta G}{nF} \tag{1.4}$$

#### 1.1.5.2 Nernst Equation

The Nernst equation describes how the reversible electrochemical cell voltage varies with as a function of species concentration, gas pressure and temperature. For an arbitrary number of

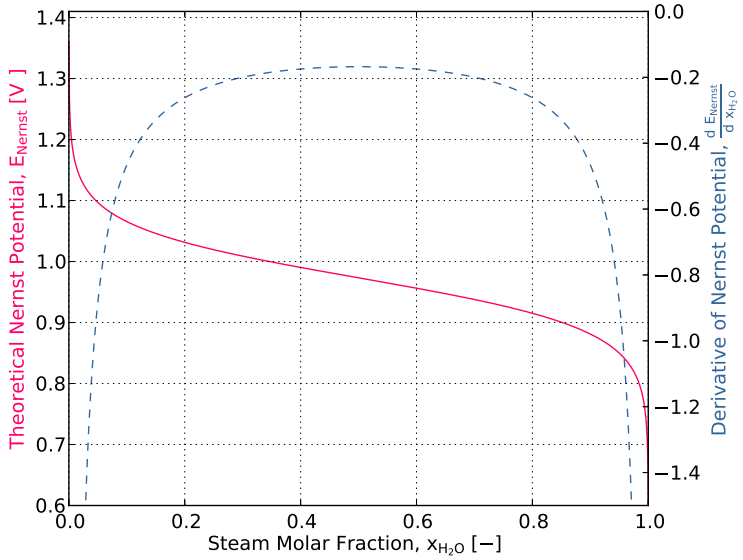


Figure 1.4: Theoretical Nernst potential as a function of steam molar fraction calculated at $T = 700°C$.

products the Nernst equation is given in Equation 1.5. The Nernst equation for the hydrogen oxygen fuel cell reaction (Euation 1.1) is given by Equation 1.6 [1]. $R_g\ \left[\frac{J}{mol\,K}\right]$ is the gas constant, $T\ [K]$ is the temperature, $n\ [-]$ is the number of moles of electrons, $F\ \left[\frac{C}{mol}\right]$ is the Faraday constant and $x\ [-]$ molar fractions for the species.

$$U_N = E_{Nernst} = E^0 - \frac{R_g\,T}{n\,F}\ln\left(\frac{\prod x_{products}^{\nu_i}}{\prod x_{reactants}^{\nu_i}}\right) \tag{1.5}$$

$$U_N = E_{Nernst} = E^0 - \frac{R_g\,T}{2\,F}\ln\left(\frac{x_{H_2O}}{x_{H_2}\,x_{O_2}^{\frac{1}{2}}}\right) \tag{1.6}$$

As $x_{H_2} = 1 - x_{H_2O}$ the derivative of the Nernst equation is given by Equation 1.7. The Nernst potential plottet versus the steam content and its derivative at $700°C$ is shown in Figure 1.4.

$$\frac{d\,U_N}{d\,x_{H_2O}} = \frac{R_g\,T}{2\,F\,x_{H_2O}\,(x_{H_2O} - 1)} \tag{1.7}$$

#### 1.1.5.3 Faraday Law

Electrons are either generated or consumed by electrochemical reactions. The current $I\,[A]$ in an electrochemical reaction is a measure of the rate of the electrochemical reaction. The unit for current is ampere, $[A]$, which is equal to charge (Coulomb) per second, $\left[\frac{C}{s}\right]$, as given by Faraday law in Equation 1.8, where $Q\ [C]$ is the charge and $t\ [s]$ is the time in seconds [1].

$$I = \frac{d\,Q}{d\,t} \tag{1.8}$$

Current expresses the rate of charge transfer. If the electrochemical reaction results in the transfer of $n$ electrons then the current is given by Equation 1.9 where $F\ \left[\frac{C}{mol}\right]$ is the Faraday constant and $\upsilon\ \left[\frac{mol}{s}\right]$ is the molar conversion rate [1]. Since two moles of electrons are transferred for every mole of $H_2$ gas reacted, $n = 2$ if the fuel is $H_2$.

$$I = n\,F\,\upsilon \tag{1.9}$$

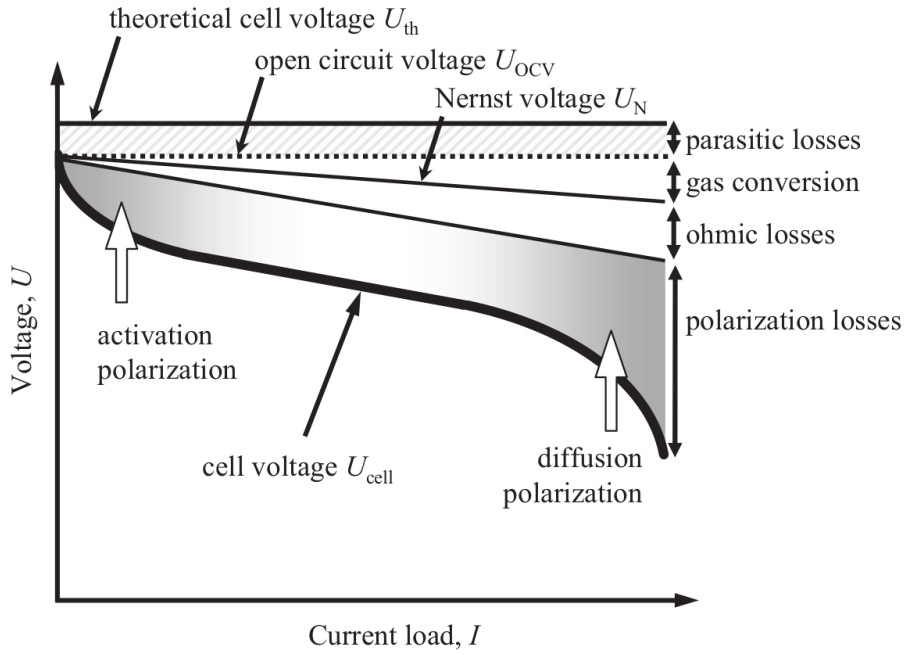


Figure 1.5: Schematic representation of the current-voltage characteristics of a SOFC. The individual loss processes cause a decrease in cell voltage with increasing current. From Ref. [3].

## 1.2 Polarization losses and SOFC performance

The power delivered by a fuel cell is given by the product of the current and voltage as given in Equation 1.10. The current supplied by a fuel cell is directly proportional to the amount of fuel consumed (Faraday law. See Section 1.1.5.3 on the facing page). When current is applied the measured voltage experience a decrease which in electrochemistry is referred to as polarization. As the fuel cell voltage decreases, the electric power produced per unit of fuel also decreases.

$$P = U\,I \tag{1.10}$$

The polarization losses can by classified as to their physical origin. There are three major types of fuel cell polarization losses. Activation losses describes the charge transfer reactions at the electrode (electrochemical reactions). Ohmic losses due to ionic and electronic conductivity. Concentration losses due to mass transport limitations in the electrode electrode structure which includes gas conversion and gas diffusion. The real fuel cell voltage output is written in Equation 1.11 starting with the thermodynamically predicted voltage output [1].

$$U_{cell} = U_{th} - \eta_{act} - \eta_{ohmic} - \eta_{conc} \tag{1.11}$$

The performance of a fuel cell can be summarized by the schematic representation of the current-voltage (polarization) characteristics illustrated in Figure 1.5. The open circuit voltage, $U_{OCV}$, is lower than theoretical thermodynamically voltage, $U_{th}$ predicted in Equation 1.4 on page 3. The gap may be caused by parasitic losses such as electron leakage across the electrolyte or gas leakage through the sealant gaskets. The Nernst potential, $U_N$, decreases as a function of fuel utilization explained in Section 1.1.5.2 on page 3.

### 1.2.1 Ohmic Losses

The ohmic losses is due to electrical resistance of the electrodes, contact points of the interconnects, and the resistance due to conduction of ions through the electrolyte [10]. The size of the voltage drop is proportional to the current given by Ohms law in Equation 1.12.

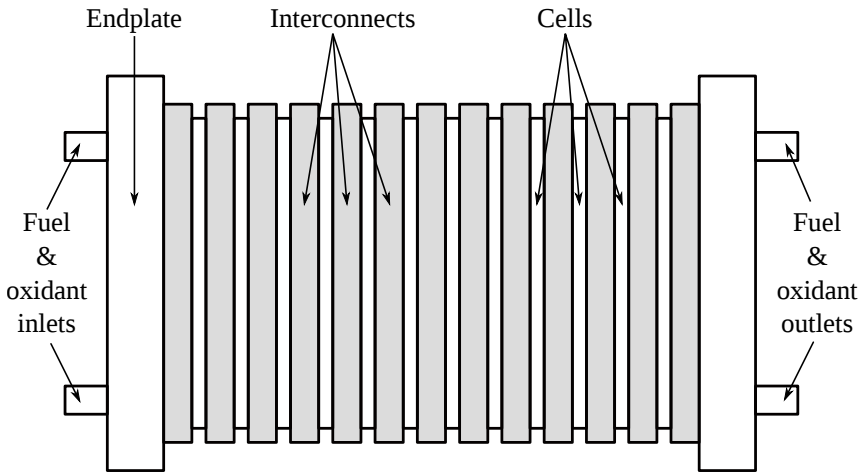


Figure 1.6: Illustration of a SOFC stack in a planar design.

$$U = R\,I \tag{1.12}$$

In the case where the electronic conductivity of the electrodes is sufficiently high the ohmic losses are mainly caused by resistance due to conduction of ions through the electrolyte, though the degree of contact between the cell and the interconnects can also be important.

### 1.2.2 Activation losses

Activation polarization losses (due to the fuel oxidation and oxidant reduction reactions taking place at the electrodes) and gas concentration polarization losses. The activation polarization losses are related to the charge transfer reactions at the electrodes and are strongly dependent on the exchange current density relating to the specific electrode material and its microstructure. Higher exchange current density reflects more facile electrode reactions, and produces lower polarization resistances. Therefore the exchange current densities of the electrodes are crucial in controlling the performance of a fuel cell [10].

### 1.2.3 Concentration Losses

The gas concentration losses are related to the gas transport within the electrode structure and reflects the coupled processes of the diffusion polarization and gas conversion [11]. Nernst potential in Figure 1.5 is illustrated as a linear function, which is a simplification of the real case. It is only approximately linear for steam molar fractions between $\sim 20\%$ and $\sim 80\%$ as shown in Figure 1.4.

## 1.3 Solid Oxide Fuel Cell Stacks

The voltage difference between the electrodes of the fuel cell is $\sim 1\,V$ at open circuit conditions. In order to obtain a useful voltage a number of fuel cells are connected in series to form a fuel cell stack. A schematic representation of a fuel cell stack can be seen in Figure 1.6. The cells are separated by interconnect plates which provide electrical contact between the cells, efficiently contacts the fuel cell electrode or current collection layers, and distribute fuel at one side and oxidant at the other side. To make the stack gas tight it is sealed at the edges between interconnects and cells. The fuel cell stack is provided with end plates with inlets and outlets for fuel and oxidant.

### 1.3.1 Interconnect materials

As the interconnects used in a stack not only provides electrical contact between the cells but also ensures that air and fuel flows are separated in the cell stack, this means that the interconnect material must withstand both reducing and oxidizing atmospheres at high temperature. When stack operating temperatures are lower than $800°C$ it is possible to use metallic interconnects, which lowers the raw material and fabrication cost significantly compared to the ceramic interconnect materials available for use at higher operating temperatures [2]. The interconnects must be highly resistant to surface oxidation and corrosion in a dual atmosphere. The metallic interconnects are usually coated with protective layers which decrease corrosion scale growth [2] and reduce chromium evaporation [12, 13].

### 1.3.2 Sealant materials

Sealant materials used in planar stacks with planar cells and interconnects must prevent leakage of fuel and oxidant as well of mixing of fuel and oxidant inside the stack. The sealant must be able to withstand thermal cycling from cell operational temperature to room temperature and the coefficient of thermal expansion must be similar to the other stack components [2]. The sealant materials must also be able to withstand both reducing and oxidizing atmospheres at high temperatures.

### 1.3.3 Flow configurations

The flow configuration used in a stack has a strong influence on the horizontal and vertical temperature profile of the stack. Furthermore the temperature profile is strongly dependent on the operating point which includes parameters such as the choice of fuel gas, fuel and oxidant flow rates, inlet temperature, and current density. The SOFC stack temperature profile has a great influence on the performance and lifetime of the stack and is therefore a high priority within research and development of SOFC stacks. During operation under DC current load more heat is generated than the stack loses to the surroundings. In order to cool the stack the gases fed to the stack are colder than the average stack temperature. The type of fuel has a strong influence on the temperature profile, and it is particularly influenced by whether it is a reforming (methane and other hydrocarbons) or non-reforming fuel (hydrogen or carbon monoxide) that is being used. Reforming is an endothermic process and when using such fuels additional cooling of the stack may take place, primarily near the fuel inlet of the each cell. When using non-reforming the stack is heated due the exothermic nature of the fuel cell reaction. The balance of the different heat inputs (cooling or heating), the flow configuration and the current load determines the temperature profile across each cell and across the stack. The three main flow configurations used in planar SOFC stacks are illustrated in Figure 1.7.

In a **cross flow configuration** the fuel and oxidant are supplied perpendicular to each other. The complexity in building SOFC stacks with a cross flow configuration is lower relative to the co- and counter-flow configuration, especially if an external air manifold is desired. The disadvantage of the cross flow configuration is that the hottest zone is at the outlet corner and the coldest zone is at the inlet corner as illustrated by the red and blue circles in Figure 1.7. This yields a skewed temperature profile which increases the thermal and mechanical stresses of the stack.

For a **counter flow configuration** the fuel and oxidant flow are supplied parallel in the opposite directions. This gives a better temperature profile compared to the cross flow configuration. The disadvantage is that the hottest and coldest zones are inside the stack which means that one need to rely on proper numerical stack models to ensure safe operation of the stack. For non reforming fuels the coldest zone is approximately $1/4$ of the cell width from the oxidant inlet and the hottest zone is approximately $1/4$ of the cell width from the fuel inlet as illustrated in Figure 1.7. For reforming fuels the coldest zone is approximately $1/4$ of the cell width from the fuel inlet and the hottest zone is approximately $1/4$ of the cell width from the oxidant inlet, which is opposite of the hot and cold zones illustrated for counter flow in Figure 1.7.

For a **co flow configuration** the fuel and oxidant are supplied in parallel, flowing in the same direction, which means that in a co-flow configuration the hottest zone is typically the outlet and

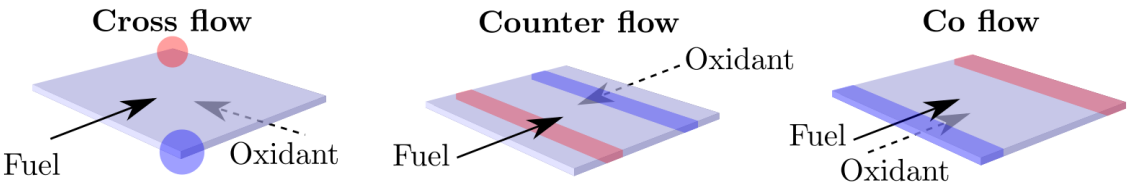


Figure 1.7: Illustration of flow configurations for planar SOFC stacks. Red indicate possible hot zones and blue indicate possible cold zones.

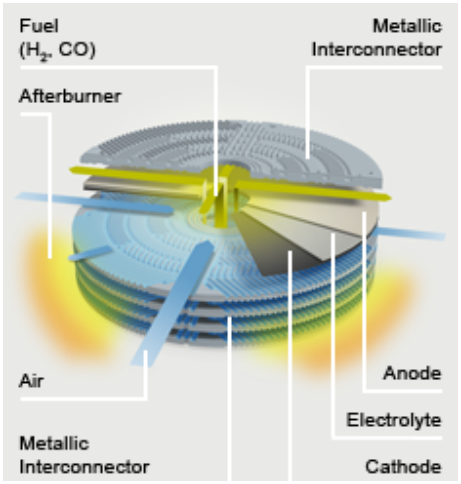


Figure 1.8: Illustration of the Hexis AG SOFC stack design. From Ref. [17].

coldest zone is typically at the inlet as illustrated in Figure 1.7. Since the temperature profile of the co-flow configuration typically is hottest at the outlet simplifies the operation of the SOFC stack since it is relatively easier to control of the temperature profile compared to cross and counter flow configurations which reduces the dependency of the numerical models [14].

SOFC stacks from Hexis AG, Switzerland have a more sophisticated flow configuration as illustrated in Figure 1.8. The Hexis AG SOFC stacks consists of 60 repeat units containing disk-shaped planar electrolyte supported cells (area $100\,cm^2$) and metallic interconnects. The fuel is supplied from a round hole in the center of the cells/stack and preheated oxidant is supplied from the an external manifold through four channels. Excess fuel is burned in a post-combustion zone surrounding the stack which minimizes the demands on seals [15, 16]. The disadvantage with this stack configuration is that the stack will have a very hot zone in the post combustion zone surrounding the stack which increases the thermal and mechanical stresses of the stack.

## 1.4 Electrochemical Impedance Spectroscopy

In this section a brief description of the theory of electrochemical impedance spectroscopy is given. More comprehensive descriptions are given in the following literature: Ref. [1, 18, 19].

Electrochemical impedance spectroscopy (EIS) provides information about different losses in an electrochemical device as a function of the frequency, or characteristic time-scale of the responsible process. An EIS measurement involves imposing a sinusoidal AC current or voltage signal on the test object at different frequencies. From the input signal and the response signal the impedance can then be calculated.

There are two fundamental types of electrochemical characterization techniques to obtain the frequency dependent impedance: potentiostatic technique and galvanostatic technique. With the *potentiostatic technique* the voltage is controlled and the response of the current is measured. The

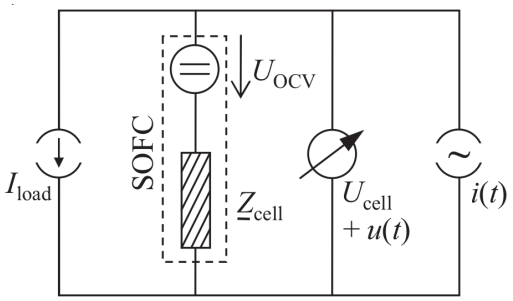


Figure 1.9: Electrical schematic of a measurement setup for a single SOFC with the internal impedance $Z_{cell}$. From Ref. [3].

potentiostatic technique is often chosen for high impedances since unintentional high currents is avoided at high impedances. For the *galvanostatic technique* the current is controlled and the voltage is measured. This method is especially appropriate when measuring very small impedances [1, 3].

The basic measurement setup for impedance measurements on SOFCs is illustrated in Figure 1.9. A sinusoidal current of small amplitude $i(t) = i_0 \sin(\omega\, t)$ at a fixed angular frequency $\omega = 2\,\pi\, f$ is superimposed on the (DC) load current, $I_{load}$. The resulting voltage response is measured, from which the sinusoidal component $u(t) = u_0(\omega)\sin(\omega\, t + \theta)$ as illustrated in Figure 1.10. The sinusoidal voltage signal, $U$, and corresponding current response, $I$ with absolute impedance, $|Z|$, and phase, $\theta$ is illustrated in Figure 1.11.

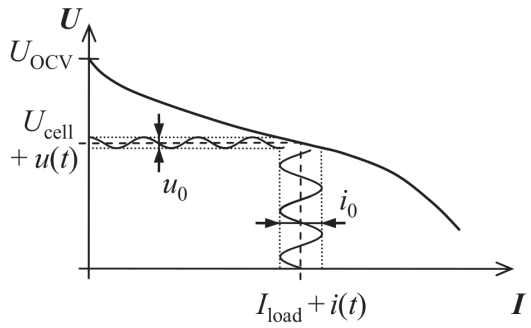


Figure 1.10: Illustration of impedance measurement and corresponding polarization curve. From Ref. [3].

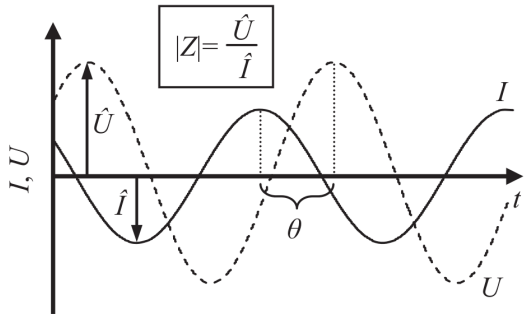


Figure 1.11: Sinusoidal voltage signal, $U$, and corresponding current response, $I$ with absolute impedance, $|Z|$, and phase, $\theta$. From Ref. [20].

From the measured current amplitude, voltage amplitude, and the phase shift the impedance can be calculated. The complex impedance is given for the potentiostatic method by Equation 1.15 technique and for the galvanostatic technique by Equation 1.14 . $Z_0\,[\Omega\, cm^2]$ is the complex impedance, $u_0$ $[V]$ and $i_0\,[\frac{A}{cm^2}]$ are the voltage and current density amplitudes respectively. $\omega$ $\left[\frac{rad}{s}\right]$ is the radial frequency and $\theta$ $[-]$ is the phase shift.

$$Z = \frac{u_0 e^{j\omega t}}{i_0 e^{j\omega t - j\theta}} = \frac{u_0}{i_0} e^{j\theta} = Z_0\,(\cos\theta + j\sin\theta) = Z_{re} + jZ_{im} \tag{1.13}$$

$$Z = \frac{u_0 e^{j\omega t - j\theta}}{i_0 e^{j\omega t}} = \frac{u_0}{i_0} e^{-j\theta} = Z_0\,(\cos\theta - j\sin\theta) = Z_{re} - jZ_{im} \tag{1.14}$$

The obtained impedance can be visualized many different ways. Usually one or a few of a number of two-dimensional representations are chosen, e.g. a complex plane, or Nyquist, plot

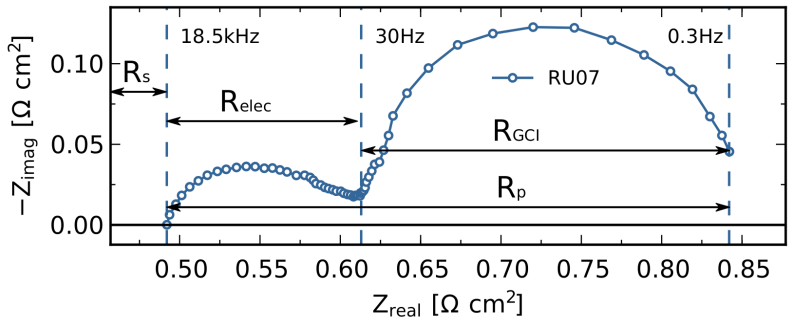


Figure 1.12: Impedance spectra for repeating unit (interconnect - seal - cell - seal - interconnect) in a SOFC at $700°C$ Fuel: $20\%$ $H_2O$ and $80\%$ $H_2$ Oxidant: Air. With definitions of the series resistance, $R_s$, the polarization resistance, $R_p$, the gas concentration resistance, $R_{GCI}$, and the electrochemical resistance $R_{elec}$.

in which the real and imaginary impedance is plotted, or a Bode plot in which the phase and the magnitude (or the real and imaginary parts of the impedance) are plotted versus the logarithm of the frequency. Figure 1.12 shows an impedance spectra of a repeating unit (interconnect - seal - cell - seal - interconnect) together with definitions of the series resistance, $R_s$, describing the ohmic losses, the polarization resistance, $R_p$, describing the polarization losses, the gas concentration resistance, $R_{GCI}$, describing the losses due to gas transport, and the electrochemical resistance, $R_{elec}$, describing the electrochemical losses such as the activation losses amongst other things. For fast computer simulations of SOFCs, equivalent circuit models (ECM) can be used to calculate the impedance spectra expected in different situations. For quantitative analysis, or parameterization, of data in terms of an equivalent circuit model, the model can be fitted to the data using algorithms for complex non-linear least squares minimization. The equivalent circuit models consist of different impedance elements. Three simple impedance elements are explained in the following section together with two parallel equivalent circuits used in this work.

### 1.4.1 Impedance elements

To describe the behavior of the impedance measured, different impedance elements can be used for equivalent circuit modeling. In this section only a few simple impedance elements are described such as resistance, inductance, capacitance and the constant phase element. For equivalent circuit modeling, other frequency dependent elements are used as well. Frequency-dependent elements consist among others of the Warburg element describing mass transport losses and the constant-phase element describing the double layer capacitance at the electrodes and the Gerischer element. For description of the frequency-dependent elements see the following literature [1, 19, 21].

The simplest impedance element is the resistor. Resistors are used to describe ohmic resistance in terms of electron conduction and ion conduction. The impedance of a resistor is the resistance as given in Equation 1.15.

$$Z_R = R \tag{1.15}$$

The inductance, $L\,[H]$, is used to describe the high frequency inductance. The high frequency inductance is often caused by self-inductance in the device under test, and may also be caused by inductance originating from the leads used to connect to the test object. The impedance of an inductor is given by equation 1.16. Where $\omega\,[Hz]$ is the angular frequency given by $\omega = 2\pi\, f$ where $f\,[Hz]$ is the frequency.

$$Z_L = j\omega L \tag{1.16}$$

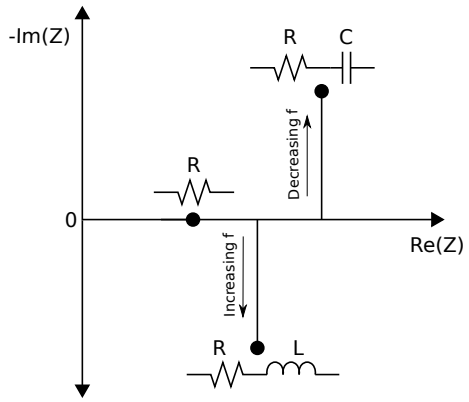


Figure 1.13: Illustration of the impedance elements.

The capacitor, $C\,[F]$, is used to describe the double layer capacitance at the anode-electrolyte and the cathode-electrolyte interfaces and the chemical capacitance associated with concentration impedances. The impedance of a capacitor is imaginary and is described by Equation 1.17. Impedance spectra of the three explained impedance elements are illustrated in Figure 1.13.

$$Z_C = \frac{1}{j\omega C} \tag{1.17}$$

#### 1.4.1.1 Parallel RC Circuit

A parallel connection between a resistor and a capacitor is known as a Voigt element and is illustrated in Figure 1.14. The parallel RC circuit is a fundamental combination which can describe interfacial processes electrochemical systems. Its complex impedance is given by Equation 1.18 (See also Figure 1.15) where $\tau$ is the time constant $\tau = RC$ which is inverse of the angular frequency $\omega = 2\pi\, f$ [19].

$$Z_{RC} = \frac{R_{RC}}{1 + j\omega\,\tau_{RC}} \tag{1.18}$$

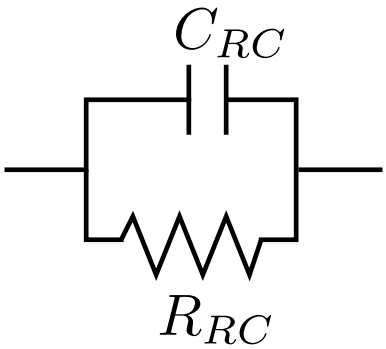


Figure 1.14: RC equivalent circuit element.

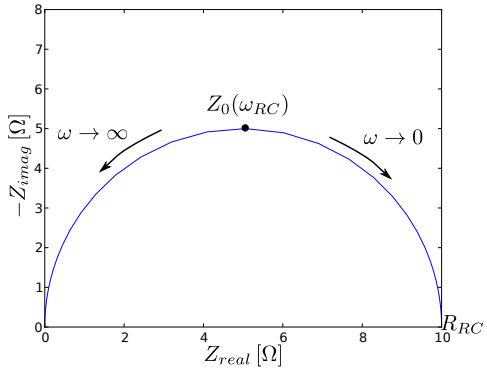


Figure 1.15: Nyquist plot of a RC circuit.

#### 1.4.1.2 Parallel RQ Circuit

The electrochemical impedance response of a real electrode or device typically reflects a distribution of reactivity that is often represented in equivalent circuit by a constant phase element (CPE

denoted as Q). A CPE assumes a specific distribution of time constants that may apply only approximately to a given electrochemical system [19]. The complex impedance of a CPE is given by Equation 1.19.

$$Z_Q = \frac{1}{(j\omega)^\alpha Q} \tag{1.19}$$

The CPE connected in parallel with a resistor (parallel RQ circuit) is illustrated in Figure 1.16 and its complex impedance is given by Equation 1.20. A Nyquist plot of a RQ circuit with varying is illustrated in Figure 1.17.

$$Z_{RQ} = \frac{R_{RQ}}{1 + (j\omega)^\alpha Q_{RQ}\, R_{RQ}} \tag{1.20}$$

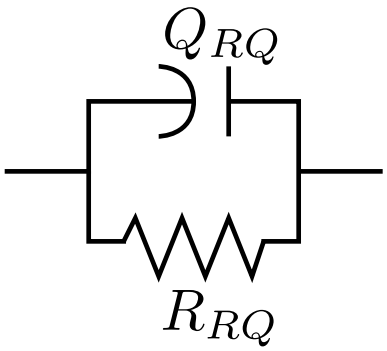


Figure 1.16: RQ equivalent circuit.

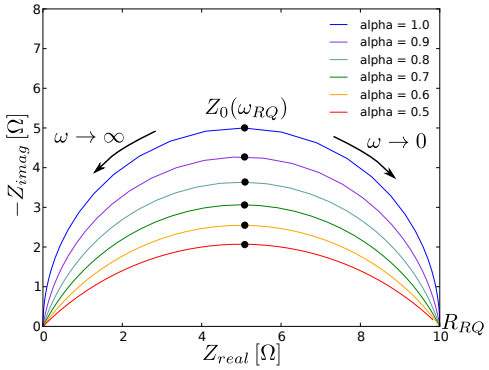


Figure 1.17: Nyquist plot of a RQ circuit with different values of $\alpha$.

### 1.4.2 Impedance data validation

The Kramers-Kronig test is a powerful tool to test the quality of electrochemical impedance measurements. In this section the Kramers-Kronig relations are presented together with an explanation of how the Kramers-Kronig test is used to validate the impedance data in this work.

#### 1.4.2.1 Kramers-Kronig Relations

The Kramers-Kronig relations allows one to calculate the real part of the impedance from the imaginary part and the imaginary impedance from the real part. To satisfy the Kramers-Kronig relations the complex impedance measurement must fulfill the following criteria:

**Linearity** The system is measured in the linear regime and be independent of amplitude.

**Causality** The measured response signal is entirely determined by perturbation.

**Stability** The sample did not change it electrochemical properties during the measurement.

**Finiteness** The impedance values must tend to a constant real value for $\omega \to 0$ and $\omega \to \infty$.

complies to the Kramers-Kronig relations and the real impedance can be reproduced by the imaginary impedance as given in Equation 1.21 and the imaginary impedance can be reproduced by the real impedance as given in Equation 1.22 [21].

$$Z_{real} = R_\infty + \frac{2}{\pi}\int_0^\infty \frac{xZ_{imag}(x) - \omega Z_{imag}(\omega)}{x^2 - \omega^2} dx \tag{1.21}$$

$$Z_{imag} = -\frac{2\omega}{\pi}\int_0^\infty \frac{Z_{real}(x) - Z_{real}(\omega)}{x^2 - \omega^2}dx \tag{1.22}$$

#### 1.4.2.2 Kramers-Kronig Test

The linear Kramers-Kronig test was presented by Boukamp [22]. To conduct a linear Kramers-Kronig test, a model consisting of a large number of series connected RC circuit elements, $n$, is fitted to the data by complex nonlinear least squares minimization. The initial guesses for the time constants of the RC circuit elements used are usually logarithmically spaced and cover the frequency range of the measurement. The residuals between the measured impedance and the equivalent circuit model gives a measure of the adherence of the data to the requirements that needs to be fulfilled for the Kramers-Kronig relations to work and will be referred to as Kramers-Kronig residuals [20, 22].

- **Low residuals** indicate good measurement quality.
- **Randomly distributed residuals** show that a certain measurement noise is present
- **Systematically distributed residuals** can occur if the Kramers-Kronig relations is violated or the number of RC circuit elements used in the linear Kramers-Kronig test was too small.

The linear Kramers-Kronig test is applied to the impedance measurements by fitting seven parallel RC circuit elements (Voigt elements) per decade to the impedance data using a complex non-linear least squares fitting routine in the data analysis software RAVDAV [23]. This software is using Scipy's leastsq() least-squares minimizer, which wraps MINPACK's lmdif (Levenberg-Marquardt) algorithm [24]. The data quality, expressed as the relative Kramers-Kronig test residuals, of impedance measurements on single cells ($16\,cm^2$) are usually in the range of $\pm 0.5\%$ and are considered to be low residuals at DTU Energy Conversion [25, 26].

### 1.4.3 Distribution of Relaxation Times

The distribution of relaxation times (DRT) is a valuable preidentification method that separates the polarization processes with different time constants directly from the impedance data [27, 28, 29, 30]. The DRT method uses the fact that every impedance that obeys the Kramers-Kronig relations can be represented as a differential sum of infinitesimal small RC-elements as illustrated in Figure 1.18. This sum goes from $0$ to $\infty$ [30]. The measured impedance $Z(\omega)$ can be expressed by an integral equation (Equation 1.23) containing the approximated distribution function $\gamma(\tau)$ which satisfies Equation 1.24. $R_s$ represents the ohmic resistance and $R_p$ represents the total polarization resistance as illustrated in Figure 1.12 on page 10.

$$Z(\omega) = R_s + R_p\int_0^\infty \frac{\gamma(\tau)}{1 + j\omega\,\tau}\mathrm{d}\tau \tag{1.23}$$

$$\int_0^\infty \gamma(\tau)\mathrm{d}\tau = 1 \tag{1.24}$$

The expression $\gamma/(1 + j\omega\,\tau)$ specifies the fraction of the overall polarization with relaxation time between $\tau$ and $\tau + \mathrm{d}\tau$. The area under each peak in the DRT equals the polarization resistance of the corresponding loss mechanism [20]. For practical reasons the continous distribution function $\gamma(\tau)$ is approximated by the discrete function in Equation 1.25.

$$Z(\omega) = R_s + R_p\sum_{n=1}^{N}\frac{\gamma_n}{1 + j\omega\,\tau_n} \tag{1.25}$$

DRT has been applied to the impedance measurement data in this work using a complex non-linear least squares fitting routine in the data analysis software RAVDAV [23]. This software is using Scipy's leastsq() least-squares minimizer, which wraps MINPACK's lmdif (Levenberg-Marquardt) algorithm [24].

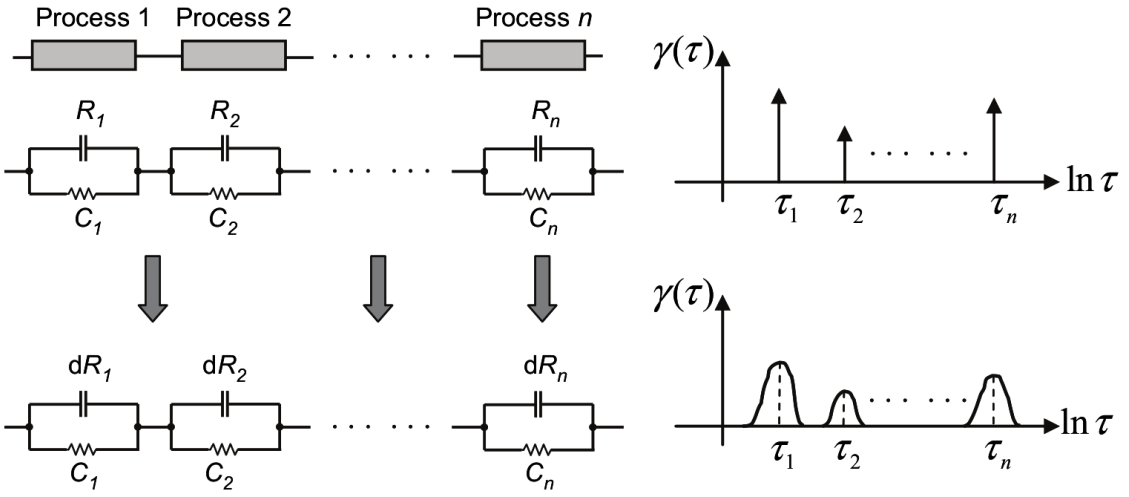


Figure 1.18: Interpretation of EIS data in terms of equivalent circuit models and distribution of relaxation times. From Ref. [30].

### 1.4.4 Impedance measurements on solid oxide fuel cell stacks

Electrochemical Impedance Spectroscopy (EIS) measurements on SOFC stacks are not straightforward due to the high active cell areas and low impedances which makes it difficult to get an error free high frequency response and thereby be able to determine the series resistance, and thus also the polarization resistance of a stack as shown in Figure 1.12 on page 10. Until now only a few research institutions have presented impedance measurements on SOFC stacks with an active cell area above $50\,cm^2$ [31, 32, 33, 34, 35, 36, 37, 38, 39].

Dekker et al. [33] from Energy research Centre of the Netherlands (ECN) conducted EIS measurements of a cell groups of 3 repeating units each in a 30 cell stack with an active area of $81\,cm^2$ and in this way investigated the fuel flow distribution in the SOFC stack.

Lang et al. [31, 32, 34, 35] and Westner et al. [36] from German Aerospace Center (DLR) presented EIS measurements on single repeating units of SOFC short stacks active cell area of $84\,cm^2$ with decent high frequency impedance responses. They divided the loss processes with equivalent circuit modeling, impedance measurements on different cathodes and the dependence on temperature. Ebbesen et al. [37] from Technical University of Denmark presented the impedance response of five repeating units in a Solid Oxide Electrolysis (SOE) stacks (active cell area $\sim 90\,cm^2$) during co-electrolysis (steam and carbon-dioxide) and showed good high frequency response even though they were not able to accurately determine the series resistance at approximately $100\,kHz$ since their equipment was limited to $50\,kHz$. Schefold et al. [38] from European Institute for Energy Research (EIFER) presented impedance measurements of three repeating units in a 5 cell SOE stack (active cell area $\sim 100\,cm^2$) operating in water electrolysis. The impedance measurements were subject to noise at low frequencies and did not catch series resistance at high frequencies. Comminges et al. [39] presented impedance measurements of 5 repeating units in a 5-cell SOFC stack supplied by HTceramix/SOFCpower with an active cell area of $50\,cm^2$. The 5-cell SOFC stack was tested during $10,000\,h$ operation in a hydrogen, carbon-dioxide, steam mixture. The impedance spectra recorded by Comminges et al. [39] was able to intersect with the real axis though the high frequency impedance response for the different repeating units did not show the same trend.

This review presented some of the challenges with the high frequency impedance response of SOFC stack with active cell areas larger than $50\,cm^2$. This thesis will continue the work on improving high frequency impedance response on SOFC stacks with large active cell areas.

## 1.5 Goal of this Thesis

The overall goal of the work behind thesis is to develop advanced techniques for electrochemical characterization and diagnoses of Solid Oxide Fuel Cell (SOFC) stacks with focus on Electrochemical Impedance Spectroscopy (EIS) and Total Harmonic Distortion (THD) with the aim to improve measurement geometries, measurement setups, measurement time, parameter identification and tracking of evolving parameters.

The combination of advanced (Electrochemical Impedance Spectroscopy) and simple (Total Harmonic Distortion) electrochemical characterization techniques for SOFC stacks gives the possibilities to track activation and degradation and their sources in SOFC stacks in the research and development departments of the SOFC stack suppliers and as an on-line diagnostic tool during operation of SOFC systems at the end user. These techniques, in particular EIS, can also yield valuable input for further development of SOFC stack technology.

## 1.6 Outline

**Chapter 2** gives a detailed description of the electrical considerations needed for improving SOFC stack electrochemical impedance measurements. Optimization of the SOFC stack measurement geometry and measurement setups for electrochemical impedance spectroscopy are presented as well.

**Chapter 3** gives a description of the experimental test rig and a sequential impedance measurement setup for a cross-flow stack and a parallel impedance measurement setup for a co-flow stack.

**Chapter 4** is focused on stack degradation monitoring using electrochemical impedance spectroscopy. It is divided into two parts. The first part is about cathode related time dependent performance changes of a 13-cell stack each with different types of protective coatings on the metallic interconnects. The stack was operated for $2500$ hours. The second part is about anode related time dependent degradation and focuses on the results of a test of a 14-cell experimental stack for $667$ hours of operation . The latter degradation test was carried out with a high steam content in the fuel.

**Chapter 5** is revolving around the use of electrochemical impedance spectroscopy on SOFC stacks for detection of minor differences in the fuel flow rate at the individual cells in a stack, an aspect which is of vital importance when operating a stack at high fuel utilizations. The distribution of fuel flow rates in a stack, derived from the measured gas conversion impedance, is presented and existing gas conversion impedance models are compared with the measured gas conversion impedance.

**Chapter 6** focuses on fuel starvation detection from the stack sum voltage using total harmonic distortion (THD). It offers simple system monitoring which could reduce the cost of the fuel cell control system. An experimental study of THD as a function of AC amplitude, frequency, and fuel utilization is presented, and the potential of the technique for system monitoring is discussed.

**Chapter 7** summarizes the thesis with a general discussion on the results presented throughout the report. It stresses the most important conclusions in the context of how Solid Oxide Fuel Cell stack diagnostics and finally comments on how the research of this topic could be continued.

## 1.7 List of included publications

**A** *Detailed electrochemical characterisation of large SOFC stacks*
Rasmus Rode Mosbæk, Johan Hjelm, Rasmus Barfod, Jens Høgh and Peter Vang Hendriksen
B1006, Conference proceeding for the 10th European SOFC Forum, 26-29 June 2012, Lucerne, Switzerland. See page 131.

**B** *Electrochemical Characterization and Degradation Analysis of Large SOFC stacks by impedance spectroscopy*
Rasmus Rode Mosbæk, Johan Hjelm, Rasmus Barfod, Jens Høgh and Peter Vang Hendriksen
FUEL CELLS 13, 2013, No. 4, 605-611. See page 143.

**C** *Fuel flow distribution in SOFC stacks revealed by impedance spectroscopy*
Rasmus Rode Mosbæk, Johan Hjelm, Rasmus Barfod and Peter Vang Hendriksen
A0902, Conference proceeding for the 11th European SOFC and SOE Forum, 1-4 July 2014, Lucerne, Switzerland. See page 152.

CHAPTER 2

# Improving the stack impedance response

The challenge of using Electrochemical Impedance Spectroscopy (EIS) on large area SOFCs is, from a measurement perspective, that the impedance of the cells is very small. When the cell resistances decreases the AC cell voltage response decreases respectively, which increases the influence of electrical noise and stray impedances. This chapter addresses the experimental challenges when going from small area to large area SOFCs. It also covers cable and signal configurations which needs to be considered when using EIS on SOFC stacks. Two automated EIS measurement setups for SOFC stacks developed in this PhD study are described as well as how to improve the stack measurement geometry on SOFC stacks when using EIS.

This chapter consists of four parts. The first part introduces the scaling effect when going from small SOFC cell areas to large cell areas and its decrease in resistance which makes EIS challenging. The second part introduces electrical considerations needed for low impedance measurements on SOFC stacks. The third part describes the EIS equipment and measurement setups and its modifications for making EIS on large area SOFC stacks. The fourth part describes the optimization of the stack measurement geometry for reducing the systematic errors of the impedance response from SOFC stacks.

## 2.1 EIS on SOFCs - A matter of Scale

One of the big challenges when performing Electrochemical Impedance Spectroscopy on SOFCs is that the measured resistance of the fuel cell decreases dramatically when going to larger cell areas. When the resistance decreases the voltage response will consequently decrease when running galvanostatic mode at fixed current. This challenge can be explained in the simplest case by having a piece of resistive material with electrical contacts on both ends as illustrated in Figure 2.1. The resistive material has a length, $l$, and a cross-sectional area, $A$. The resistance of the given material is given by Equation 2.1. The resistance measured over a piece of material will increase with the length, but decrease with increasing cross-sectional area [40].

$$R = \rho \frac{l}{A} \tag{2.1}$$

Figure 2.2 shows an illustration of three different SOFC sizes. A symmetrical cell, a single cell and a stack. Ebbehøj et al. [41] measured a symmetrical anode cell (Ni-YSZ/YSZ/Ni-YSZ). The area of the symmetrical cell was $\sim 0.36\,cm^2$ and the absolute series resistance was $228\,m\Omega$ measured at $1\,MHz$. Barfod et al. [42] measured at single cell (Ni-YSZ/YSZ/LSM-YSZ). The

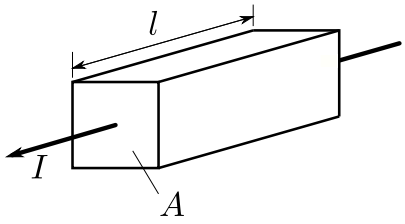


Figure 2.1: A uniform conductor of length, $l$, and cross-sectional area $A$, with a current, $I$,flowing through the conductor.

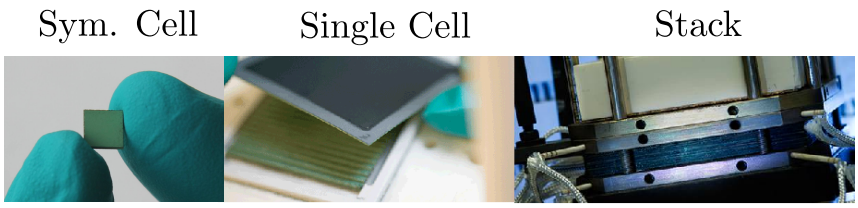


Figure 2.2: Illustration of a symmetrical cell, single cell and a stack. Pictures from DTU Energy Conversion.

| | Sym. Cells | Single Cells | RU cell in a Stacks |
|---|---|---|---|
| Area | $\sim 0.36\,cm^2$ | $\sim 16\,cm^2$ | $\sim 90\,cm^2$ |
| Temperature | $750°C$ | $700°C$ | $750°C$ |
| Rel. series resistance, $R_s$ | $0.08\,\Omega\,cm^2$@$1\,MHz$ | $0.2\,\Omega\,cm^2$@$100kHz$ | $0.2\,\Omega\,cm^2$@$100kHz$ |
| **Abs. series resistance,** $\lvert R_s \rvert$ | $228\,m\Omega$ @ $1\,MHz$ | $12m\Omega$@$100kHz$ | $3\,m\Omega$ @ $100\,kHz$ |
| Reference | [41] | [42] | Paper A.2 on page 143 |
| $V$ @ $60\,mA$ from $\lvert R_s \rvert$ | $14\,mV$ | $720\,\mu V$ | $180\,\mu V$ |

Table 2.1: Overview of absolute series resistance for different sizes of SOFCs.

area of the single cell was $\sim 16\,cm^2$ and the absolute series resistance was $12\,m\Omega$ measured at $100\,kHz$. In paper A.2 on page 143 a repeating unit cell (Ni-YSZ/YSZ/LSM-YSZ) in a stack was measured. The area of the cells in the stack was $\sim 90\,cm^2$ and the absolute series resistance was $3\,m\Omega$ measured at $100\,kHz$.

The absolute impedance for the three different sizes is compared in Table 2.1 with references. The cells in all three references has a approximately the same electrolyte thickness. The single cell is measured at $50°C$ lower temperature which will give rise to a slightly higher resistance than if it was measured at $750°C$. The last line of Table 2.1 voltage response of the three different types of cells if the amplitude was $60\,mA$ (Maximum amplitude for Solartron 1260). This shows that the voltage response will decrease significantly when going to larger cell areas which will also lower the signal to noise ratio significantly, due to an increased influence of stray impedances.

## 2.2 Electrical Considerations

This section describes relevant electrical considerations which needs to be taken into account when performing low impedance measurements. It starts with explaining the electromagnetic considerations such as magnetic flux, mutual and self inductance, skin and proximity effects. Definitions of noise and signals, and different relevant cable configurations are given as well.

### 2.2.1 Electromagnetic Considerations

An AC current is imposed on the fuel cell under test when performing electrochemical impedance spectroscopy. The AC current in a given conductor induce a magnetic field in the conductor and adjacent conductors. The time-varying magnetic field leads to an increased inductance and resistance in the conductors. For a single conductor the self-induced magnetic field leads to an increased inductance called self-inductance and an increased resistance described by the skin effect. For two adjacent conductors the current in one conductor induces magnetic flux in the adjacent conductor. This leads to an increased inductance called mutual inductance and an increased resistance described by the proximity effect.[1]

More information about electromagnetic fields and its related effects can be found in the following references [40, 43, 44, 45].

[1]This section was also a part of the unpublished master thesis "Investigation of the high frequency response from large solid oxide fuel cell stacks on model systems" written by the author.

#### 2.2.1.1 Magnetic flux

The magnetic flux, $\Phi_B\,[Wb]$, is the normal component of the magnetic field, $\vec{B}\,\left[\frac{Wb}{m^2}\right]$, passing through a surface. The contribution to a magnetic field due to a differential length of the current $I\,d\vec{s}$. At a distance $r$ given by the direction vector, $\vec{a}_r$, the differential contribution to the magnetic flux density vector, $\vec{B}\,\left[\frac{Wb}{m^2}\right]$, is given by the Biot-Savart law given in Equation 2.2. An illustration of the Biot-Savart law can be seen in Figure 2.3. The direction of the resulting flux density vector is perpendicular to the plane with a current element and a direction vector according to the right-hand-rule [43].

$$d\vec{B} \;=\; \frac{\mu_0\,I}{4\,\pi}\frac{d\vec{s}\times\vec{a}_r}{r^2} \tag{2.2}$$

For a given magnetic field $\vec{B}\,\left[\frac{Wb}{m^2}\right]$ the magnetic flux through an area $d\vec{A}\,[m^2]$ where $d\vec{A}$ is a vector perpendicular to the surface and has a magnitude equal to the area $dA$. The total magnetic flux $\Phi_B\,[Wb]$ is given by Equation 2.3. For a uniform magnetic field $\vec{B}\,\left[\frac{Wb}{m^2}\right]$ that makes an angle $\theta$ with the $d\vec{A}$ the magnetic flux through the plane is given by Equation 2.4.

$$\Phi_B \;=\; \int \vec{B}\cdot d\vec{A} \tag{2.3}$$

$$\Phi_B \;=\; B\,A\,\cos(\theta) \tag{2.4}$$

When the magnetic field $B$ is parallel to the plane surface as illustrated in Figure 2.4 a), the angle between the magnetic field $B$ and the vector $d\vec{A}$ is $\theta = 90°$. The induced magnetic flux is then $\Phi_B = 0$. For a magnetic field perpendicular to the plane as illustrated in Figure 2.4 b), the angle between the magnetic field $B$ and the vector $d\vec{A}$ is $\theta = 0°$ and the induced magnetic flux is then $\Phi_B = B\,A$ [40]. When relating the magnetic flux to any given measurement setup, it is important that current conducting wires are perpendicular to wires for voltage measurements to prevent induced magnetic flux. The induced magnetic flux will genrate an electromotive force in an adjacent conductor given by the mutual inductance.

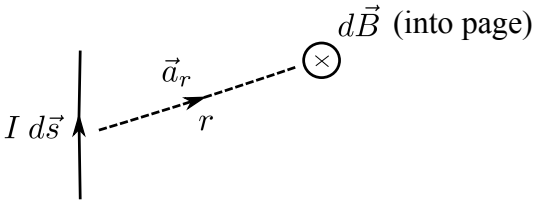


Figure 2.3: Illustration of the Biot-Savart law for determining the magnetic field vector $d\vec{B}$. Adapted from Ref. [40].

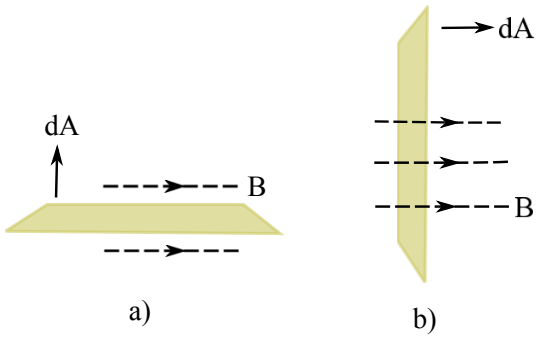


Figure 2.4: Magnetic flux through a plane. a) When the magnetic field is parallel to the plane the magnetic flux is zero. b) When the magnetic flux is perpendicular to the plane the magnetic flux is at maximum. Adapted from Ref. [40].

#### 2.2.1.2 Mutual inductance

The magnetic flux through a closed circuit varies with time if the currents in nearby circuits varies with time. This induces an electromotive force (EMF) in the closed circuit through a process called

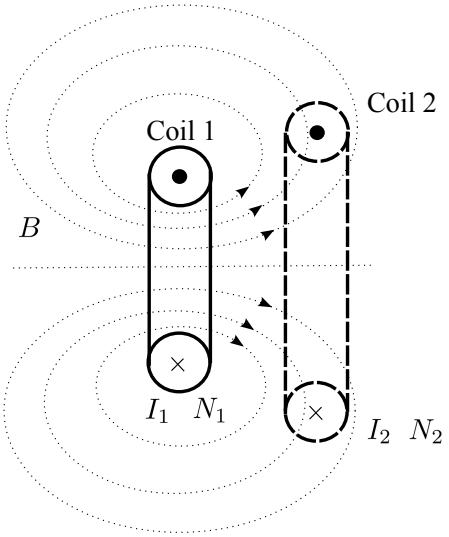


Figure 2.5: Illustration of mutual inductance. A cross sectional view of two adjacent coils. The current in coil 1 generate a magnetic field and some of the field lines passes through coil 2. Adapted from Ref. [40].

mutual induction. Two closely wound coils of wire are shown in Figure 2.5. The current $I_1$ in Coil 1 with $N_1$ turns creates a magnetic field $B$. Some of the magnetic field lines caused by the current in coil 1 passes through coil 2 with $N_2$ turns. These magnetic field lines are represented by the magnetic flux $\Phi_{B,12}$. The mutual inductance with respect to coil 1, $M_{12}\,[H]$, is defined by Equation 2.5 [40].

$$M_{12} \equiv \frac{N_2\,\Phi_{B,12}}{I_1} \tag{2.5}$$

The electromotive force induced in coil 2, $e_2\,[V]$ is given by the time varying current in coil 1, $I_1\,[A]$, and the mutual inductance, $M_{12}\,[H]$ shown in Equation 2.6.

$$e_2 = -M_{12}\,\frac{dI_1}{dt} \tag{2.6}$$

The mutual inductance and the induced EMF is important to keep in mind when setting up measurements. A wire conducting a time-varying current induces EMF in a nearby wire for voltage measurements. This has an influence on the voltage measured using these wires.

#### 2.2.1.3 Self-inductance in a straight wire

The self-inductance is a special case of mutual inductance and is caused by a self-induced magnetic flux. When the current, $I\,[A]$, in the wire changes with time, an electromotive force, $e_L\,[V]$, is generated in the wire as described by Equation 2.7 where $L\,[H]$ is the self-inductance.

$$e_L = -L\frac{dI}{dt} \tag{2.7}$$

The magnetic flux generates eddy currents in the conductors as well. When the frequency increases the magnetic flux will fluctuate more, resulting in larger eddy currents. This leads to an increased resistance in the conductors described by the so called skin effect and the proximity effect.

#### 2.2.1.4 Skin effect

Magnetic flux induces eddy currents in a AC current conducting wire. Eddy currents can lead to resistances significantly higher than the value predicted due to a decreased utilization of the cross-sectional area of the conductor. Figure 2.6 illustrates an AC current $i(t)\,[A]$ through a wire. The current induces a magnetic flux $\Phi_B(t)\,[Wb]$ with circular flux lines around the current. The magnetic flux induces eddy currents in the wire. The eddy currents oppose the current $i(t)\,[A]$ in the middle of the conductor and increase the current at the surface of the conductor as shown in Figure 2.7. The current density is exponentially decaying as a function of distance into the conductor with the characteristic length $\delta\,[m]$ called skin depth. The skin depth $\delta\,[m]$ is given by Equation 2.8 and is a function of frequency, $f\,[Hz]$, and the resistivity of the material, $\rho\,[\Omega\,m]$ [44]. $\mu\,[\frac{H}{m}]$ is the permeability of the material (the measure of the ability of a material to support the formation of a magnetic field within itself) given by $\mu = \mu_r\,\mu_0$ where $\mu_r\,[-]$ is the relative permeability of the material and $\mu_0$ is the permeability of free space given by $\mu_0 = 4\,\pi \cdot 10^{-7}\frac{H}{m}$ [40].

$$\delta = \sqrt{\frac{\rho}{\pi\,\mu\,f}} \tag{2.8}$$

For a round single wire far away from the return conductor the skin effect resistance is given by Equation 2.9, where $R_{DC}\,[\Omega]$ is the DC resistance. The dimensionless variable $\xi\,[-]$ is given by Equation 2.10 where $d\,[m]$ is the diameter of the wire and $\delta\,[m]$ is the skin depth [46].

$$R_{skin} = \frac{R_{DC}\,\xi}{2}\,\frac{\sinh\,\xi + \sin\,\xi}{\cosh\,\xi - \cos\,\xi} \tag{2.9}$$

$$\xi = \frac{\sqrt{\pi}}{2}\,\frac{d}{\delta} \tag{2.10}$$

The equivalent circuit of a straight wire influenced by skin effect and self inductance is illustrated in Figure 2.8. To show an example of skin effect and self-inductance for a wire with circular cross section. The impedance of a copper wire with a diameter of $d = 2.5\,mm$ and a length of $l = 20\,mm$ was measured. The real and imaginary impedance as a function of frequency for the copper wire with circular cross section are shown in Figure 2.9.

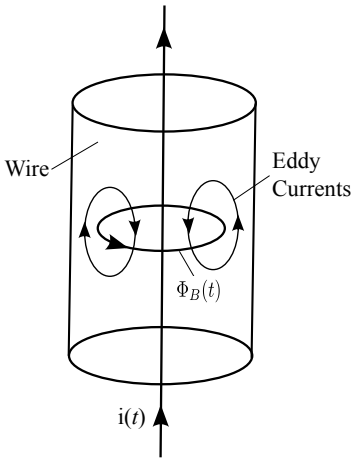


Figure 2.6: The current $i(t)$ induces flux $\Phi(t)$ which generates eddy currents. Adapted from Ref. [44].

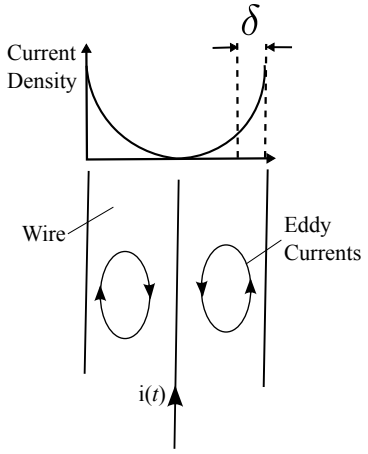


Figure 2.7: The eddy currents oppose the current $i(t)$ in the middle of the conductor and increase the current on the surface of the conductor described by the skin depth $\delta\,[m]$. Adapted from Ref. [44].


Figure 2.8: Equivalent circuit of a straight wire influenced by skin effect and self-inductance.

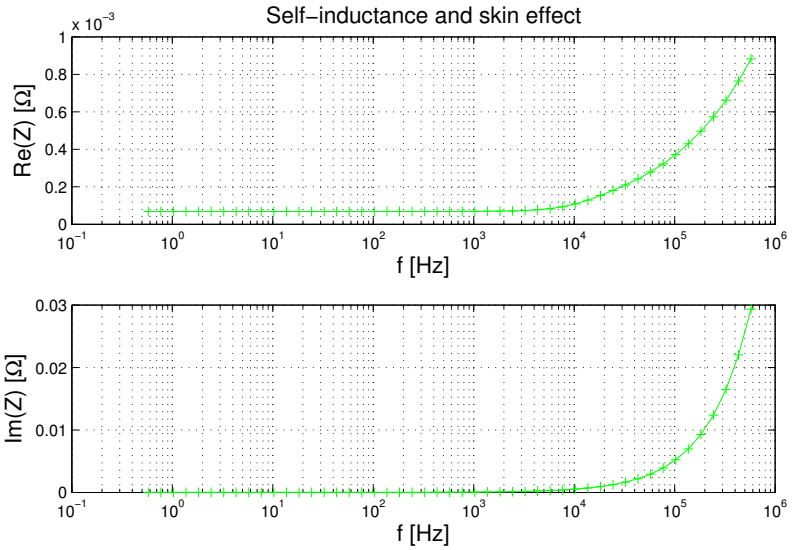


Figure 2.9: Real and imaginary impedance as a function of frequency for a round copper wire with a diameter of $d = 2.5\,mm$ and a length of $l = 20\,mm$.

#### 2.2.1.5 Proximity effect

The magnetic flux through a closed circuit varies with time because of time varying currents in nearby circuits. The time-varying magnetic flux will generate local eddy currents in the conductor. Due to eddy currents, the overall current distribution will be constrained to smaller regions. If two parallel AC current conductors are closely spaced the conductors will experience a higher magnetic flux compared to a single wire since the conductors will experience the magnetic flux generated within itself (explained in Section 2.2.1.4) and the magnetic flux from the adjacent conductor. The increased magnetic flux will increase the extent of eddy currents. This effect is called proximity effect.

An illustration of the proximity effect can be seen in Figure 2.10. For the skin effect explained in the previous section the current distribution was constrained to a smaller region described by the distance $\delta\,[m]$ due to self-induced magnetic flux. The current distribution is illustrated by the gray area. For two adjacent conductors carrying an AC current in the same direction the induced magnetic flux, which also leads to mutual inductance, cause the current distribution to be constrained to the surface of the conductor far from each other. For two adjacent conductors carrying an AC current in the opposite direction the induced magnetic flux causes the current distribution to be constrained at the surface of the conductor close to each other.

When the frequency increases, the magnetic flux increases resulting in larger eddy currents. Larger eddy currents cause stronger proximity effects and thereby an increased resistance [45]. For a wire with circular cross section influenced by proximity effect and mutual-inductance has the same characteristics as skin effect and self-inductance shown in Figure 2.9 though the increase in real impedance and imaginary impedance with increasing frequency would be higher.

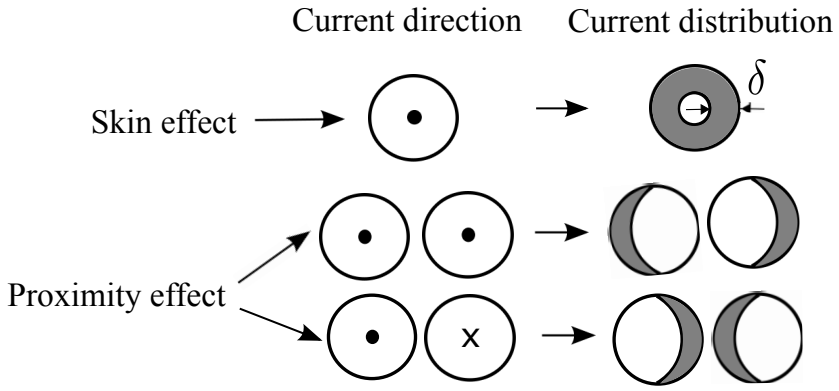


Figure 2.10: Current direction: Dot is out of the plan and x is into the plane. Current distribution: utilized area marked gray, ineffective area marked white. The skin effect is described by the skin depth, $\delta\,[m]$. For to adjacent conductors the utilized area is further reduced. Adapted from Ref. [45].

### 2.2.2 Noise and Signals

This section explains and defines signals and cable configurations relevant to consider when applying electrochemical impedance spectroscopy to any electrochemical cell. This includes the definitions of signal to noise ratio and total harmonic distortion. Different cable configurations are explained for canceling electromagnetic noise. Different signal-modes are defined which are of relevance for accurate measurements with frequency response analyzers.

#### 2.2.2.1 Explaining noise and signals

Consider a sinusoidal signal of a given frequency as the original signal in Figure 2.11 (A). If there is nonlinearities in the system, higher harmonics will be generated as an integer multiple of the fundamental frequency, $f$, of the original signal. The harmonic frequencies are $2f$, $3f$, $4f$ etc. Nonlinearities can occur in fuel cell during fuel or air starvation due to an increase in concentration losses which result in a nonlinear polarization losses in the current voltage characteristics. The original signal and the 2nd, 3rd and 4th harmonics of the original signal is shown in Figure 2.11 (B) and the sum of the original signal and the 2nd, 3rd and 4th harmonics in Figure 2.11 (C). Electrical noise is unavoidable in electronic devices. Typical electrical noise includes noise generated from switch-mode power supplies, microprocessor clocks and contact switching [47], as well as thermal noise from a resistor or shot noise from diodes [48]. Figure 2.11 (D) illustrates electrical noise from three different sources. The sum of the electrical noise from the three different sources is shown in Figure 2.11 (E). Static (random) noise is atmospheric noise cause by natural atmospheric processes, primarily lightning discharges.[2] Static noise is illustrated in Figure 2.11 (F). The sum of the original signal, its harmonics (C) and the static noise (F) is given in Figure 2.11 (G). The sum of the original signal and its harmonics (C), the static noise (F) and the electrical noise from the three sources (E) is given in Figure 2.11 (H). By applying Fast Fourier transform, FFT, on the recorded signal (H) one can convert the signal from the time to the frequency domain and vice versa. Fast Fourier Transform, FFT, is an algorithm based on Discrete Fourier Transform developed by Cooley and Tukey [50]. Figure 2.11 (I) shows the FFT of the recorded signal. Here the frequency components from the signals and the static noise are visible. A zoom of the FFT spectrum in Figure 2.11 (J) reveals the frequency components from the original signal, its harmonics and the three electrical noise sources.

[2] According to National Oceanic and Atmospheric Administration, USA the global lightning flash frequency is on the order of 40 flashes per second [49].

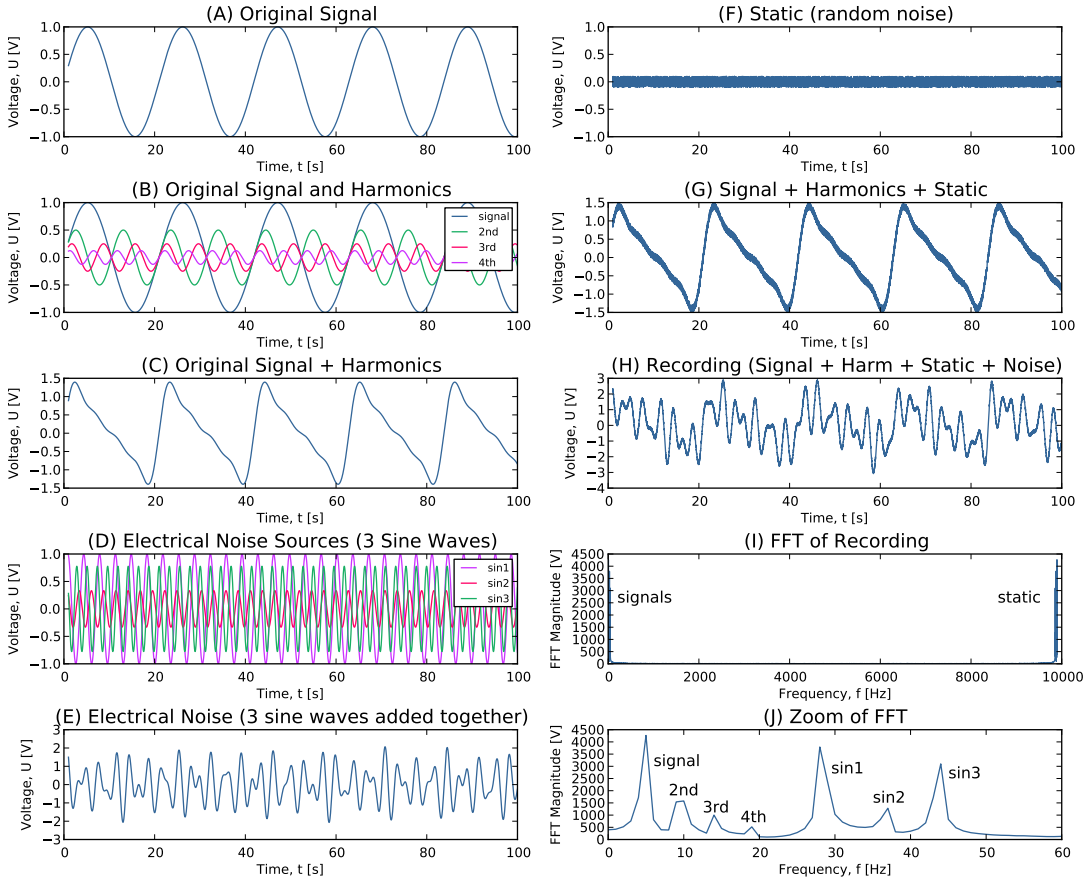


Figure 2.11: Illustration of signal, harmonics, electrical noise and static noise. **(A)** Original signal. **(B)** Original signal (A) and 2nd, 3rd and 4th harmonics. **(C)** Original signal (A) and harmonics (B) added together. **(D)** Some electrical noise. 3 sine waves of different amplitudes and frequencies. **(E)** Electrical noise. 3 sine waves added together from (D). **(F)** Static random noise. **(G)** Signal plus harmonics (C) plus static (F). **(H)** Signal plus harmonics (C) plus static (F) plus electrical noise (E). **(I)** Total FFT. **(J)** Zoom of total FFT. Adapted from Ref. [51].

#### 2.2.2.2 Definition of signal to noise ratio and total harmonic distortion

The signal-to-noise ratio, SNR, is the ratio between input signal, $U_{Signal}$ $[V]$ (Example in Figure 2.11 (A)). and the noise level, $U_{Noise}$ $[V]$ (Example in Figure 2.11 (E) and (F)), given by Equation 2.11 [52]. It is important to point out that the signal harmonics (Example in Figure 2.11 (B)) needs to be excluded from the calculation of SNR, leaving only the noise term [53].

$$SNR = \frac{U_{Signal}}{U_{Noise}} \tag{2.11}$$

*Total harmonic distortion* (THD) is the ratio of the root-mean-square, RMS, of the waveform not included the fundamental, to the RMS amplitude of the fundamental frequency (signal), $U_1 = U_S$ (Example illustrated in Figure 2.11 (B)). The THD $[-]$ is given in Equation 2.12 [44].

$$THD = \frac{\sqrt{\sum_{n=2}^{\infty} U_n^2}}{U_1} \tag{2.12}$$

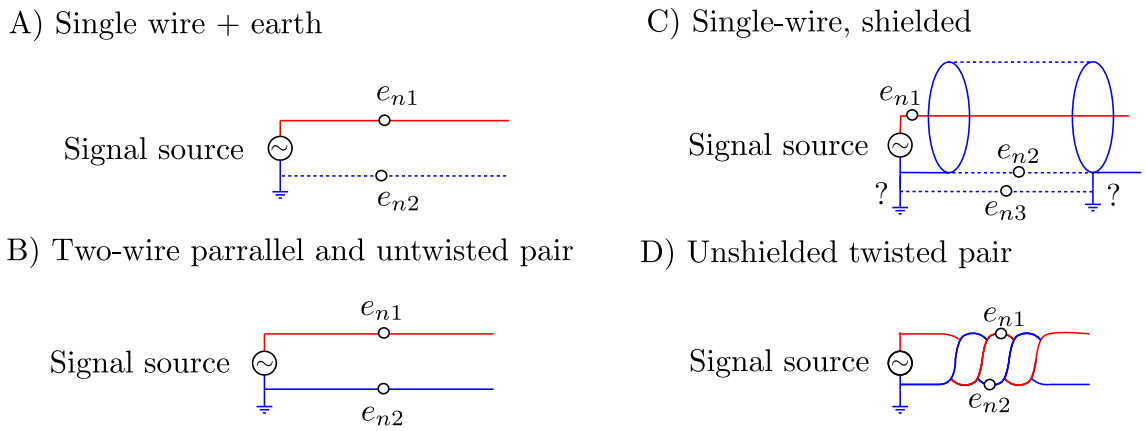


Figure 2.12: Cable configurations and locations of possible noise sources. Adapted from Ref. [55].

#### 2.2.2.3 Cable configurations

Selecting the right cable configuration is of high importance for impedance measurements since the cables transfers the sensitive low voltage signal from the repeating unit of the stack to the measurement device (frequency response analyzer or potentiostat). Impedance measurements can be divided into three groups: **Standard impedance measurements** ($1\,\Omega$ to $100\,M\Omega$) where single- wire shielded cables are recommended. **High impedance measurements** ($100\,M\Omega$ and higher) here special equipment and a Faraday cage (surrounding the device under test connected to shield of the equipment) is needed . For high impedance measurements stray capacitances needs to be considered carefully [54].

For **low impedance measurement** setups (less than $1\,\Omega$) mutual inductance needs to be considered carefully. Unshielded twisted paired wires are recommended for low impedance measurements since they reduces the mutual inductance [54]. For all cable configurations the following is always valid: the shorter the cables the better the quality of the measurements .

Mutual inductance (explained in Section 2.2.1.2 on page 19) in signals are generated from surrounding magnetic fields and changes the measured voltage by the electromotive force, $e_n$. Figure 2.12 illustrates different cable configurations and locations of possible noise sources. In this case the signal source could be the AC voltage response from a cell in a SOFC stack during an electrochemical impedance measurement.

For a single wire plus ground given in Figure 2.12 A) the signal return route is through earth [3]. The measurement device must be insensitive to the electromotive force generated in the signal conducting cable, $e_{n1}$, and the earth conducting cable $e_{n2}$ when using this cable configuration. Two parallel and untwisted paired wire shown in Figure 2.12 B), $e_{n1}$and $e_{n2}$ will partially cancel out if the lines are parallel and closely spaced. Single shielded wires shown in Figure 2.12 C) A copper shield is ineffective for mutual inductance (inductive coupled noise). The electromotive force $e_{n1}$ is insignificant if the inductive coupling is absent [55]. Shielded cables will increase the parasitic capacitance, but decreases the coupling capacitance (relevant for normal and high impedance measurements [54]). $e_{n3}$ is noise induced in conduction of electrical currents in the external ground path if both ends are grounded. If a potentiostat has an active current-driven shield[4] then the shield of single shielded wire should only be connected potentiostat. Unshielded twisted pair cables shown in Figure 2.12 D) makes $e_{n1}$and $e_{n2}$ equal in phase and amplitude and reduce the mutual inductance significantly in low impedance measurements ($< 1\Omega$). Each straight (untwisted) piece of cable of a few centimeters in length is long enough to produce a magnetic field interfering with the signals [55, 54].

[3] Also known as ground or common and refers to the reference point in an electrical circuit from which the voltage is measured.

[4] A current-driven shield carrying an equal and opposite current to reduce generated noise by reducing the magnetic field around the conductor [56].

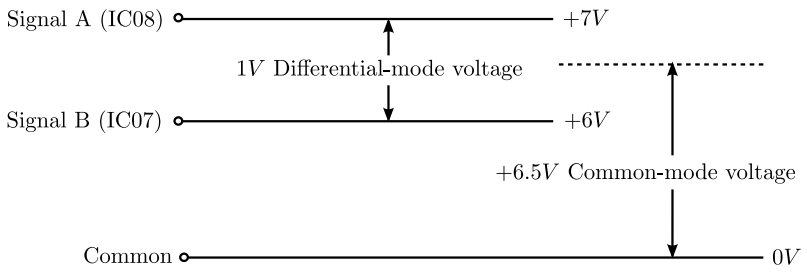


Figure 2.13: Common and differential mode signals explained for a SOFC stack measurement. Adapted from Ref. [55].

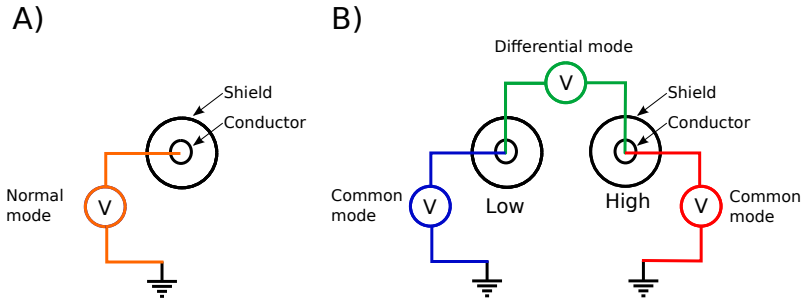


Figure 2.14: Illustration of a normal mode signal A), and differential and common mode signals B) for a single wire shielded cable configuration.

#### 2.2.2.4 Signal-mode definitions on frequency response analyzers

Understanding the different signal modes is relevant for optimizing the measurement accuracy of the frequency response analyzers explained in the next section. This section describes the three relevant signal-modes.

A **normal-mode signal** is any type of signal (other than common mode) that appears between a pair of wires, or on a single wire referenced to (or returned through) the earth, ground, common or shield. Signal A and signal B in Figure 2.13 are normal-mode signals with respect to common.

A **differential-mode signal** appears differentially on a pair of wires in an ungrounded cable configuration. The voltage between signal A and signal B in Figure 2.13 is a differential-mode voltage.

A **common-mode voltage** appears equally (with respect to local circuit common) on both lines of a 2-wire cable not connected to earth, shield or local common. Usually, but not always, this is an unwanted signal that should be rejected by the receiving circuit. The common-mode voltage, $U_{CM}$, is expressed mathematically by Equation 2.13 as the average of the two signal voltages with respect to local ground or common.

$$U_{CM} = \frac{U_A + U_B}{2} \tag{2.13}$$

The common-mode voltage can be AC, DC, or a combination of AC and DC. Figure 2.13 represents the simplest case where the DC common-mode voltage for signal A and signal B is $6.5\,V$ with no AC component [55]. Figure 2.14 A) illustrate a normal mode signal and Figure 2.14 B) illustrate a differential mode signal and common mode signals for a single wire shielded cable configuration.

### 2.2.3 Conclusion on electrical considerations

Electrical and electromagnetic considerations relevant for low impedance measurements were discussed. To minimize errors by the induced magnetic flux from the magnetic field is most easily ensured by requiring that current conducting wires are placed perpendicular to the wires

| Analyzer | | Frequency | | Excitation Signal | | Input | | CMR | Ref. |
|---|---|---|---|---|---|---|---|---|---|
| | | Min | Max | Volt. | Current | Volt. | Res. | | |
| Solartron | 1260 | $10\,\mu$Hz | $32\,MHz$ | $0$ to $3\,V$ | $0$ to $60\,mA$ | $30\,mV$ to $300\,mV$ to $3\,V$ | $1\,\mu$V to $10\,\mu$V to $100\,\mu$V | $5\,V$ | [57] |
| | 1255B | $10\,\mu Hz$ | $1\,MHz$ | $0$ to $3\,V$ | N/A | $30\,mV$ to $300\,mV$ to $3\,V$ | $1\,\mu$V to $10\,\mu$V to $100\,\mu$V | $5\,V$ | [58] |
| Zahner | IM6 | $10\,\mu Hz$ | $8\,MHz$ | $1\,mV$ to $1\,V$ | $\pm 3\,A$ | $\pm 1\,V$ to $\pm 2\,V$ to $\pm 4\,V$ | $7.8\,\mu$V to $15.6\,\mu$V to $31.3\,\mu$V | $100\,V$ | [59] |

Table 2.2: Overview of key specifications of the three FRAs used in this work.

for voltage measurements. Magnetic flux generates mutual and self inductance in wires resulting in skin and proximity effects which increases the measured real and imaginary impedance. The effect of different noise sources was discussed together with a discussion of cable configurations that could limit the induced mutual inductance for low impedance measurements. Furthermore, this section described three signal-modes (normal-mode, differential-mode and common-mode) relevant for optimizing the measurement accuracy for low impedance SOFC stack measurements using frequency response analyzers as described in the next Section.

## 2.3 Measurement Equipment and Modifications

This section describes the different frequency response analyzers and the measurements setups used in this work. Two overall measurement setups are described. One impedance measurement setup with sequential acquisition and one impedance measurement setup with parallel acquisition. It explains optimizations of the setups for improving measurement accuracy and acquisition time. This includes current transducers for current measurements, DC and common mode cancellation circuits as well as automation of the recording of impedance measurements.

### 2.3.1 Frequency Response Analyzers

Frequency response analyzers (FRA) measure the real and imaginary impedance response characteristics with respect to frequency of the device under test, by applying a frequency swept sine wave to it and examining its response signal. In this section, the FRAs used for this work are presented together with their characteristics. An overview of the important equipment characteristics is shown in Table 2.2. The information is taken from the specifications published by the manufactures of the devices.

#### 2.3.1.1 Solartron 1260

The *Solartron 1260* shown in Figure 2.15 is a widely used FRA and has been produced in the current configuration for decades. It has a very large frequency range. However, the maximum current excitation signal is limited to $I_{RMS} = 60\,mA$. If a higher current excitation signal needs to be connected to a booster (current amplifier) as explained in Section 2.3.2.1 on page 29. The input voltage ranges are $30\,mV$, $300\,mV$ and $3\,V$. For the best measurement accuracy possible the $30\,mV$ range should be used in the complete measurement sequence. This can be done by help of a DC cancellation circuit as explained in Section 2.3.2.3. The common mode rejection (CMR) voltage of the Solartron 1260 is $5\,V$ in all the ranges. This means that a signals with common mode voltages higher than $5\,V$ are rejected which limits impedance measurements to the first four repeating units in a SOFC stack at open circuit voltage. This is an issue when measuring on SOFC stacks greater than 5 cells. Section 2.3.2.4 on page 33 describes the design of a common-mode cancellation circuit that removes the common-mode voltage.

#### 2.3.1.2 Solartron 1255B

The *Solartron 1255B* is also applied in this work and is almost identical to the *Solartron 1260* except that it has no generator for current excitation signals and there is no hardware user interface on the front panel of the device as shown in Figure 2.16 . The maximum frequency is limited to $1\,MHz$ as shown in Table 2.2.

Figure 2.15: Solartron 1260.

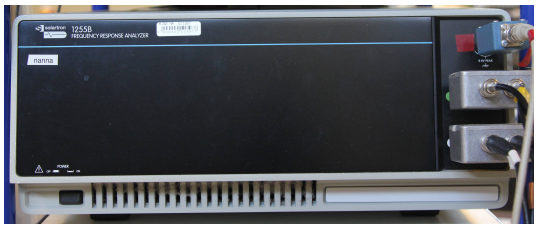

Figure 2.16: Solartron 1255B.

#### 2.3.1.3 Zahner IM6

The *Zahner IM6* shown in Figure 2.17 is also a widely used FRA and a full potentiostat/galvonostat. It can handle similar frequency ranges as the *Solartron 1260* as shown in Table 2.2, but can provide a larger current excitation signal of $\hat{I} = 3\,A$. Control is provided via the *Thales* software package. The *Zahner IM6* has active driven shields. This means, that the device tries to reproduce the measurement signal on the shields, in order to minimize stray capacitance in the cables (relevant for high impedance measurements). To avoid damage in the active driven shields, the shields must not be connected to ground or the cell [54]. The main channel with active driven shield is not used in this work. Instead twisted paired wires connected to the *Zahner PAD4* add-on cards are used.

#### PAD4

The *Zahner IM6* can be extended with up to four *Zahner PAD4* add-on cards which are 4-channel synchronous A/D converters which makes the *Zahner IM6* able to measure the impedance on up to 17 differential signals in parallel. Each channel on the *Zahner PAD4* add-on cards has a common mode rejection voltage of $100\,V$ which makes the *Zahner IM6* able to do impedance on stacks with a large number of cells without the use of external circuitry to cancel the common mode voltage. The four *Zahner PAD4* add-on cards are shown on the *Zahner IM6* in Figure 2.17 where the green and blue twisted paired wires are connected.

#### EL1000

With an additional *Zahner EL1000* electronic load shown in Figure 2.18 the *Zahner IM6* can excite a fuel cell stack with a peak AC current up to $3\,A$ and $100\,kHz$ on top of a DC current up to $50\,A$. The EL1000 makes the IM6 suitable for impedance measurements under higher loads.

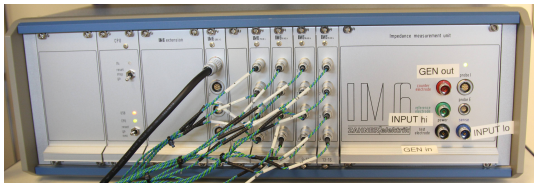


Figure 2.17: Zahner IM6 with 4xPAD4 extension cards.


Figure 2.18: Zahner EL1000.

### 2.3.2 Sequential Measurement Setup for EIS on SOFC stacks

An illustration of the test set-up when using a *Solartron* FRAs is shown in Figure 2.19. The EIS computer controls a *Solartron 1260* or a *Solartron 1255B*, via a GPIB communication bus. The FRA sends an AC voltage signal from the generator output to the programmable input (Prg. Input) of a *Kepco Bipolar Operational Amplifier 20-20D* (Op-Amp) . The Op-Amp converts the AC voltage signal to a corresponding AC current signal with a current-to-voltage ratio of $1\frac{A}{V}$. The generated AC current through the SOFC stack is superimposed on the DC current provided by the electronic load of the test rig. Four terminal measurements were used to measure the (time-dependent) currents and voltages of the RUs. The voltage of a RU was measured by a differential probe connected to the differential input V1 on the FRA.

The *Keithley 2750* is able to multiplex differential signals from the different cells in the stack. The combined DC and common mode cancellation box (DC + CMR Box) is an active electric circuit designed at *DTU Energy Conversion* which minimizes the common mode voltage and cancels out the DC contribution for utilizing the best resolution on the voltage input. The cables from the SOFC stack to the Keithley multiplexer was two wire parallel untwisted paired. All the other cables for voltage measurements was single wire shielded (also called coaxial or BNC) and the shields from the wires was connected in a star ground configurations together with the shield from the measurement equipment. The current through the stack was measured with an active current transducer (*LEM ITN 600-s*) which has a linear response up to $100\,kHz$. The DC voltage (which correspond to the measured current) from the current transducer generated in the Rm Box was minimized by additional active electrical circuit, a DC cancellation box (DC Box), in order to utilize the highest measurement resolution on the voltage input on the Solartron. The operation of the Solartron 1260 or the Solartron 1255B was controlled by the Elchemea 6.0.4 software developed at DTU Energy Conversion by Søren Koch and Karin Vels Hansen.

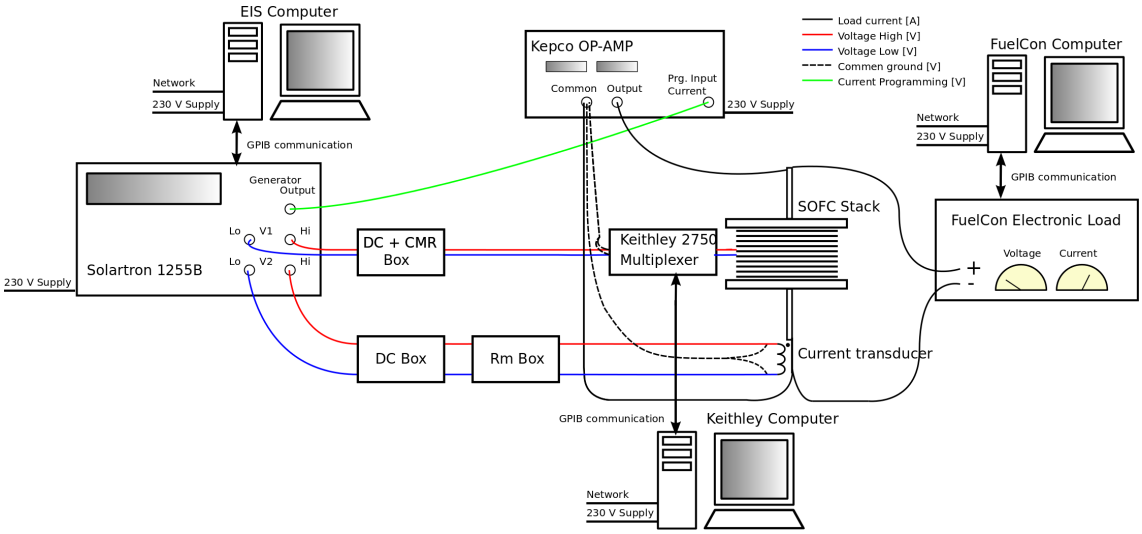


Figure 2.19: Illustration of the test setup when using Solartron 155B or Solartron 1260.

#### 2.3.2.1 Amplifying the AC signal

The amplifier used, Kepco 20-20D Bipolar operational power supply/amplifier, shown in Figure 2.20. It is a $400\,W$ amplifier with a max current of $20\,A$ and a max voltage of $20\,V$. The amplifier work as a booster which amplifies the output signal of the Frequency Response Analyzer, FRA, with a amplification of $1\,\frac{A}{V}$. The FRA (Solartron 1260 or 1255B) generates an AC voltage signal in the range $0-3\,V$ which is amplified to $0-3\,A$ by the amplifier. The slew rate (rise time, $t_r$) from $10\%$ to $90\%$ load of the Kepco 20-20D is $76\,\mu$S [60] which from Equation 2.14 gives an amplifier bandwidth of $f_B = 4.6\,kHz$ [61].

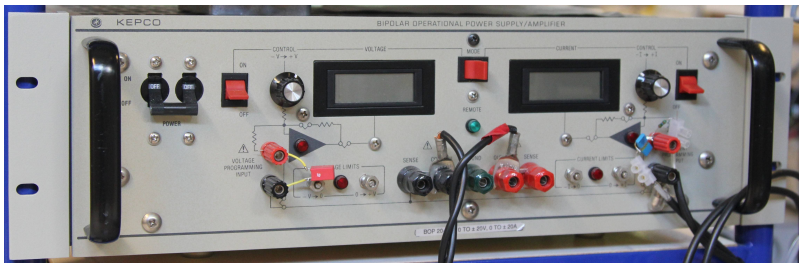


Figure 2.20: Kepco 20-20D operational amplifier.

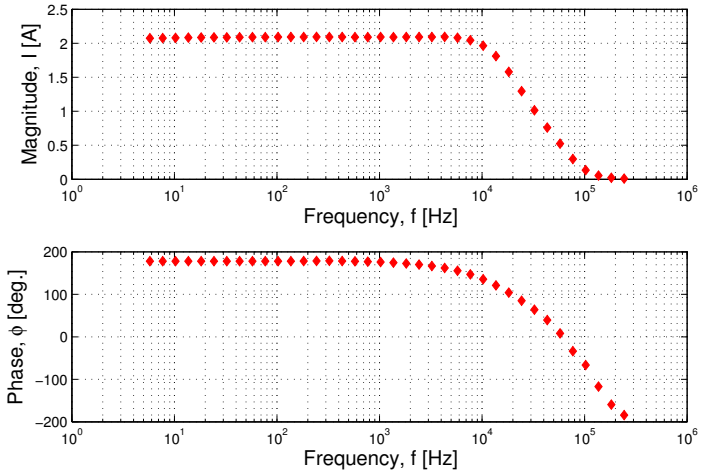


Figure 2.21: Measured output current as a function of frequency for the Kepco 20-20D.

$$f_B = \frac{0.35}{t_r} \tag{2.14}$$

The actual bandwidth is higher when not going to $90\%$ of full load ($20\,A$). The actual bandwidth measured with at $I_{AC,peak} = 3\,A$ ($I_{AC,RMS} = 2.1\,A$) is around $10\,kHz$ as shown in Figure 2.21. For frequencies above $10\,kHz$ the current amplitude decreases significantly due to limitations in the power supply. This means the the voltage response from the cell/stack under test decreases significantly as well. The impedance can still be measured since the current through the stack is measured by a current transducer.

#### 2.3.2.2 Current measurements

Small metal strip resistors are normally used as shunt for measuring the current through the cell for single cell tests (cell active area $\sim 4x4\,cm^2$) at DTU Energy Conversion. For SOFC stack tests (cell active area $\sim 90\,cm^2$), where higher DC currents is needed, metal strip resistors are not suitable. When using metal strip resistors a lot of energy will be dissipated in the resistor which makes the resistor hot and increases its resistance.

A current transducer is used instead, which measure the current passing by sensing the magnetic field generated by the current. The placement of the current transducer is illustrated in Figure 2.19. It is important to place the current transducer as close to the SOFC before connecting the FuelCon Electronic DC load in order to get the exact current through the stack. The impedance response of the current transducer was recorded by a Solartron 1260 with the current generator output set to $60\,mA$. The impedance response of the current transducer is measured (at identical frequencies as the cell/stack measurements) as $\left(\frac{V_2}{I}\right)_{CT,measured}$ where $V_2$ is the measured volt-


Figure 2.22: Current transducer used for measuring the current through the stack: LEM ITN 600-S Ultrastab.

age response from the current transducer and $I$ is the current from the generator output of the Solartron 1260. The impedance response of the current transducer is multiplied to the RU/stack measurement to compensate for the non linear impedance response of the current transducer at high frequencies. The calculation of the compensation is shown in Equation 2.15. $V_1$ is the measured voltage response of the repeating unit and $V_2$ is the measured voltage response from the current transducer representing the current through the stack.

$$Z_{cell} = \left( \left( \frac{V_1}{V_2} \right)_{RU,measured} \right) \left( \frac{V_2}{I} \right)_{CT,measured} \tag{2.15}$$

The current transducer used for the measurements is a LEM ITN 600-S Ultrastab shown in Figure 2.22. An electric circuit with a measurement reference resistor for the current transducer was made by Martin Nielsen, DTU Energy Conversion. The circuit schematic for the Rm Box consisting the measurement reference resistor, $R_m$, is shown in Figure 2.23 in between the current transducer on the left and the DC compensation (cancellation) box on the right. The current, $I$, through the current transducer is given by Equation 2.16. $U_{R_m}$ is the voltage across the measurement resistor with the resistance $R_m$. The conversion ratio, $K_N = 1500$ is the ratio between the primary and secondary windings of the current transducer [62].

$$I = \frac{U_{R_m}}{R_m} K_N \tag{2.16}$$

According to the data sheet (Ref. [62]) the measurement resistor should be, $R_m \leq 5\,\Omega$. A measurement resistor of $R_m = 5\,\Omega$ was selected to keep a high resolution of the measured signal. A measurement resistor $R_m = 12\,\Omega$ was also tried. It worked fine at OCV, but the magnetic coil in the current transducer got saturated at nominal DC current. The frequency response of the current transducer is shown in Figure 2.24. The imaginary impedance response, $-Z_{imag}$, is linear up to $100\,kHz$ and the relative residuals from the Kramers-Kronig test [22] are reasonable ($\leqq 1\%$) up to $200\,kHz$. When current measurements are recorded by the current transducer during RU impedance measurement a DC cancellation circuit is used between the current transducer and the input of the Solartron FRA to remove the DC component of the signal. DC cancellation is explained in the next section.

#### 2.3.2.3 DC cancellation to improve measurement resolution

As explained in Section 2.2.2.4 on page 26 a differential-mode signal appears differentially on a pair of wires in an ungrounded cable configuration. Figure 2.25 illustrates the differential-mode

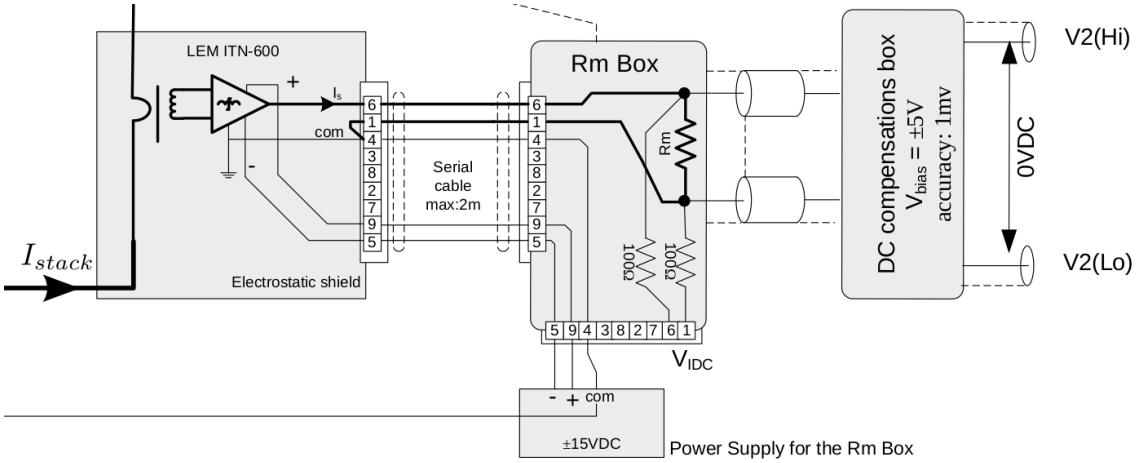


Figure 2.23: Schematic of the current transducer, reference resistor box (Rm Box) and the DC compensation (cancellation) box. $V_{IDC}$ is for measuring the DC current through the current transducer.

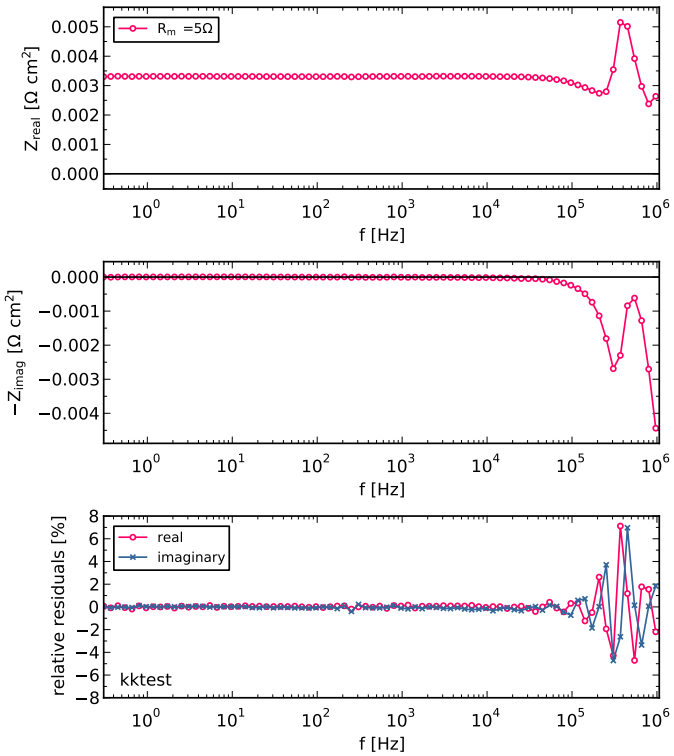


Figure 2.24: Real and imaginary impedance response of the current transducer with a measurement resistor of $R_m = 5\,\Omega$.

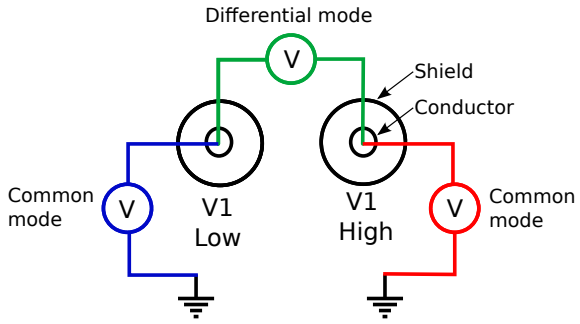


Figure 2.25: Illustration of differential and common mode signals at the voltage inputs of an Solartron FRA.

signal (green) between voltage measurement response inputs V1 Low and V1 High of a Solartron FRA. The DC voltage in the differential mode needs to be canceled to be in the lowest voltage range ($30\,mV$) with the highest resolution ($1\,\mu V$). Figure 2.26 illustrates the voltage response signal for a cell/repeating unit without DC cancellation where the AC signal is superimposed on the DC signal (red line). For ease of explanations differential DC voltage was selected to be $1\,V$ which fit approximately to the open circuit voltage of a cell. With DC cancellation the DC differential voltage response signal is canceled (Figure 2.26 green line).

There are three ranges at the voltage response inputs in the Solartron 1255B and 1260: $30\,mV$, $300\,mV$ and $3\,V$ [57, 58]. In order to utilize the highest resolution of $1\,\mu V$, the $30\,mV$ range needs to be used. To make sure that the voltage response is in the $30\,mV$ range, the DC RU voltages are canceled out electronically by an active DC cancellation circuit attached between the device under test and the voltage response input at the Solartron (either $V1$ or $V2$).

In the Solarton 1260 Operating Manual (Ref. [57]) the following description is given about the ranges:

- [auto] Auto ranging selects the most accurate range for the signal amplitude being measured. Each measurement starts on the most sensitive range. If an overload is detected the result is discarded and measurement restarts on the next range up; this procedure is continued until a valid result is obtained. Auto ranging should be used when the signal amplitudes being measured cover more than one input range, or are unpredictable.
- [30mV] Fixed range for signal amplitudes between $0\,V$ and $30\,mV$.
- [300mV] Fixed range for signal amplitudes between $0\,V$ and $300\,mV$.
- [3V] Fixed range for signal amplitudes between $0\,V$ and $3\,V$.
- The use of a fixed range avoids the range search time penalty incurred with auto ranging. Select the most sensitive range possible, to obtain the finest measurement resolution.

With DC cancellation the Solartron is kept fixed in the $30\,mV$ range during the complete measurement sequence. The DC cancellation circuit is combined with the common mode rejection circuit explained in the following section.

#### 2.3.2.4 Common mode cancellation for SOFC stack measurements

As explained in Section 2.2.2.4 a common-mode voltage appears equally (with respect to local circuit common) on both lines of a 2-wire cable not connected to earth, shield or local common. Figure 2.25 illustrates the common mode voltages for V1 Low (blue) and V1 High (red) of a Solartron FRA. The common mode rejection voltage of the Solartron 1255B and 1260 are only $5\,V$ in all the ranges [57, 58], therefore the common mode voltage on the voltage response signal needs to be canceled in order to measure single repeating units in SOFC stacks with more than four repeating units. Figure 2.27 illustrates the cancellation of the common mode signals with

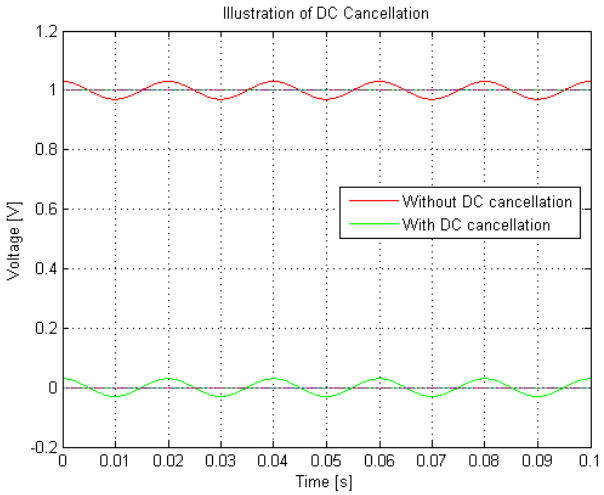


Figure 2.26: Illustration of the voltage response signal with and without DC cancellation.

respect to earth for $V1_{High}$ and $V1_{Low}$ for the ninth repeating unit, RU09, in a SOFC stack. For ease of explanations differential DC voltage was selected to be $1\,V$ which fit approximately to the open circuit voltage of a cell. Without common mode cancellation the common mode DC voltages are $V1_{High,CM,RU09} = 10\,V$ (magenta) and $V1_{Low,CM,RU09} = 9\,V$ (cyan). With common mode cancellation the common mode DC voltages becomes $V1_{High,CM,RU09} = 1\,V$ (red) and $V1_{Low,CM,RU09} = 0\,V$ (blue) and differential voltage response signal from RU09 can then be measured by the Solartron FRA. The AC component for $V1_{Low,CM,RU09}$ is removed since it would be connected to ground in the combined DC and common mode cancellation box.

DC and common mode cancellation are done by one single active circuit which is referred to as the DC + CMR Box in the illustration of the test setup in Figure 2.19 on page 29. The circuit was specified by the author and constructed by development engineer, Martin Nørby Nielsen, DTU Energy Conversion. The essential part of the circuit is the high common-mode voltage difference amplifier, INA117 from Texas Instruments Inc. [63]. The output voltage of the INA117 high common-mode voltage difference amplifier is given by Equation 2.17.

$$U_{out,INA117} = U_{High} - U_{Low} \tag{2.17}$$

The circuit schematic of the combined DC and common mode cancellation circuit is shown in Figure 2.28. The circuit has two switches, shown as K1 and K2 in the circuit schematic in Figure 2.28 witch can bypass the DC and common mode cancellation circuit when AC coupling mode is needed. DC and AC coupling modes are explained in the next section.

The impedance response of the combined DC and common mode cancellation box is given in Figure 2.29. The real response is linear up to $30\,kHz$ and the imaginary response is linear up to $3\,kHz$. The response of the DC and common mode cancellation circuit is compensated in the DC coupling mode given in Equation 2.19 as $\left(\frac{V_2}{V_1}\right)_{cmrbox,measured}$ in the next section.

#### 2.3.2.5 AC and DC coupling modes of the Frequency Response Analyzer

AC and DC coupling modes is two different ways to couple of the measured signal to the analyzer input. Figure 2.30 shows the equivalent circuit of the analyzer input of the Solartron 1255B. When DC coupling is active the DC/AC switches are closed and the capacitors are inactive allowing the AC and DC components of the signal to measured. When AC coupling is active the DC/AC switches are open and the capacitors are active and rejects the DC component of the signal. DC coupling introduces minimum phase shift and should be used whenever possible, particularly at

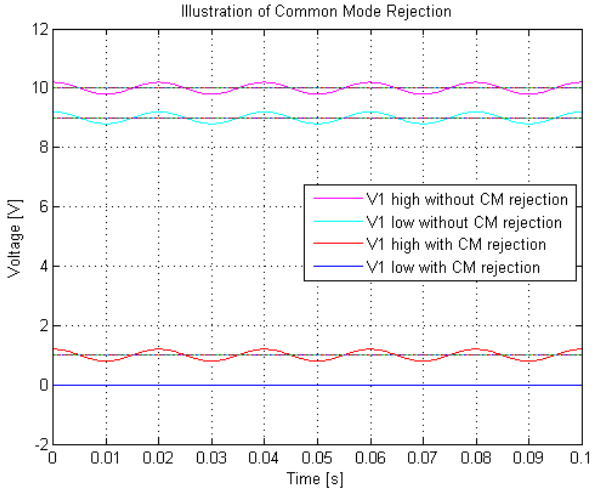


Figure 2.27: Illustration of the cancellation of common mode signals for the voltage response of the ninth repeating unit of a SOFC stack.

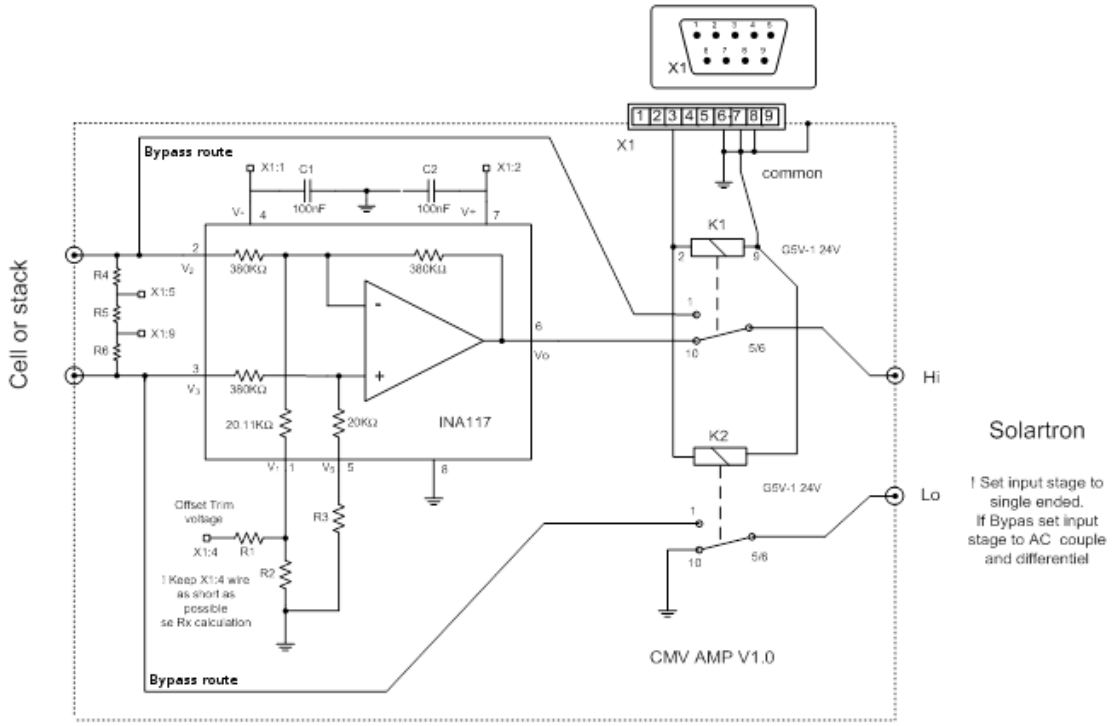


Figure 2.28: Electronic schematic of the combined DC cancellation and Common mode rejection circuit with bypass.

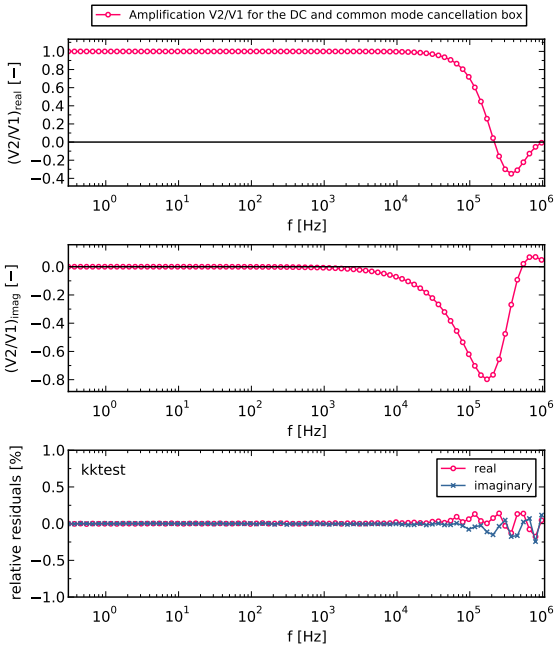


Figure 2.29: Impedance response of the combined DC and common mode cancellation box.

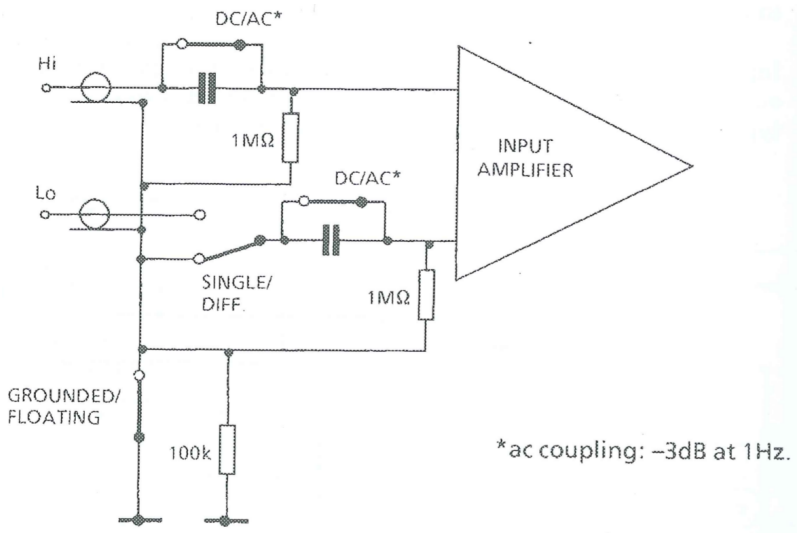


Figure 2.30: Equivalent circuit of the analyzer input of Solartron 1255B. Illustration taken from [58].

low frequencies. AC coupling can be used to reject an unwanted DC component. This may allow a more sensitive input range to be selected [57, 58].

To get the best impedance measurement of a repeating unit in a SOFC stack with a Solartron FRA is to do a sequential AC and DC coupling measurement. The AC coupling has the best precision at high frequencies and is recorded from $1\,MHz$ to $8\,Hz$ with 12 points per decade. It takes about $3.5\,minutes$ (integration time of 200 measure periods from $969\,kHz$ to $6.7\,Hz$) to record the AC coupling measurement. The DC coupling measurement has the best precision at low frequencies and is recorded from $1\,MHz$ to $0.3\,Hz$ with 12 points per decade (200 measure periods from $969\,kHz$ to $6.7\,Hz$, 100 measure periods from $6.6\,Hz$ to $670\,mHz$, 50 measure periods

from $60\,mHz$ to $300\,mHz$). It takes about $35\,minutes$ to record the DC coupling measurement. Measurement points between $969\,kHz$ and $\sim 200\,kHz$ are removed by the data analysis software. The compensated impedance signal for the AC coupling impedance can be calculated as given by Equation 2.18 . The compensated DC coupling impedance can be calculated as given by Equation 2.19 which also takes the response of the combined DC and common mode cancellation circuit into account.

$$Z_{RU,ac} = \left( \left( \frac{V_1}{V_2} \right)_{RU,measured} \right) \left( \frac{V_2}{I} \right)_{CT,measured} \tag{2.18}$$

$$Z_{RU,dc} = \left( \frac{\left( \frac{V_1}{V_2} \right)_{RU,measured}}{\left( \frac{V_2}{V_1} \right)_{DC+CMR\,Box,measured}} \right) \left( \frac{V_2}{I} \right)_{CT,measured} \tag{2.19}$$

The AC coupling (Red) and DC coupling (blue) impedance spectra are shown in Figure 2.31. The AC coupling and DC coupling impedance spectra are combined to a single impedance spectrum (green). The AC coupling and DC coupling measurements obtained identical impedances in the range $100\,Hz$ to $10\,kHz$. For the combined impedance measurement the impedances measured above $300\,Hz$ is the AC coupling measurement and below $300\,Hz$ it is the DC coupling measurement. Real and imaginary impedances as a function of frequency for the AC coupling, DC coupling and Combined impedance spectra are shown in Figure 2.31 B) and C) respectively. The recorded impedance data from AC coupling and DC coupling measurements are combined to a single impedance data file using a Python script developed by Christopher Graves, DTU Energy Conversion. When carrying out an AC coupling measurement together with the DC + CMR Box, a bypass switch was applied to the circuit shown as K1 and K2 in Figure 2.28. The bypass switch will disconnect the circuit, since it is only needed for DC coupling measurements. The state of the bypass switch can be set automatically in the Elchemea software enabling automated impedance measurements as explained in the Section 2.3.2.7 on page 39.

#### 2.3.2.6 Short circuit compensation measurement

To minimize the effects of stray resistance and mutual inductance in wires from measurement equipment to the SOFC stack a short circuit measurement can be performed and subtracted from the repeating unit measurements. The short circuit measurement can be done by replacing the stack with a short circuit bracket shown in Figure 2.32 which is normally used for short circuit measurements in single cell testing at DTU Energy Conversion. The short circuit bracket is then mounted in the furnace as shown in Figure 2.33 and a short circuit measurement was performed at room temperature with nearly the same wire connections as used for the SOFC stack measurements. Figure 2.34 shows the impedance spectra for the second repeating unit, RU02 at $750°C$ with Anode gas: $96\%\ H_2$ $4\%\ H_2O$ and $96\%$ air and $4\%\ H_2O$ at the cathode and a current density of $0.2\,A\,cm^{-2}$. "no SC compensation" is without short circuit compensation. "with SC compensation" is where the short circuit measurement is subtracted to the short circuit measurement as shown in Equation 2.20.

$$Z_{cell} = \left( \left( \frac{V_1}{V_2} \right)_{cell,measured} - \left( \frac{V_1}{V_2} \right)_{short,measured} \right) \left( \frac{V_2}{I} \right)_{CT,measured} \tag{2.20}$$

It was selected not to correct the impedance measurements with the short circuit measurement since the short circuit bracket does not represent the wire connections for a SOFC stack perfectly and add extra uncertainty to the estimation of the series resistance, $R_s$. It is estimated that this will give a measurement error of less than $10\%$ for the series resistances and a measurement error of less than $3\%$ for the polarization resistances. One needs to make a "short circuit stack" for making representative short circuit measurement. This could be by replacing cells with conductive rubber sheets and measure at room temperature or make some "short circuit cells" for a "short circuit stack" to do short circuit measurements at operating temperature.

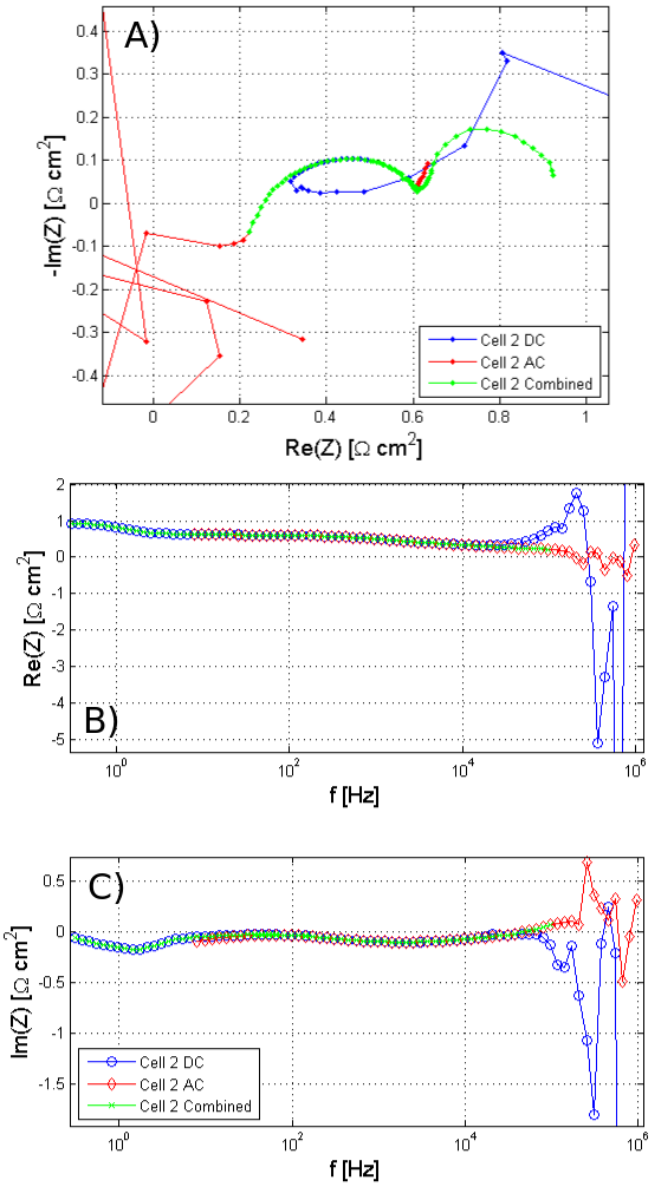


Figure 2.31: **A)** Impedance spectra of the AC coupling and DC coupling measurement and the combined and where points with high noise are removed. **B)** Real impedance as a function of frequency **C)** Imaginary impedance as a function of frequency.

As an alternative to short circuit compensation measurements, the high frequency inductance was removed by subtraction. The inductance to be subtracted can be determined for each spectra by comparison of the imaginary data generated from the experimental real part of the impedance using the Kramers-Kronig transforms [22]. An inductance of $2\,nH$ subtracted determined by the Kramers-Kronig transforms and subtracted in the impedance spectrum shown in Figure 2.34. The high frequency inductance was only removed by subtraction when using Distribution of Relaxation Times, DRT.

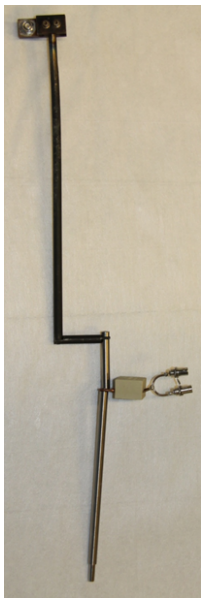

Figure 2.32: The short circuit bracket configuration.

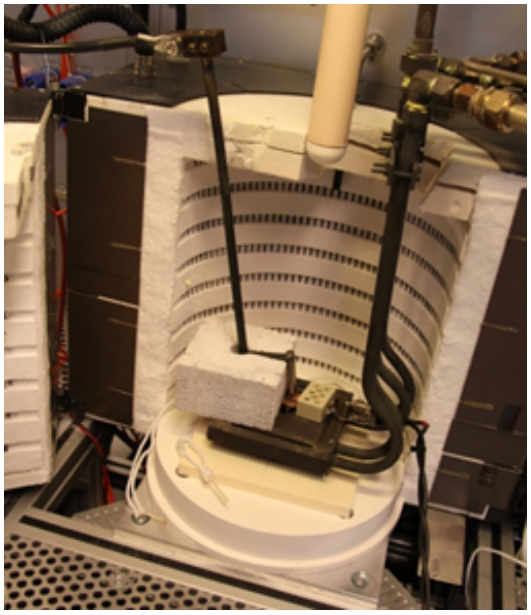

Figure 2.33: Short circuit bracket configuration mounted in the FuelCon rig for SOFC stack measurements.

#### 2.3.2.7 Automation of impedance measurements

Manual impedance spectroscopy on a stack is very time consuming since the EIS measurements are carried sequentially and one needs to change cables for the RUs between each impedance measurement manually. By making automated impedance measurements, utilization of the stack test time will improve significantly. Central to automation of impedance measurements using a single channel instrument is a multiplexer which switches between different RUs automatically, and can be programmed to switch between RUs sequentially. The selected multiplexer is a Keithley 2750 (data logging system with 5 slots for modules) with two Keithley 7700 20-channel Differential Multiplexer Modules. A picture of the Keithley 2750 is shown in Figure 2.35. An illustration of the test setup is given in Figure 2.36 where multiplexer is added in between the DC + CMR Box and the SOFC stack.

An overview of the programming blocks for automation of sequential impedance measurements is given in Figure 2.37. The multiplexing of the Keithley is controlled by a simple Perl program (PERL GPIB Socket Client) made the author and Søren Koch, DTU Energy Conversion, on a Linux PC (Keithley Computer on Figure 2.36). The Keithley computer (slave) communicates with test rig control computer (Master) through a Perl LAN server. The test rig control computer (Windows PC) will then send a command by the EIS Subroutine VisualBasic program, made by the author and Martin Nørby Nielsen, DTU Energy Conversion, through the TCP/IP (LAN connection) via Visual Basic LAN client to the Keithley computer, that it needs to access a given channel on the Keithley. When the channel is changed the FuelCon Computer will send a command by the Visual Basic EIS Subroutine program, through the TCP/IP (LAN connection) to

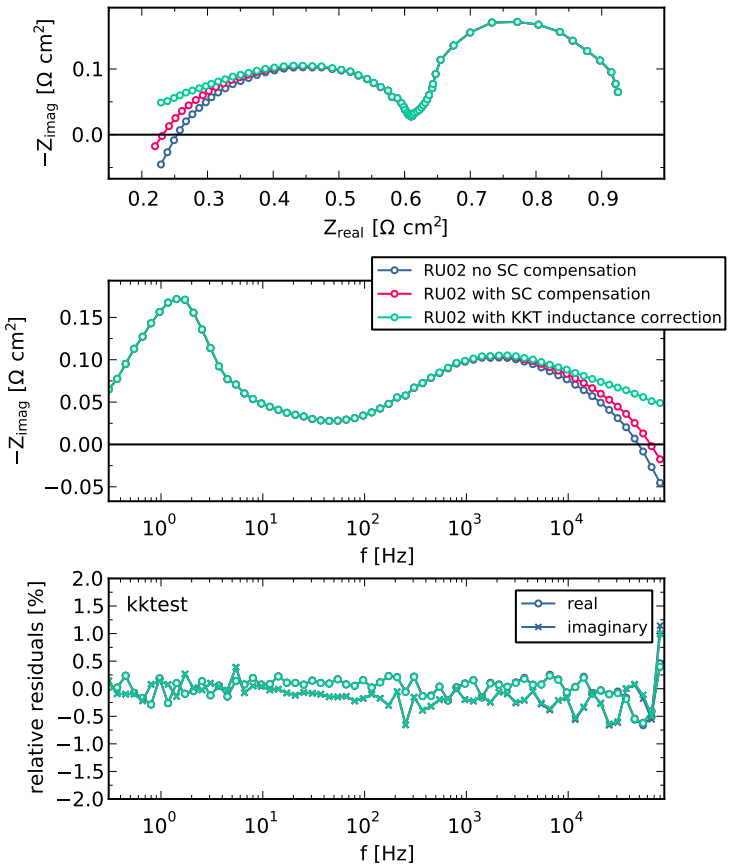


Figure 2.34: Impedance response with and without short circuit compensation. Measurement recorded at $750°C$ with Anode gas: $96\%$ $H_2$ $4\%$ $H_2O$ and $96\%$ air and $4\%$ $H_2O$ at the cathode and a current density of $0.2\,A\,cm^{-2}$. SC = short circuit.

the EIS computer (Linux PC) that it need to start a AC coupling measurement. The command is received by a Perl LAN Server to the Perl GPIB client that communicate with the Solartron FRA. These two programs was made by Søren Koch, DTU Energy Conversion. When the AC coupling measurement is done, a subsequent DC coupling measurement will start. After the DC coupling measurement, the multiplexer switches to a new repeating unit and so forth. All the impedance data are saved on both the EIS computer and the FuelCon Computer.

Multiplexing RUs from the stack to the FRA had a negative effect on the precision of the impedance measurements. Figure 2.38 shows the difference between a manual and automated impedance. The automated impedance loses precision from $20\,kHz$. The reasons to the lower precision was investigated. Impedance measurements done without the multiplexer showed that the loss in precision was due to the combined DC and Common mode cancellation. The impedance measurement with red line and markers in Figure 2.39 was recorded without the multiplexer and the DC and common mode cancellation circuit was bypassed. The impedance measurement shows poor precision at high frequencies together with high relative residuals for the Kramers-Kronig test [22] indicating a significant systematic error. The impedance measurement with blue line and markers in Figure 2.39 was recorded without multiplexer and DC and common mode cancellation circuit and shows good precision at high frequencies together with good relative residuals for the Kramers-Kronig test. The cause bad precision from the combined DC and common mode cancellation circuit in AC coupling mode must be the bypass switch illustrated in the

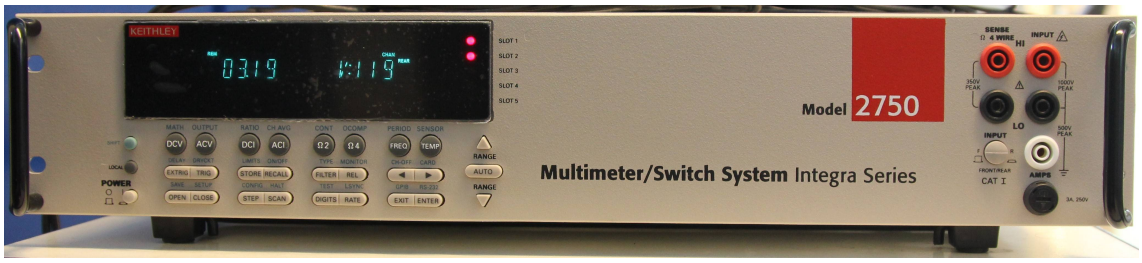


Figure 2.35: Keithley 2750 data logging system with 5 slots. 2 slots are used for multiplexing repeating units (Keithley 7700 cards) and 3 slots can be used for logging 120 temperature and voltage measurements (Keithley 7702 cards) .

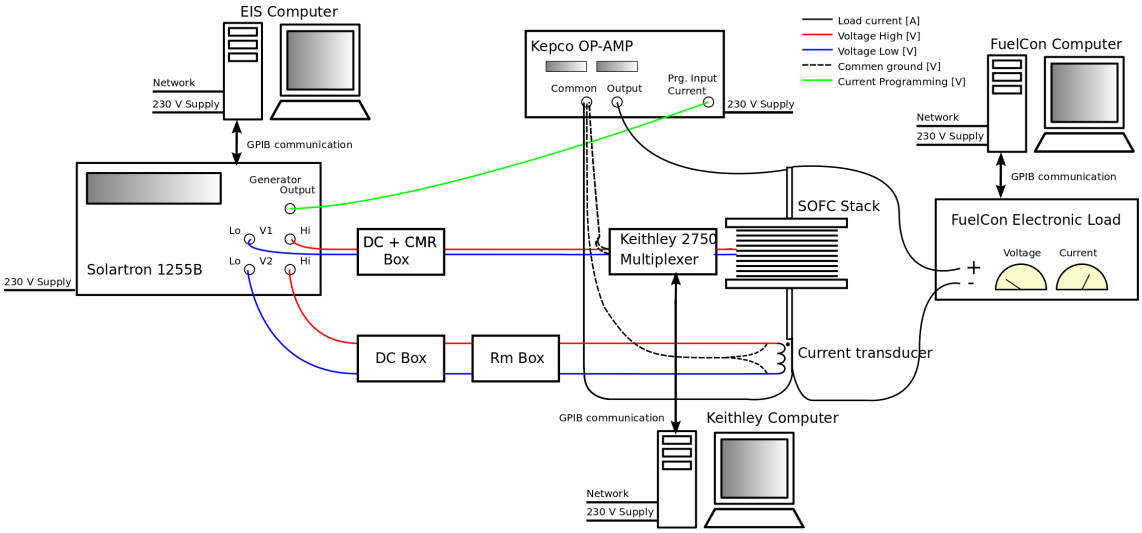


Figure 2.36: Illustration of the test setup when using a Keithley 2750 multiplexer with Solartron 1255B or Solartron 1260.

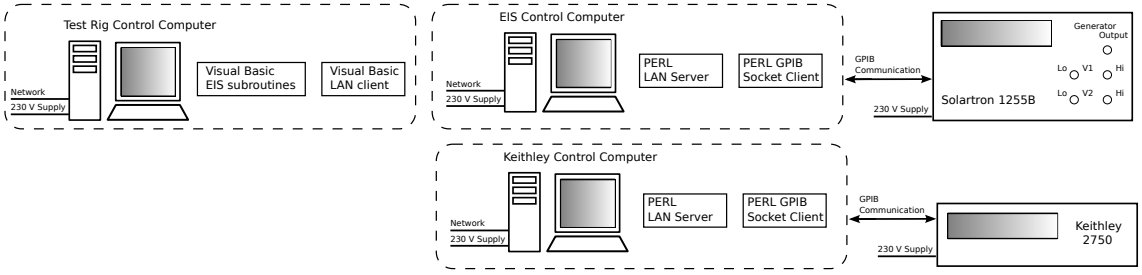


Figure 2.37: Programming blocks for automation of sequential impedance measurements.

circuit schematic as K1 and K2 in Figure 2.28 on page 35.

Due to the big loss in precision at high frequencies with the bypassed DC and common mode cancellation box the automation of impedance measurements was discontinued. Instead the DC and common mode cancellation box was removed manually each time AC coupling impedance measurements was recorded. This made the sequential impedance measurement setup very time consuming and limited the amount of repeating units characterized within normal working hours and thereby limited the amount of repeating units that could effectively monitored during long term degradation of SOFC stacks.

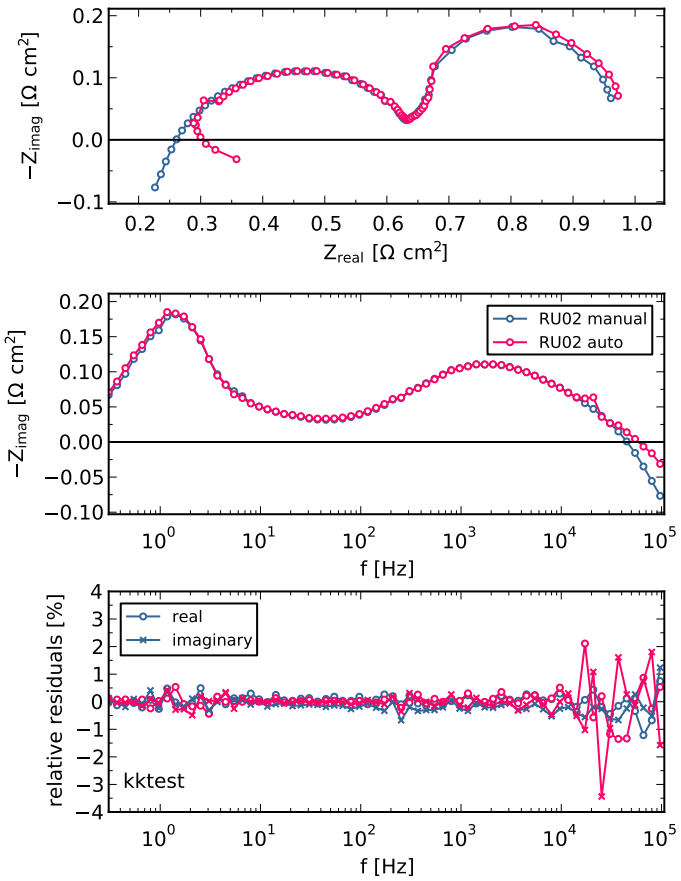


Figure 2.38: Impedance response recorded manually and automatically with the multiplexer. Recorded on stack J-102 at Temperature:750°$C$ Fuel: $96\%\, H_2$ $4\%\, H_2O$ Oxidant: $96\%\, Air$ and $4\%\, Air$ at a current density of $0.2\, A\, cm^{-2}$.

#### 2.3.2.8 Conclusion on Sequential Impedance Measurement Setup

A sequential impedance measurement setup was constructed and tested. Several initiatives were made to improve the accuracy of measurements at high frequency. The AC current signal was boosted from $60\, mA$ to $3\, A$ with a bipolar operational power supply/amplifier. The current through the stack was measured with a current transducer with reasonable impedance response up to $200\, kHz$.

A combined DC and common mode cancellation circuit was designed and implemented in the test setup. The DC and common mode cancellation circuit removed the common mode voltage and DC differential voltage which improved the measurement accuracy significantly. A combination of AC and DC coupling measurements made it possible to improve the high frequency impedance response significantly.

A short circuit compensation measurement was made to subtract the high frequency stray resistance and stray inductance. It was however decided not correct the impedance measurements with the short circuit measurement since the short circuit bracket did not represent the wire connections for a SOFC stack perfectly.

Automation of the impedance measurements was carried out with the implementation of multiplexer which switched between repeating units in the stack for automated sequential impedance measurements. It was found that the DC and common mode cancellation circuit when bypassed in the AC coupling mode lead to a significant decrease in precision. The automation of impedance

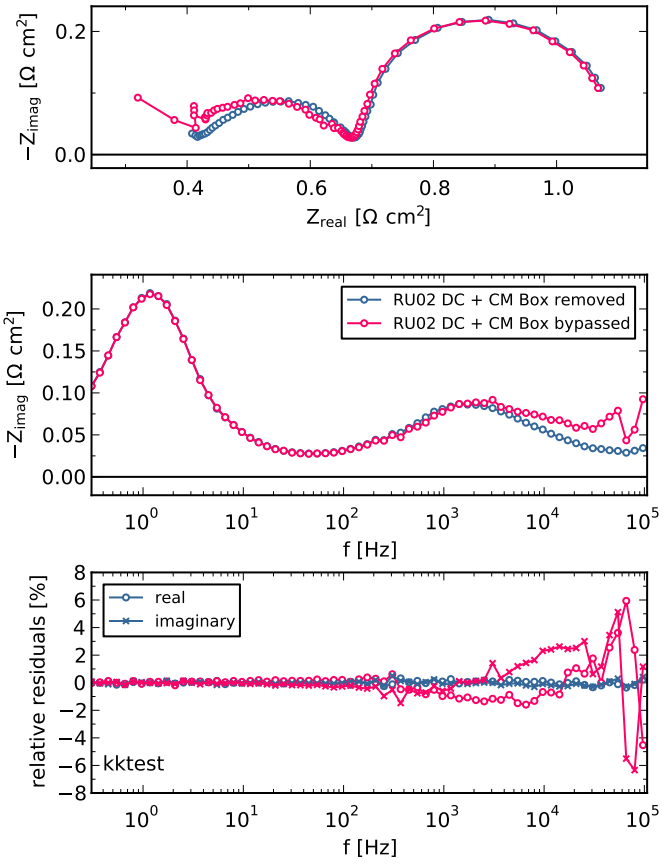


Figure 2.39: Difference in impedance measurements with and without the DC and common mode cancellation box. Recorded on stack K-571 at Temperature:$750°C$ Fuel: $80\%\ H_2\ 20\%\ H_2O$ Oxidant: $100\%\ Air$ at OCV.

measurements was therefore discontinued and the sequential impedance measurements were recorded manually. Validation of the data quality of the impedance measurements for the sequential impedance measurement setup is given in Section 3.2.0.1 on page 63.

### 2.3.3 Parallel Impedance Measurement Setup for EIS on SOFC stacks

A disadvantage with the Solartron setup explained in Section 2.3.2 on page 29 is that it is a sequential measurement setup is only capable of measuring one repeating unit voltage response at a time. Impedance measurements on a SOFC stack with 16 repeating units would take approximately 13 hours for 16 repeating units (RU) including a measurement of the full stack impedance using the sequential setup described. With the parallel impedance measurement setup explained in this section one is capable of carrying out EIS measurements of up to 16 RUs and the full stack simultaneously in $1.5\,h$. This reduces any drift in temperature and fuel supply and minimizes any changes in the internal resistance of the stack and its RUs during the measurement period and makes one able to compare the impedance measurements for up to 16 RUs and the stack directly. With the this setup there is no need for additional AC/DC coupling measurements and DC and common mode cancellation circuits as this is taken care of by the Zahner IM6 and Zahner EL1000. Furthermore, the test setup can be operated in a fully automated manner and allows measurement sequences to be carried out at any time of the day.

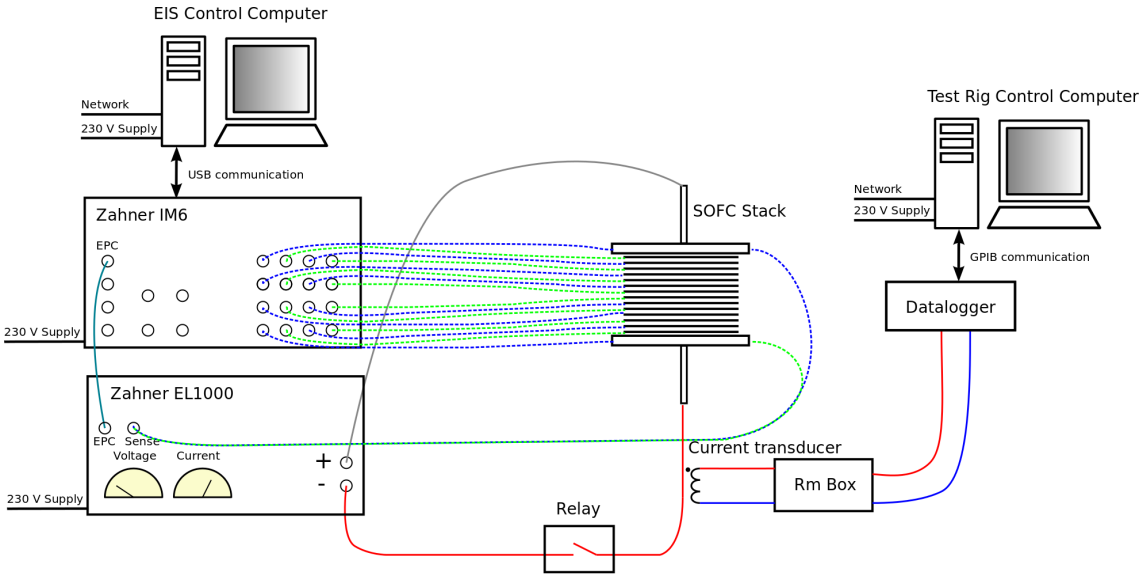


Figure 2.40: Illustration of the test setup when using Zahner IM6 and the *Zahner EL1000*.

#### 2.3.3.1 Test setup

An illustration of the Zahner set-up is shown in Figure 2.40. The test rig computer controls the EIS computer via a network connection. The EIS computer controls the Zahner IM6 Potentiostat via a USB connection through the Zahner software: "Thales". The Zahner IM6 controls the Zahner EL1000 Electronic Load via an EPC connection which is a custom cable with a D-Sub9 plug and a 8 pin Lemosa plug made by ZAHNER-elektrik GmbH & Co. KG. The Zahner EL1000 can be controlled in the "Potentiostat Control" menu in Thales. The Zahner IM6 is extended with 4x Zahner PAD4 cards. Each Zahner PAD4 card has 4 parallel AD converters and with 4x Zahner PAD4 cards the Zahner IM6 is able to measure the impedance of 16 channels in total. At the sense input of the Zahner EL1000 the AC voltage response of the whole stack is measured. In combination, the Zahner IM6 and the Zahner EL1000 can record EIS measurements of the stack and 16 RUs simultaneously which reduces the measurement time significantly. When the Zahner IM6 and the EL1000 is recording impedance measurements it is not possible to communicate, measure the DC current or shut off the Zahner system. This is critical if the Test Rig Control computer goes into an alarm mode. The DC current is therefore measured by a current transducer, LEM ITN-600s, as explained in Section 2.3.2.2 on page 30 and the data is logged by the test rig control computer via a data logger using a data logging script programmed in Visual Basic on the FuelCon test rig computer. A power relay is implemented in the set-up in order to disconnect the Zahner IM6 and the Zahner EL1000 if the cell voltages exceeds the set over- or under-voltage limits ($0.6V$ and $1.5V$, respectively) e.g. if shortage in the fuel supply occur. The power relay is explained in Section 2.3.3.3 on the facing page.

Suitable software was developed for automation of impedance measurement acquisition. The automation software is explained in Section 2.3.3.2. The software, Thales, also allows measurements of the harmonic distortion from the $2^{nd}$ to the $10^{th}$ order higher harmonic frequencies from the main voltage channel and is used in this work for fuel starvation detection which is discussed in Chapter 6 on page 103.

#### 2.3.3.2 Automation of the parallel impedance setup

Suitable software was developed for automation of impedance acquisition which reduced the measurement time significantly. An overview of the different software program blocks needed

| Remote instruction | Description |
|---|---|
| setGenMode(“gal”) | Set the generator on the IM6/EL1000 in galvanostatic mode |
| setGenMode(“pot”) | Set the generator on the IM6/EL1000 in potentiostatic mode |
| setCurrent(setpoint) | Sets the DC current to the specified setpoint (galvanostatic mode) |
| setPotential(setpoint) | Sets the DC current to the specified setpoint (potentiostatic mode) |
| output(“on”) | Turn on the generator on the IM6/EL1000 |
| output(“off”) | Turn off the generator on the IM6/EL1000 |
| measureCurrent() | Measures the current through the IM6/EL1000 |
| measurePotential() | Measures the voltage at the IM6/EL1000 |
| startImpedance() | Start EIS measurement |
| isImpedance_finish() | Check if the EIS measurement is finished on the IM6/EL1000 |

Table 2.3: Remote instruction functions programmed in VisualBasic to control the Zahner IM6 and EL1000 from the test rig control computer .

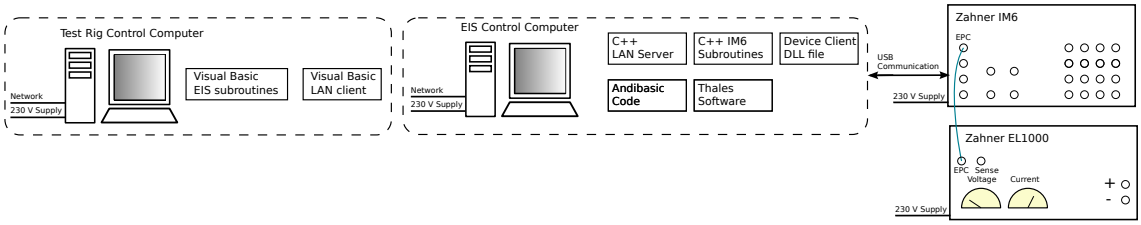


Figure 2.41: Programming blocks for automation of the parallel impedance measurement setup.

for the automation is given in Figure 2.41. The Visual Basic EIS subroutines, made by Martin Nørby Nielsen, sends a message through the Visual Basic LAN Client from www.chilkatsoft.com to the EIS control computer. When the parallel impedance measurements are done the Visual Basic EIS subroutines will continue to next step in the test plan. The C++ LAN Server from “Chillkat Software” receives the messages from software program blocks were written on the Test Rig Control Computer and forward it to the C++ IM6 subroutines which are made by the author, Martin Nørby Nielsen and the software team at Zahner. The Device Client DLL file is a Microsoft Dynamic Link Library (DLL) file developed by Zahner and is the link between the AndiBasic Code used for scripting and automation of the Zahner system and the and the C++ IM6 subroutines. AndiBasic is a programming language developed by Zahner for making custom programs for Thales. The AndiBasic Code communicate with Thales software which controls the the Zahner IM6 and the Zahner EL1000. The EIS settings for automated impedance measurements are read by the AndiBasic Code from earlier recorded impedance measurement and cannot be set remotely by the Test Rig Control computer. In Table 2.3 a list of instructions available to be set in VisualBasic software from the test rig computer for automated control of the EIS computer.

#### 2.3.3.3 Power Relay

When impedance measurements are recorded by the Zahner IM6 and the EL1000 it is not possible to communicate with the Zahner Thales software. This could become critical if the RU voltages exceed set over- or under-voltage limits e.g. due to insufficient of fuel supply. A power relay is implemented in the set-up in order to disconnect the Zahner IM6 and the Zahner EL1000 if the RU voltages exceed set over- or under-voltage limits ($0.6V$ and $1.5V$, respectively) e.g. if shortage in the fuel supply occur. The implementation of the power relay in the test rig is shown in Figure 2.42.

The power relay used is a BDS-A Battery Disconnect Switch (V23130-C2421-A431) originally designed for automotive applications [64] which can switch DC currents up to $260\,A$. The power relay is the black component in Figure 2.42. The power relay can be remote controlled from the test rig control computer via a Visual Basic program made by Martin Nørby Nielsen, or by a trip

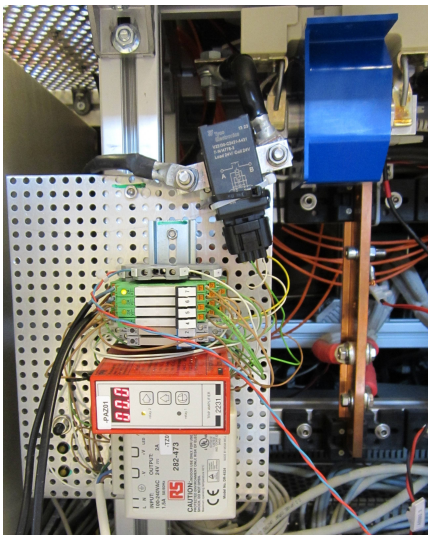

Figure 2.42: Implementation of the power relay in the test rig.

amplifier. A Visual Basic program monitor all the repeating unit voltages. If one of the RU voltages exceeds the set over- or under-voltage limit the power relay will disconnect by receiving a digital signal from the test rig. The response time is $40\,s$ due to limitations of the implementation of the data logger monitoring of the repeating unit voltages. Therefore a trip amplifier (red component in Figure 2.42) was implemented which monitor a single repeating unit voltage. If the selected RU voltage exceeds the set over- or under-voltage limit, the power relay will disconnect with a response time of $250\,ms$. The used trip amplifier is 2231 from PR electronics A/S [65].

#### 2.3.3.4 Conclusion on Parallel Impedance Measurement Setup

A parallel impedance measurement setup was constructed and tested. The impedance setup record 16 repeating unit and the stack impedance simultaneously and could be operated fully automated by the test rig computer resulting in a significantly reduced measurement time. Software in several programming languages was made in order to set up automated communication between the test rig computer and the computer recording the EIS measurements. A power relay was implemented in the test rig to cut of the impedance equipment from the SOFC stack if repeating unit voltages exceed set over- or under-voltage limits. Validation of the data quality of the impedance measurements for the parallel impedance measurement setup is given in Section 3.3.0.2 on page 66.

## 2.4 Optimizing stack measurement geometries for EIS

As introduced in Section 2.2 the current conducting rods needs to be perpendicular to the voltage probes minimize the effect of magnetic fields which are very important for the achievable accuracy. Four different experimental stack measurement geometries have been tested with electrochemical impedance spectroscopy. Table 2.4 gives an overview of the different stack configurations tested. The stack serial number is specified together with $\alpha$ or $\delta$. $\alpha$ indicate that the stack flow configuration is cross-flow and $\delta$ indicates that the stack flow configuration is Co-flow. The Cell Column gives the cell generation. $2.0G$ refers to planar anode-supported SOFCs (Ni-YSZ/YSZ/LSM-YSZ). The cell details can be found elsewhere [66]. $2.5G$ refers to planar anode supported cells with Ni/YSZ anode support, Ni/YSZ anode, YSZ electrolyte, CGO barrier layer and LSCF/CGO composite cathode [67]. The operator column indicate who operated the stack, jehq is Development Engineer, Jens Høgh from DTU Energy Conversion and rasmo is Rasmus Rode Mosbæk, the author. The column "$R_S$?" indicates if the corresponding stack measurement

| Conf | $R_s$? | Stack | Cell | Temp. | Fuel | Oxidant | Load | Operator |
|---|---|---|---|---|---|---|---|---|
| A | No | J-10 ($\alpha$) | $2.0G$ | $817\,°C$ | $30\%\,H_2O$ $70\%\,H_2$ | $Air$ | $OCV$ | jehq |
| B | No | J-50 ($\alpha$) | $2.0G$ | $750\,°C$ | $50\%\,H_2O$ $50\%\,H_2$ | $Air$ | $OCV$ | jehq |
| C | Yes | J-102 ($\alpha$) | $2.0G$ | $750\,°C$ | $4\%\,H_2O$ $96\%\,H_2$ | $Air$ | $18.5\,A$ | rasmo |
| C1 | Yes | J-102 ($\alpha$) | $2.0G$ | $750\,°C$ | $20\%\,H_2O$ $80\%\,H_2$ | $Air$ | $OCV$ | rasmo |
| C2 | No | K-581 ($\delta$) | $2.5G$ | $700\,°C$ | $20\%\,H_2O$ $80\%\,H_2$ | $Air$ | $OCV$ | rasmo |
| D | Yes | K-708 ($\delta$) | $2.5G$ | $700\,°C$ | $20\%\,H_2O$ $80\%\,H_2$ | $Air$ | $4\,A$ | rasmo |

Table 2.4: Overview of the different stack configurations.

| Conf | $R_s$? | Stack | In-plane effects in end plates avoided | Current rod effects avoided | Area between wires avoided |
|---|---|---|---|---|---|
| A | No | J-10 ($\alpha$) | No | No | No |
| B | No | J-50 ($\alpha$) | No | Partially | Partially |
| C | Yes | J-102 ($\alpha$) | Yes | Yes | Partially |
| C1 | Yes | J-102 ($\alpha$) | Yes | Yes | Partially |
| C2 | No | K-581 ($\delta$) | No | Partially | Partially |
| D | Yes | K-708 ($\delta$) | Yes | Yes | Yes |

Table 2.5: Overview of the results for the different stack configurations in reducing the magnetic fields.

geometry allowed an accurate measurement of the series resistance of the stack. Even though the stack configurations are not tested at the same conditions it is still possible to compare the behavior of the high frequency response.

The magnetic fields in a SOFC stack measurement setup has a high influence on the high frequency impedance response from the repeating units in a SOFC stack. The magnetic fields for SOFC stack impedance measurements can be divided into four categories. The first category is the magnetic fields generated inside the repeating units, $B_{RUs}$, from AC current conducted in the interconnects and the cells. These effects cannot be reduced since the current conducted in the interconnects will always be parallel to the voltage probes. The second category is the magnetic field generated from in-plane AC currents conducted in the end plates, $B_{End\ plate}$, of the stack. The magnetic fields generated in from in-plane currents in the end plate can be reduced by correct attachment of the rod. The third category is the magnetic fields generated by the AC current conducted in the current rods, $B_{Rods}$, attached to the stack. The magnetic field generated from the current in the current rods can be reduced if the current rodes are perpendicular to the voltage probes. The fourth category is the difference in magnetic fields observed by the wires for repeating unit voltage measurements, $B_{Area\ between\ wires}$, which can be reduced by reducing the area between the wires, e.g. by making twisted paired wires. Ideally the sum of the magnetic fields from the four categories should by zero as given by Equation 2.21. Table 2.5 gives an overview of the results for the different stack configurations in reducing the magnetic fields from second to the fourth category.

$$B_{RUs} + B_{End\ plate} + B_{Rods} + B_{Area\ between\ wires} = 0 \tag{2.21}$$

### 2.4.1 Configuration A

The experimental stack configuration A is shown in Figure 2.43. The impedance spectra for two different RU's in the stack are shown in Figure 2.44. A large difference in the high frequency impedance response of neighbouring repeating units was observed. The difference in the high frequency response can be explained by that odd and even RU's were influenced by mutual inductance in opposite direction (i.e. an either positive or negative inductance).

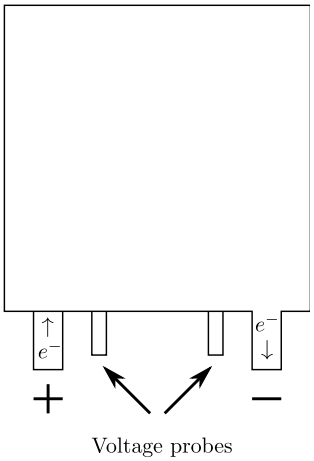


Figure 2.43: Experimental stack Configuration A seen from above.

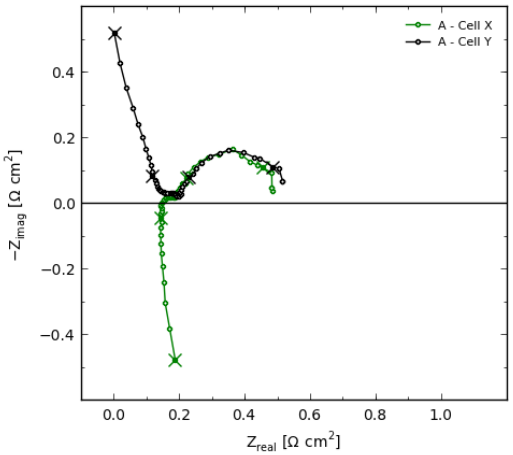


Figure 2.44: Impedance spectra for two RUs with experimental stack configuration A. X corresponds to $50\,kHz$, $5\,kHz$, $500\,Hz$, $50\,Hz$, $5\,Hz$, and $0.5\,Hz$.

When measuring the impedance for odd RUs, $Z_{RU,x}$, for stack configuration A illustrated in Figure 2.45, the magnetic flux, $\Phi_B(t)$ generated by the AC current, $I_{AC}$, will generate mutual inductance as explained in Section 2.2.1.2 on page 19 and thereby induce a voltage change by the electromotive force, $e_{n,x}$ and $e_{n,x+1}$, in the wires from the interconnects below and above the cell, $IC_{RU,x}$(left) and $IC_{RU,x+1}$(right) respectively. This will change the measured differential voltage, $U_{RU,x}$, which will then not be identical to the voltage across the impedance of the RU in question, $Z_{RU,x}$. This leads to a decrease of the measured impedance, $Z_{RU,x,measured}$ which becomes smaller than the actual impedance, $Z_{RU,x,actual}$ for frequencies greater than approximately $1\,kHz$ as given in Equation 2.22.

$$for\ f\ > 1\,kHz\ \Rightarrow\ Z_{RU,x,measured} < Z_{RU,x,actual} \tag{2.22}$$

For odd RUs the interconnect below the cell $IC_{RU,x}$ the voltage flap was on the left side whereas the interconnect above the cell $IC_{RU,x+1}$ the voltage flap was on the right side. For even RUs the interconnect below the cell $IC_{RU,y}$ the voltage flap was on the right side and the interconnect above the cell, $IC_{RU,y+1}$, the voltage flap was on the left side as illustrated in Figure 2.46. This causes the measured impedance, $Z_{RU,y,measured}$ to become greater than the actual impedance, $Z_{RU,y,actual}$, as given in Equation 2.23.

$$for\ f\ > 1\,kHz\ \Rightarrow\ Z_{RU,y,measured} > Z_{RU,y,actual} \tag{2.23}$$

The impedance measurement of stack configuration A showed that the placement of the current path and voltage measurement wires is of great importance. With experimental stack configuration B elimination of the mutual inductance was attempted.

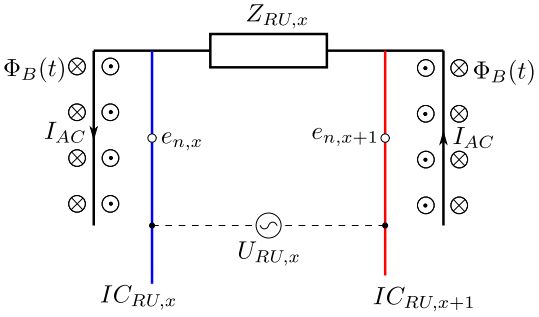


Figure 2.45: Illustration of current and voltage paths when measuring the impedance of odd RUs in stack configuration A.

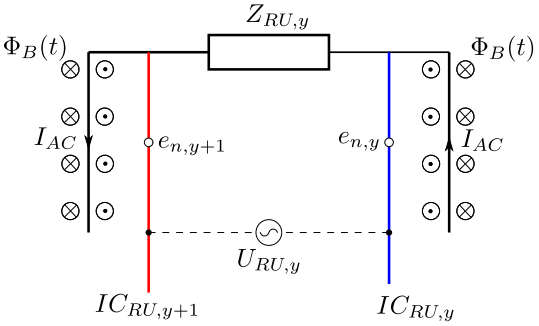


Figure 2.46: Illustration of current and voltage paths when measuring the impedance of even RUs in stack configuration A.

### 2.4.2 Configuration B

Stack configuration B is illustrated in Figure 2.47. The probes for RU voltage measurements connected to the interconnects was placed on top of each other which removed the problem of an alternating measurement configuration between odd and even RUs from configuration A and reduced the area between the voltage probes for the RU voltage measurements. Furthermore, the current connections were moved to the sides of the stack (i.e. further away from the voltage probes), to decrease the interaction with the voltage probes. The impedance spectra for two neighboring RUs from the SOFC stack test of Configuration B is shown in Figure 2.48. A significant difference in the high frequency impedance response was still observed between neighboring RUs, but the systematic error was of a smaller magnitude than observed for the high frequency impedance response in Configuration A in Figure 2.44. Even though the error was reduced in configuration B it was still not possible to accurately measure the series resistance of the RUs.

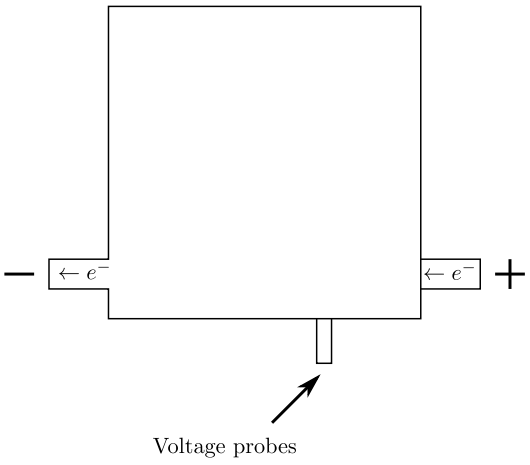


Figure 2.47: Stack Configuration B seen from above

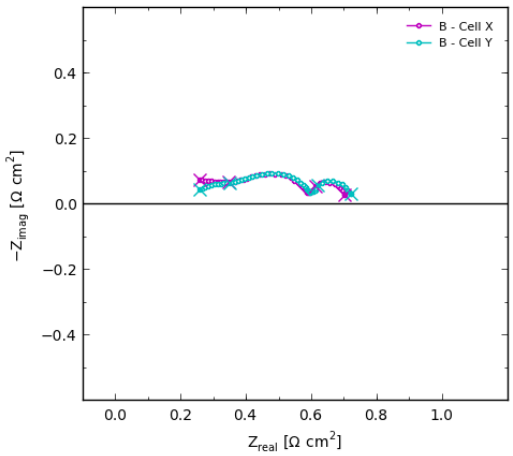


Figure 2.48: Impedance spectra for two RUs with stack configuration B. X corresponds to $50\,kHz$, $5\,kHz$, $500\,Hz$, $50\,Hz$, $5\,Hz$, and $0.5\,Hz$.

### 2.4.3 Configuration C

Stack configuration C is illustrated in Figure 2.49. The geometry of configuration C makes use of the formula given in Equation 2.4 in Section 2.2.1.1 on page 19. The current conduction path which

generates the magnetic flux is perpendicular to the voltage probes, the net induced magnetic flux is zero and hence the mutual inductance is zero (in theory).

The current rod needs to be placed in the diagonal center of the end plate as illustrated in Figure 2.51. The arrows illustrates the current distribution. The AC current from the current rod is equally distributed over the end plate. For ease of explanation it is illustrated in two dimensions only in Figure 2.53. If the current rod is placed in the diagonal center of the current collection plate the two currents will be flowing in opposite directions, therefore the magnetic field, $\Phi_B$, will be equal in magnitude and of opposite directions, thus canceling each other out. This is illustrated in Figure 2.53. If the current rod is placed, e.g, on the left side of the current collection end plate as illustrated in Figure 2.54 the current, $I_{AC}$, in the current collector is flowing in only one direction, the magnetic field will not be canceled out, resulting in a larger magnetic field experienced at the voltage probes. Therefore the best solution for minimizing the magnetic field experienced by the voltage probes is by placing the current rod in the diagonal center of the current plate.

New voltage flaps were designed and placed at the center of one of the interconnect edges. A photo of a voltage flap with a spot welded wire for voltage measurements is shown in Figure 2.52. The impedance spectra of two neighboring RUs obtained in measurement configuration C are shown in Figure 2.50. The two RUs shows similar behavior in the high frequency impedance response. The difference in high frequency impedance response for the two RUs, and the difference in $R_p$ of the two RUs are related to different coatings on the interconnects in the two RUs. With this stack configuration the impedance measurements shows a good high frequency impedance response where the influence of mutual inductance is limited to a minimum and accurate $R_s$ determination and thus an accurate break down of losses can be made.

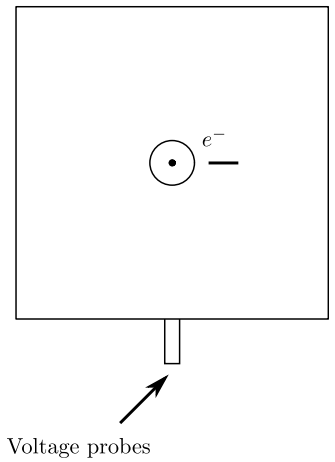


Figure 2.49: Stack Configuration C seen from above

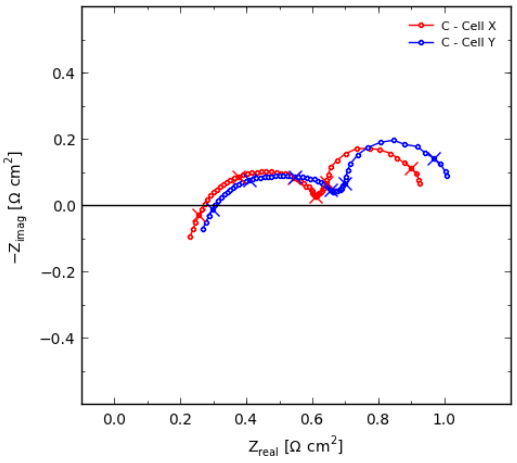


Figure 2.50: Impedance spectra for two RUs with stack configuration C. X corresponds to $50\,kHz$, $5\,kHz$, $500\,Hz$, $50\,Hz$, $5\,Hz$, and $0.5\,Hz$.

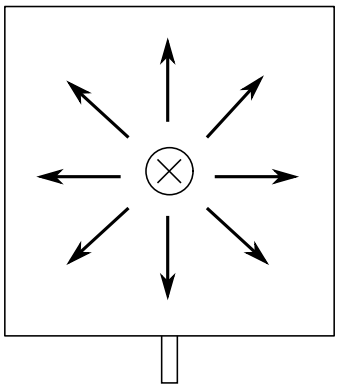

Figure 2.51: Stack Configuration C seen from above. Current direction into the plane. Arrows illustrates current distribution.

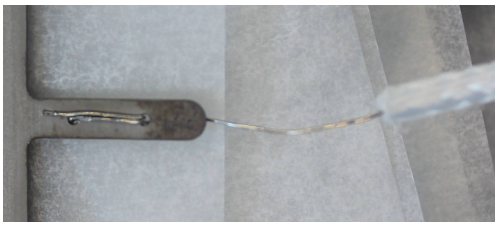

Figure 2.52: Optimized voltage flap for EIS with spot welded wire developed for experimental stack measurement geometry configuration C.

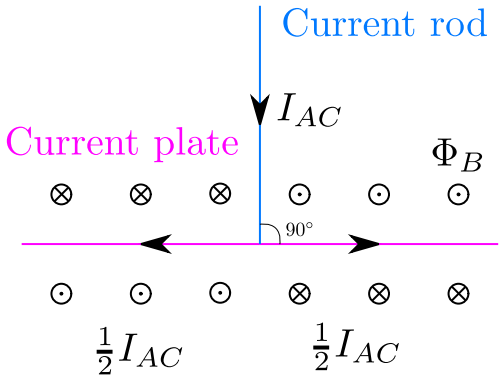


Figure 2.53: 2D illustration of current rod placed in the diagonal center of the current plate. $I_{AC}$ is the AC current and $\Phi_B$ is the magnetic flux. Circle and dot: field lines out of the plane. Circle and cross: field lines into of the plane.

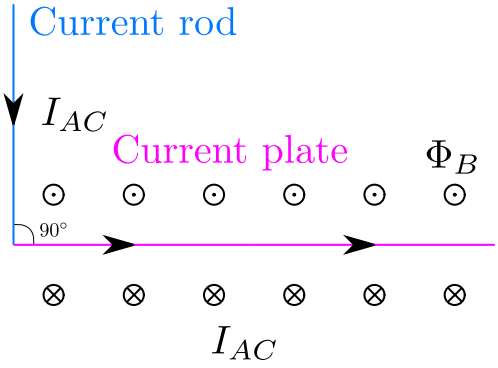


Figure 2.54: 2D illustration of current rod placed in the left side of the current plate. $I_{AC}$ is the AC current and $\Phi_B$ is the magnetic flux. Circle and dot: field lines out of the plane. Circle and cross: field lines into of the plane.

#### 2.4.3.1 Configuration C1 and C2

In order to make space for the mechanical load, the current rod mounted onto the top plate of the stack needs to bended twice. Figure 2.55 shows two different ways to bend the current rod mounted to the top plate. For configuration C1 the second bend is pointing away from the RU voltage probes. In configuration C2 the second bent is pointing towards the RU voltage flaps. Impedance measurements of RUs carried out with Configuration C1 and Configuration C2 are shown in Figure 2.56. Even though the measurements are performed at different temperatures and were thus not truly comparable there is a significant difference in the high frequency response between $40\,kHz$ and $100\,kHz$. Configuration C2 does not intersect the real axis as Configuration C1 does. Configuration C2 might be influenced by a significant contribution of unwanted stray impedances from the current rod. This makes it difficult to estimate $R_s$ for configuration C2. An explanation for the significant influence of unwanted stray impedances could be that bend 2 for Configuration C2 in Figure 2.55 is pointing towards the voltage outlets and parallel current rod is closer to the voltage probes. Right angle bends in a current trace can cause more magnetic flux since the capacitance increases in the region of the corner. Therefore $90°$angle bend should

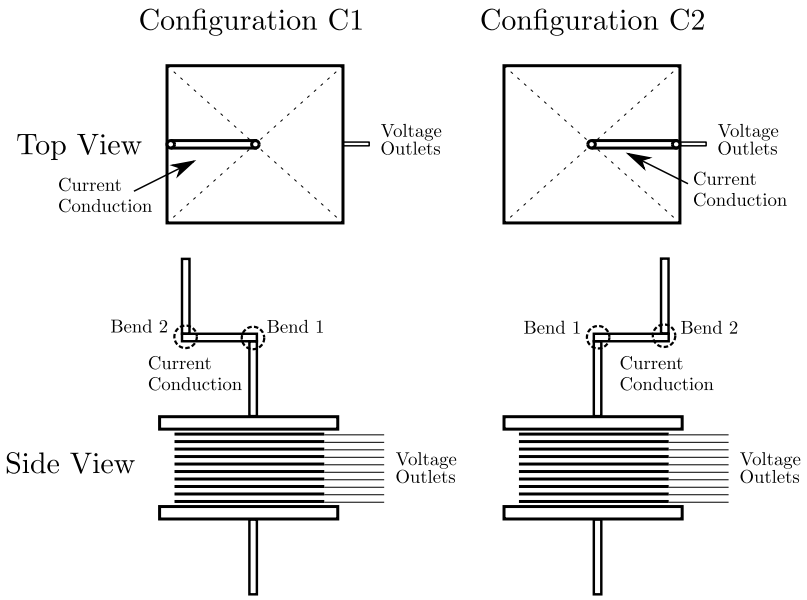


Figure 2.55: Configuration C1 and C2.

be avoided in current traces according to Ref. [68] when designing AC current traces in printed circuit boards. In Figure 2.57 shows recommendations for good right angle bends for traces in printed circuit boards.

### 2.4.4 Configuration D

Configuration C1 yielded a good high frequency response for electrochemical impedance spectroscopy. Experimental stack configuration D shown in Figure 2.58 is an additional improvement to configuration C1 in order to make the experimental stack more technologically relevant.

The experimental SOFC stack optimized for EIS was assembled with frame, insulation plate and current collector plate. To minimize in-plane currents in the stack the top current rod needs to be attached to the current collector plate directly. The current collector plate is thin metal plate which makes it hard to attach a current rod. However, this could be done by welding a nut to the current collector plate. When the nut is mounted to the current collector plate the current rod can be mounted to the nut. With the top current rod mounted to the current collector plate a hole needs to made in the isolation plate and the top plate. To prevent in plane currents, it is important that the current rod does not touch the top plate. This can be done by insulating the current rod with an alumina tube.

Impedance measurements recorded for the complete stack is shown in Figure 2.59. Three repeating units (RU04, RU08 and RU12) seems to have a higher inductance compared to the rest of the repeating units. A possible cause of this may be found by the twisted pair configuration of the stack illustrated in Figure 2.60. IC01-IC15 is the interconnect wires for the 14 RUs. IC00 is the wire connected to the bottom plate and IC16 is the wire connected to the top plate. IC01 and IC02 measures the differential voltage across RU01 and IC02 and IC03 measures the differential voltage across RU02 and so forth. The wires are twisted paired into four bundles. The wires to measure the differential voltages across RU04, RU08 and RU12 are not twisted paired into any bundle for practical reasons. A future improvement for the stack measurement geometry could be to have two wires for each interconnects, which makes single twisted paired possible for each differential voltage measurement.

Impedance measurements for configuration D recorded at four different DC current amplitudes are shown in Figure 2.61. The Kramers-Kronig test relative residuals showed to increase between $10\,kHz$ and $30\,kHz$ with increasing DC current amplitudes. A possible explanation could be that the electronic load (Zahner EL1000) changes AC characteristics with changing DC

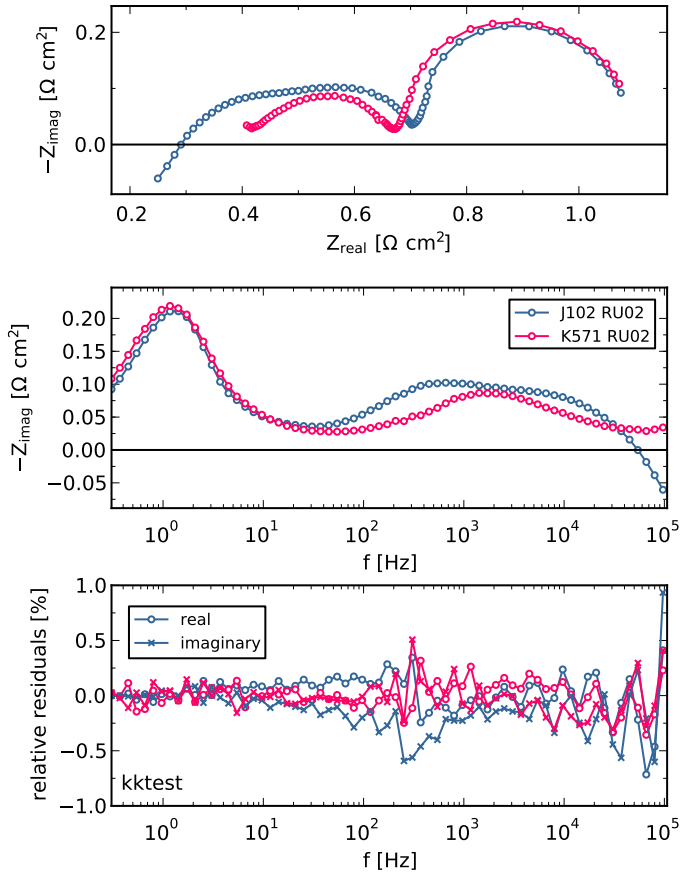


Figure 2.56: RU impedance spectra for configuration C1 and C2.

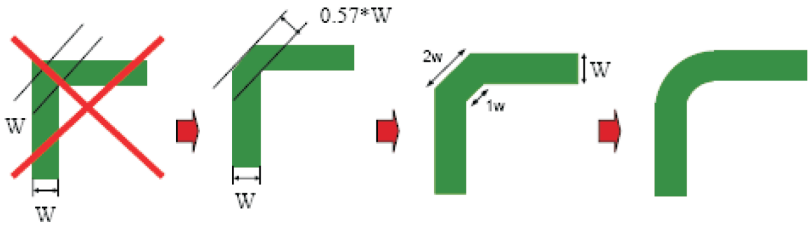


Figure 2.57: Poor and good right angle bends recommended by [68] for printed circuit board design. From Ref. [68].

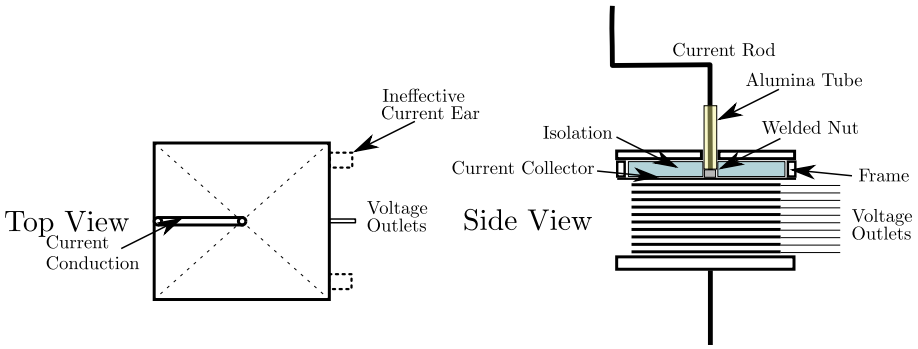


Figure 2.58: Illustration of experimental stack configuration D.

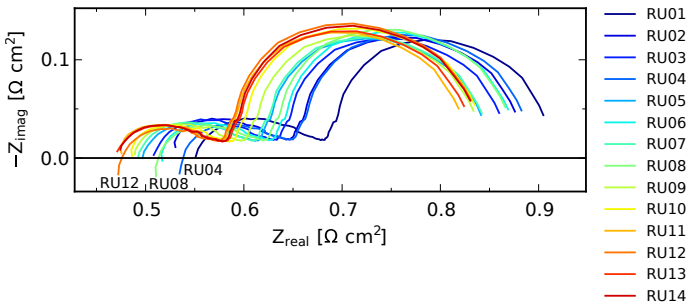


Figure 2.59: Impedance measurements for the 14 RUs in the stack measured at recorded at DC current of $4\,A$ and AC peak current at $3.8\,A$ Temperature: $700°C$ Fuel: $20\%\,H_2O$ and $80\%\,H_2$ Oxidant: Air.

characteristics.

### 2.4.5 Conclusion on optimizing stack measurement geometries

Four different stack measurement geometries configurations were tested by carrying out electrochemical impedance spectroscopy to investigate the high frequency response from the repeating units (RU) in the stack. In configuration A the current path was placed close to the RU wires for voltage measurements and showed large differences in the high frequency impedance response between neighboring RUs. The current rods induced mutual inductance in the RU wires for voltage measurements which had a large influence on the impedance measured at high frequencies. The distance between the current path and the wires for voltage measurements was increased in Configuration B which decreased the deviation at high frequencies, but there was still a deviation in the observed high frequency impedance between neighboring RUs which made it very challenging to accurately determine the series resistance. In configuration C the current feed was placed in the diagonal center of the current plate and perpendicular to the RU wires for voltage measurement which gave a significant improvement to the uniformity in high frequency impedance response from the different RUs. Configuration D was an additional improvement to configuration C to make the experimental stack more technological relevant while keeping the uniformity in high frequency impedance response from the different RUs. Configuration D showed a very weak decrease in measurement quality with increasing DC current which cause has not been found in this work.

## 2.5 Conclusion and discussion on improving EIS on SOFC stacks

This section summarizes the main conclusions for improving electrochemical impedance spectroscopy (EIS) on SOFC stacks. The improvements includes electrical considerations, two impedance

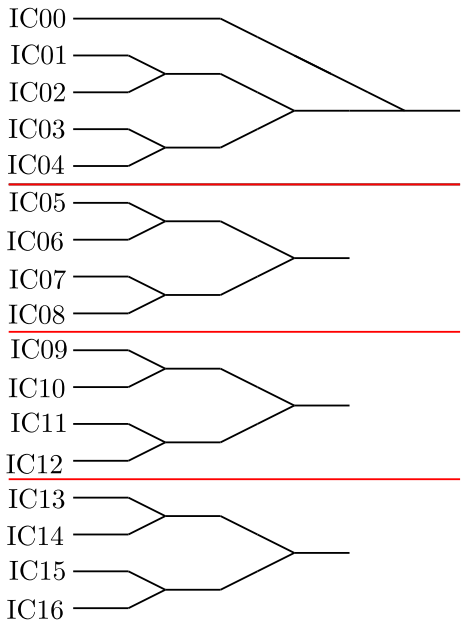


Figure 2.60: Twisted pair configuration for experimental stack configuration D.

measurement setups optimized for EIS on SOFC stacks together with the main conclusions for optimizing the stack measurement geometry for EIS.

### 2.5.1 Electrical considerations

Electrical and electromagnetic considerations relevant for low impedance measurements were discussed. To minimize the induced magnetic flux in any given measurement setup, it is important that current conducting wires are perpendicular to wires for voltage measurements to prevent induced magnetic flux. Magnetic flux generates mutual- and self-inductance in wires together with skin and proximity effects. The effect of different noise sources was discussed together with a discussion of cable configurations that could limit the induced magnetic flux for low impedance measurements. Furthermore three signal-modes relevant for optimizing the measurement accuracy of the frequency response analyzers were described .

### 2.5.2 Sequential Impedance Measurement Setup

A sequential impedance measurement setup was constructed and tested. Several modifications were made to improve the high frequency impedance response with Solartron FRAs. The AC current signal was boosted from $60\,mA$ to $3\,A$ with a bipolar operational power supply/amplifier. The current through the stack was measured with a current transducer with a linear impedance response up to $200\,kHz$. A combined DC and common mode voltage cancellation circuit was designed and implemented in the test setup. The DC and common mode voltage cancellation circuit removed the common mode voltage and DC differential voltage which improved the measurement accuracy significantly. With a combination of measurements carried out using AC and DC coupling it was possible to improve the high frequency impedance response significantly. Automation of the impedance measurements was done with the implementation of multiplexer which switched between repeating units in the stack for automated sequential impedance measurements. It was found that when bypassing the combined DC and common mode cancellation circuit in the AC coupling mode this lead to a significant decrease in precision. The multiplexer solution was therefore discontinued and the sequential impedance measurements were recorded manually, in order to maintain satisfactory measurement accuracy.

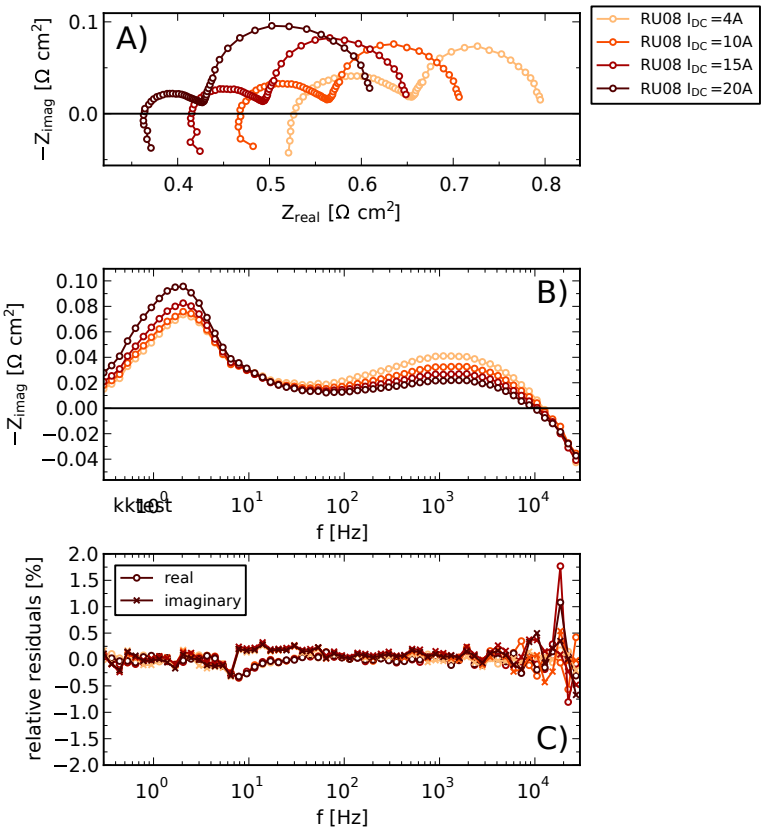


Figure 2.61: Impedance measurements for RU08 at a AC peak current of $3.8\,A$ four different DC currents, $4\,A$, $10\,A$, $15\,A$ and $20\,A$ measured at $700°C$ Fuel: $50\%\,H_2O$ and $50\%\,H_2$ Oxidant: Air. A) EIS spectra B) Corresponding imaginary impedance vs frequency C) Corresponding relative residuals from the linear Kramers-Kronig transform test.

### 2.5.3 Parallel Impedance Measurement Setup

A parallel impedance measurement setup was constructed and tested. The impedance setup was capable of recording the impedance of 16 series connected repeating units and the stack impedance simultaneously and could be operated in a fully automated fashion by the test rig computer. The parallel acquisition of impedance data results in a significantly reduced measurement time, with a complete characterization of the stack and all RUs in less than one hour, which would take at least 16 hours of measurement time using the sequential set-up. Software was written in several programming languages in order to set up automated communication between the test rig computer and the computer recording the EIS measurements. A power relay was implemented in the test rig to cut off the impedance equipment from the SOFC stack if repeating unit voltages exceed set over- or under-voltage limits. The setup eliminated the need for: manual operation, DC and common mode cancellation boxes, AC and DC coupling procedures.

### 2.5.4 Optimizing stack measurement geometries

Four different stack measurement geometries were tested with EIS to investigate the high frequency response from the repeating units (RUs). In configuration A the current path was placed to close to the RU wires for voltage measurements and showed large deviations in the high frequency impedance response between neighboring RUs. The current rods induced mutual induc-

tance in the RU wires for voltage measurements which had a large influence on the impedance measured at high frequencies. The distance between the current path and the wires for voltage measurements was increased in Configuration B and although this decreased the deviation at high frequencies significantly, there was still a deviation in the RU high frequency measurement between neighboring cells which made it very challenging to accurately determine the series resistance. In configuration C the current path was placed in the diagonal center of the current plate and perpendicular to the RU wires for voltage measurement which gave a significant improvement of the uniformity in the high frequency impedance response from the different RUs. Configuration D was an additional improvement to configuration C to make the experimental stack more technological relevant while keeping the uniformity in high frequency impedance response from the different RUs. Configuration D showed a decrease in measurement quality with increasing DC current the cause of which has not been established in this work. Based on the results obtained it is highly recommended to place the current rods in the diagonal center of the current plates and perpendicular to twisted paired wires for voltage measurements.

CHAPTER 3

# Experimental Setups

This chapter describes the test rig used for operating the SOFC stacks in this work. Descriptions of the two experimental setups based on the results given in the previous chapter are given. The first experimental setup is for a Cross-flow stack monitored with sequential acquisition of impedance measurements using a Solartron Frequency Response Analyzer. The second experimental setup is for a Co-flow stack monitored with parallel acquisition of impedance measurements using a Zahner IM6 potentiostat and a Zahner EL1000 electronic load. Both measurement test setup is described including the stack configuration and a validation of the quality of the impedance measurements.

## 3.1 Test rig

All the SOFC stacks tested in this work was operated in custom build SOFC stack test rig supplied by FuelCon AG. The name of the test rig is FuelCon Evaluator-S with test stand number 70390. For more information about SOFC test rigs from FuelCon AG take a look at reference [69]. A picture of one of the tested SOFC stacks mounted in the FuelCon test rig is shown in Figure 3.1. For operation, the test rig is supplied with the FuelWork Enterprise Edition software. Figure 3.2 shows a screen shot of the main view of the FuelWork software. For full automation of the test rig Visual Basic programs can be made. The Visual Basic programs can be activated through the FuelWork Task Window and communication with the rig parameters is done by writing to the FuelWork variables called tags. Important parameters and its ranges for the test rig is given in Table 3.1.

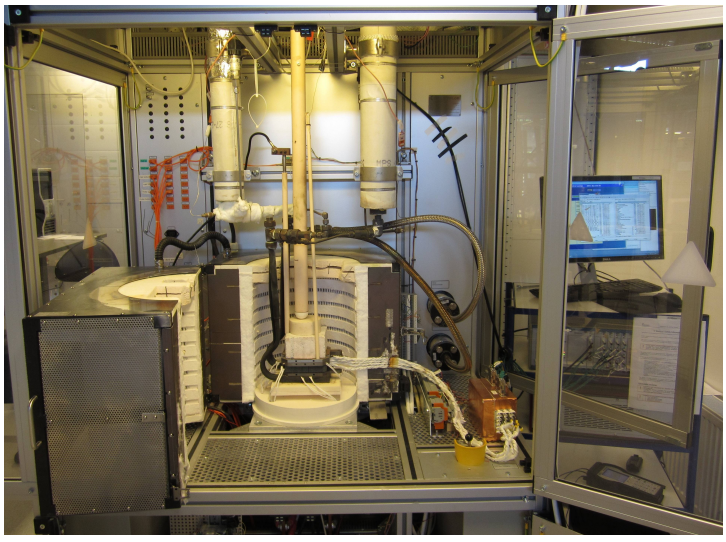

Figure 3.1: SOFC stack mounted in the FuelCon test rig.

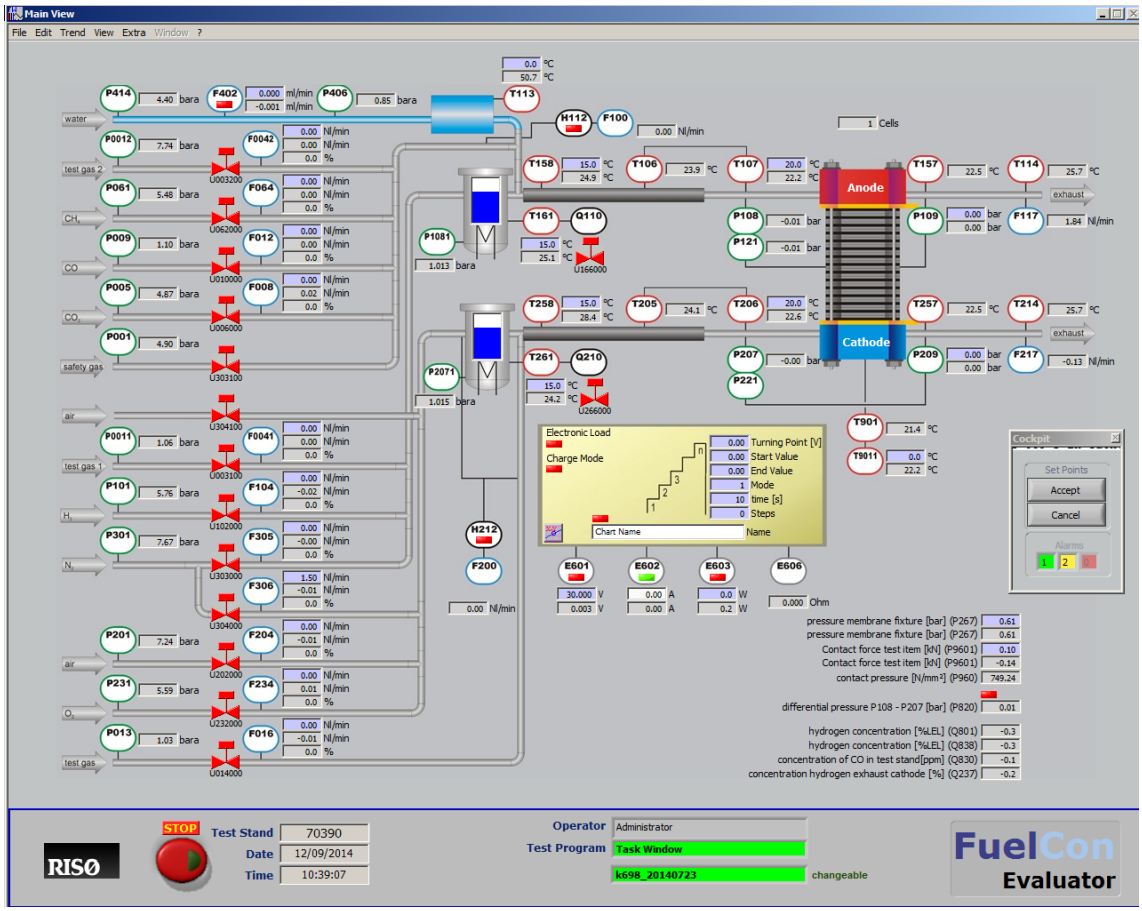


Figure 3.2: Screenshot of the main view of the FuelCon test rig.

## 3.2 Cross-flow stack monitored with sequential impedance measurements

The solid oxide fuel cells (SOFC) used for the 13-cell experimental cross flow fuel cell stack were planar anode-supported SOFCs (Ni-YSZ/YSZ/LSM-YSZ) of $12\,cm$ x $12\,cm$ footprint and an active area of approximately $90\,cm^2$. The cell details can be found elsewhere [66]. Interconnects were made of commercial stainless steel. Different coatings were used on the interconnects in the stack (see Table 3.2) to prevent chromium poisoning on the cathode side [70]. The nickel oxide in the Ni-YSZ electrode was reduced to nickel in hydrogen at start-up and the stack was subsequently tested for performance and durability. The stack testing was performed at DTU Energy Conversion with an experimental stack (serial number J-102) manufactured by Topsoe Fuel Cell A/S (TOFC).

The stack was sealed along the edges with a glass seal designed by TOFC. The fuel cell stack can be considered to consist of a number of repeating units (RU). Each repeating unit contains interconnects, glass seals and a cell. A schematic representation of the experimental stack is shown in Figure 3.3.

An illustration of the test set-up is shown in Figure 3.4. The EIS computer controls the Solartron 1255 or 1260 Frequency Response Analyzer (FRA), via a GPIB communication bus. Explanation of the FRAs are given in Section 2.3.1 on page 27. The FRA sends an AC voltage signal from the generator output to the programmable input (Prg. Input) of a Kepco Bipolar Operational Amplifier 20-20D (Op-Amp) explained in Section 2.3.2.1 on page 29. The Op-Amp converts the AC voltage signal to a corresponding AC current signal with a current-to-voltage ratio of $1\,AV^{-1}$. The generated AC current through the SOFC stack is superimposed on the DC current provided by the electronic load of the test rig. Four terminal measurements were used to measure

| **Supplied to the:** | **Parameter** Name | Variable | **Range** From | To | Unit |
|---|---|---|---|---|---|
| Anode | Water supply | $\dot{V}_{\mathrm{H_2O}}$ | 0 | 10 | $\frac{mL}{min}$ |
| | Methane flow | $\dot{V}_{\mathrm{CH_4}}$ | 0 | 5 | $\frac{NL}{min}$ |
| | Carbon monoxide flow | $\dot{V}_{\mathrm{CO}}$ | 0 | 2.5 | $\frac{NL}{min}$ |
| | Carbon dioxide flow | $\dot{V}_{\mathrm{CO_2}}$ | 0 | 5 | $\frac{NL}{min}$ |
| | Hydrogen flow | $\dot{V}_{\mathrm{H_2}}$ | 0 | 15 | $\frac{NL}{min}$ |
| | Nitrogen flow | $\dot{V}_{\mathrm{N_2}}$ | 0 | 5 | $\frac{NL}{min}$ |
| | Safety gas flow | $\dot{V}_{safety,anode}$ | 0 | 50 | $\frac{NL}{h}$ |
| | Bubbler temperature | $T_{bubler,anode}$ | 0 | 85 | $^{\circ}C$ |
| | Temperature Preheat 1 | $T_{Pre1,anode}$ | 0 | 200 | $^{\circ}C$ |
| | Temperature Preheat 2 | $T_{Pre2,anode}$ | 0 | 800 | $^{\circ}C$ |
| Cathode | Air | $\dot{V}_{Air}$ | 0 | 50 | $\frac{NL}{min}$ |
| | Oxygen | $\dot{V}_{\mathrm{O_2}}$ | 0 | 10 | $\frac{NL}{min}$ |
| | Safety | $\dot{V}_{safety,cath}$ | 0 | 50 | $\frac{NL}{h}$ |
| | Bubbler temperature | $T_{bubler,cath}$ | 0 | 60 | $^{\circ}C$ |
| | Preheat 1 | $T_{Pre1,cath}$ | 0 | 200 | $^{\circ}C$ |
| | Preheat 2 | $T_{Pre2,cath}$ | 0 | 800 | $^{\circ}C$ |
| Stack | Furnace temperature | $T_{Furnace}$ | 20 | 1000 | $^{\circ}C$ |
| | Mechanical load | $F_{Load}$ | 0 | 10 | $kN$ |
| | DC load current | $I_{DC}$ | 0 | 400 | $A$ |

Table 3.1: Important parameters and ranges for the FuelCon FuelCon Evaluator-S with test stand number 70390 used in this work for SOFC stack testing.

| RU | IC Coating | RU | IC Coating | RU | IC Coating |
|---|---|---|---|---|---|
| #1 | st.cer.coat | #6 | Cu | #11 | Cu LSM ws |
| #2 | st.cer.coat | #7 | LSM ws | #12 | Cu |
| #3 | Co | #8 | st.cer.coat | #13 | Co |
| #4 | Co LSM ws | #9 | LSM ws | | |
| #5 | Co LSM ws | #10 | Co LSM ws | | |

Table 3.2: RUs and the corresponding interconnect (IC) coating towards the cathode side. Abbreviations: Wet sprayed, ws, Standard ceramic coat, st.cer.coat.

the (time-dependent) currents and voltages of the RUs. The voltage of a RU was measured by a differential probe connected to the differential input V1 on the FRA. The current through the stack was measured with an active current transducer (LEM ITN 600-s) which has a linear response up to $200\,kHz$. The DC voltages were minimized by additional active electrical circuits in order to utilize the highest measurement resolution on the FRA. The DC + CMR Box is a combined DC cancellation and common mode rejection box 2.3.2.3 on page 31. The DC box is a DC cancellation box and the Rm Box is a box containing the measurement resistor for the current transducer for measuring the current through the SOFC stack as explained previously in Section 2.3.2.2 on page 30. Figure 3.5 and Figure 3.6 shows the cross flow stack mounted in the furnace. The wires for voltage measurements of the RUs passes through the vertical gas pipes for the manifold. All the other wires were custom made temperature probes for internal stack temperature measurements. The temperature measurements was unsuccessful and are therefore not described in this work. The impedance measurements were not corrected for wire inductances and stray capacitances in the test setup. It is estimated that this will give a measurement error of less than $10\%$ for the series resistances and a measurement error of less than $3\%$ for the polarization resistances as explained in Section 2.3.2.6 on page 37. EIS spectra were recorded from $97\,kHz$ to $0.3\,Hz$ with an AC current modulation of $0.8\,A$ $\left(8.7\,mA\,cm^{-2}\right)$ at OCV or on top of the nominal DC current of $20\,A$ $\left(0.2\,A\,cm^{-2}\right)$ during the galvanostatic long term degradation test. The settings for the

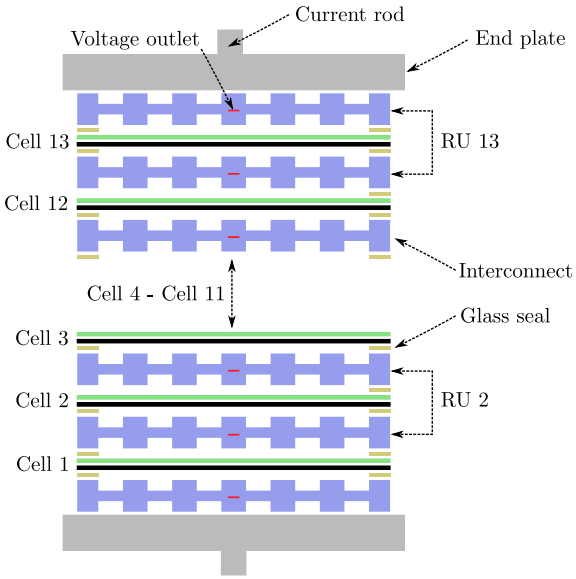


Figure 3.3: Schematic representation of the experimental cross-flow stack.

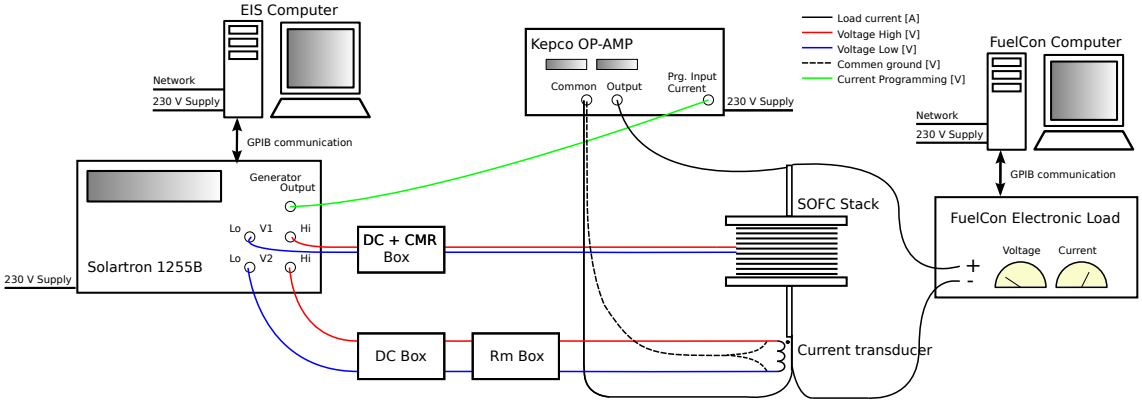


Figure 3.4: Illustration of the test set-up for the cross flow stack measured with sequential impedance measurements.

impedance measurements and and the selection of the AC current amplitude are given in the next section.

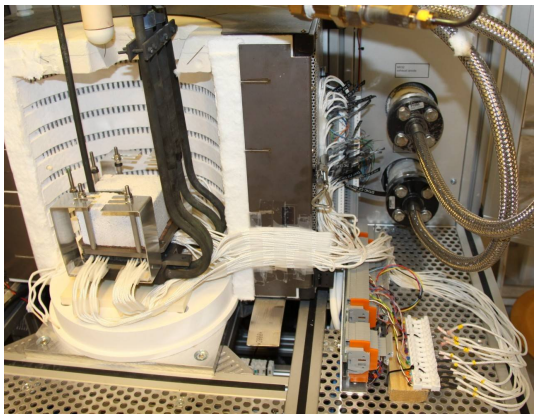

Figure 3.5: Side view of the cross flow stack mounted in the furnace.

Figure 3.6: Zoom of the cross flow stack mounted in the furnace.

#### 3.2.0.1 EIS settings and selection of AC amplitude

Impedance measurements was recorded from $969\,kHz$ to $300\,mHz$. From $969\,kHz$ to $66\,Hz$ measurements was recorded with $12$ points per decade with an integration time of $200$ measure periods. From $66\,Hz$ to $300\,mHz$ measurements was recorded with $12$ points per decade with an integration time of $75$ measure periods. Measurements from $969\,kHz$ to $100\,kHz$ was removed in the data analysis software. Three different AC current amplitudes was tested with Kramers-Kronig test [22] at OCV to find the AC current amplitude with the lowest Kramers-Kronig test relative residuals. Figure 3.7 shows impedance measurement at AC RMS current amplitudes of $0.25\,A$, $0.5\,A$ and $1.0\,A$. Figure 3.7 C) shows relative residuals from the Kramers-Kronig test. Impedance measurements for the $14$ RUs in the stack in Figure 3.13 shows relative residuals below $\pm 0.5\%$ for the Kramers-Kronig test in the frequency range from $0.3\,Hz$ to $100\,kHz$. Impedance measurements for all three amplitudes gives nearly the same relative residuals. It was selected to use an AC RMS amplitude of $0.8\,A$.

## 3.3 Co-flow stack monitored with parallel impedance measurements

The solid oxide fuel cells (SOFC) used were planar anode supported cells with Ni/YSZ anode supports, Ni/YSZ anodes, YSZ electrolytes, CGO barrier layers and LSCF/CGO composite cathodes [67]. The cells were used in a 14-cell fuel cell stack in a co-flow configuration with an active area of approximately $90\,cm^2$. The interconnect plates were made of commercial stainless steel. Coatings were used on the interconnects in the stack to prevent chromium poisoning on the cathode side [70]. The stack was heated up with flowing nitrogen fed to the anode and flowing air fed to the cathode. The nickel oxide in the Ni-YSZ electrodes was reduced to nickel in hydrogen at start-up at a temperature greater than normal operating temperature and the stack was subsequently tested for performance and durability. The stack testing was performed at DTU Energy Conversion using an experimental stack with serial number K-708 manufactured by Topsoe Fuel Cell A/S (TOFC). The fuel cell stack can be considered to consist of a number of repeating units (RU). Each repeating unit consists of interconnects, glass seals and a cell. A schematic representation of the experimental stack is shown in Figure 3.8.

The stack was tested using an automated test rig purchased from FuelCon AG, and characterized using Electrochemical Impedance Spectroscopy (EIS) and Total Harmonic Distortion (THD). An illustration of the EIS test set-up is shown in Figure 3.9. The test rig computer controls the EIS computer via a network connection. The EIS computer controls the Zahner IM6 Potentiostat via a USB connection. The Zahner IM6 controls the Zahner EL1000 Electronic Load via an EPC connection which is a custom cable with a D-Sub9 plug and a Lemosa plug made by ZAHNER-

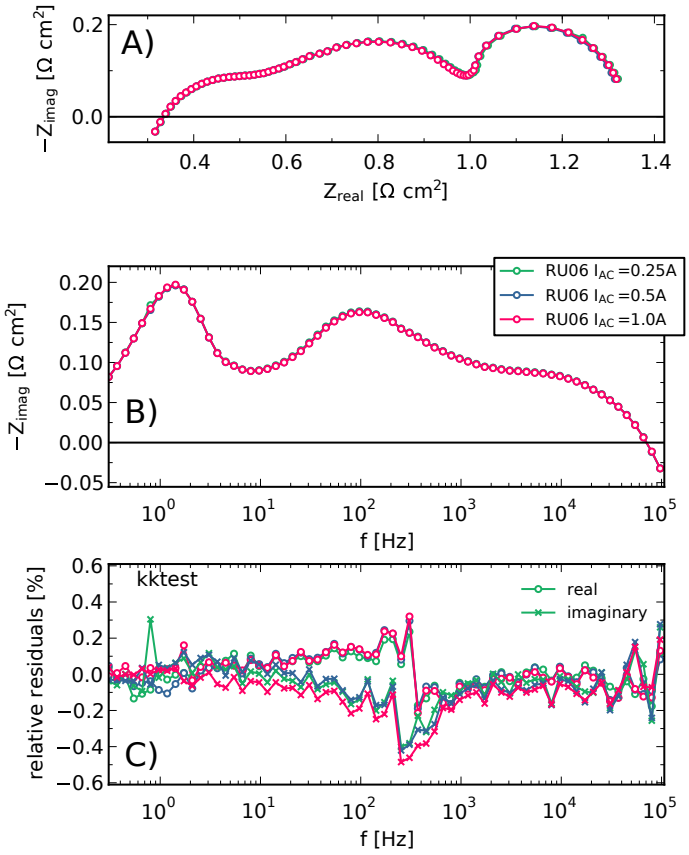


Figure 3.7: Impedance measurements for RU08 at three different AC RMS amplitudes, $0.25\,A$, $0.5\,A$ and $1.0\,A$. A) EIS spectra for the 14 RUs in the stack measured at OCV and $750°C$ Fuel: $20\%\,H_2O$ and $80\%\,H_2$and Oxidant: Air B) Corresponding imaginary impedance vs frequency C) Corresponding relative residuals from the linear Kramers-Kronig transform test.

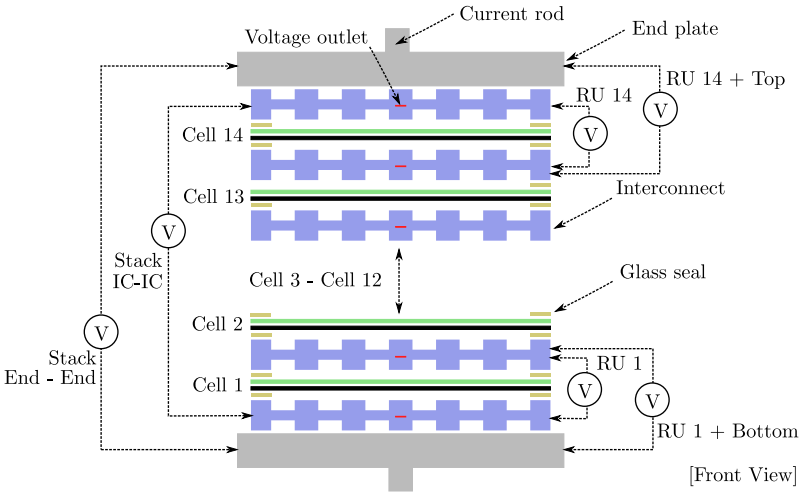


Figure 3.8: A schematic representation of the experimental co-flow stack.

elektrik GmbH & Co. KG. In combination the Zahner IM6 and the Zahner EL1000 can record EIS measurements of the stack and 16 RUs simultaneously. The DC current is measured by a current transducer, LEM ITN-600s, and the data is logged by the test rig control computer via a data logger using a data logging script running programmed in Visual Basic. A power relay is implemented in the set-up in order to disconnect the Zahner IM6 and the Zahner EL1000 if the cell voltages exceed set over- or under-voltage limits ($0.6V$ and $1.5V$, respectively). The power relay is explained in Section 2.3.3.3 on page 45. The complete test set-up is fully automated. The automation software is explained in Section 2.3.3.2 on page 44. EIS measurements were recorded on $14$ RUs and the stack simultaneously. EIS settings and the selection of the AC current amplitude is given in the next section. The software from ZAHNER-elektrik GmbH & Co. KG allows measurements of the harmonic distortion (THD) from the $2^{nd}$ to the $10^{th}$ order higher harmonic frequencies from the main voltage channel.

A harmonic of a sine wave is a frequency component of the signal that is an integer multiple of the fundamental frequency, e.g if the fundamental frequency is $f\,[Hz]$, the harmonics of the fundamental frequency is $2f$, $3f$, to $n\,f$. When the device under test is linear the voltage response of the higher harmonics $U_2$, $U_3$ to $U_n$ is ideally zero. If the device under test becomes nonlinear voltage response of the higher harmonics $U_2$, $U_3$ to $U_n$ increases.

For the current test the stack sum voltage (top to bottom interconnect) shown in Figure 3.8 was connected to the main channel in order to obtain the THD of the whole stack. The general equation for the THD can be calculated as given in Equation 3.1 [44]. The higher harmonics recorded by the Zahner system are prepossessed in a way that they can be used directly for second harmonic analysis or harmonic distortion analysis [54]. The THD in percent from the preprocessed $2^{nd}$ to the $10^{th}$ order harmonics which are already normalized to the fundamental frequency from the Zahner system can be calculated as given in Equation 3.2 [71].

$$\%THD = \frac{\sqrt{\sum_{n=2}^{\infty} U_n^2}}{U_1} \cdot 100\% \tag{3.1}$$

$$\%THD_{Zahner} = \sqrt{U_2^2 + U_3^2 + \ldots + U_{10}^2} \cdot 100\% \tag{3.2}$$

An investigation of the optimal geometrical placement of the current probes and voltage probes was carried out in order to minimize measurement errors caused by stray impedances. The voltage probes needed to be placed perpendicular to the current feeds to minimize the effect of stray impedances as much as possible. Details on optimizing this set-up was reported previously in Section 2.4 on page 46. Figure 3.10 and Figure 3.11 show the experimental stack mounted in the furnace. Wires for the repeating unit voltage measurements was twisted paired to reduce the mutual inductance as explained in Section 2.2.2.3 on page 25.

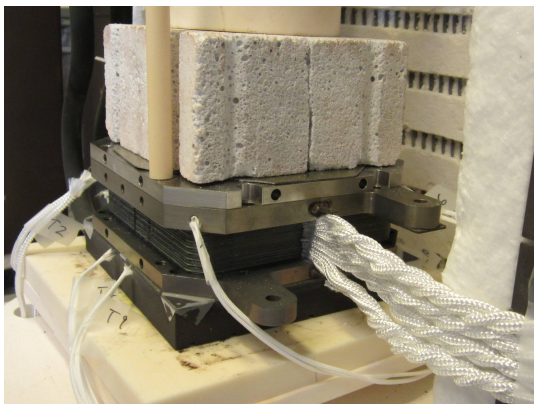

Figure 3.10: Front view of the stack mounted in the furnace.

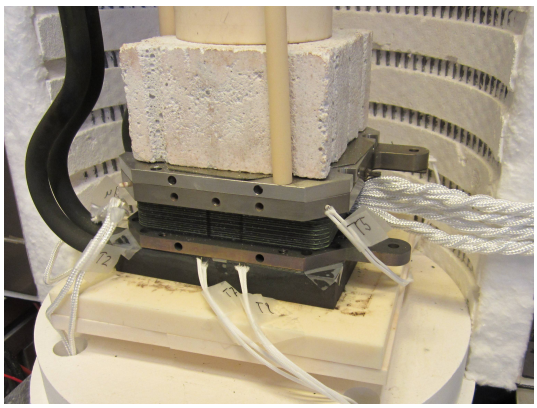

Figure 3.11: Side view of the stack mounted in the furnace.

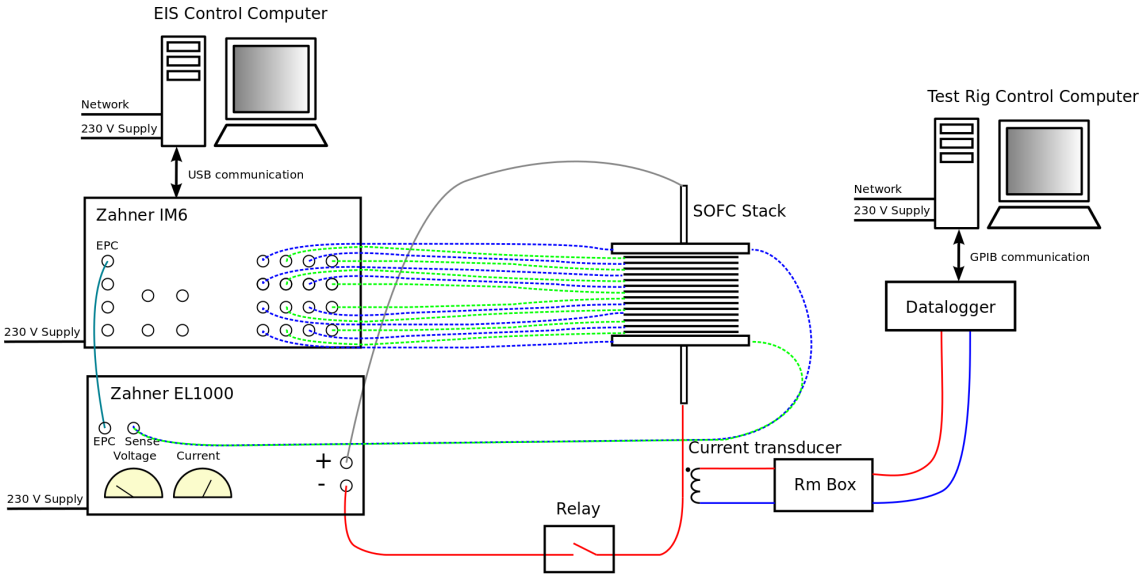


Figure 3.9: Illustration of the test set-up for parallel impedance and THD measurements on SOFC stacks.

#### 3.3.0.2 EIS settings and selection of AC current amplitude

Impedance measurements was recorded from $969\,kHz$ to $300\,mHz$ with $12$ points per decade. From $969\,kHz$ to $66\,Hz$ measurements was recorded with an integration time of $200$ measure periods. From $66\,Hz$ to $300\,mHz$ measurements was recorded with an integration time of $75$ measure periods. Measurements from $969\,kHz$ to $20\,kHz$ was removed in the data analysis software. The DC current applied when recording impedance measurements was minimum $4\,A$. Three different AC current amplitudes was tested with Kramers-Kronig test [22] to find the AC current amplitude with the lowest relative residuals. Figure 3.12 show impedance measurement at AC peak current amplitudes of $0.9\,A$, $1.9\,A$ and $3.8\,A$. Figure 3.12 C) shows relative residuals from the Kramers-Kronig test. The AC peak current amplitude of $3.8\,A$ shows the lowest relative residuals at high frequencies and is therefore selected as the amplitude for the parallel impedance measurement setup. Impedance measurements for the 14 RUs in the stack in Figure 3.13 shows relative residuals below $\pm 0.5\%$ for the Kramers-Kronig test in the frequency range from $0.3\,Hz$ to $20\,kHz$.

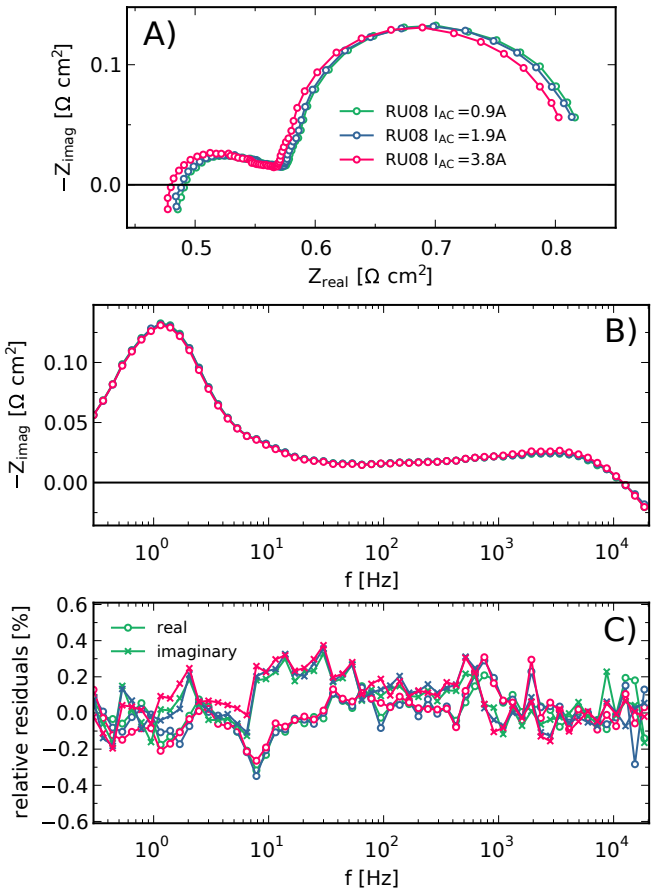


Figure 3.12: Impedance measurements for RU08 at three different AC peak amplitudes, $0.9\,A$, $1.9\,A$ and $3.8\,A$. A) EIS spectra for the 14 RUs in the stack measured at $700°C$ Fuel: $20\%\,H_2O$ and $80\%\,H_2$and with a DC load of $4\,A$ Oxidant: Air B) Corresponding imaginary impedance vs frequency C) Corresponding relative residuals from the linear Kramers-Kronig transform test.

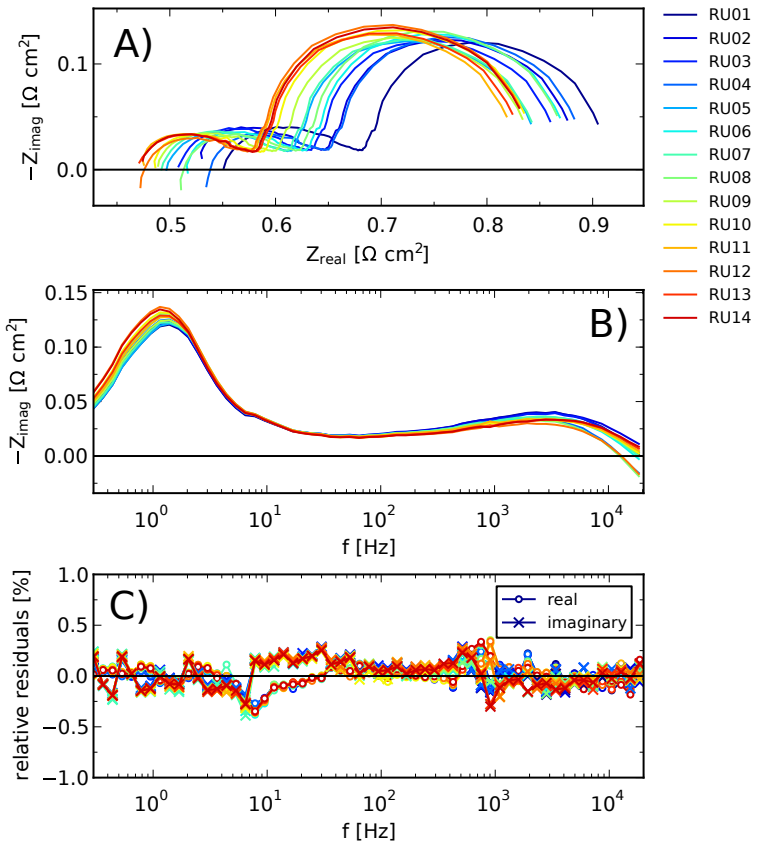


Figure 3.13: Impedance measurements for the 14 RUs in the stack measured at recorded at DC current of $4\,A$ and AC peak current at $3.8\,A$ Temperature: $700°C$ Fuel: $20\%\,H_2O$ and $80\%\,H_2$ Oxidant: Air A) EIS spectra B) Corresponding imaginary impedance vs frequency C) Corresponding relative residuals from the linear Kramers-Kronig transform test.

CHAPTER 4

# Stack Degradation Monitoring

The promotion and marketing of power generation, regardless of technology, requires demonstrated ability to convert fuel to electric energy at low amortized cost. Given the high capital costs of most fuel cell technologies, low amortized costs can only be achieved with long lifetimes. Therefore, degradation behavior remains a key concern for all fuel cell types (PEMFC, AFC, PAFC, SOFC, MCFC, etc.). Past research in solid oxide fuel cell stack degradation assessment and improvement has mainly focused on cell operating voltage (efficiency) [72]. Related to this metric, but distinct and equally important, is performance degradation related to resistance increases in the different layers of the SOFC stack. This chapter examines repeating units and stack degradation by electrochemical impedance spectroscopy and indicate electrode specific degradation phenomena. The chapter is divided into two main parts: 1) Cathode related time stack degradation monitoring. The purpose of this test was to investigate cathode degradation of cells in the stack when different protective coatings was applied to the oxidant side of the interconnects. 2) Anode related stack degradation monitoring. The purpose of this test was to investigate the rapid degradation observed after constant current was applied to the stack.

## 4.1 Cathode related stack degradation monitoring

The section about cathode related time dependent stack degradation monitoring and investigate the performance changes detail by the characterization of a 13-cell stack each with different types of protective coatings on the metallic interconnects. The stack was tested for more than $2,500$ hours at steady operating conditions. EIS was used to examine the long-term behavior and monitor the evolution of the series and polarization resistances for four out of the $13$ repeating units during the first $1,400$ hours of operation. The losses for the four selected repeating units are reported and discussed. All text and figures related to the cathode related stack degradation monitoring was published in the conference proceeding Paper A on page 131 and was later upgraded to a peer reviewed journal as Paper B on page 143.

### 4.1.1 Experiments

Prior to the long term degradation test the performance of the stack was determined by measuring polarization curves and electrochemical impedance spectra at 700, 750, and $800°C$ with $80\%$ $H_2$ + $20\%$ $H_2O$ as fuel and air as the oxidant. Temperature monitoring was performed using four type S (Pt/Pt-Rh) thermocouples mounted in the top and bottom end plates in the cold and hot corners which are illustrated for a cross flow configuration in Figure 1.7 on page 8. The long term degradation test was carried out at constant current (galvanostatic) conditions at $0.2\,A\,cm^{-2}$ and the average stack temperature set to $750°C$. The fuel was $H_2$ with $4\%$ $H_2O$ the oxidant was air. After $200\,h$, $4\%$ $H_2O$ was added to the air. The fuel and oxygen utilization was $52\%$ and $19\%$, respectively. Further details regarding the stack and the experimental setup is given in Section 3.2 on page 60.

### 4.1.2 Results

This section presents the results for the cathode related time dependent stack degradation test. The initial performance is presented together with the long term degradation behavior. Impedance

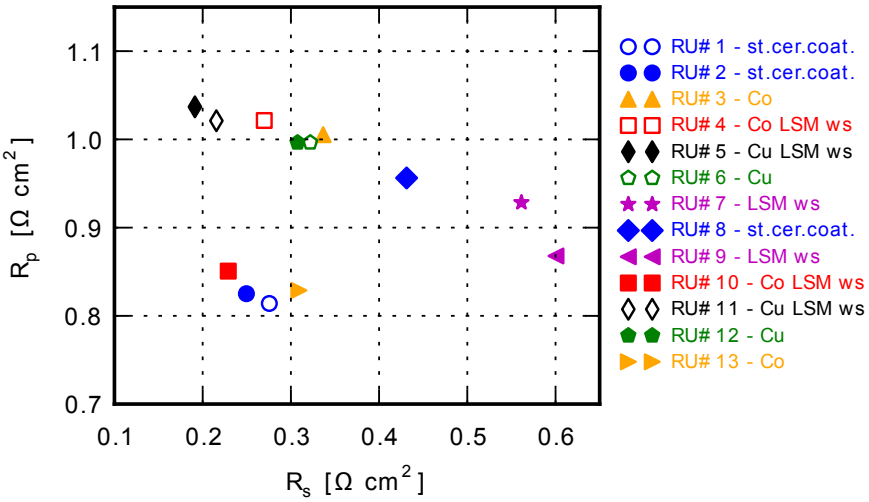


Figure 4.1: Initial performance of the cells in the stack measured at OCV with EIS. Temperature: $750°C$ Fuel: $80\%$ $H_2$ with $20\%$ $H_2O$. Oxidant: Air.

| RU | IC Coating | $E_a$ for $R_s$ | $E_a$ for $R_p$ |
|---|---|---|---|
| #2 | st.cer.coat | $0.70\,eV$ | $0.62\,eV$ |
| #4 | Co LSM ws | $0.74\,eV$ | $0.85\,eV$ |
| #6 | Cu | $0.78\,eV$ | $1.04\,eV$ |
| #11 | Cu LSM ws | $0.77\,eV$ | $1.06\,eV$ |

Table 4.1: Activation energies, $E_a$, for $R_s$ and $R_p$ for the different cells.

measurements from four repeating units are monitored and analyzed using resistance normalization.

#### 4.1.2.1 Initial performance

Figure 4.1 shows the initial performance and scattering in resistance of the different cells in the stack measured by EIS. The series resistance, $R_s$, and the polarization resistance, $R_p$, were derived from the EIS data and the data for the different RUs are grouped in colors which represent the different coatings. The $R_s$ and $R_p$ data presented here were extracted from the real part of the impedance at the highest and lowest frequency ($f_{high}$ and $f_{low}$, respectively).

RU#5 and RU#11 with Cu LSM wet spray coating have a low $R_s$ value but a high $R_p$ value. RU#1 and RU#2 with standard ceramic coating have the lowest total resistance, yields the lowest $R_p$ values. RU#8, with the same interconnect coating, displays a significantly higher $R_s$ and $R_p$ than RU#1 and RU#2. Most of the increased impedance of RU#8 is in the $R_s$ (increased by more than $60\%$), while $R_p$ is only moderately increased (by $\approx 20\%$). This observation is consistent with the predicted behavior when partial contact loss (detachment) occurs at the cathode-interconnect interface in a repeating unit (RU) as shown by Gazzarri's PhD thesis page 86 [73].

Due to the time-consuming nature of the impedance characterization carried out, with manual multiplexing between cells and measurements carried out sequentially, four cells were selected for detailed impedance and degradation analysis. The RU (#2,4,6,11) were selected based on physical placement in the stack, and on the interconnect coating material. The temperature dependence in $R_s$ and $R_p$ for the four cells of interest is shown in Figure 4.2. The corresponding activation energies for $R_s$ and $R_p$ are listed in Table 4.1.

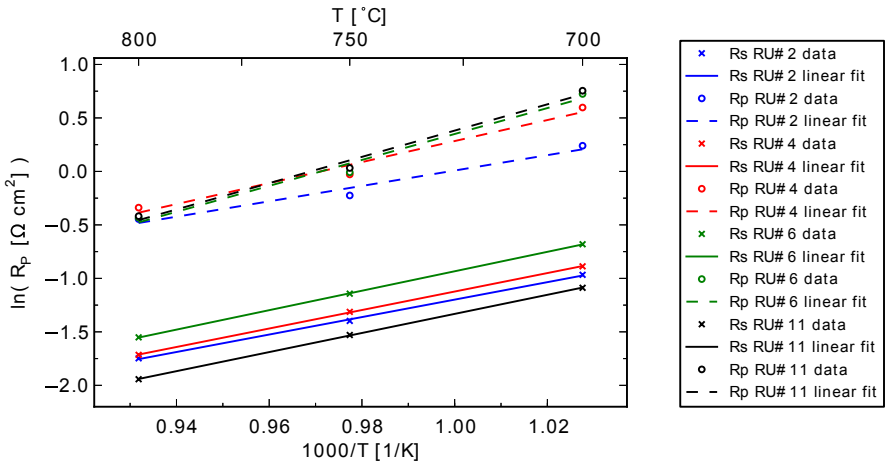


Figure 4.2: Arrhenius plot for the four RUs of interest. RU#2 – st.cer.coat, RU#4 – Co LSM ws, RU#6 – Cu and RU#11 – Cu LSM ws. Fuel: $80\%\ H_2$ with $20\%\ H_2O$. Oxidant: Air.

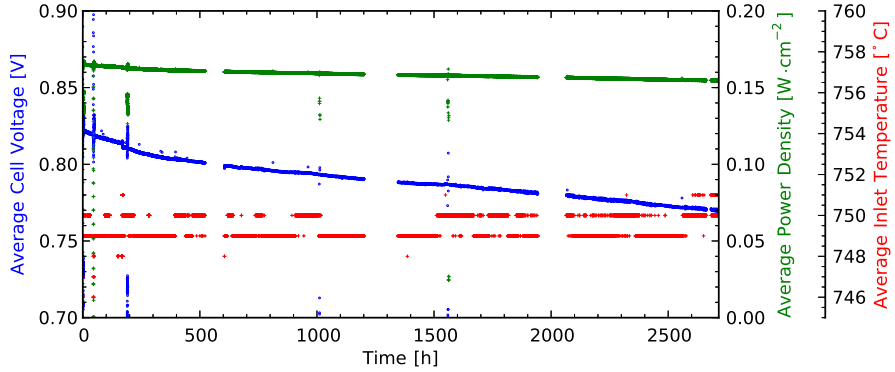


Figure 4.3: Overall stack performance during long term degradation.

#### 4.1.2.2 Long term degradation behavior

The cell voltage history plot in Figure 4.3 shows the average cell voltage for the stack RUs. It can be split into four periods separated by shorter periods in which the data-logging system was off-line. In the middle of degradation period 1 the air humidification was initiated. The galvanostatic test was continuous however, also in periods without data-logging. The average degradation rate is not constant during the test, but is greatest in period 1. When examining individual RU voltages (Figure 4.4), it is clear that RUs with different coating materials display very different degradation behavior. In period 2 the degradation rate vary from RU#2 with $-4.5\,mV\,kh^{-1}$ to RU#6 with $-18.4\,mV\,kh^{-1}$. In period 4 the degradation rate vary from Ru#2 with $-1.1\,mV\,kh^{-1}$ to RU#11 with $-84.2\,mV\,kh^{-1}$. RU#11 displays a progressive degradation trend (accelerating degradation)[14]. The origin of the progressive degradation in this experiment is not known to us. The RU with the standard ceramic coating (RU#2) displays a linear degradation in periods 2-4 after the initial nonlinear voltage drop in period 1. The orange dashed lines on Figure 4.4 indicate where EIS spectra were recorded during the long term test.

#### 4.1.2.3 EIS monitoring

EIS spectra were recorded regularly on the four selected cells. Figure 4.5 shows EIS spectra of the four RUs just after the air humidification was initiated. The absolute value for $R_s$ for the

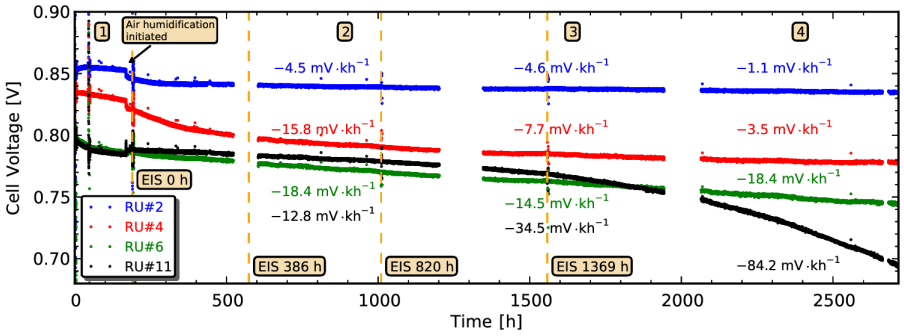


Figure 4.4: RU voltages versus time. Annotation 1-4 corresponds to 4 different degradation periods. RU#2 – st.cer.coat, RU#4 – Co LSM ws, RU#6 – Cu and RU#11 – Cu LSM ws.

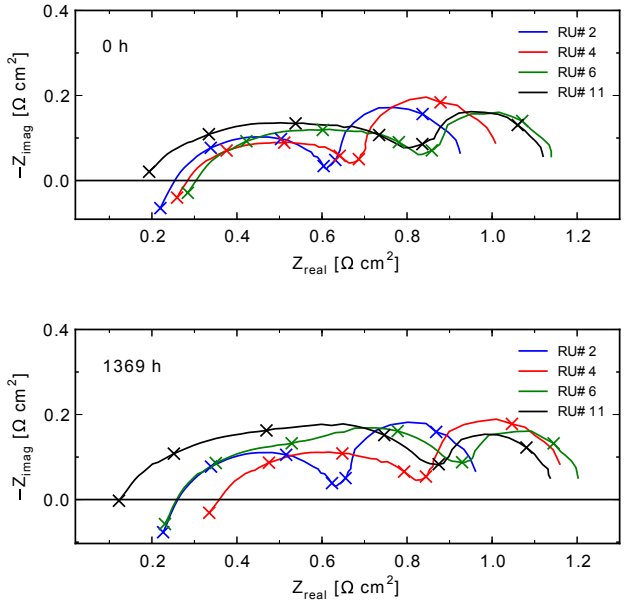


Figure 4.5: EIS spectra at $0.2\,A\,cm^{-2}$ just after air humidification was initiated ($0\,h$) and the last EIS spectra recorded ($1369\,h$). RU#2 – st.cer.coat, RU#4 – Co LSM ws, RU#6 – Cu and RU#11 – Cu LSM ws. Temperature: $750°C$ Fuel: $96\%\ H_2$ with $4\%\ H_2O$. Oxidant: $96\%$ Air with $4\%\ H_2O$. X corresponds to $97\,kHz$, $9.7\,kHz$, $970\,Hz$, $97\,Hz$, $9.7\,Hz$ and $0.97\,Hz$.

displayed impedance spectra s in the range between 2 to $3\,m\Omega$.

Figure 4.6 shows the resistance behavior versus time for the series resistance, $R_s$ and the polarization resistance, $R_p$, measured at $0.2\,A\,cm^{-2}$.

#### 4.1.2.4 Degradation analysis

The degradation analysis proposed by Gazzarri et al. [74] referred to as "Degradation mode tracking", involving visualization of the evolution of the degradation by plotting the inverse normalized series and polarization resistances. Figure 4.7 shows the normalized polarization resistance, $R_p^0\,/\,R_p$ versus normalized series resistance, $R_s^0\,/\,R_s$ where point $(1,1)$ corresponds to the initial situation *i.e.* the initial performance. Plotting the evolution of normalized series and polarization resistance starting at $(1,1)$ provides a useful visualization of the change in performance which carries information about the nature and extent of degradation. A degradation mode that

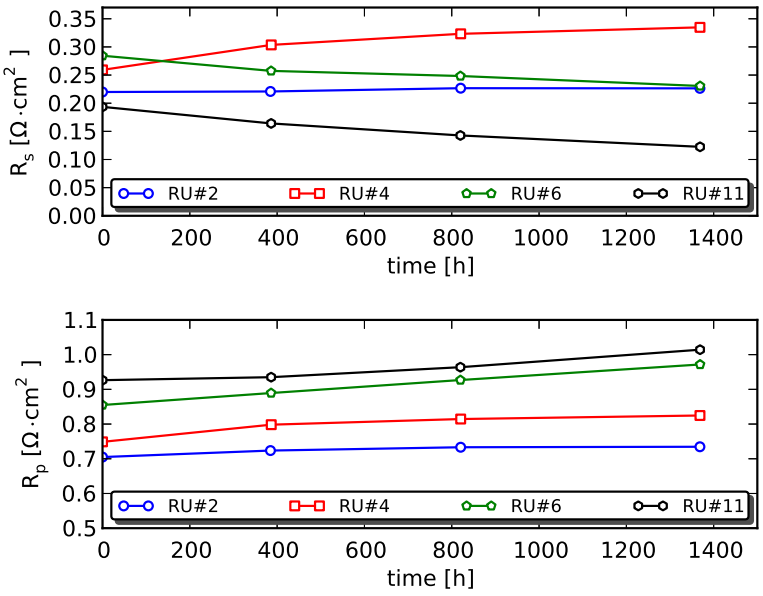


Figure 4.6: Resistance behavior versus time. RU#2 – st.cer.coat RU#4 – Co LSM ws, RU#6 – Cu and RU#11 – Cu LSM ws. Current: $0.2\,A\,cm^{-2}$. Temperature: $750°C$. Fuel: $96\%$ $H_2$ with $4\%$ $H_2O$. Oxidant: $96\%$ Air with $4\%$ $H_2O$.

mainly affects $R_s$, *e.g.* oxide layer growth on the metallic interconnects, yields a horizontal progression towards smaller values of $R_s^0$ / $R_s$ with increasing extent of degradation [74]. Processes that mainly affects $R_p$, such as nickel coarsening (at shorter time-scales) [75], chromium poisoning [76] and/or water induced changes on the cathode side [77], is reflected as a vertical line down from $(1, 1)$ since it is mainly affects the $R_p$.

If the normalized resistance trajectory follows the $45$ degree line it is an indication that a degradation process that changes the active area of the RU (e.g. delamination at one or both of the electrode/electrolyte interface) may be dominating the degradation [74]. It is important to note that this way of visualizing the data does not identify the degradation specifically, it only aids in identifying the main types of degradation, $R_s$ only, $R_p$ only or usually both in various proportions.

Figure 4.7 illustrates that the degradation of RU#2, which has interconnects with the "standard coating" is characterized by occurring at the same relative rate for both $R_s$ and $R_p$ which could indicate a mechanism that changes the active area of the RU. For RU#4 one also observes that both resistances increase, but here $R_s$ increases at a faster rate than $R_p$ – this could indicate a combination of a change of the active area of the RU and a "$R_s$-only process" *e.g.* oxide layer growth. RU#6 and RU#11 behave differently; for these RUs $R_s$ decreases over time, but $R_p$, which dominates the total resistance, increases. Figure 4.7 shows the relative changes for $R_s$ and $R_p$. For absolute changes of $R_s$ and $R_p$ see Figure 4.6.

Already at the initial characterization stage of the stack shown in Figure 4.1, RU#4, RU#6 and RU#11 showed a high $R_p$ compared to RU#2. This indicates that significant chromium poisoning takes place during start-up, which has also been reported by Kornely et al. [76].

RU#4 has a slightly lower $R_p$ value compared to RU#6 and RU#11 at $0\,h$ in Figure 4.6, even though RU#4, RU#6 and RU#11 have the nearly the same relative change in $R_p$ which is significantly higher than RU#2 as shown in Figure 4.7. This indicates that the coatings on the interconnects used in RU#4, RU#6 and RU#11 are not as good chromium barriersas those used in RU#2.

To arrive at a more detailed understanding of the underlying degradation processes in the specific stack the analysis presented here analysis needs to be supplemented by post test microscopy

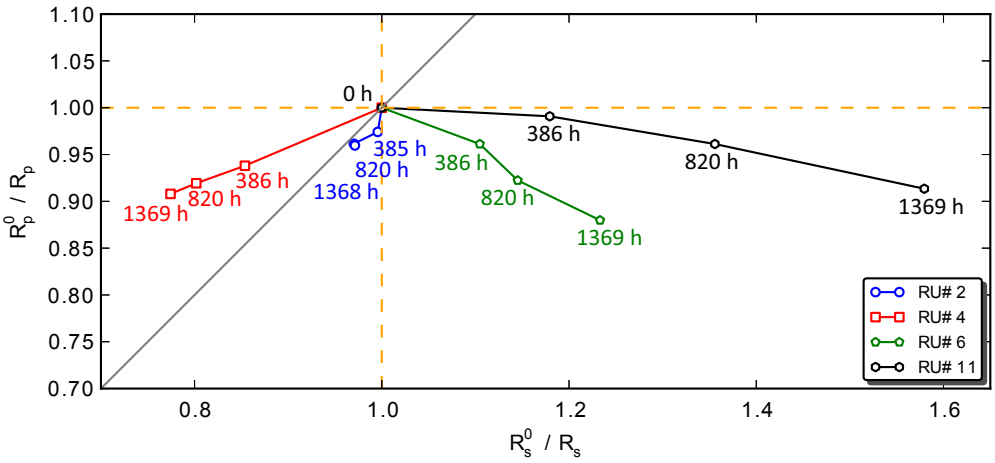


Figure 4.7: Resistance normalization plot. RU#2 – st.cer.coat, RU#4 – Co LSM ws, RU#6 – Cu and RU#11 – Cu LSM ws. Current: $0.2\,A\,cm^{-2}$. Temperature: $750°C$. Fuel: $96\%$ $H_2$ with $4\%$ $H_2O$. Oxidant: $96\%$ Air with $4\%$ $H_2O$.

and other characterization, which are beyond the scope of the present work.

### 4.1.3 Conclusion on cathode related time dependent degradation

A 13-cell experimental SOFC stack was tested during $2,500$ hours of continuous operation with hydrogen as fuel with $52\%$ fuel utilization and constant current load ($0.2\,A\,cm^{-2}$) at $750°C$. Stack interconnects were coated with six different coatings to prevent chromium poisoning on the cathode side.

The stack geometry, in terms of current path and voltage probe placement, was optimized for electrochemical impedance spectroscopy (EIS). The results illustrate that detailed EIS is possible on large area stacks and a de-convolution of the total loss into an ohmic and a non-ohmic part can be made.

The linear Kramers-Kronig test was used for validation of the impedance data. Four RUs were selected for detailed impedance analysis. RU#2 with the standard ceramic coating displayed the lowest long term degradation. The degradation of RU#4 with Co LSM wet sprayed coating was dominated by an increase of the series resistance with time, which could indicate that oxide layer growth was relatively rapid in the RU. RU#6 and RU#11 showed increasing $R_p$ values but decreasing $R_s$ values. Analysis of all RU impedances in the stack was only carried out at zero bias (OCV) before and after the galvanostatic durability test further supports the interpretation that the difference in behavior between the four RUs lies mainly in the different interconnect coatings, as the other RUs with the same coatings displayed the same degradation trends. Whereas the performance of the experimental coatings was unsatisfactory the experiment was successful in terms of characterization – the EIS allowed a clear distinction to be made in terms of the degradation between the four RU types that is not possible from IV-data only.

## 4.2 Anode related stack degradation monitoring

The anode related time dependent performance changes focus on the characterization of a 14-cell experimental stack with electrochemical impedance spectroscopy. The stack was tested galvanostatically (at constant current) for more than 667 hours with $50\%$ steam in the fuel gas ($H_2$) supplied to the stack. EIS was used to examine the long-term behavior and monitor the evolution of series and polarization resistances for one repeating unit and the whole stack. The observed impedance was analyzed in detail and the losses reported and discussed in the following.

### 4.2.1 Experiments

The stack was operated at a constant current of $20\,A$ $\left(0.22\,A/cm^2\right)$ at a average cathode gas temperature $\overline{T}_{cath,gas} = 720°C$ (measured by the inlet and outlet cathode gas temperature in the gas manifold) and fuel composition of $50\%$ $H_2O$ and $50\%$ $H_2$, and air as the oxidant. The fuel flow was set so that the fuel utilization was $56\%$ at $20\,A$. EIS measurements were recorded between $20\,kHz$ and $0.3\,Hz$ with an AC current (zero-to-peak) amplitude of $I_{AC} = 3.8\,A$ with 12 points per decade and with an integration time of 75 cycles below $66\,Hz$ and 200 cycles above $66\,Hz$. Further details regarding the stack and the experimental setup are given in Section 3.3 on page 63.

### 4.2.2 Results

This section presents the results for the anode related stack degradation monitoring. Presenting the long term degradation behavior, single sided gas changes, parameterization of the losses and an investigation of the anode degradation. The section is completed with resistance normalization of one repeating unit and the stack impedance.

#### 4.2.2.1 Long term degradation behavior

The RU voltage history plot in the top plot of Figure 4.8 shows the average RU voltage for the 14 RUs in the stack. The sudden increase in RU voltage after $100\,h$ of operation was caused by malfunction of a magnetic valve in the test rig that controls re-filling of the temperature controlled fuel humidification unit, a stainless steel gas wash bottle that allows saturation of the fuel gas with water. This lead to a temporary decrease in steam content of the fuel gas, and is the reason for the observed concurrent increase in average cell voltage of the stack. The galvanostatic test was continuous however, also in periods without data-logging. After $620\,h$ there was a power outage. Jitter on the RU voltage occur each time EIS measurements was recorded. The stack temperature measured as the average temperature of the inlet and outlet cathode gas measured in the stack manifold showed a slight increase in temperature due to the resistance increase caused by the degradation of the stack.

As a measure of change in degradation the Area-Specific-Resistance, ASR, is important for fuel cell developers since ASR is shown to be insensitive to certain variations in test conditions. Whereas Degradation Rate, DR, is the preferred parameter for determining changes in the efficiency over the lifetime of the cell or stack which is a key concern for end users [72]. Due to the lack of degradation measurement standards, there presently exists a variety of methods and metrics used to quantify and report degradation of cells and stacks. Within the SOFC area, calculation of degradation rates are done in a number of different ways, using both relative and absolute metrics. Several authors report the degradation rate in $[mV/kh]$ [67, 78, 79]. Horita et al. [80] calculate the degradation rate as a voltage change rate from initial values as $\left(-\left(U_0 - U\right)/U_0\right) \cdot 100$ where $U$ is the measured voltage and $U_0$ is the initial voltage. Comminges et al. [39] calculate the degradation rate as the differential voltage with respect to time in $[\%/kh]$. Gemmen et al. [72] proposed two ways of how the degradation rates should be calculated: 1) the instantaneous, degradation rate, $\mathrm{DR}\,(t)$, and 2) the average degradation rate, $\overline{DR}\,(t)$. These two ways of calculating the degradation rates are further explained in the following.

Without degradation, the cell voltage and area specific resistance, ASR, are constant for a particular system at a constant operating current density, $j_c$ $\left[\frac{A}{cm^2}\right]$, and with constant reactant flows. At a given time, $t_0$, and a constant operating current density, $j_c$, the fuel cells starts to degrade. The ASR, and thus also the voltage, begins to change with time. For an infinitesimal time change the instantaneous degradation rate is given by Equation 4.1 [72].

$$\frac{\mathrm{d}\,U\,(j_c, t)}{\mathrm{d}\,t} \tag{4.1}$$

The relative instantaneous voltage degradation rate at a current density, $j_c$, and time $t$ in expressed in $\%$ per hour is given by Equation 4.2. The relative average degradation rate in terms of $\%$ per hour is given by Equation 4.3.

$$\mathrm{DR}\,(t) = -100 \cdot \left( \frac{\frac{\mathrm{d}U(j_C,t)}{\mathrm{d}t}}{\mathrm{d}U\,(j_c,t_0)} \right) \tag{4.2}$$

$$\overline{\mathrm{DR}}\,(t) = 100 \cdot \frac{U\,(j_c,t_0) - U\,(j_c,t)}{U\,(j_c,t_0) \cdot (t-t_0)} \tag{4.3}$$

A relative voltage degradation as given in Equation 4.2 and 4.3 directly relates to changes in fuel efficiency. Increase in fuel consumption (and cost) from startup is a very relevant concern for end users. On the other hand the normalization of the degradation rate as shown in Equation 4.2 and 4.3 has been considered by Steinberger-Wilckens et al. [81] that relative voltage degradation can result in higher apparent degradation rate values for fuel cells operated at lower voltages / higher currents.

Dividing Equation 4.2 and 4.3 by the constant current density, $j_c$, the degradation rate can be calculated as area specific resistances. This assumes that the OCV is constant throughout the durability test, but this is an assumption that can be verified in each test. The absolute instantaneous degradation rate expressed in $\Omega\,cm^2$ per hour is given by Equation 4.4. The absolute average degradation rate in terms of $\Omega\,cm^2$ per hour is given in Equation 4.5.

$$\mathrm{DR}_{\mathrm{ASR}}\,(t) = \frac{1}{j_c}\frac{\mathrm{d}U\,(j_c,t)}{\mathrm{d}t} \tag{4.4}$$

$$\overline{\mathrm{DR}}_{\mathrm{ASR}}\,(t) = \frac{1}{j_c}\frac{U\,(j_c,t_0) - U\,(j_c,t)}{(t-t_0)} \tag{4.5}$$

The instantaneous degradation rates, $\mathrm{DR}\,(t)$, and the average degradation rates, $\overline{DR}\,(t)$ for the long term degradation test are shown in Figure 4.8. Jitter that occur on the RU voltage each time EIS measurements was recorded are masked away as well as the increase in RU voltage after $100\,h$ that was caused by the stuck magnetic valve which supplied water to the water bubbler and the power outage at $620\,h$. For the absolute degradation rate, $\mathrm{DR}\,(t)$, data was smoothed with a moving average of $10\%\ (66\,h)$ of the dataset.

When examining the individual RU voltages in Figure 4.9 the RU voltages from the bottom part of the stack show lower performance compared to the top part of the stack. A rapid degradation occurs during the first $100\,h$ after which the degradation rate decreases out from $100\,h$ to $600\,h$. The purpose of this test was to investigate the rapid degradation observed after constant current was applied to the stack. Therefore the intervals between impedance measurements are shorter in the beginning of the test compared to the end of the test. RU01+Bottom is the first repeating unit including the bottom plate and RU14+Top is last repeating unit and the top plate illustrated on Figure 3.8 on page 64. These voltage measurements were performed in order to monitor the effect of contact loss at the end plates. RU01+Bottom showed a large constant degradation compared to RU14+Top. Due to time limitations in this work the effect of contact loss at the end plates is not analyzed in detail.

The polarization curve of the stack before and after the Long Term Degradation Test, LTD, are shown in Figure 4.10. The UI curves were recorded at $50\%\,\mathrm{H_2O}$ and $50\%\,\mathrm{H_2}$as fuel and air as oxidant. The stack voltage is measured between top and bottom interconnect. It is clearly shown that the stack power output has decreased the long term degradation. The power decrease at $20\,A$ is $12.5\,W$.

#### 4.2.2.2 Single sided gas changes

The strategy of using impedance spectra recorded as a function of a number of single sided gas changes to obtain information about electrode specific and reactant partial pressure sensitive processes, and has been used in several studies to aid separation of electrode processes [82, 83, 25], a form of pre-identification that can provide physically reasonable constraints for deconvolution of individual processes from full cell spectra by complex nonlinear least squares fitting of equivalent circuit models to the data. An overview of the single sided gas changes carried out before

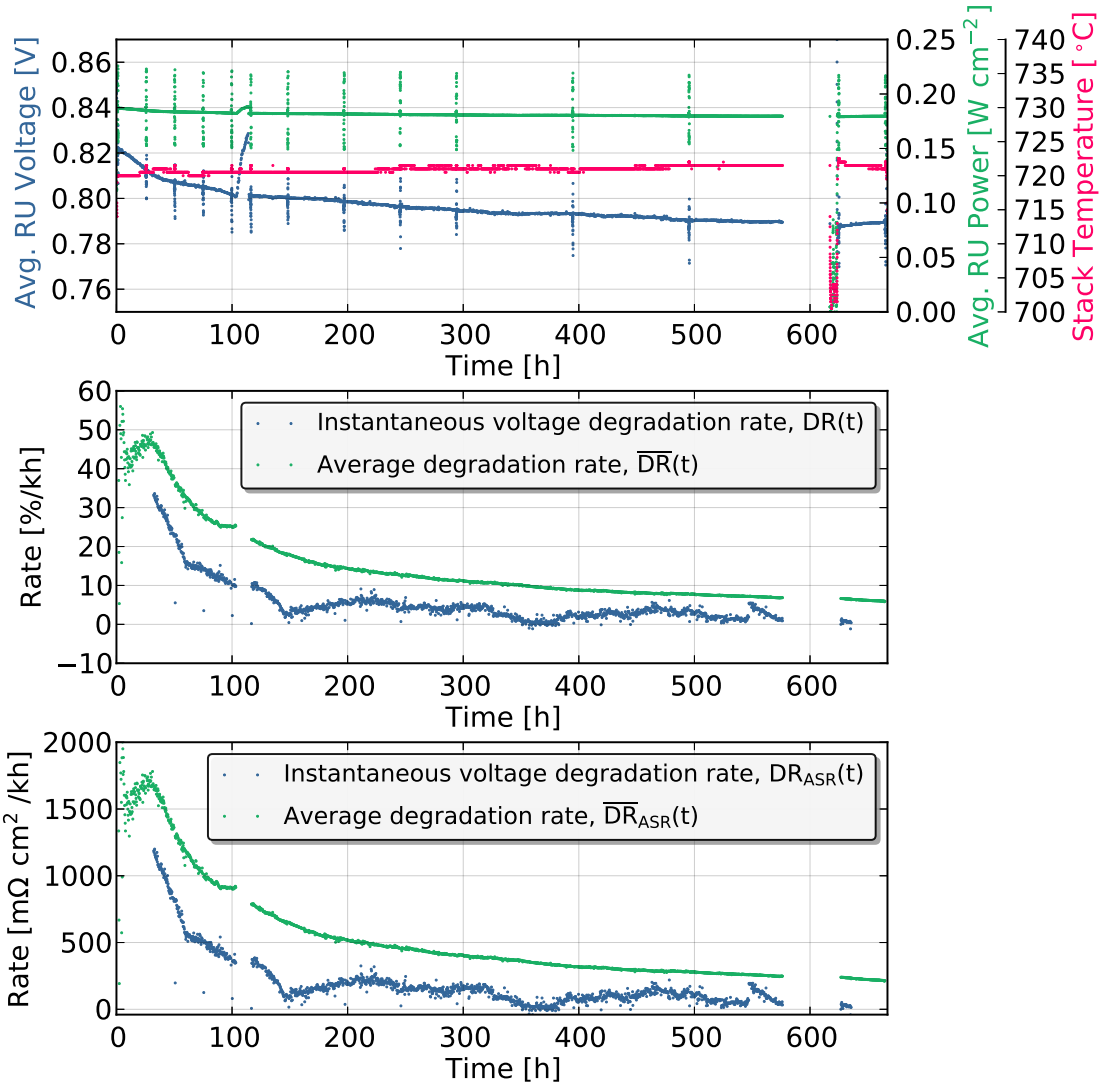


Figure 4.8: Top plot: Overall stack performance during long term degradation. Center plot: Instantaneous and average degradation rates given in $[\%/kh]$. Bottom plot: Instantaneous and average degradation rates given in $[m\Omega\, cm^2]$.

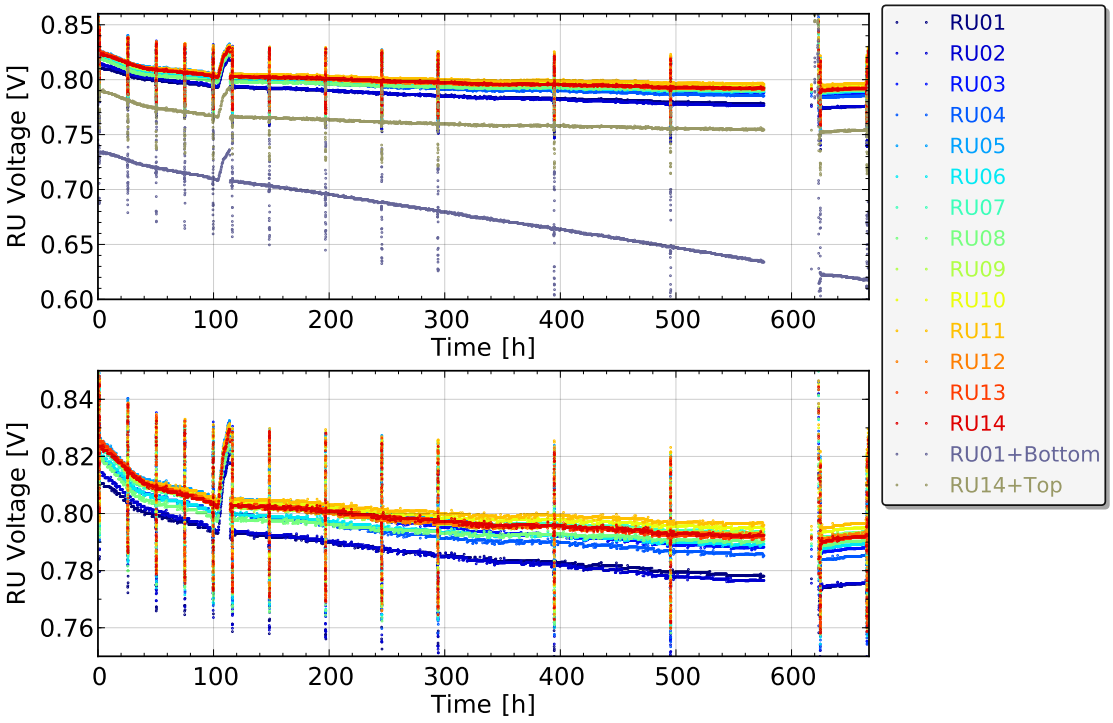


Figure 4.9: RU voltages versus time. Jitter voltages indicate where EIS measurements were recorded. RU01+Bottom is the first repeating unit including the bottom plate. RU14+Top is last repeating unit and the top plate.

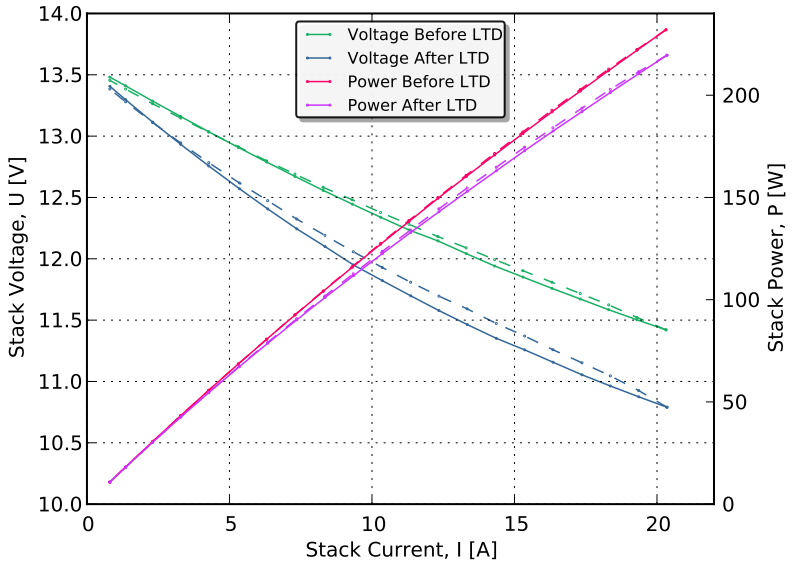


Figure 4.10: Polarization curve before and after Long Term Degradation Test, LTD. Dashed line indicate decreasing current.

| Temperature | Fuel | | | Oxidant | | | Current | |
|---|---|---|---|---|---|---|---|---|
| $T$ | $x_{H_2}$ | $x_{H_2O}$ | $\dot{V}_{anode}$ | $x_{O_2}$ | $x_{N_2}$ | $\dot{V}_{cathode}$ | $I_{DC}$ | $I_{AC}$ |
| $[°C]$ | $[\%]$ | $[\%]$ | $\left[\frac{NL}{min}\right]$ | $[\%]$ | $[\%]$ | $\left[\frac{NL}{min}\right]$ | $[A]$ | $[A]$ |
| 700 | 80 | 20 | 4.4 | 20.8 | 79.2 | 36.0 | 4.3 | 3.8 |
| 700 | 50 | 50 | 7.1 | 20.8 | 79.2 | 36.0 | 4.3 | 3.8 |
| 700 | 80 | 20 | 4.4 | 20.8 | 79.2 | 10.0 | 4.3 | 3.8 |
| 700 | 80 | 20 | 4.4 | 100.0 | 0.0 | 10.0 | 4.3 | 3.8 |

Table 4.2: Overview of the single sided gas changes used before and after long term degradation for the 14 RU stack.

and after long term degradation is shown in Table 4.2. This can provide insight into which process or electrode is dominating the degradation of the repeating units in the stack. The result of the analysis of the cathode side gas changes before and after long term degradation for RU08 is shown in Figure 4.11. Hardly any changes are observed in the DRT spectrum between $30\,Hz$ and $90\,Hz$ which represents the cathode. The impedance for two different anode side gas compositions recorded before and after long term degradation for RU08 are shown in Figure 4.12. It is clearly seen in the DRT plot that the conversion arc between $0.3\,Hz$ and $7\,Hz$ and the diffusion arc between $8\,Hz$ and $30\,Hz$ changes with changing steam molar fractions. It is clearly seen that the anode impedance increases between $100\,Hz$ and $4000\,kHz$ after the long term degradation test and that it reacts on changing steam molar fractions. The anode performance change is by far the biggest and it is selected to focus the detailed degradation analysis on the anode.

#### 4.2.2.3 Parameterization of losses

Figure 4.13 shows the evolution of the impedance measurements of RU08 during the long term degradation test. Figure 4.13 A) shows the impedance spectra of RU08 recorded from $2\,h$ to $665\,h$. Figure 4.13 B) shows the imaginary impedance vs frequency. Figure 4.13 C) shows the corresponding relative residuals of the linear Kramers-Kronig transform test [84]. The Kramers-Kronig Transform test gave relative residuals is in the range of $\pm 0.5\%$ which is in the same range as what has been reported for single cell measurements at DTU Energy Conversion [25, 26]. Figure 4.13 D) shows the distribution of relaxation times - DRT. This preidentification method separates the polarization processes with different time constants directly from the impedance data [27, 28, 29]. A first tentative assignment of the various processes observed can be carried out using available data from Leonide et al. [28] who used similar anode supported cells in a single cell set-up although the anode support thickness is different in Leonide et al. [28] and a LSCF/CGO composite cathode was used whereas Leonide et al. [28] used a LSCF cathode and based on previous work on the present anode-supported half-cell as exemplified in Barfod et al. [85]. The DRT spectra can be divided into five processes, **P1** to **P5**. **P1** is the gas conversion impedance at $1Hz$, **P2** is a gas diffusion impedance at $10Hz$ related to the inhibited gas diffusion within the Ni/YSZ anode substrate [30]. **P3** is the activation polarization at the cathode ($100Hz$ to $1kHz$). **P4** and **P5** are according to [28, 29, 30] related to gas diffusion coupled with charge transfer reactions at the triple phase boundary and ionic transport in the anode functional layer. Prior to calculation of DRT from the impedance spectra the high frequency inductance was removed by subtraction. The inductance subtracted was determined for each spectra by comparison of the imaginary data generated from the experimental real part of the impedance using the Kramers-Kronig transforms [84]. The negative DRT observed between the conversion and diffusion arc is not fully understood and it is not found described in the literature. It is observed that the gas conversion impedance, P1, drifts to higher frequencies and the DRT peak increases in size over time, but the reason for this is not clear at the present. From the Nyquist, Bode and DRT plots it is clear that it is mainly the electrode polarization part of the impedance spectrum that is increasing over time. This could be related to changes in the tortuosity over time which are concurrent with particle coarsening [86].

The following equivalent circuit was used to fit the impedance data: $L-R_s-(RQ)_2-(RQ)_3-$

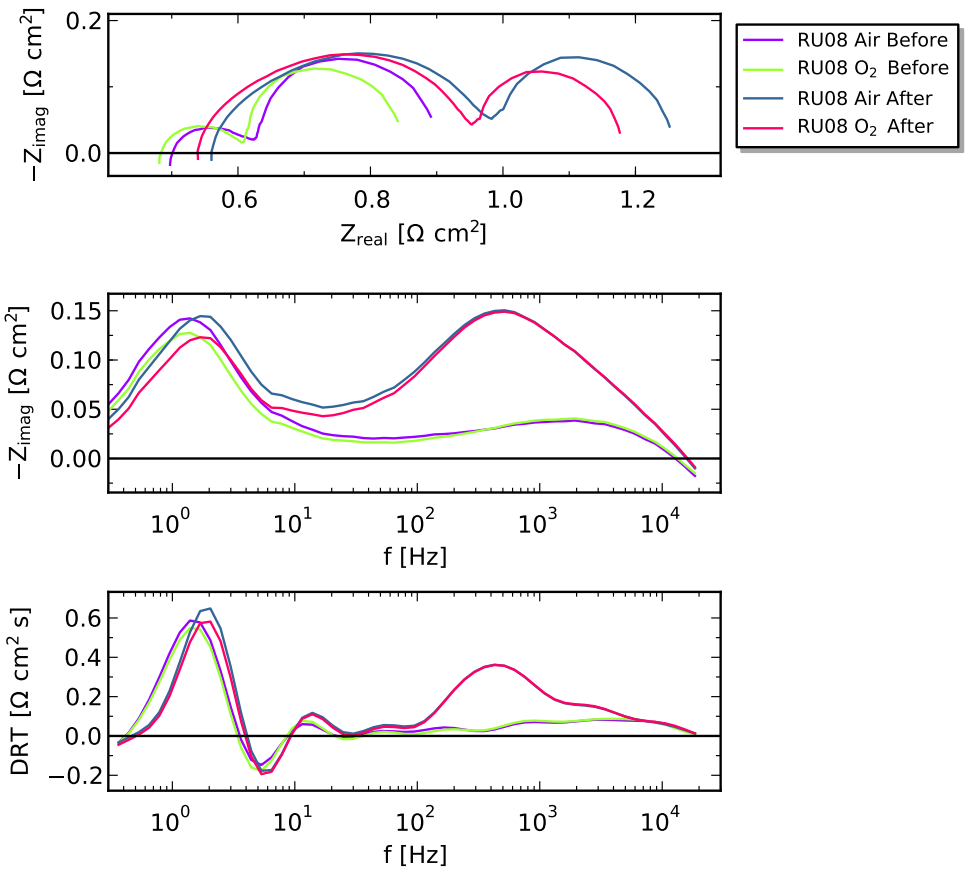


Figure 4.11: Cathode gas change before and after long term degradation for RU08.

$(RC)_4$. The corresponding schematic of the equivalent circuit is shown in Figure 4.14. $L\ [H]$ represents the high frequency inductance. The inductance was determined using the Kramers-Kronig transform test [84]. The values for $L\ [H]$ was fixed and therefore not fitted. $R_s\ \left[\Omega\, cm^2\right]$ is the series resistance which represents the ohmic loss from the ionic transport in the electrolyte and any contact/current collection losses. $(RQ)_2$ represents the losses in the anode (fuel electrode). $(RQ)_3$ represents the losses in the cathode (air electrode). $(RC)_4$ represents the gas concentration impedance, the sum of gas conversion and gas diffusion impedance [11]. For practical reasons $(RC)_4$ was fitted with a $RQ$ circuit with $\alpha$ value locked to $\alpha = 1$ which is equivalent to an ideal capacitor. The circuit model was fitted to the data using a complex non-linear least squares fitting routine in the data analysis software RAVDAV [23]. This software is using Scipy's leastsq() least-squares minimizer, which wraps MINPACK's lmdif (Levenberg-Marquardt) algorithm [24].

The impedance measurement, the total fit and the individual arcs for RU08 at $2\,h$ is shown in Figure 4.15. A simplified model circuit was used in order to get a first parametrization of the losses, which means that the deconvolution of the impedance spectra is limited and multiple processes may be hidden under $(RQ)_2$, $(RQ)_3$ and $(RC)_4$. The anode processes are described by $(RQ)_2$ although according to [30], the arc accommodate several processes. The hidden processes are process P4 and P5 shown in Figure 4.13 which are related to gas diffusion coupled with charge transfer reactions at the triple phase boundary and ionic transport in the anode functional layer [28, 29, 30]. The cathode process described by $(RQ)_3$ describes the activation polarization at the cathode (P3 on Figure 4.13). According to Nielsen et al. consensus within literature is that Mixed Ionic Electronic Conductor (MIEC) SOFC cathodes such as the LSCF cathode used in this study

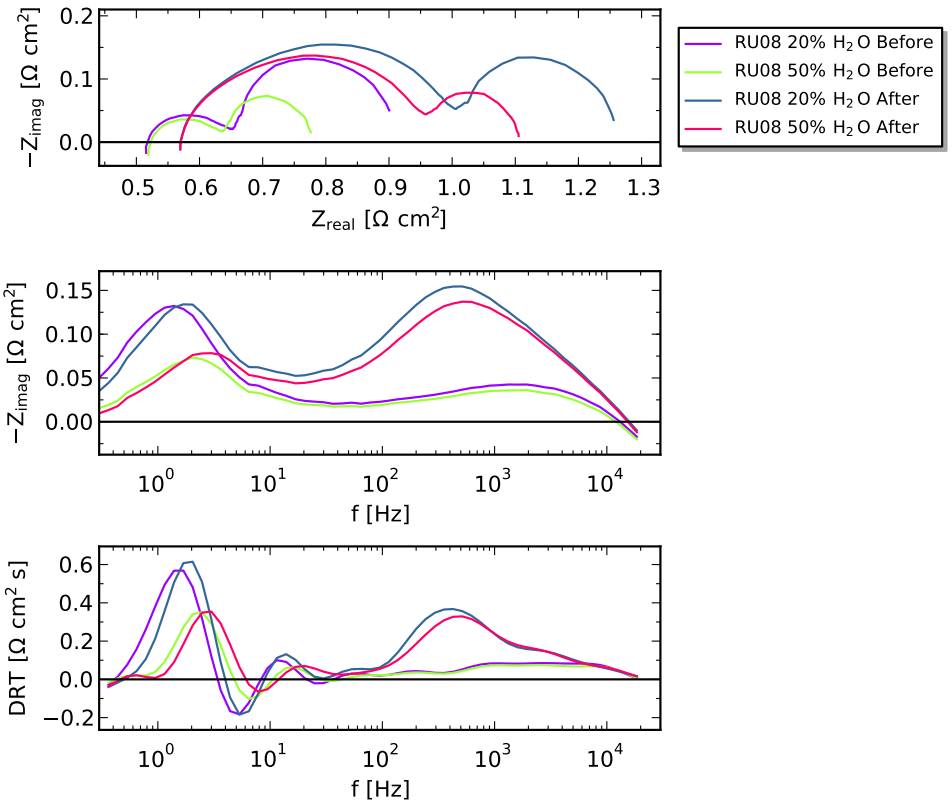


Figure 4.12: Anode gas change before and after long term degradation for RU08.

can appropriately be described by a Gerischer impedance, describing the co-limiting situation of coupled bulk oxide ion diffusion and surface reaction [87]. This would also ensure less interaction between the anode impedance and the cathode impedance due to the skewed semicircle behavior of a Gerischer element. The reason for choosing a Constant Phase Element, CPE, $(Q)$ was to obtain a simple equivalent circuit with a focus on monitoring the total anode impedance. The concentration impedance is fitted with one arc, but it actually consist two arcs, the diffusion and the conversion impedance [11].

The series of impedance measurements for RU08 recorded from $2\,h$ to $665\,h$ during the long term degradation was batch fitted using the data analysis software RAVDAV [23]. Based on the observed changes of the cathode process denoted P3 in the DRT plot in Figure 4.13 the cathode loss is nearly unchanged during the long term degradation test. Therefore bounds on the resistance for $(RQ)_2$ describing the cathode (P3) were implemented restricting changes of the cathode polarization resistance to within $\pm 5\%$ during the complete batch fit. Making the bounds narrower than $\pm 5\%$ would result in a improper fit. Impedance data and the corresponding fits for RU08 for the series of impedance measurements from $2\,h$ to $665\,h$ are shown in Figure 4.16.

#### 4.2.2.4 Investigation of the anode degradation

Faes et al. [88] presented a model for describing the degradation of a Nickel-Zirconia anode. The degradation followed an exponential growth model presented to describe Nickel coarsening. Hauch et al. [83] later investigated the change of anode resistance in single cell tests. The degradation followed the same exponential growth and was likely to describe Nickel coarsening as well. Hauch et al. [83] investigated anode resistance, $R_{Ni,TPB}$, for a Ni/YSZ - YSZ - LSM/YSZ SOFCs during $250\,h$ tests at three different steam molar fractions: $0.2$, $0.4$ and $0.6$. The develop-

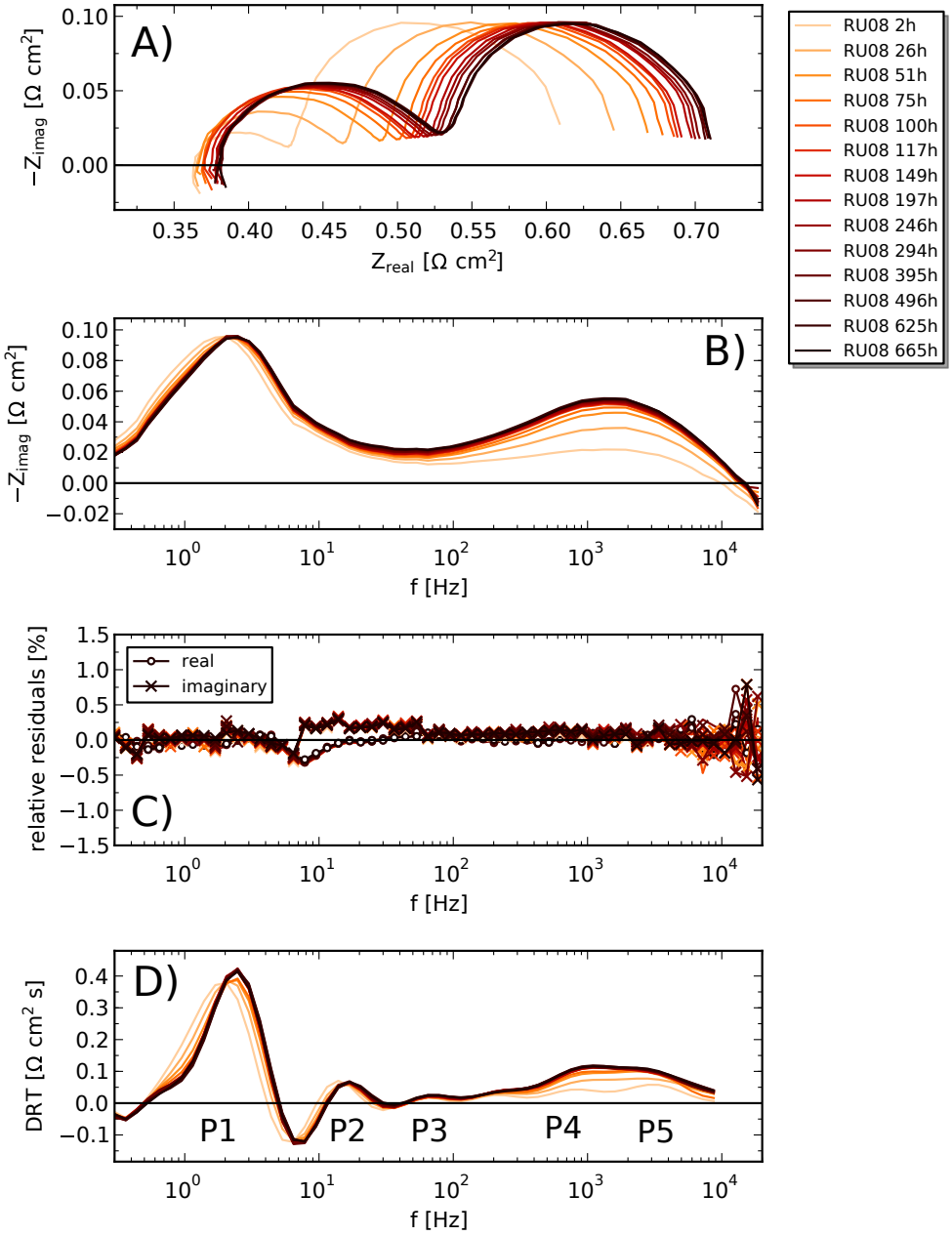


Figure 4.13: Development of EIS spectra during the long term degradation for RU08. $\overline{T}_{cath,gas} = 720°C$ with $50\%\,H_2O$ and $50\%\,H_2$ as fuel and air as oxidant

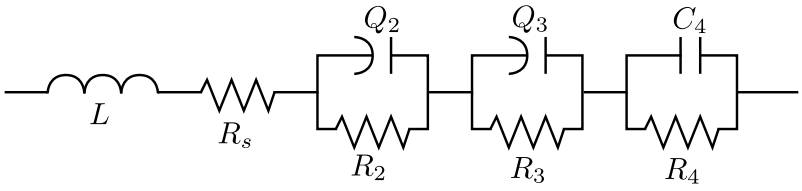


Figure 4.14: The equivalent circuit for deconvolution of losses for the RUs and the stack.

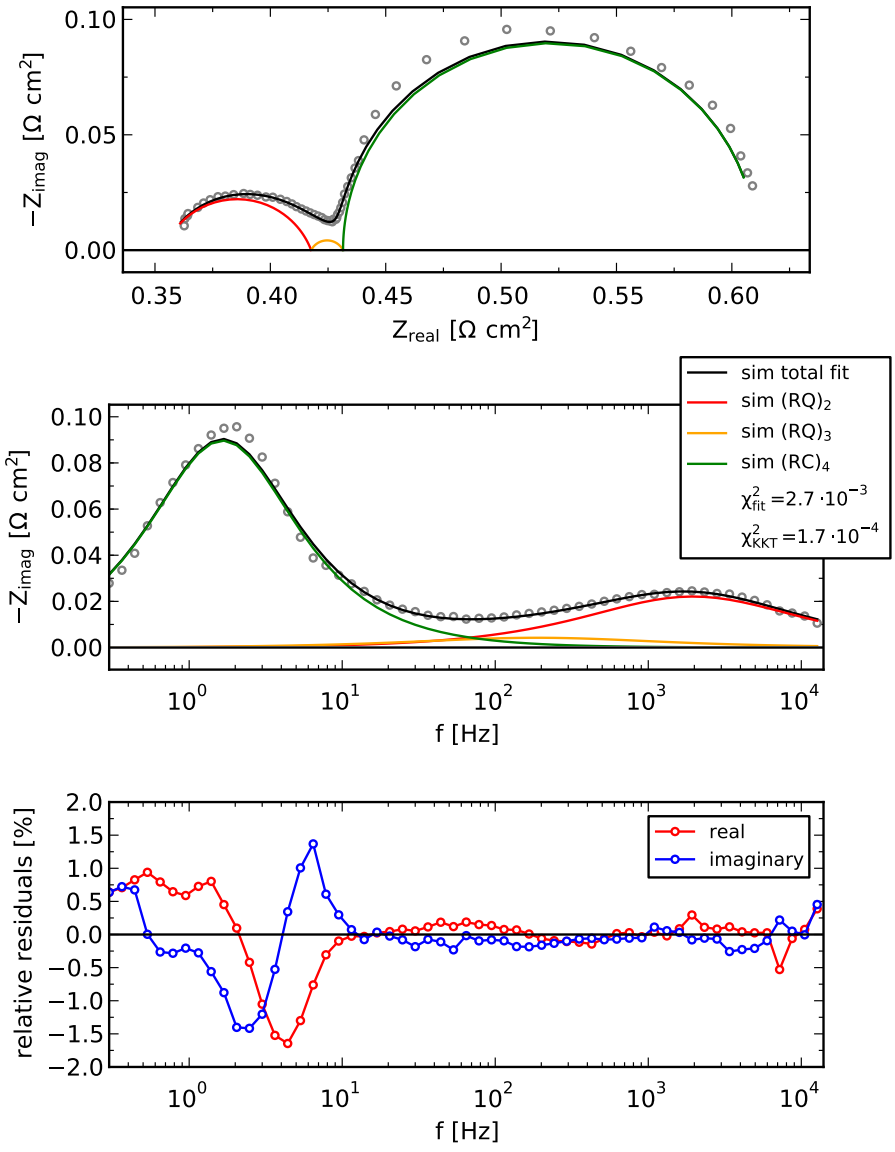


Figure 4.15: Fit of impedance spectrum for RU08 2h after long term degradation was initiated together with the relative residuals of the fit.

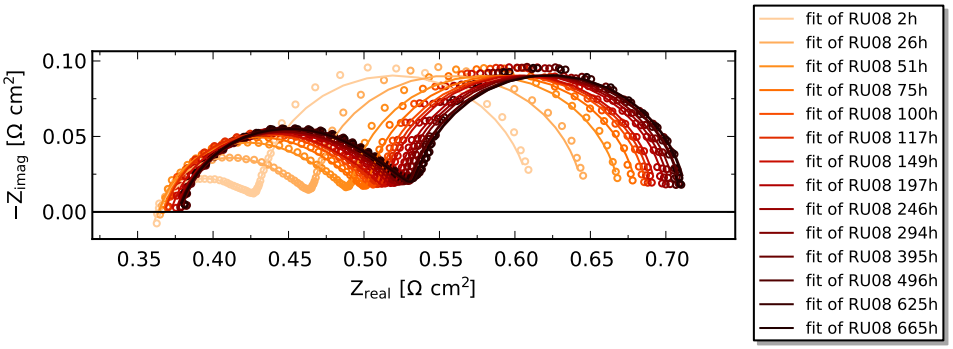


Figure 4.16: Development of impedance spectra during the long term degradation for RU08 including fits.

| | $A_{active}$ $[cm^2]$ | $x_{H_2O}$ $[-]$ | $R_{Ni,0}$ $[\Omega\, cm^2]$ | $\Delta R$ $[\Omega\, cm^2]$ | $\tau$ $[h]$ | Ref. |
|---|---|---|---|---|---|---|
| RU08 | 90 | 0.5 | 0.064 | 0.088 | 49 | |
| Stack | 90 | 0.5 | 0.819 | 1.289 | 60 | |
| Test B | 16 | 0.4 | 0.061 | 0.062 | 17 | [83] |
| Test C | 16 | 0.6 | 0.077 | 0.077 | 34 | [83] |

Table 4.3: Results of fits of $R_{Ni,TPB}\,(t)$ for RU08 and Stack compared with results from Test B and Test C from Hauch et al. [83].

ment of anode resistance over time, $R_{Ni,TPB}\,(t)$ was fitted to Equation 4.6 using CNLS fit. $R_{Ni,0}$ is the initial Ni-YSZ charge transfer resistance, $\Delta R$ is the total increase in $R_{Ni,TPB}$ and $\tau$ is the characteristic time for the Ni/YSZ electrode degradation. The change in anode resistance over time was assigned to Ni particle growth.

$$R_{Ni,TPB}\,(t) = R_{Ni,0} + \Delta R(1 - e^{(\frac{-t}{\tau})}) \tag{4.6}$$

The anode resistance, $R_{Ni,TPB}\,(t)$ given in Equation 4.6 was fitted to the results of $R_2$ in $(RQ)_2$ from the equivalent circuit described in previous section. The fit of the anode resistance over time is shown in Figure 4.17. The anode resistance for the stack was fitted as well. The anode resistance fit data and the $R_{Ni,TPB}\,(t)$ fit is shown in Figure 4.18. Results of fits of $R_{Ni,TPB}\,(t)$ for RU08 and Stack compared with results from Test B and Test C from Hauch et al. [83] are shown in Table 4.3. The initial anode resistance, $R_{Ni,0}$, for RU08 and Test B is very similar. The characteristic time, $\tau$, for RU08 is in the same range as Test B and Test C. Comparison between the anode resistance for RU08 and the stack and the single cell test data from Hauch et al. [83] definitely following the often observed exponential change with time, that is likely caused by nickel coarsening.

#### 4.2.2.5 Resistance normalization

Gazzarri et al. [74] proposed normalization of the resistances by taking $R_0$ / $R$ referred to by them as "Degradation mode tracking" and while there is some virtue to this approach, we instead use normalization by taking $R$ / $R_0$ , to better visualize the relative magnitude of the evolution of the degradation. Figure 4.19 shows the normalized polarization resistance, $\Delta R_p$ / $R_p^0$ versus normalized series resistance, $\Delta R_s$ / $R_s^0$ where point $(0, 0)$ correspond to the initial situation . Plotting the evolution of normalized series and polarization resistance starting at $(0, 0)$ provides useful visual information about the nature and extent of degradation. A degradation mode that mainly affects $R_s$ like oxide layer growth appears as an almost horizontal progressing leftward with increasing extent of degradation [74]. Nickel coarsening (at shorter time-scales) [75, 83], chromium poisoning [76] and/or water induced changes on the cathode side [77], is reflected as a vertical line up

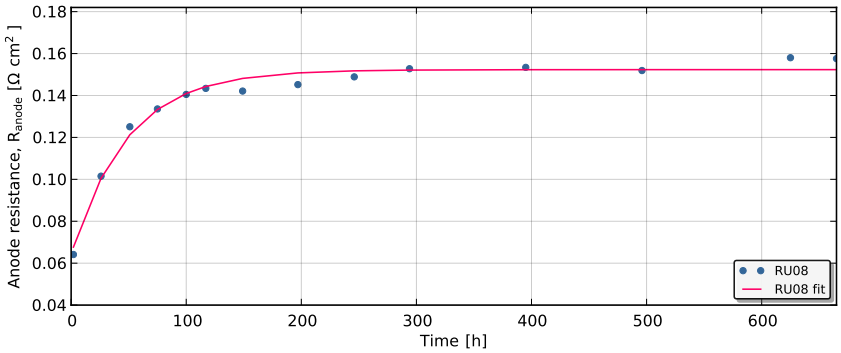


Figure 4.17: Development of anode resistance, $R_{anode} = R_{Ni,TPB} = R_2$, for RU08 over time obtained from CNLS fits of Equation 4.6. The applied equivalent circuit are shown in Figure 4.14.

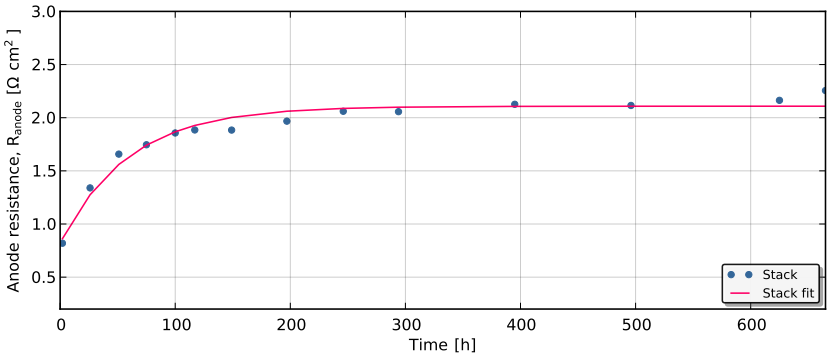


Figure 4.18: Development of anode resistance, $R_{anode} = R_{Ni,TPB} = R_2$, for the stack impedance over time obtained from CNLS fits of Equation . The applied equivalent circuit are shown in Figure 4.14.

from $(0, 0)$ since it imainly affects the $R_p$.

If the normalized resistance trajectory follows a $45$ degree line (equal changes of $\Delta R_p/R_p^0$ and $\Delta R_s/R_s^0$) it is an indication that a degradation process that changes the active area of the RU (e.g. delamination) may be dominating the degradation [74]. It is important to note that this way of plotting does not identify the degradation specifically, it only aids in identifying main types of degradation, $R_s$ only, $R_p$ only or usually both in various proportions.

The resistance normalization plot is shown in Figure 4.19 on the following page for RU08 and the stack indicate a clearly $R_p$ only process. The change in polarization resistance$\Delta R_p/R_p^0$ is the change of the of the total polarization losses which includes electrode and gas concentration losses. The polarization resistance increases $\sim 40\%$ during the $667\,h$ test, whereas the change in electrode resistance $\Delta R_{elec}/R_{elec}^0$ which is the sum of the electrode losses increases $120\%$ and $130\%$ for the stack and RU08 respectively. The electrode resistance, $R_{elec}$, is the main source for degradation and it was likely caused by nickel coarsening at the anode as described in previous section.

### 4.2.3 Conclusion on anode related time dependent degradation

A $14$-cell experimental stack was tested during $667$ hours of continuous operation with $50\%$ hydrogen and $50\%$ steam as fuel with $56\%$ fuel utilization and a constant current load ($0.2\,A\,cm^{-2}$)

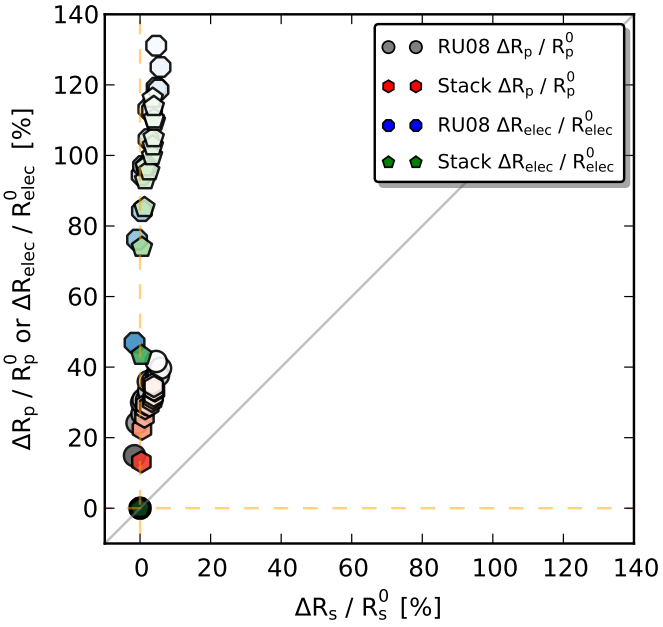


Figure 4.19: Resistance normalization plot for RU08 and the stack. Current: $20\,A$. Temperature: $720°C$. Fuel: $50\%$ $H_2$ with $50\%$ $H_2O$. Oxidant: Air.

at $720°C$. Different measures (metrics) of degradation rates were discussed. This included normalized instantaneous and average degradation rates given in $\%/kh$ and in $m\Omega\,cm^2\,/\,kh$. The greatest part of the degradation occurred in the first $200$ hours of operation with the chosen operating conditions.

The stack geometry, in terms of current path and voltage probe placement was optimized for electrochemical impedance spectroscopy (EIS). The results illustrate that detailed EIS is possible on large area stacks and a deconvolution of the total loss into an ohmic and a non-ohmic part can be made. The linear Kramers-Kronig Transform test was used for data validation of the impedance spectra and the relative residuals was in same range as seen for single cell measurements at DTU Energy Conversion. By comparing the distribution of relaxation times obtained from the impedance data with literature observations it was possible to identify the different processes in a RU. These assignments were further supported by observations made as a function of single-sided gas changes.

Analysis of RU and stack impedances (carried out at specific times only) show that the degradation followed an exponential growth model as suggested by Faes et al. [88] and later also observed by Hauch et al. [83] in a single cell test was dominated by the anode and likely caused by nickel coarsening.

The experiment is successful in terms of characterization – the EIS allowed indication of a specific degradation phenomenon at one electrode that is not possible from IV-data only.

## 4.3 Conclusion on stack degradation monitoring

A $13$-cell experimental SOFC stack was tested during $2,500$ hours of continuous operation with hydrogen as fuel with $52\%$ fuel utilization and constant current load ($0.2\,A\,cm^{-2}$) at $750°C$. Stack interconnects were coated with six different coatings to prevent chromium poisoning on the cathode side.

RU#2 with the standard ceramic coating displayed the lowest long term degradation. The

degradation of RU#4 with Co LSM wet sprayed coating was dominated by an increase of the series resistance with time, which could indicate that oxide layer growth was relatively rapid in the RU. RU#6 and RU#11 showed increasing $R_p$ values but decreasing $R_s$ values. Analysis of all RU impedances in the stack (carried out at specific times only) show that the difference in behavior between the four RUs lies mainly in the different interconnect coatings.

A $14$-cell experimental stack was tested during $667$ hours of continuous operation with $50\%$ hydrogen and $50\%$ steam as fuel with $56\%$ fuel utilization and a constant current load ($0.2\,A\,cm^{-2}$) at $720°C$. Different measures of degradation rates was discussed. This included normalized instantaneous and average degradation rates in $\%/kh$ and in $m\Omega\,cm^2\,/\,kh$. Common to all of the degradation rates was that the greater part of the degradation occurred in the first $200$ hours of operation.

The stack geometry, in terms of current path and voltage probe placement was optimized for electrochemical impedance spectroscopy (EIS). The results illustrate that detailed EIS is possible on large area stacks and a deconvolution of the total loss into an ohmic and a non-ohmic part can be made. The linear Kramers-Kronig Transform test was used for data validation of the impedance spectra and the relative residuals was in same range as seen for single cell measurements at DTU Energy Conversion. Analysis of RU and stack impedances (carried out at specific times only) show that the degradation followed an exponential growth model as suggested by Faes et al. [88] and later also observed by Hauch et al. [83] in a single cell test was dominated by the anode and likely caused by nickel coarsening.

The two experiments is successful in terms of characterization – the EIS allowed indication of a specific degradation phenomenons at the electrodes that is not possible from IV-data only.

CHAPTER 5

# Detection of fuel gradients

An operating stack is subject to steep compositional gradients in the gaseous reactant streams, and significant temperature gradients along each cell and across the stack, which makes it a complex system to analyze in detail [89]. Today one is forced to use mathematical modeling to extract information about existing gradients and cell resistances in operating stacks, as mature techniques for local probing are not available. This type of spatially resolved information is essential for model refinement and validation, and can assist further technological stack development. More detailed information obtained from operating stacks is essential for developing appropriate process monitoring and control protocols for stack and system developers.

An experimental stack from Topsoe Fuel Cell A/S was characterized using Electrochemical Impedance Spectroscopy (EIS). The stack measurement geometry was optimized for EIS by careful selection of the placement of current feeds and voltage probes in order to minimize measurement errors. It was demonstrated that with the improved placement of current feeds and voltage probes it is possible to separate the loss contributions in an ohmic and a polarization part and that the low frequency response is useful in detecting mass transfer limitations. This methodology can be used to detect possible minor changes in the supply of gas to the individual cells, which is important when operating at high fuel utilizations. The fuel flow distribution provides important information about the operating limits of the stack when high electrical efficiency is required.

The impedance spectra were used to monitor the series, polarization, electrochemical and gas conversion resistances for all the repeating units and the stack simultaneously. The losses for the repeating units are reported and discussed. The gas concentration resistances from the different repeating units are compared in order to investigate the fuel flow distribution in the stack. The measured gas concentration impedance for one repeating unit is compared with predicted gas concentration resistances by a Continuously Stirred Tank Reactor model and a Plug Flow Reactor model model.

All text and figures related from Section 5.2.1 to Section 5.2.3 in this chapter was published in the conference proceeding Paper C on page 152.

## 5.1 Experiments

An experimental 14-cell stack was assembled with an optimized stack measurement geometry where the current feed is perpendicular to the voltage probes which minimizes stray impedances as explained in Chapter 2 on page 17. The metallic interconnects used in the stack were coated with protective layers to prevent chromium poisoning. EIS measurements for 14 repeating units and the stack were recorded simultaneously. This has several advantages such as reduced measurement time and a limited drift in temperature and fuel flow which gives a better comparison between repeating units compared to EIS measurements recorded sequentially. The test measurement setup and the stack are described in detail in Section 3.3 on page 63. All impedance measurements in this chapter was measured at a DC current of $4\,A$ $\left(0.046\,A\,cm^{-2}\right)$.

## 5.2 Results

This section presents the quality of impedance measurements and a parameterization of the losses. A comparison of the gas concentration resistances of the 14 repeating units is given together with single sided gas change analysis for one repeating unit. An equivalent circuit was

fitted to the measured gas concentration impedances for the 14 repeating units and the fuel distribution of the stack is revealed. The measured gas concentration impedance for one repeating unit is compared with predicted gas concentration resistances by a Continuously Stirred Tank Reactor model and a Plug Flow Reactor model model.

### 5.2.1 Quality of impedance measurements

EIS spectra were recorded from $18.5\,kHz$ to $0.3\,Hz$ with $12$ points per decade with an AC current modulation of $4\,A$, on top of a DC current of $4\,A$. The absolute value of the series resistance, $R_s$, for the displayed impedance spectra was between $5$ and $6\,m\Omega$. Figure 5.1 A) shows the impedance spectra for the 14 RUs recorded at $700^{\circ}\mathrm{C}$ with $20\%$ steam and $80\%$ hydrogen as fuel and air as oxidant. Figure 5.1 B) shows the imaginary impedance vs frequency. Figure 5.1 C) shows corresponding relative residuals of the linear Kramers-Kronig Transform test [22]. The Kramers-Kronig Transform test gave relative residuals in the range of $\pm 0.5\%$ which is in the same range as seen for single cell measurements at DTU Energy Conversion [25, 26]. Figure 5.1 D) shows the distribution of relaxation times, DRT, calculated from the impedance spectra. This preidentification method separates the polarization processes with different time constants directly from the impedance data [27, 28, 29]. A first tentative assignment of the various processes observed can be carried out using available data from Leonide et al. [28] (who used similar anode supported cells in a single cell set-up although the anode support thickness is different in Leonide et al. [28] and a LSCF/CGO composite cathode was used, where Leonide et al. [28] used a LSCF cathode) and from previous work on the present anode-supported half-cell as exemplified in Barfod et al. [42]. The DRT spectra can be divided into five processes, **P1** to **P5**. **P1** is the gas conversion impedance peaking at $1Hz$, **P2** is a gas diffusion impedance peaking at $10Hz$, **P3** is the activation polarization at the cathode ($100\,Hz$ to $1\,kHz$), **P4** and **P5** are according to [28, 29, 30] related to gas diffusion coupled with charge transfer reactions at the triple phase boundary and ionic transport in the anode functional layer. Prior to calculation of the DRT from the impedance spectra the high frequency inductance was removed by subtraction. The inductance subtracted was determined for each spectra by comparison of the imaginary data generated from the experimental real part of the impedance using the Kramers-Kronig transforms [21]. The negative DRT observed between the conversion and diffusion arc is not fully understood and it is not found described in the literature.

### 5.2.2 A first parameterization of losses

As a first step in the analysis a simplified parameterization was carried out. The loss for each impedance spectrum was divided into a series resistance, $R_s$, a polarization resistance, $R_p$, a gas conversion resistance, $R_{GCI}$, and an electrochemical polarization resistance, $R_{elec}$. See Figure 5.2. The series resistance, $R_s$, is the ohmic resistance and includes the resistance of the YSZ electrolyte [42], the CGO inter diffusion barrier layer, and losses associated with in-plane charge transport (current collection losses) and possibly a contribution from constriction at the interconnect/electrode interface. $R_s$ was determined as the $Z_{real}$ at the highest frequency $(18.5\,kHz)$. The polarization resistance, $R_p$, includes electrochemical polarization losses from the anode and cathode together with the gas diffusion and conversion losses. $R_p$ was determined as as the difference in $Z_{real}$ between $18.5\,kHz$ and $0.3\,Hz$. The gas diffusion and conversion impedance is the low frequency arc on the impedance spectra and has been described in several studies on single cells [11, 90, 91, 92, 93], only few studies describe the low frequency arc in detail on the stack level with large area cells [33]. $R_{GCI}$ is the real part of the gas diffusion and conversion impedance. $R_{GCI}$ was determined as the difference in $Z_{real}$ between $30\,Hz$ and $0.3\,Hz$. $R_{elec}$ was determined as the difference in $Z_{real}$ between $18.5\,kHz$ and $30\,Hz$ and reflects the electrochemical losses in the anode and cathode. The above analysis of the data is fast to do and represents a first approximate deconvolution of the losses in the repeating unit.

Figure 5.3 shows $R_s$, $Rp$, and $R_{GCI}$, and $R_{elec}$ as a function of the repeating units. $R_s$ decreases with increasing RU number. $R_s$ is decreasing by $16\%$ from RU01 to RU14. Temperature probes mounted at the top and at the bottom of the stack yield a temperature difference of $12^{\circ}C$

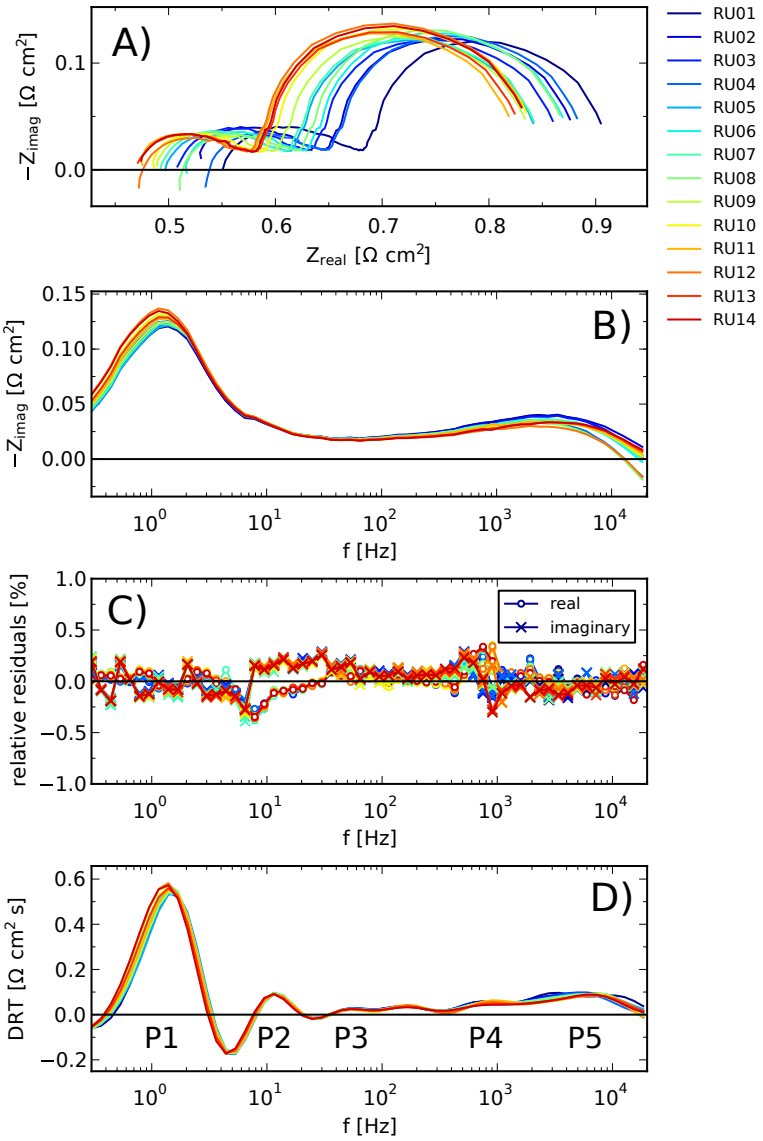


Figure 5.1: A) EIS spectra for the 14 RUs in the stack measured at a DC current of $4\ A$ and a temperature of $700°C$ Fuel: $20\%\ H_2O$ and $80\%\ H_2$ Oxidant: Air B) Corresponding imaginary impedance vs frequency C) Corresponding relative residuals from the linear Kramers-Kronig transform test. D) Corresponding DRT spectra with electrochemical processes, P1-P5.

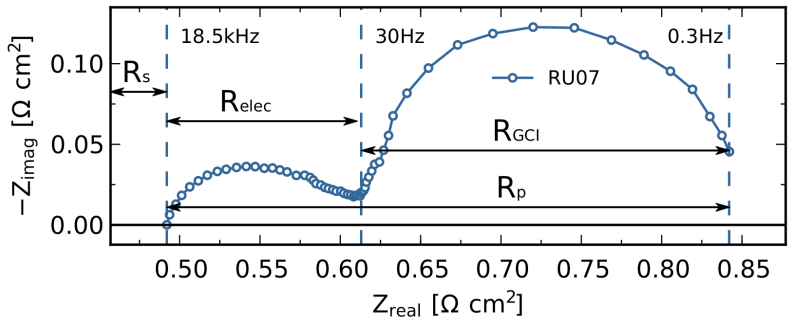


Figure 5.2: Impedance spectra for RU07 at $700°C$ Fuel: $20\%$ $H_2O$ and $80\%$ $H_2$ Oxidant: Air. The series resistance, $R_s$, is extracted at 18.5 kHz, the polarization resistance, $R_p$, is extracted between 18.5 kHz and 0.3 Hz. The gas concentration resistance, $R_{GCI}$, is extracted between $30\,Hz$ and $0.3\,Hz$.

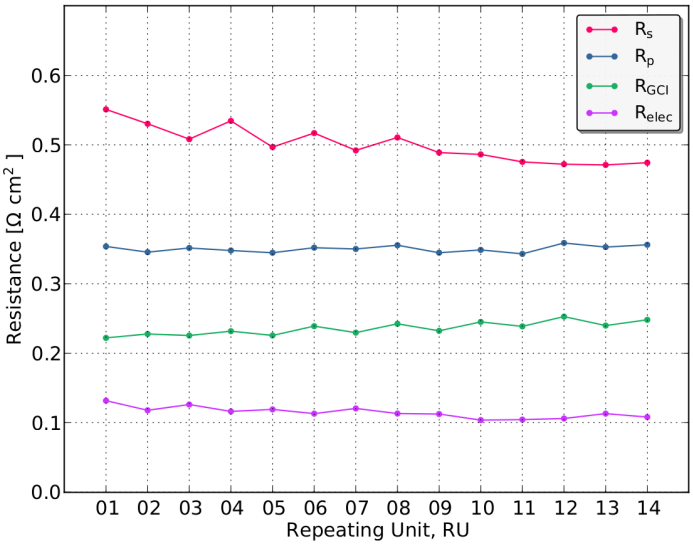


Figure 5.3: $R_s$, $R_p$, $R_{GCI}$ and $R_{elec}$ vs repeating unit at $700°C$ Fuel: $20\%$ $H_2O$ and $80\%$ $H_2$ Oxidant: Air.

between the top and bottom of the stack, with the top being the warmer end. The observed series resistance decreases from bottom (RU01) to top (RU14) by $16\%$. Estimating the expected temperature difference using a simple Arrhenius expression and the observed activation energy of $R_s$, the difference should be $12\%$. Thus, the trend in $R_s$ appears to primarily reflect the gradient in average RU temperature across the stack. The variations in $R_s$ observed from RU03 to RU09 indicate variations in stray impedances and/or systematic variation in cell/IC contact. $R_p$, shows similar values for all the cells in the stack. $R_{GCI}$ increases with increasing RU number. This is explained in detail in Section 5.2.3. $R_{elec}$ decreases from the bottom to the top of the stack. The $R_{elec}$ decreases by $22\%$ from RU01 to RU14. It is consistent with the activation energies of the electrodes and the electrolyte that the variation from top to bottom of the stack, if predominantly a temperature effect, is more pronounced for $R_{elec}$ than for $R_s$ [42].

Figure 5.4 shows a comparison between the stack resistance and the sum of the RU resistances. The difference in the series resistance for the stack, $R_s$ Stack, and repeating units, $R_s$ RUs, is $0.8\%$. The difference in the polarization resistance for the stack, $R_p$ Stack, and repeating units, $R_p$ RUs, is $0.5\%$. The difference in the gas conversion resistance for the stack, $R_{GCI,Stack}$, and the sum

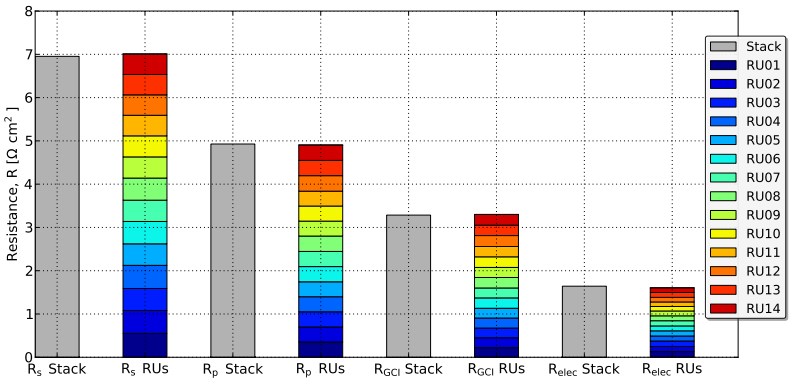


Figure 5.4: $R_s$, $R_p$, $R_{GCI}$ and $R_{elec}$ for the stack and the repeating units. Recorded at $700°C$ Fuel: $20\%$ $H_2O$ and $80\%$ $H_2$ Oxidant: Air.

over the repeating units, $R_{GCI}$ RUs, is $0.5\%$. The difference in electrochemical resistance for the stack, $R_{elec,Stack}$, and the sum over the repeating units, $R_{elec}$, is $2\%$.

### 5.2.3 Gas concentration impedance

In simple models the gas conversion and diffusion impedance are treated separately, can each be split into a resistive part and a capacitive part, and are strongly dependent on parameters such as gas composition, temperature, gas flow rate and interconnect geometry [90, 94, 93]. Jacobsen et al. [11] presented a coupled model of the gas diffusion and gas conversion impedance which depended on the gas concentration gradient. In this work the gas concentration impedance is sum of the gas diffusion and gas conversion impedance. Figure 5.5 shows the gas concentration resistance, $R_{GCI}$, as a function of repeating unit number. The dashed line is the average gas concentration resistance. The difference between the lowest $R_{GCI}$ from RU01 and the highest $R_{GCI}$ from RU12 is $\sim 12\%$. The general trend is that $R_{GCI}$ increases with increasing RU. An estimate using simple expressions for gas conversion resistances [90, 93] with a measured temperature difference of $12°C$ between top and bottom of the stack shows that the difference should be $\sim 1\%$ if it was a pure temperature effect. Hence, the observed variation is not due to the temperature gradient in the stack. The variation can be explained by a variation in fuel flow between the cells. The results indicate that slightly less fuel is supplied to the top of the stack compared bottom of the stack. The stack was a co-flow stack with internal fuel and oxidant manifolding and the fuel and oxidant was supplied from below. In order to understand the fuel flow distribution in more detail gas diffusion and conversion models must be fitted to the observed gas conversion impedance. An estimate of the fuel flow can be obtained from the gas concentration impedance. This has been shown with gas conversion impedance models on single cells [90, 91, 11, 93]. In simple gas conversion impedance models the gas conversion resistance is inversely proportional to the fuel flow [90, 93]. This means that the observed $\sim 12\%$ variation in $R_{GCI}$ corresponds to $\sim 12\%$ variation in fuel flow (if the temperature and partial pressures are constant).

#### 5.2.3.1 Single sided gas change

EIS recorded as a function of a series of single-sided gas changes is a useful method for identification of electrode and process specific parts of the impedance spectrum [82]. Barfod et al. [95] have tested single SOFC and observed a low-frequency arc with a summit frequency of $1\,Hz$ and showed that this was due to a gas-conversion resistance at the Ni electrode and it was strongly dependent on steam partial pressure. The gas concentration impedance for all repeating units was recorded at different steam partial pressures during a single sided gas change. The single sided gas change is shown in Table 5.1. The EIS spectra for RU08 at varying steam partial pressure,

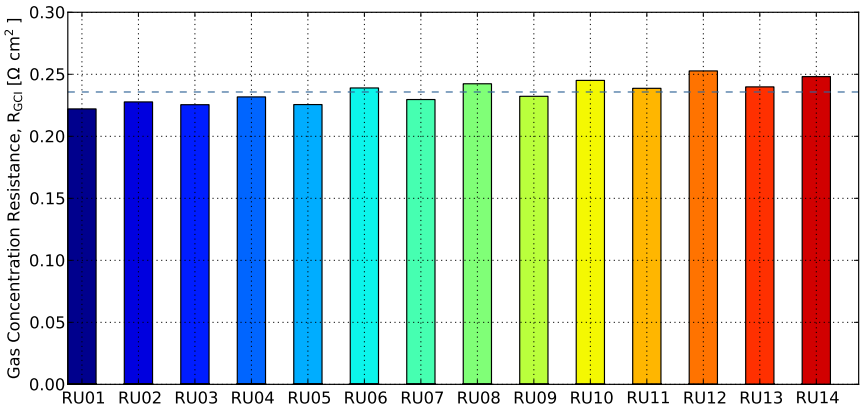


Figure 5.5: Gas concentration resistance, $R_{GCI}$, vs Repeating Unit at $700°C$ Fuel: $20\%$ $H_2O$ and $80\%$ $H_2$ Oxidant: Air. Dashed line is the average gas concentration resistance.

| Temp. $T$ | Hydrogen $x_{H_2}$ | Steam $x_{H_2O}$ | Oxidant $x_{Air}$ | DC Current $I_{DC}$ | AC Current $I_{AC,0-peak}$ |
|---|---|---|---|---|---|
| $700°C$ | $96\%$ | $4\%$ | $100\%$ Air | $4\,A$ | $3.85\,A$ |
| $700°C$ | $92\%$ | $8\%$ | $100\%$ Air | $4\,A$ | $3.85\,A$ |
| $700°C$ | $80\%$ | $20\%$ | $100\%$ Air | $4\,A$ | $3.85\,A$ |
| $700°C$ | $50\%$ | $50\%$ | $100\%$ Air | $4\,A$ | $3.85\,A$ |

Table 5.1: Anode single sided gas change.

$4\%$, $8\%$, $20\%$ and $50\%$ $H_2O$, are shown in Figure 5.6. The fuel electrode gas conversion, diffusion and activation polarization impedances changes with steam partial pressure. Again, the negative DRT observed between the conversion and diffusion arc is not fully understood and it is not found described in the literature.

#### 5.2.3.2 Equivalent circuit fitted to the gas concentration impedance

The gas concentration impedance which includes the diffusion and conversion impedance for all the repeating units, $14$ impedance measurement simultaneously at four different steam molar fractions, during the single sided gas change test given in Table 5.1 was fitted between $20\,Hz$ and $0.1\,Hz$ with a $R-RQ$ circuit as given in Figure 5.7. The $Q$ element is a constant phase element described in Section 1.4.1.2 on page 11. It is an approximate parameterization as the chosen equivalent circuit lumps the conversion and diffusion impedance into one element to get the gas concentration resistance, $R_{GCI}$. The fits for the 14 RUs are shown in Figure 5.8. The $\alpha$ values for the $Q$ element for all the fits was close to one. The circuit was batch fitted to the measured impedance using the data analysis software RAVDAV [23]. The fitted $R_{GCI}$ values for the complete single side gas change as a function of incoming steam molar fractions are shown in Figure 5.9. The incoming steam molar fraction for each RU was calculated using OCV and the Nernst equation given in Section 1.1.5.2 on page 3 since it will give the most correct gas composition for each RU in the stack.

#### 5.2.3.3 Fuel Distribution

The gas concentration resistance, obtained from fits, as a function of repeating unit number at four different steam partial pressures, $4\%$, $8\%$, $20\%$ and $50\%$ are shown in Figure 5.10. Two trends are observed. Trend 1: An increasing gas concentration resistance, $R_{GCI}$, with increasing RU number. This is due to a decrease in fuel flow from RU01 to RU14, since the fuel is supplied from

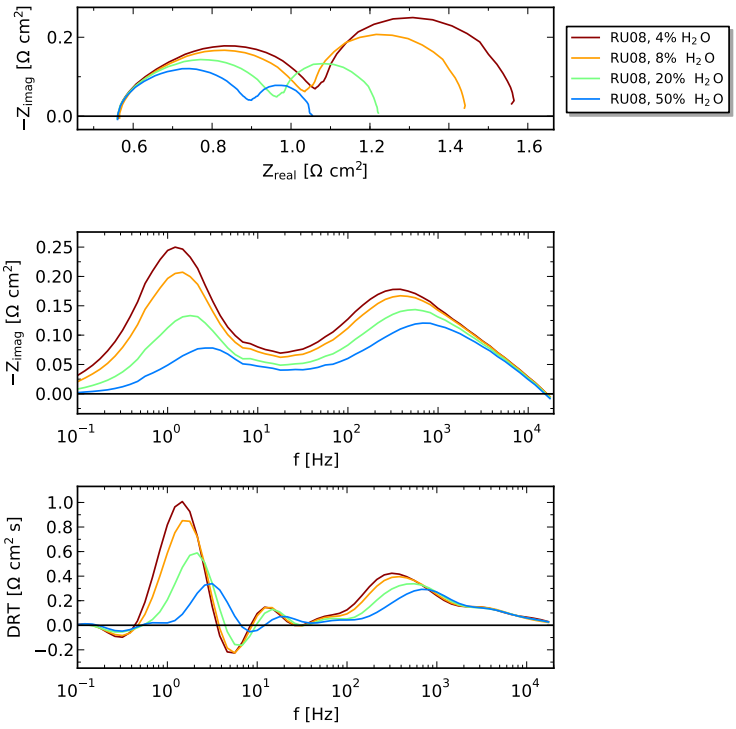


Figure 5.6: EIS measurements for RU08 at $700°C$ during single sided gas change with $H_2$ as fuel at varying steam partial pressure, $4\%$, $8\%$, $20\%$ and $50\%$ $H_2O$. Oxidant: $100\%$ $Air$

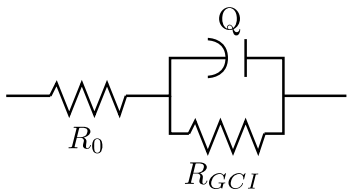


Figure 5.7: RQ circuit used for fitting the gas conversion impedance.

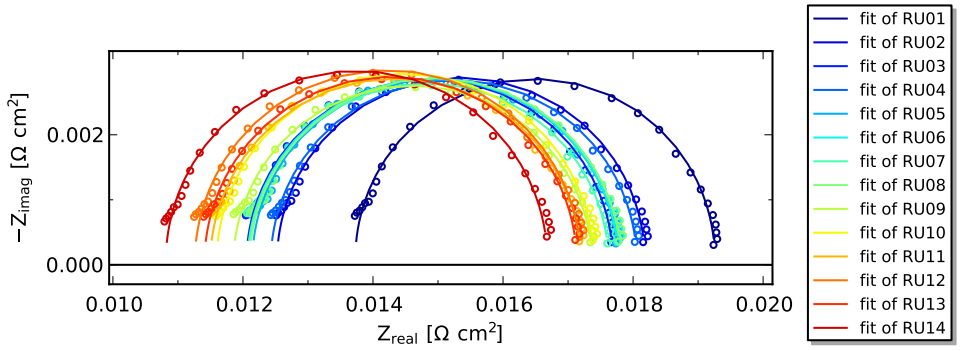


Figure 5.8: The fitted gas concentration resistance for the 14 repeating units at DC current: $4\,A$ Temperature: $700°C$ Fuel: $96\%$ $H_2$ $4\%$ $H_2O$ Oxidant: $100\%$ $Air$.

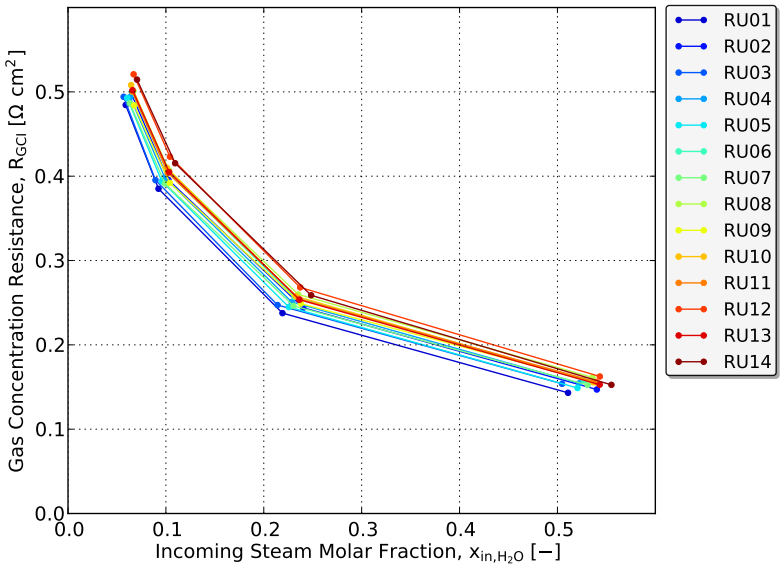


Figure 5.9: Gas concentration resistances from fits vs incoming steam molar fractions obtained from OCV.

RU01 to RU14. Trend 2: Alternating increase/decrease between neighboring RUs. This has been observed before on cell voltage measurements, but with electrochemical impedance spectroscopy it can be clarified that it relates to the fuel flow. The cause of the alternating increase/decrease between neighboring RUs are not fully understood. It may somehow reflect that flow resistance varies from cell to cell in a periodic manner. Figure 5.11 shows the deviation from average gas conversion resistance, $\overline{R}_{GCI}$. The deviation in fuel flow is in the range of $\pm 7\%$. Dekker et al. [33] reported in 2009 that the flow distribution varied from $-9\%$ to $14\%$ between 10 cell blocks in a 30 cell stack. The deviation from perfect distribution is thus slightly smaller in the experimental stack, tested in this work, than in the stack from Energy research Centre of the Netherlands (ECN) tested by Dekker et al. [33].

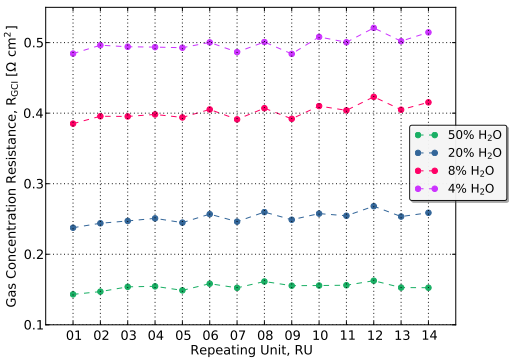


Figure 5.10: Gas concentration resistance as a function of repeating unit at different steam partial pressures.

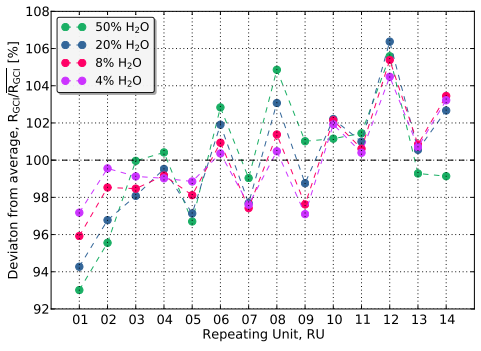


Figure 5.11: Deviation in gas concentration resistance as a function of repeating unit at different steam partial pressures.

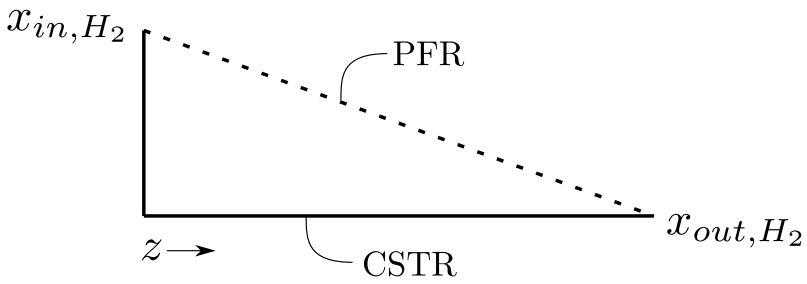


Figure 5.12: Difference in change composition, $x_{gas}$, between Plug Flow Reactor (PFR) and Continuously Stirred Tank Reactor (CSTR) models.

#### 5.2.3.4 Gas conversion impedance models

A detailed understanding of the fuel flow and the corresponding gas concentration impedance in SOFC stacks is highly desirable from an optimization point of view. Particularly when fuel utilization (stack efficiency) is the main concern for commercialization, efforts should be made to create an efficient gas flow field design so that differences in the gas flow distribution across the cells and the stack are minimized. Several models exist for describing the gas concentration impedance including the gas conversion and gas diffusion impedance [11, 90, 91, 96]. So far these models have not been applied to SOFC stack impedance measurements. In this section different gas conversion models are evaluated together with the fitted gas concentration impedance values from the single sided gas change. The gas diffusion impedance is not taken into account even though it is observed in between $6\,Hz$ and $20\,Hz$ on the DRT plot in Figure 5.6. This means that the calculated gas conversion impedance should be a little bit smaller than the measured gas concentration impedance. Two types of models are considered, the Continuously Stirred Tank Reactor (CSTR) and the Plug Flow Reactor (PFR). The difference in change in gas composition between the CSTR and PFR model is illustrated in Figure 5.12. The CSTR model assumes that the complete cell works with the outlet composition . The PFR model assume uniform current density on the electrode surface. The electrochemical reactions with the gas composition, $x_{gas}$, changes uniformly along the $z$-axis.

**Continuously Stirred Tank Reactor Model**

Primdahl et al. [90] studied an anode electrode in a three-electrode setup. The electrode was examined in a $H_2/H_2O$ gas, and a low-frequency impedance arc with summit frequency around $1\,Hz$ was assigned to gas conversion. The Continuously Stirred Tank Reactor model (CSTR) assume the that the complete cell works with the outlet composition as illustrated in Figure 5.12 based on well convected gas flow. The gas conversion resistance is described by Equation 5.1 where $R_g\,[\frac{J}{mol\,K}]$ is the gas constant, $T\,[K]$ is the absolute temperature, $F\,[\frac{C}{mol}]$ is Faraday's constant. $x_{in,H_2O}\,[-]$ and $x_{in,H_2}\,[-]$ are the inlet steam and hydrogen mole fractions respectively. $J_{in}\,[\frac{mol}{m^2\,s}]$ is the total area specific incoming molar gas flux. The gas compositions $x_{in,H_2O}\,[-]$ and $x_{in,H_2}\,[-]$ for each cell needs to be calculated using OCV and the Nernst equation given in Section 1.1.5.2 on page 3 since it will give the most correct gas composition for each cell in the stack.

$$R_{GCI,CSTR} = \frac{R_g\,T}{4\,F^2 J_{in}} \left( \frac{1}{x_{in,H_2O}} + \frac{1}{x_{in,H_2}} \right) \tag{5.1}$$

When hydrogen is transported through a bubbler for humidifying the hydrogen the total area specific reaction rate, $J\,[\frac{mol}{m^2\,s}]$, can be calculated as Equation 5.2 from the molar flow of hydrogen, $\upsilon_{H_2}\,\left[\frac{mol}{s}\right]$, the steam mole fraction, $x_{H_2O}\,[-]$ and the active area, $A_{active}\,\left[m^2\right]$.

$$J = \frac{\upsilon_{RU,total}}{A_{active}} \tag{5.2}$$

Equation 5.1 assume that the gas conversion impedance is recorded at OCV where $x_{in,H_2O} = x_{out,H_2O}$ is valid since no hydrogen is converted to steam. Under load $x_{in,H_2O} \neq x_{out,H_2O}$ since steam is produced through the electrochemical reaction of hydrogen. As the CSTR model assumes perfectly mixed gas the gas conversion impedance under load is given by Equation 5.3.

$$R_{GCI,CSTR} = \frac{R_g\,T}{4\,F^2 J_{out}} \left( \frac{1}{x_{out,H_2O}} + \frac{1}{x_{out,H_2}} \right) \tag{5.3}$$

If the gas conversion impedance is measured under load the molar flow of hydrogen, $\upsilon_{H_2}$ $\left[\frac{mol}{s}\right]$, and the steam molar fraction, $x_{H_2O}$ $[-]$, needs to be adjusted using Faraday law given in Section 1.1.5.3 on page 4. The CSTR model assumes that the complete cell works with the outlet composition, the molar flow rate at the outlet for a given repeating unit, $\upsilon_{H_2\,at\,I,CSTR,RU}$ $\left[\frac{mol}{s}\right]$, is given by Equation 5.4. $\upsilon_{H_2\,to\,H_2O}$ $\left[\frac{mol}{s}\right]$ is the molar flow of hydrogen converted to steam by the electrochemical reaction given by Faraday law.

$$\upsilon_{H_2\,at\,I,CSTR,RU} = \upsilon_{out,H_2,RU} = \upsilon_{in,H_2,RU} - \upsilon_{H_2\,to\,H_2O} \tag{5.4}$$

The molar flow of hydrogen, $\upsilon_{in,H_2,RU}$ entering a given RU is given by Equation 5.5 where $\upsilon_{in,stack,H_2}$ is the total incoming molar flow of hydrogen entering the stack, $n_{cells}$ is the number of cells in the stack. $\frac{R_{GCI}}{\overline{R}_{GCI}}$ $[-]$ is the deviation from the average gas conversion impedance shown in Figure 5.11 in order to correct for changes in the flow distribution.

$$\upsilon_{in,H_2,RU} = \frac{\upsilon_{in,stack,H_2}}{n_{cells}} \left( \frac{R_{GCI}}{\overline{R}_{GCI}} \right)^{-1} \tag{5.5}$$

The molar flow rate of steam under load for the CSTR model, $\upsilon_{H_2O\,at\,I,CSTR}$ is given by Equation 5.6. $\upsilon_{RU,total}$ is the total molar flow of hydrogen for a given repeating unit entering a given RU is given by Equation 5.7. $x_{H_2O\,at\,OCV}$ $[-]$ is the steam molar fraction at OCV.

$$\upsilon_{H_2O\,at\,I,CSTR,RU} = \upsilon_{RU,total}\,x_{H_2O\,at\,OCV} + \upsilon_{H_2\,to\,H_2O} \tag{5.6}$$

$$\upsilon_{RU,total} = \frac{\upsilon_{in,H_2,RU}}{1 - x_{H_2O\,at\,OCV}} \tag{5.7}$$

The steam molar fraction under load is then given by Equation 5.8. The total area specific molar flux under load, $J_{total\,at\,I}$ $\left[\frac{mol}{m^2\,s}\right]$, can be calculated by Equation 5.9.

$$x_{H_2O\,at\,I} = \frac{\upsilon_{H_2O\,at\,I}}{\upsilon_{H_2\,at\,I} + \upsilon_{H_2O\,at\,I}} \tag{5.8}$$

$$J_{total\,at\,I} = \frac{\upsilon_{H_2\,at\,I}}{(1 - x_{H_2O\,at\,I})\;A_{active}} \tag{5.9}$$

**Plug Flow Reactor Model**

Jensen et al. [96] studied a nickel electrode in a single cell SOEC setup with an active cell area of $16\,cm^2$. The electrode was examined in a $H_2/H_2O$ gas, and the low frequency arc at around $1\,Hz$ was described as gas-conversion and the expression for the gas-conversion resistance in a plug-flow reactor setup (PFR), $R_{GCI,PFR}\,[\Omega\,cm^2]$ as given in Equation 5.10 measured under current load. The plug-flow reactor model (PFR) for the gas-conversion resistance assume uniform current density on the electrode surface leading to a linear change in gas composition as illustrated in Figure 5.12.

$$R_{GCI,PFR} = \frac{R_g\,T}{8\,F^2 J_{in}} \left( \frac{1}{x_{in,H_2O}} + \frac{1}{x_{in,H_2}} \right) \tag{5.10}$$

The PFR model given in Equation 5.10 assumes that the gas conversion impedance is recorded at OCV. Under load the molar flow of hydrogen, $\upsilon_{H_2\,at\,I,PFR,RU}$ $\left[\frac{mol}{s}\right]$, for the PFR model is given by Equation 5.11 . $\upsilon_{in,H_2,RU}$ $\left[\frac{mol}{s}\right]$ molar flow of hydrogen entering the RU given in Equation 5.5.

$\upsilon_{H_2\,to\,H_2O}\left[\frac{mol}{s}\right]$ is the molar flow of hydrogen converted to steam through the electrochemical fuel cell reaction calculated by Faraday law given in Section 1.1.5.3 on page 4. The molar flow rate of steam, $\upsilon_{H_2O\,at\,I,PFR,RU}$, for given repeating unit can then be calculated by Equation 5.12

$$\upsilon_{H_2\,at\,I,PFR,RU} = \upsilon_{in,H_2,RU} - \frac{1}{2}\,\upsilon_{H_2\,to\,H_2O} \tag{5.11}$$

$$\upsilon_{H_2O\,at\,I,PFR,RU} = \frac{\upsilon_{in,H_2,RU}}{1 - x_{H_2O\,at\,OCV}}\,x_{H_2O\,at\,OCV} + \frac{1}{2}\,\upsilon_{H_2\,to\,H_2O} \tag{5.12}$$

The steam molar fraction, $x_{H_2O\,at\,I}$, and the total area specific molar flux, $J_{total\,at\,I}$, for the PFR model can then be calculated as Equation 5.8 and Equation 5.9 respectively.

**Comparison between gas conversion impedance models and test data**

The gas conversion impedance for the CSTR model and the PFR model are compared with the measured gas concentration impedances for RU08 at varying incoming steam molar fraction in Figure 5.13. The measured gas concentration impedance lies between the CSTR and the PFR model at all incoming steam molar fractions. This is to be expected in the sense that the CSTR assumes perfect mixing of the gases (thereby overestimating mixing by diffusion) and the plug flow neglects any mixing in the sense that the local gas composition is a function of local current and the upstream composition only. This means that effect of mixing by diffusion is neglected. Hence, the two models represents extremes.

Further work on modeling of the gas conversion impedance still needs to be done in order to get a better description of the gas concentration impedance at various steam molar fractions inside the SOFC stacks. Specifically to take into account backwards diffusion. The relevant flow profile for the measured gas concentration impedance would a priori be expected to be plug flow since the stack is running in a co-flow configuration where the fuel gas enters at one edge of the cell and the channel height is significantly smaller than the cell length. The difference in the measured gas concentration impedance and the calculated gas conversion from the PFR could indicate a measurement error in the fuel flow. The steam molar fraction is measured at OCV and calculated from the Nernst equation which should not lead to any measurement error. The incoming fuel flow for the PFR model was varied in the model calculations to obtain a better agreement with the observed gas concentration impedance as shown in Figure 5.14. If the actual molar fuel flow was $81\%$ of the nominal fuel flow then the PFR model shows good agreement with the measured gas concentration impedance at low steam molar fraction. On the other hand if the molar fuel flow was only $63\%$ of the nominal fuel flow assumed one to account for the discrepancy between model and experimental value. The deviation could indicate that the stack receives less gas than the set gas flow (a systematic error in the flow controller or loss of gas through leaks).

## 5.3 Conclusion

A 14-cell experimental SOFC stack was tested with electrochemical impedance spectroscopy. The stack measurement geometry, in terms of current path and voltage probe placement was optimized for electrochemical impedance spectroscopy (EIS). The linear Kramers-Kronig transform test was used for data validation of the impedance spectra. The results illustrate that detailed EIS is possible on large area stacks and a de-convolution of the total loss into an ohmic, a non-ohmic part, and a part describing the gas conversion and diffusion, is possible. The sum of the RU resistances agreed well with the stack resistances. The experiment was successful in terms of characterization – the EIS allowed a distinction to be made in terms of differences between the RUs that is not possible from IV-data only. The gas conversion resistance increased with increasing RU number (from bottom to top). This indicates that top cells got slightly less fuel than the bottom cells ($\sim 12\%$). The measured gas concentration impedance was smaller than predicted by the Continuously Stirred Tank Reactor model (CSTR) and above the prediction of the Plug Flow Reactor model (PFR). The incoming molar fuel flow was varied for the PFR model to see if the deviation between the real flow and the set-point value could be the cause of disagreement with

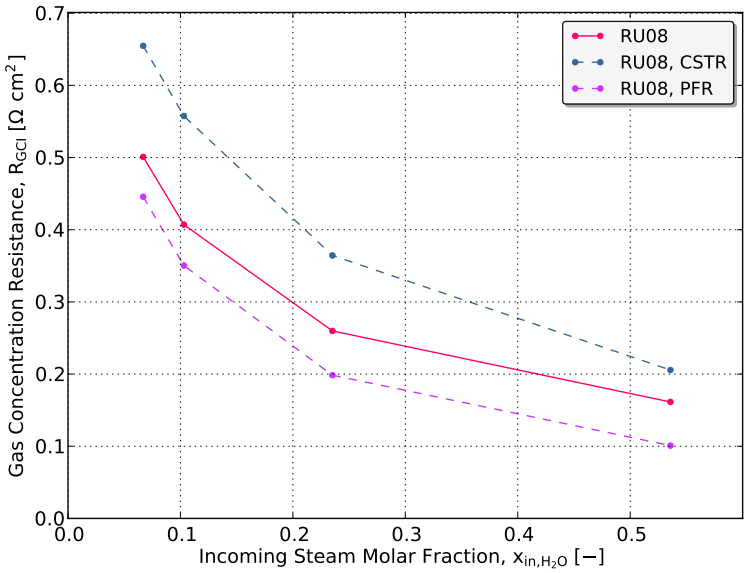


Figure 5.13: Observed gas concentration resistance of RU08 for a range of molar fractions of steam and calculated gas conversion impedance using three different models: Continuously Stirred Tank Reactor model (CSTR) and Plug Flow Reactor model (PFR).

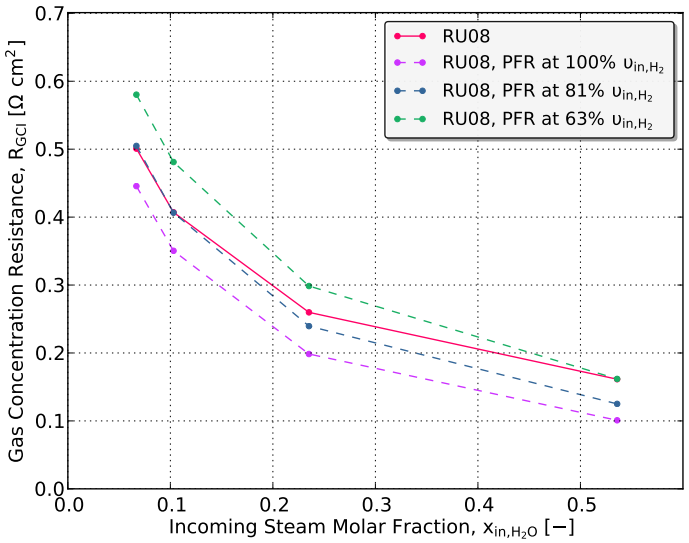


Figure 5.14: Gas concentration resistance measured for RU08 and corresponding gas conversion impedance models Plug Flow Reactor Model (PFR). The molar fuel flow of hydrogen, $\nu_{in,H_2}$, was varied in the model calculations to obtain a better agreement with the observed gas concentration impedance.

the measured gas concentration impedance for RU08. The PFR model showed good agreement with the measured gas concentration impedance if the incoming molar fuel flow was $81\%$ of the actual flow for low steam molar fractions. If the incoming molar fuel flow was assumed to be only $63\%$ of the setpoint value the PFR model showed good agreement with the measured gas concentration resistance at high steam molar fractions. This indicate that the fuel flow supplied to the cell is lower than expected. Work on gas conversion impedance modeling still needs to be done in order to get a better description of the gas concentration impedance at various steam molar fractions inside the SOFC stacks.

CHAPTER 6

# Fuel starvation detection

In state of the art fuel cell stack monitoring techniques such as electrochemical impedance spectroscopy and cell voltage monitoring, single cell or cell-block voltages are monitored separately, whereas in the Total Harmonic Distortion (THD) approach derives information about critical cell and stack conditions, such as fuel starvation, from the stack sum voltage using a superimposed AC current signal on the DC current load. The THD signal arises from non-linearities in the current-voltage curve. It offers a simple system monitoring which could reduce the cost of the fuel cell control system. In this chapter an experimental study of THD as a function of AC amplitude, frequency, and fuel utilization is presented, and the potential of the technique for system monitoring is discussed.

## 6.1 Introduction

The electrical efficiency of a fuel cell is dictated by thermodynamics, irreversible kinetic losses, and fuel losses due to finite fuel utilization and can be written as Equation 6.1. Only a part $(\Delta G)$ of the total energy $(\Delta H)$ of the overall reaction can be extracted by the electrochemical process giving an upper limit for the cell efficiency described by the thermodynamic efficiency, $\epsilon_{thermo}\,[-]$, as given Equation 6.2. For a fuel cell the maximum amount of energy available to do work is given by Gibbs free energy, $\Delta G\,\left[\frac{J}{mol}\right]$. For a hydrogen-oxygen fuel cell above $100°C$ one should recognize that calculating $\Delta G\,\left[\frac{J}{mol}\right]$ based on water vapor, while simultaneously using $\Delta H_{HHV}\,[J]$ based on liquid water for efficiency calculations does not represent a contradiction but says that a fuel cell operating above $100°C$ is losing the ability to convert latent heat of vaporization of the product water into useful work [1]. The voltage efficiency of a fuel cell, $\epsilon_{voltage}$, incorporates the losses due to irreversible kinetics effects in the fuel cell. The voltage efficiency of a fuel cell (Equation 6.3) is the ratio between the operating voltage, $U\,[V]$, and the thermodynamically reversible voltage of the fuel cell, $E_{rev}\,[V]$. The thermodynamically reversible voltage of the fuel cell, $E_{rev}\,[V]$ is given by Equation 6.4, where $n$ is the number of moles, $F\,\left[\frac{C}{mol}\right]$ is the Faraday constant. The fuel utilization efficiency accounts for the fact that not all fuel provided to the fuel cell will not participate in generating power through the electrochemical reaction. Some of the fuel will undergo side reactions that do not produce power and some fuel will simply pass through the fuel cell without ever reacting. The fuel utilization efficiency, $\epsilon_{FU}$, is the ratio between the fuel used to generate electric current versus the total fuel provided to the fuel cell as written in Equation 6.5, where $i\,[A]$ is the current generated by the fuel cell, where $\dot{n}_{fuel}\,[\frac{mol}{s}]$, is the total fuel supplied to the fuel cell [1].

$$\epsilon_{real} = \epsilon_{thermo} \cdot \epsilon_{voltage} \cdot \epsilon_{fuel} \tag{6.1}$$

$$\epsilon_{thermo} = \frac{\Delta G}{\Delta H_{HHV}} \tag{6.2}$$

$$\epsilon_{voltage} = \frac{U}{E_{rev}} \tag{6.3}$$

$$E_{rev} = -\frac{\Delta G}{n\,F} \tag{6.4}$$

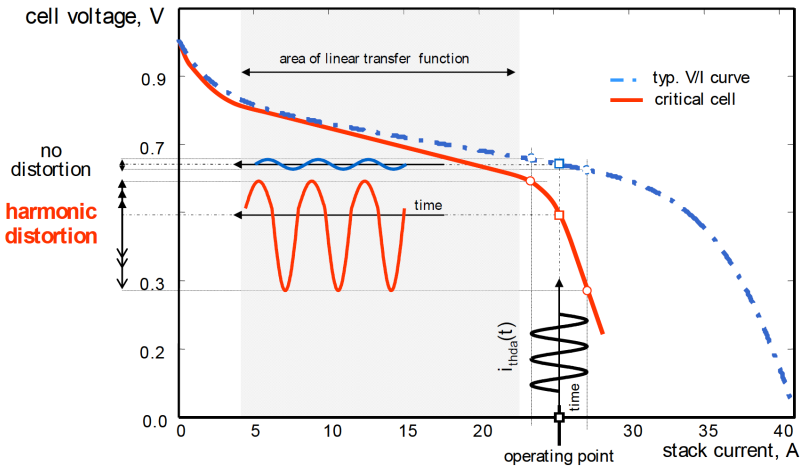


Figure 6.1: Distortion of a Sinusoidal Signal in a Fuel Cell (Principle). From Ref. [97].

$$\epsilon_{FU} = \frac{\frac{i}{nF}}{\dot{n}_{fuel}} \tag{6.5}$$

For an operating fuel cell stack the fuel utilization efficiency is a key parameter to obtain high electrical efficiency. When operating a real stack at high fuel utilization some cells in a fuel cell stack may suffer from too low fuel supply, leading to local fuel starvation, e.g. due to an uneven fuel flow distribution in the fuel cell stack. Detecting fuel starvation would therefore be of great importance from a fuel cell system control point-of-view for maintaining high fuel utilizations, but at the same time make sure there are no problems with starvation at any of the cells. In state of the art fuel cell stack monitoring techniques the voltage of either single cells, or cell-blocks, are monitored separately. This complicates system integration and has a negative impact on the cost of the fuel cell system as a large number of voltage channels may have to be monitored. Total Harmonic Distortion Analysis is a promising low cost technique for detecting critical cell and stack operation status, such as fuel starvation, from the stack sum voltage only.

If critical cell operation conditions occur, *e.g.* if too low fuel flow causes a sharp voltage drop at a particular cell current can be detected by THD. If in such case the current is superposed by a AC current signal with a specific frequency pattern (e.g. sinusoidal), then the stack voltage will be harmonically distorted. This means that even if just one single cell is in a critical status, it will cause frequency distortion and an increase in the amount of harmonics in the stack (AC) voltage. The amount of higher harmonics are analyzed in the frequency domain and are compared to the originally superposed frequency pattern, which provides information on whether one or more cells are operated in a critical mode [97]. This technique has been investigated on low temperature PEM fuel cell stacks in several studies [97, 98, 99, 100, 101], but has so far only been investigated to a limited extent on SOFC stacks [98].

Figure 6.1 illustrates the AC current response for two cases where the fuel flow and DC current is such that one is either in a range where the transfer function is linear or (with too small fuel or oxidant flow with respect to the running DC current) where it is non-linear. Generally, harmonic distortion of the AC current signal occurs at conditions with insufficient fuel or oxidant supply which cause mass transport limitations and where the Nernst expression becomes nonlinear in the composition. The general term for monitoring the harmonic distortion is Total Harmonic Distortion, THD. Total Harmonic Distortion Analysis, THDA, is an AVL List GmbH trademark. Since this new approach is based on the detection of harmonic distortion in the AC voltage response, the acronym "THDA" (Total Harmonic Distortion Analysis) is used for this technology [97].

Figure 6.2 shows a schematic of the hardware setup for THDA. An auxiliary signal source (controlled source) is generating a small AC current amplitude, $I_{THDA}$. On average, the stack

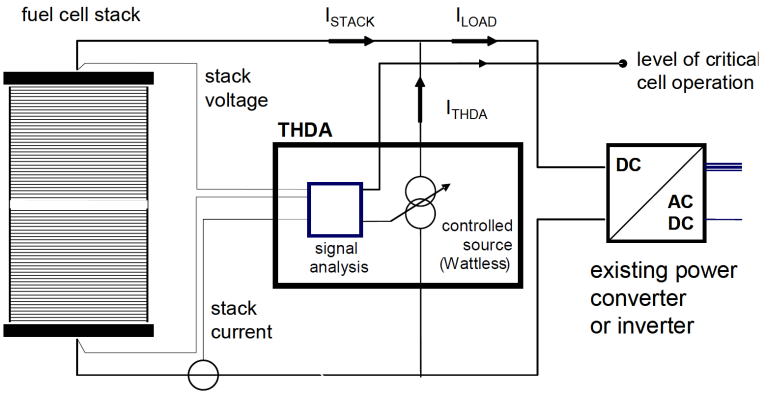


Figure 6.2: Schematic realization of the AVL THDA measurement system. From Ref. [97].


Figure 6.3: The AVL THDA hardware device. Photo: AVL List GmbH.

output power is not influenced by the THDA device. From the stack voltage only the AC part is measured in order to utilize the full range of the analogue to digital converter. Signal measurement, de-noising and the transformation into the time-frequency and the frequency domain is carried out by an embedded digital signal processor (DSP) [97]. Figure 6.3 shows the AVL THDA hardware device and its graphical user interface.

Figure 6.4 shows THDA results for an fuel gas starvation experiment reported by Ramschak et al. [97] who have reported a number of studies of THDA applied to PEM fuel cells [97, 98, 99]. The fuel flow anode of the tested PEM fuel cell was decreased slowly from a fuel utilization of $50\%$ until the first drops in the cell voltage were detected. This measurement shows that the THDA technology can detect when critical conditions occur at the anode. Similar measurements were made for the case of oxidant starvation at the cathode [97].

The focus of this work was on THD of a SOFC stack and was carried out by investigating the frequency, AC amplitude, and fuel utilization dependence of the THD signal. EIS spectra and THD was recorded simultaneously at selected DC currents, using a range of fuel flow rates (corresponding to $20\%$ up to $98\%$ fuel utilization) and AC amplitudes ($1$ to $4\ A$). Tests with changing DC current from the linear region to the non-linear region at a single fuel flow rate were also performed.

## 6.2 Experiments

The stack was tested at a stack temperature of $700°C$ at OCV with a gas mixture of $48\%\ H_2$, $32\%\ N_2$ and $20\%\ H_2O$ as fuel and air as oxidant. The stack temperature was determined by calculating the average of the measured cathode gas inlet and outlet temperatures from mounted thermocouples

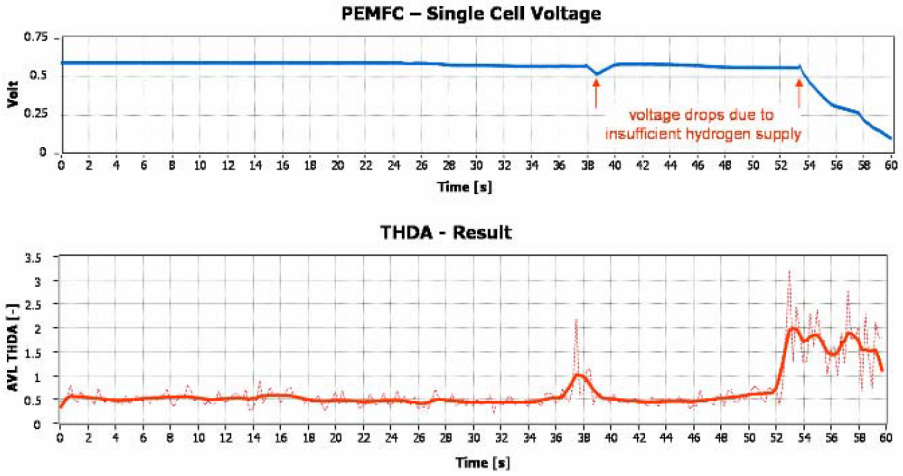


Figure 6.4: AVL THDA output for critical conditions on anode (PEMFC). From Ref. [97].

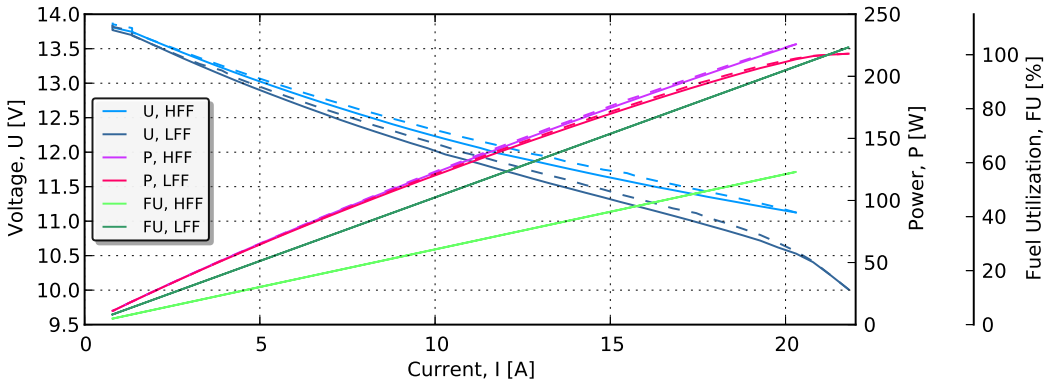


Figure 6.5: UI curve for high fuel flow, HFF, and low fuel flow , LFF, and corresponding power and fuel utilization. Dashed line indicate decreasing current.

in the gas manifold. Further details regarding the stack and the experimental setup are given in Section 3.3 on page 63. The UI curve and corresponding power and fuel utilization for the $14$-cell experimental stack are shown in Figure 6.5 for high fuel flow, HFF, and low fuel flow, LFF. Above $20\,A$ the UI curve obtained at LFF becomes nonlinear due to fuel starvation.

A zoom of the UI curve at HFF for each repeating unit are shown in Figure 6.6. All RU voltages are linear towards $20.5\,A$ for fuel utilizations (stack average) up to $\approx 56\%$. A zoom of the UI curve at LFF for each repeating unit are shown in Figure 6.7. RU12 shows signs of fuel starvation already at $19.2A$ at $\approx 91\%$ fuel utilization, and half of the cells in the stacks will suffer from fuel starvation at $21.7\,A$ and $\approx\ 102\%$ (nominal) fuel utilization. The variation in the onset of fuel starvation among the different cells reflects a slightly uneven fuel flow distribution in the stack. That a greater apparent fuel utilization than $100\%$ was observed is likely due to a small systematic error in the mass flow controllers used to control the fuel flow. RU10, RU12 and RU14 have degraded during the starvation period since the RU voltages observed during the decreasing current ramp (dashed lines) are lower than the RU voltages during the increasing current ramp (solid lines). If one would apply an AC current superimposed on the DC current in the fuel starvation area it would be possible to detect non-linearities from the stack sum voltage by measuring the THD as explained in Section 6.1 on page 103. Detecting the starvation from the sum voltage by THD not only allows for cheaper monitoring system it is also potentially is less harmful than detecting

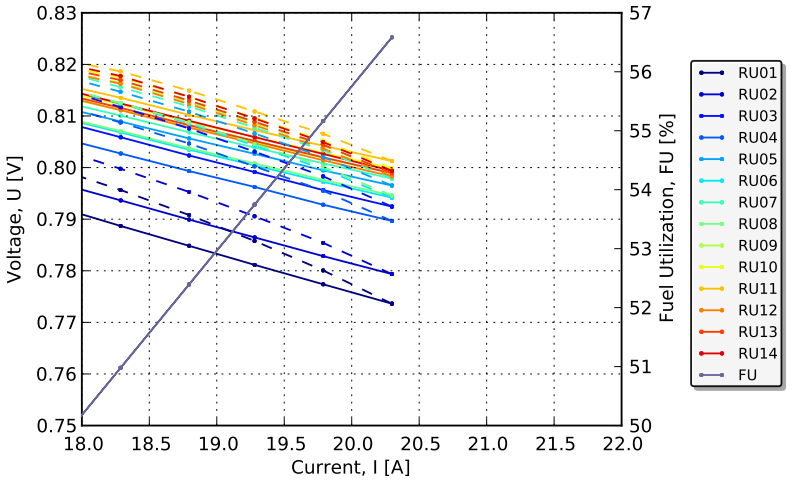


Figure 6.6: UI curve for high fuel flow, HFF. Dashed line indicate decreasing current.

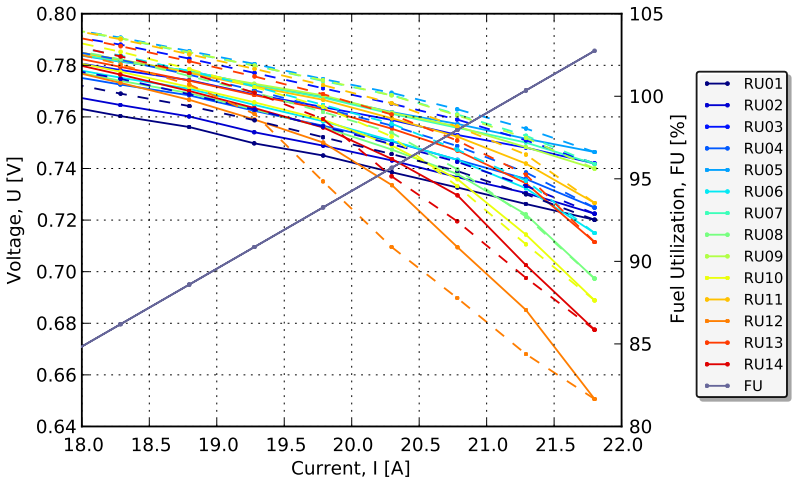


Figure 6.7: UI curve low fuel flow, LFF. Dashed line indicate decreasing current.

starvation from the DC voltage response. It was selected to apply AC current at a DC current of $20.5\,A$. By setting the DC current to $20.5\,A$ when using LFF conditions and applying AC current amplitudes in the range $1-4A$ current excursions of varying depths into the non-linear region were made.

## 6.3 Results

This section presents the results obtained by measuring the total harmonic distortion of a SOFC stack carried out by investigating the frequency, AC amplitude, and fuel utilization dependence of the THD signal.

### 6.3.1 THD - Dependence on frequency

Impedance spectra were recorded at a DC current of $20.5\,A$ at HFF with a fuel utilization of $57\,\%$ and at LFF with a fuel utilization of $98\,\%$ at three different AC peak amplitudes $0.96\,A$, $1.93\,A$ and $3.85\,A$ for monitoring the change in THD as a function of frequency as shown in Figure 6.8. At LFF with high fuel utilization the concentration impedance increases dramatically, and it also increases with increasing AC current amplitude. The increase in THD at high frequencies is due to non linearities in the stack measurement setup or the measurement equipment and could be an effect of stray impedances as explained in Chapter 2 on page 17. The THD signal increases below $3\,Hz$, which corresponds to the frequency range where the gas concentration impedance dominates and it is close to the characteristic frequency of the gas concentration impedance at HFF ($FU = 57\%$). When designing THD equipment for detecting fuel starvation in SOFC systems the superimposed signal should be lower than $3\,Hz$ for this stack technology. Considering that the gas concentration impedance varies with the dimensions of the anode side compartment (with the volume of gas over the anode) it may be at a higher or lower frequency for another stack design. The THD values increases with increasing AC current amplitude due to a greater depth of excursion into the non-linear region.

### 6.3.2 Fuel starvation and THD during a load step

At LFF a load step into the non linear region was recorded. THD was measured at $1\,Hz$ with $5$ cycles of integration time and an AC peak amplitude of $3.85\,A$. In Figure 6.9 a clear increase in THD from $2\%$ to $3.4\%$ is observed after a load step from $17.5\,A$ with a fuel utilization of $83\%$ in the linear region to $20.5\,A$ with a fuel utilization of $98\%$in the non-linear region.

### 6.3.3 THD Dependence of Fuel Utilization

Figure 6.10 shows the THD values was measured at $1\,Hz$ with $5$ cycles and an AC peak amplitude of $3.85\,A$ while varying the DC current from $4\,A$ to $20.5\,A$ at LFF. Orange points is the average THD for each for each current plateau. The average THD values (orange points) in Figure 6.10 are shown in Figure 6.11 as a function of fuel utilization. THD values at low fuel utilizations are slightly higher than between $FU = 30\%$ and $FU = 50\%$. This could be related to the nature of the Nernst potential since the change in the slope of the derivative of the Nernst equation is higher at $x_{H_2O} = 20\%$ compared to $x_{H_2O} = 50\%$ as shown in Figure 1.4 on page 4. The minimum change in slope of the Nernst equation is at $x_{H_2O} = 50\%$ which means that the $x_{H_2O} = 50\%$ should be around $FU = 50\%$.

## 6.4 Conclusion

Total harmonic distortion, THD, experiments were carried out on an experimental 14-cell SOFC stack at varying frequencies and fuel utilizations. The results illustrate that THD can be used to detect increasing non-linearities in the current-voltage characteristics of the stack when the stack suffers from fuel starvation from by monitoring the stack sum voltage only. This may reduce the need for expensive single cell or cell block monitoring in SOFC systems. The results indicate that when designing THD equipment for detecting fuel starvation in SOFC systems the superimposed signal should be sufficiently low to coincide with the frequency range in which the stack impedance is dominated by the gas concentration impedance in order to generate a THD signal. The dependence of the THD signal on fuel utilization was clarified. It was possible to detect a change in THD when going from low fuel utilization in the linear region to high fuel utilization in the non-linear region. The results provide basic guidelines for the design of THD equipment intended for use in SOFC systems. By yielding a diagnostic signal that aids in maintaining a high fuel utilization while ensuring that operation takes place within safe operating limits for all cells in the stack a THD device may improve the total efficiency of SOFC systems without risking fuel starvation induced failure of the stacks.

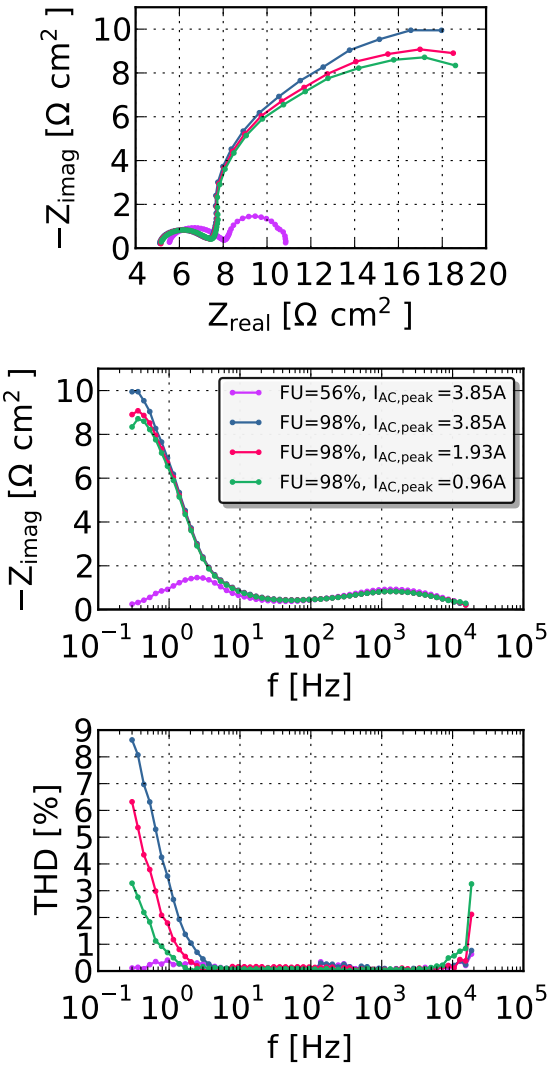


Figure 6.8: Impedance spectra and corresponding THD values vs. frequency at varies ac amplitudes. $T = 720°C$, $I_{dc} = 20.5\ A$ Anode: 20% $H_2O$ 48% $H_2$ 32% $N_2$ Cathode: Air

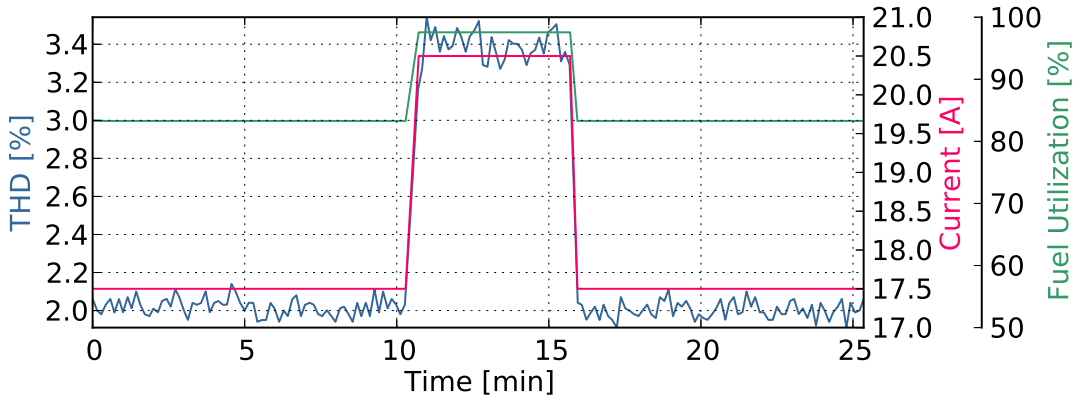


Figure 6.9: THD during load step from $I_{dc} = 17.5\,A$ to $I_{dc} = 20.5\,A$ with $I_{AC,peak} = 3.85\,A$ at $1\,Hz$ with $5$ cycles of integration time. $T = 720°C$, Anode: $20\%$ $H_2O$ $48\%$ $H_2$ $32\%$ $N_2$ Cathode: Air

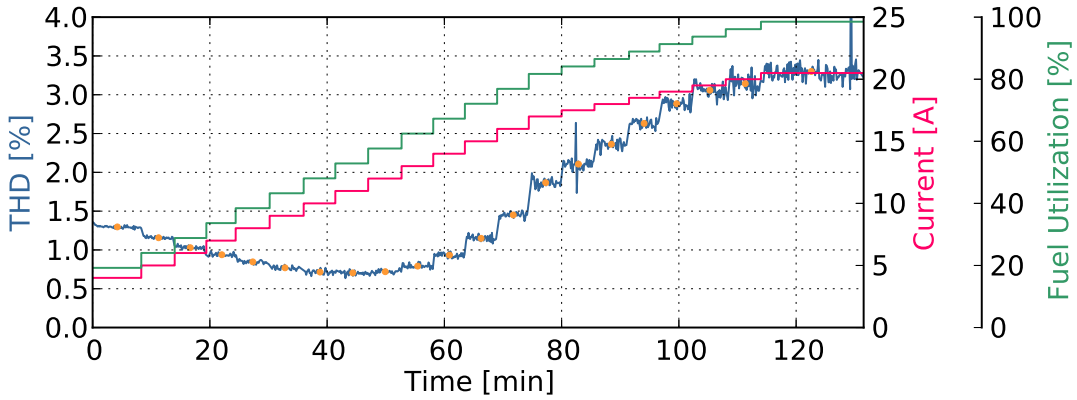


Figure 6.10: Change in THD from $4\,A$ to $20.5\,A$ with $I_{AC,peak} = 3.85\,A$ at $1\,Hz$ with $5$ cycles of integration time.$T = 720°C$, Anode: $20\%$ $H_2O$ $48\%$ $H_2$ $32\%$ $N_2$ Cathode: Air. Orange points indicates average THD for each load step

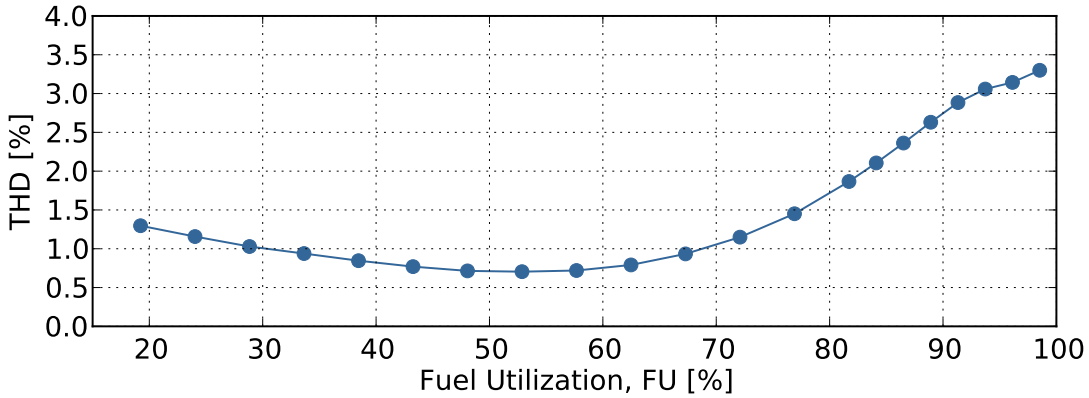


Figure 6.11: Change in THD from $4\,A_{DC}$ to $20.5\,A_{DC}$ with $I_{AC,peak} = 3.85\,A$ at $1\,Hz$ with $5$ cycles of integration time. $T = 720°C$, Anode: $20\%$ $H_2O$ $48\%$ $H_2$ $32\%$ $N_2$ Cathode: Air

CHAPTER 7

# Conclusion and Future Outlook

This thesis has its main focus on electrochemical impedance spectroscopy and total harmonic distortion measurements on solid oxide fuel cell stacks. This chapter will try to put the scientific findings of this thesis into a SOFC stack and SOFC system perspective.

## 7.1 Conclusion

From the results in the previous chapters the following main conclusion can be drawn:

- A sequential impedance measurement setup was constructed and tested. Several initiatives were made to improve the high frequency impedance response with Solartron FRAs. This included:
  - Boosting of the AC current signal from $60\,mA$ to $3\,A$ with a bipolar operational power supply/amplifier.
  - The current through the stack was measured with a current transducer with reasonable impedance response up to $200\,kHz$.
  - A combined DC and common mode cancellation circuit was designed and implemented in the test setup. The DC and common mode cancellation circuit removed the common mode voltage and DC differential voltage which improved the measurement accuracy significantly.
  - A combination of AC and DC coupling measurements made it possible to improve the high frequency impedance response significantly.
  - Automation of the impedance measurements was carried out with the implementation of multiplexer which switched between repeating units in the stack for automated sequential impedance measurements. It was found that the DC and common mode cancellation circuit when bypassed in the AC coupling mode lead to a significant decrease in precision. The automation of impedance measurements was therefore discontinued and the sequential impedance measurements were recorded manually.
- A parallel impedance measurement setup was constructed and tested. The impedance setup was able to record $16$ repeating units and the stack impedance simultaneously which reduced the measurement time significantly. The impedance setup could be operated in a fully automated fashion controlled by the test rig computer resulting in a significantly reduced total test time. The setup eliminated the need for: manual operation, DC and common mode cancellation boxes, AC and DC coupling procedures. The main development for the automated parallel impedance measurement setup included:
  - Software written in several programming languages in order to set up automated communication between the test rig control computer and the computer recording the impedance measurements.
  - A power relay implemented in the test rig to cut off the impedance equipment from the SOFC stack if repeating unit voltages exceed set over- or under-voltage limits.
- Four different stack measurement geometries were tested with EIS to investigate the high frequency response from the repeating units (RUs) :

  - For configuration A the current path was placed closed to the RU wries for voltage measurements and showed large deviation in high frequency impedance response between different RUs.
  - Configuration B decreased the deviation at high frequencies, by increasing the distance between the current path and the wires for voltage measurements. Still a deviation in the high frequency impedance between neighboring RUs was observed which made it very challenging to accurately determine the series resistance.
  - In configuration C the current feed was placed in the diagonal center of the current plate and perpendicular to the RU wires for voltage measurement which gave a significant improvement to the uniformity in high frequency impedance response from the different RUs.
  - Configuration D was an additional improvement to configuration C to make the experimental stack more technological relevant while keeping the uniformity in high frequency impedance response from the different RUs.

- A 13-cell experimental SOFC stack was tested during $2,500$ hours of continuous operation with hydrogen as fuel with $52\%$ fuel utilization and constant current load ($0.2\,A\,cm^{-2}$) at $750°C$. Stack interconnects were coated with six different coatings to prevent chromium poisoning on the cathode side. Four RUs were selected for detailed impedance analysis:

  - RU#2 with the standard ceramic coating displayed the lowest long term degradation.
  - The degradation of RU#4 with Co LSM wet sprayed coating was dominated by an increase of the series resistance with time, which could indicate that oxide layer growth was relatively rapid in the RU.
  - RU#6 with Cu coating and RU#11 Cu LSM wet sprayed coating showed increasing $R_p$ values but decreasing $R_s$ values.
  - EIS allowed a clear distinction to be made in terms of the degradation between the four RU types that is not possible from IV-data only.

- A 14-cell experimental stack was tested during $667$ hours of continuous operation with $50\%$ hydrogen and $50\%$ steam as fuel with $56\%$ fuel utilization and a constant current load ($0.2\,A\,cm^{-2}$) at $720°C$.

  - By comparing the distribution of relaxation times obtained from the impedance data with literature observations it was possible to identify the different processes in a RU. These assignments were further supported by observations made as a function of single-sided gas changes.
  - Analysis of RU and stack impedances (carried out at specific times only) show that the degradation followed an exponential growth model as suggested by Faes et al. [88] and later also observed by Hauch et al. [83] in a single cell test was dominated by the anode and likely caused by nickel coarsening.
  - EIS allowed indication of a specific degradation phenomenon at one electrode that is not possible from IV-data only.

- The fuel distribution was revealed by the gas concentration impedance and the measured gas concentration impedance was compared with existing gas conversion impedance models.

  - The gas concentration resistance increased with increasing RU number (from bottom to top). This indicates that top cells got slightly less fuel than the bottom cells ($\sim 12\%$).
  - The measured gas concentration impedance was smaller than predicted by the Continuously Stirred Tank Reactor model and above the prediction of the Plug Flow Reactor model.

- Total harmonic distortion, THD, experiments were carried out on an experimental 14-cell SOFC stack at varying frequencies and fuel utilizations.
  - The results illustrate that THD can be used to detect increasing non-linearities in the current-voltage characteristics of the stack when the stack suffers from fuel starvation by monitoring the stack sum voltage only.
  - The results indicated that when designing THD equipment for detecting fuel starvation in SOFC systems, the superimposed signal should be sufficiently low to coincide with the frequency range in which the stack impedance is dominated by the gas concentration impedance in order to generate a THD signal.
  - The results provide basic guidelines for the design of THD equipment intended for use in SOFC systems.

## 7.2 Future Outlook

After three years of work with electrochemical impedance spectroscopy and total harmonic distortion analysis on solid oxide fuel cell stacks there are still many areas that need to be explored and areas where improvements are required. Some of these are listed below:

- Detailed performance and degradation monitoring on SOFC stacks operated on reformate fuels (hydrocarbons such as methane or diesel) with parallel impedance measurements. This could monitor different degradation mechanisms which until now only has been investigated on single cell measurements. More knowledge about degradation mechanisms in SOFC stacks could possibly accelerate the development.
- Detailed performance and degradation and characterization of solid oxide electrolysis stacks under different operating conditions.
- Detailed performance monitoring with parallel impedance measurements of a SOFC stack assembled with different cell compositions for screening the performance of different fuel or oxidant electrodes or barrier layers.
- Further development of gas concentration impedance models by considering back diffusion in the plug-flow model and applying the coupled diffusion and conversion impedance model from Ref. [11] to stack impedance measurements.
- Further development of batch fitting routines impedance measurements for getting more knowledge about electrode specific degradation phenomenons faster.
- Further development of automated scripts for real time data analysis of the vast amount impedance data obtained by the parallel impedance measurement setup. This has the possibility of improving the outcome of the stack impedance measurements result.
- Being able to acquire electrochemical impedance measurements during operation of SOFC stacks in commercial systems will lead to a increased understanding of the real system degradation mechanisms. The EIS technique can be embedded on a micro controller equipped with an EIS measurement circuit for cheap implementation. This has successfully been done for Lithium-ion batteries [102].

# Bibliography


[1] R. P. O'Hayre, S.-W. Cha, W. G. Colella, and F. B. Prinz, *Fuel Cell Fundamentals*. John Wiley & Sons, Inc., 2008. ISBN: 978-0-470-25843-9.

[2] S. C. Singhal, "Solid oxide fuel cells for power generation," *WIREs: Energy Environ*, vol. 3, pp. 179–194, Mar. 2014.

[3] A. Kromp, *Model-based Interpretation of the Performance and Degradation of Reformate Fueled Solid Oxide Fuel Cells*. Phd thesis, Karlsruhe Institute of Technology, 2013.

[4] T. Tsai and S. A. Barnett, "Increased solid-oxide fuel cell power density using interfacial ceria layers," *Solid State Ionics*, vol. 98, pp. 191–196, 1997.

[5] A. Tsoga, A. Gupta, A. Naoumidis, and P. Nikolopoulos, "Gadolinia-doped ceria and yttria stabilized zirconia interfaces: regarding their application for SOFC technology," *Acta Materialia*, vol. 48, pp. 4709–4714, Dec. 2000.

[6] A. Kromp, S. Dierickx, A. Leonide, A. Weber, and E. Ivers-Tiffee, "Electrochemical Analysis of Sulfur-Poisoning in Anode Supported SOFCs Fuelled with a Model Reformate," *Journal of The Electrochemical Society*, vol. 159, no. 5, pp. B597 – B601, 2012.

[7] E. Ivers-Tiffee, H. Timmermann, A. Leonide, N. H. Menzler, and J. Malzbender, "Methane reforming kinetics , carbon deposition , and redox durability of Ni / 8 yttria-stabilized zirconia ( YSZ ) anodes," *Handbook of Fuel Cells - Fundamentals, Technology and Applications*, pp. 1–24, 2010.

[8] A. Atkinson, S. Barnett, R. J. Gorte, J. T. S. Irvine, a. J. McEvoy, M. Mogensen, S. C. Singhal, and J. Vohs, "Advanced anodes for high-temperature fuel cells.," *Nature materials*, vol. 3, pp. 17–27, Jan. 2004.

[9] Z. Zeng, M. E. Björketun, S. Ebbesen, M. B. Mogensen, and J. Rossmeisl, "Origin of electrolyte-dopant dependent sulfur poisoning of SOFC anodes.," *Physical chemistry chemical physics: PCCP*, vol. 15, pp. 6769–72, May 2013.

[10] J. Larminie and A. Dicks, *Fuel Cell Systems Explained*. John Wiley & Sons, Ltd., 2nd ed., 2003. ISBN: 978-0-470-84857-9.

[11] T. Jacobsen, P. Hendriksen, and S. Koch, "Diffusion and conversion impedance in solid oxide fuel cells," *Electrochimica Acta*, vol. 53, pp. 7500–7508, Oct. 2008.

[12] K. Nielsen, A. Persson, D. Beeaff, J. Hø gh, L. Mikkelsen, and P. Hendriksen, "Initiation and Performance of a Coating for Countering Chromium Poisoning in a SOFC-stack," *ECS Transactions*, vol. 7, no. 1, pp. 2145–2154, 2007.

[13] J. A. Schuler, Z. Wuillemin, A. Hessler-Wyser, C. Comminges, N. Y. Steiner, and J. Van herle, "Cr-poisoning in (La,Sr)(Co,Fe)O3 cathodes after 10,000h SOFC stack testing," *Journal of Power Sources*, vol. 211, pp. 177–183, Aug. 2012.

[14] Topsoe Fuel Cell A/S, "SOFC stack flow configurations - Advantages and Disadvantages." Personal telephone correspondance with Research Engineer, Thomas Heiredal-Clausen, Research and Development, Stack, October 2014.

[15] A. Mai, B. Iwanschitz, U. Weissen, R. Denzler, D. Haberstock, V. Nerlich, J. Sfeir, and A. Schuler, "Status of Hexis SOFC Stack Development and the Galileo 1000 N Micro-CHP System Andreas," *ECS Transactions*, vol. 25, no. 2, pp. 149–158, 2009.

[16] A. Mai, B. Iwanschitz, U. Weissen, R. Denzler, D. Haberstock, V. Nerlich, and A. Schuler, "Status of Hexis' SOFC Stack Development and the Galileo 1000 N Micro-CHP System," *ECS Transactions*, vol. 35, no. 1, pp. 87–95, 2011.

[17] HEXIS AG, "Galileo: Generating heat and power from natural gas." Website. `http://www.hexis.com/en/hexis-technology` Accessed 10-02-2014.

[18] Q. Huang, R. Hui, B. Wang, and J. Zhang, "A review of AC impedance modeling and validation in SOFC diagnosis," *Electrochimica Acta*, vol. 52, pp. 8144–8164, Nov. 2007.

[19] M. E. Orazem and B. Tribollet, *Electrochemical Impedance Spectroscopy*. John Wiley & Sons, Inc., 2008. ISBN: 978-0-470-04140-6.

[20] D. Klotz, *Characterization and Modeling of Electrochemical Energy Conversion Systems by Impedance Techniques*. Phd thesis, Karlsruhe Institute of Technology, 2012.

[21] A. Lasia, *Electrochemical Impedance Spectroscopy and its Applications*. Springer Science+Business Media, 2014. ISBN: 978-1-4614-8932-0.

[22] B. A. Boukamp, "A Linear Kronig-Kramers Transform Test for Immittance Data Validation," *Journal of The Electrochemical Society*, vol. 142, no. 6, p. 1885, 1995.

[23] C. Graves, "RAVDAV data analysis software." version 0.9.7, 2012.

[24] E. Jones, T. Oliphant, P. Peterson, *et al.*, "SciPy: Open source scientific tools for Python." Website, 2001–. `http://www.scipy.org/` [Online accessed 2014-09-28].

[25] S. H. Jensen, A. Hauch, R. Knibbe, T. Jacobsen, and M. Mogensen, "Modeling Degradation in SOEC Impedance Spectra," *Journal of the Electrochemical Society*, vol. 160, pp. F244–F250, Jan. 2013.

[26] C. Graves and J. Hjelm, "B1203 Advanced impedance modeling of solid oxide electrochemical cells," in *11th European SOFC and SOE Forum 2014*, pp. 16–27, 2014.

[27] H. Schichlein, A. C. Müller, M. Voigts, A. Krügel, and E. Ivers-Tiffée, "Deconvolution of electrochemical impedance spectra for the identification of electrode reaction mechanisms in solid oxide fuel cells q," *Journal of Applied Electrochemistry*, vol. 32, pp. 875–882, 2002.

[28] A. Leonide, V. Sonn, A. Weber, and E. Ivers-Tiffee, "Evaluation and Modeling of the Cell Resistance in Anode-Supported Solid Oxide Fuel Cells," *Journal of The Electrochemical Society*, vol. 155, no. 1, p. B36, 2008.

[29] V. Sonn, A. Leonide, and E. Ivers-Tiffee, "Combined Deconvolution and CNLS Fitting Approach Applied on the Impedance Response of Technical Ni-8YSZ Cermet Electrodes," *Journal of The Electrochemical Society*, vol. 155, no. 7, p. B675, 2008.

[30] A. Leonide, *SOFC Modelling and Parameter Identification by means of Impedance Spectroscopy*. Phd thesis, Karlsruher Institut für Technologie (KIT), Karlsruhe, Germany, 2010.

[31] M. Lang, C. Auer, a. Eismann, P. Szabo, and N. Wagner, "Investigation of solid oxide fuel cell short stacks for mobile applications by electrochemical impedance spectroscopy," *Electrochimica Acta*, vol. 53, pp. 7509–7513, Oct. 2008.

[32] M. Lang, T. Weckesser, C. Auer, P. Jentsch, A. C. Friedrich, and C. Westner, "SOFC Stacks for Mobile Applications," *ECS Transactions*, vol. 25, no. 2, pp. 97–104, 2009.

[33] N. J. J. Dekker, J. F. van Wees, and G. Rietveld, "Determination of the Anode Flow Distribution in a SOFC Stack at Nominal Operating Conditions by EIS," *The Electrochemical Society*, vol. 25, no. 2, pp. 1871–1878, 2009.

[34] M. Lang, C. Auer, P. Jentsch, and T. Weckesser, "SOFC Stacks for Mobile Applications," *Materials Science Forum*, vol. 638-642, pp. 1170–1175, Jan. 2010.

[35] M. Lang, C. Westner, R. Geieregger, B. Bentlohner, and R. Schwub, "SOFC Stacks for Mobile Applications," *9th European SOFC Forum, Lucerne, Switzerland*, pp. 3–72 – 3–82, 2010.

[36] C. Westner, M. Lang, and R. Geieregger, "Electrochemical Impedance Spectroscopy ( EIS ) of SOFC Short Stacks," *9th European SOFC Forum, Lucerne, Switzerland*, pp. 15–106 – 15–116, 2010.

[37] S. D. Ebbesen, J. Hø gh, K. A. Nielsen, J. U. Nielsen, and M. Mogensen, "Durable SOC stacks for production of hydrogen and synthesis gas by high temperature electrolysis," *International Journal of Hydrogen Energy*, vol. 36, pp. 7363–7373, July 2011.

[38] J. Schefold, A. Brisse, M. Zahid, J. P. Ouweltjes, and J. U. Nielsen, "Long Term Testing of Short Stacks with Solid Oxide Cells for Water Electrolysis," *ECS Transactions*, vol. 35, no. 1, pp. 2915–2927, 2011.

[39] C. Comminges, Q. Fu, M. Zahid, N. Y. Steiner, and O. Bucheli, "Monitoring the degradation of a solid oxide fuel cell stack during 10,000h via electrochemical impedance spectroscopy," *Electrochimica Acta*, vol. 59, pp. 367–375, Jan. 2012.

[40] R. A. Serway and J. W. Jewett, *Physics for Scientists and Engineers*. Brook/Cole-Thomson Learning, 6th ed., 2004.

[41] S. L. Ebbehø j, T. Ramos, and M. Mogensen, "Impact of Reduction Parameters on the Initial Performance and Stability of Ni/(Sc)YSZ Cermet Anodes for SOFCs S. L. Ebbehøj," *ECS Transactions*, vol. 45, no. 1, pp. 363–375, 2012.

[42] R. Barfod, A. Hagen, S. Ramousse, P. V. Hendriksen, and M. Mogensen, "Break Down of Losses in Thin Electrolyte SOFCs," *Fuel Cells*, vol. 6, pp. 141–145, Apr. 2006.

[43] C. R. Paul, *Electromagnetics for engineers*. John Wiley & Sons, Inc., 2004. ISBN 0-471-27180-2.

[44] R. W. Erickson and D. Maksimovic, *Fundamentals of Power Electronics*. Springer Science+Business Media, Inc., 2nd ed., 2000. ISBN 0-7923-7270-0.

[45] U. S. Gudmundsdottir, *Modelling of long high voltage AC cables in transmission systems*. PhD thesis, Aalborg University, 2010.

[46] J. A. Ferreira, "Improved Analytical Modeling of Conductive Losses in Magnetic Components," *IEEE TRANSACTIONS ON POWER ELECTRONICS*, vol. 9, no. 1, pp. 127–131, 1994.

[47] Rockwell Automation, "System Design for Control of Electrical Noise." Reference Manual, 2001. `http://literature.rockwellautomation.com/idc/groups/literature/documents/rm/gmc-rm001_-en-p.pdf` Accessed 2014-10-05.

[48] A. M. Niknejad, "University of California, Berkely, Intergrated Circuits for Communication, Lecture 11: Electrical Noise." Lecture slides, 2005. `http://rfic.eecs.berkeley.edu/~niknejad/ee142_fa05lects/pdf/lect11.pdf` Accessed 2014-10-05.

[49] National Oceanic and Atmospheric Administration, "Annual Lightning Flash Rate Map." Website, September 2014. `http://www.sos.noaa.gov/Datasets/dataset.php?id=6`.

[50] J. W. Cooley and J. W. Tukey, "An Algorithm for the Machine Calculation of Complex Fourier Series," *Mathematics of Computation*, vol. 19, no. 90, pp. 297–301, 1965.

[51] S. W. Harden, "Signal Filtering with Python." Website, January 2009. `http://www.swharden.com/blog/2009-01-21-signal-filtering-with-python/`.

[52] A. S. Sedra and K. C. Smith, *Microelectronic Circuits*. Oxford University Press, 5th ed., 2004. ISBN 0-19-514252-7.

[53] W. Kester, *MT-003: Understand SINAD, ENOB, SNR, THD, THD + N, and SFDR so You Don't Get Lost in the Noise Floor*. Tutorial, Analog Devices, October 2008. http://www.analog.com/static/imported-files/tutorials/MT-003.pdf.

[54] ZAHNER-elektrik GmbH & Co. KG, "Thales 03: EIS - Electrochemical Impedance Spectroscopy." Manual, March 2013. http://zahner.de/pdf/EIS.pdf.

[55] maxim integrated, "Tutorial 2045 Understanding Common-Mode Signals." Website, June 2003. http://www.maximintegrated.com/app-notes/index.mvp/id/2045.

[56] A. Rich, *Shielding and Guarding - How to exclude Interference - Type Noise - What to Do and Why to Do It - A Rational Approach*. Application Note, Analog Devices, 1983. http://www.analog.com/static/imported-files/application_notes/41727248AN_347.pdf Accessed 2014-10-05.

[57] Solartron Analytical, *1260 Impedance/Gain-Phase Analyzer Operating Manual*, December 1995. http://mm.ece.ubc.ca/mediawiki/images/8/8b/1260_manual.pdf.

[58] *1255 Frequency Response Analyzer Operating Manual*. Solartron Analytical, 2000.

[59] Zahner Messsysteme, *ZAHNER Solutions Electrochemical Workstations*, October 2013. http://www.zahner.de/workstations.html.

[60] KEPCO, INC., "Modification of standard KEPCO Model 20-20DC." Website, September 2014. http://www.kepcopower.com/support/bop20-20c-r4.pdf.

[61] Texas Instruments Inc., "LM108, LM118, LM741 Predicting Op Amp Slew Rate Limited Response." Website, 2002. http://www.ti.com/lit/an/snoa852/snoa852.pdf.

[62] LEM, "Current Transducer ITN 600-S ULTRASTAB." Website, February 2014. http://www.lem.com/docs/products/itn%20600-s%20ultrastab.pdf Accessed 2014-10-05.

[63] Texas Instruments Inc., "INA117 High Common-Mode Voltage Difference Amplifier." Website, December 2000. http://www.ti.com/lit/ds/symlink/ina117.pdf.

[64] TE Connectivity Ltd., "Automotive Relays High Current Devices, Battery Disconnect Switch BDS-A (Latching)." Website, 2011. http://www.farnell.com/datasheets/1717933.pdf.

[65] PR electronics A/S, "Trip amplifier 2231." Website, 2014. http://www.prelectronics.com/pdf/2231-1756-US.pdf.

[66] A. Hagen, R. Barfod, P. V. Hendriksen, Y.-L. Liu, and S. Ramousse, "Degradation of Anode Supported SOFCs as a Function of Temperature and Current Load," *Journal of The Electrochemical Society*, vol. 153, no. 6, p. A1165, 2006.

[67] N. Christiansen, S. Primdahl, M. Wandel, S. Ramousse, and A. Hagen, "Status of the Solid Oxide Fuel Cell Development at Topsoe Fuel Cell A/S and DTU Energy Conversion," *ECS Transactions*, vol. 57, no. 1, pp. 43–52, 2013.

[68] Texas Instruments Inc., "Applcation Report: High-Speed Layout Guidelines." Website, 2006. http://www.ti.com/lit/an/scaa082/scaa082.pdf.

[69] FuelCon AG, "Testing of SOFC stacks and hot-box systems." Website, 2014. http://www.fuelcon.com/cms/index.php?id=sofc_fuel_cell_stack_testing&L=1.

[70] K. A. Nielsen, A. Persson, D. Beeaff, J. Høgh, L. Mikkelsen, and P. V. Hendriksen, "Initiation and Performance of a Coating for Countering Chromium Poisoning in a SOFC-stack," *ECS Transactions*, vol. 7 (1), pp. 2145–2154, 2007.

[71] ZAHNER-elektrik GmbH & Co. KG, "Total Harmonic Distortion via Ztrace." Personal E-mail correspondance with Dr. Carl-Albrecht Schiller, July 2014.

[72] R. S. Gemmen, M. C. Williams, and K. Gerdes, "Degradation measurement and analysis for cells and stacks," *Journal of Power Sources*, vol. 184, pp. 251–259, Sept. 2008.

[73] J. I. Gazzarri, *Impedance model of a Solid Oxide Fuel Cell For Degradation Diagnosis*. Phd thesis, THE UNIVERSITY OF BRITISH COLUMBIA, Vancouver, Canada, 2007.

[74] J. Gazzarri and O. Kesler, "Short stack modeling of degradation in solid oxide fuel cells Part II. Sensitivity and interaction analysis," *Journal of Power Sources*, vol. 176, pp. 155–166, Jan. 2008.

[75] Z. Jiao, N. Shikazono, and N. Kasagi, "Study on degradation of solid oxide fuel cell anode by using pure nickel electrode," *Journal of Power Sources*, vol. 196, pp. 8366–8376, Oct. 2011.

[76] M. Kornely, A. Neumann, N. H. Menzler, A. Leonide, A. Weber, and E. Ivers-Tiffee, "Degradation of anode supported cell (ASC) performance by Cr-poisoning," *Journal of Power Sources*, vol. 196, pp. 7203–7208, Sept. 2011.

[77] D. Lee, S.-J. Ahn, J. Kim, and J. Moon, "Influence of water vapor on performance of coplanar single chamber solid oxide fuel cells," *Journal of Power Sources*, vol. 195, pp. 6504–6509, Oct. 2010.

[78] J. Malzbender, P. Batfalsky, R. Vaß en, V. Shemet, and F. Tietz, "Component interactions after long-term operation of an SOFC stack with LSM cathode," *Journal of Power Sources*, vol. 201, pp. 196–203, Mar. 2012.

[79] L. Blum, U. Packbier, I. C. Vinke, and L. G. J. de Haart, "Long-Term Testing of SOFC Stacks at Forschungszentrum Jülich," *Fuel Cells*, vol. 13, pp. 646–653, Aug. 2013.

[80] T. Horita, H. Kishimoto, K. Yamaji, M. E. Brito, Y. Xiong, H. Yokokawa, Y. Hori, and I. Miyachi, "Effects of impurities on the degradation and long-term stability for solid oxide fuel cells," *Journal of Power Sources*, vol. 193, pp. 194–198, Aug. 2009.

[81] R. Steinberger-Wilckens, L. Blum, H.-P. Buchkremer, S. Gross, L. de Haart, K. Hilpert, H. Nabielek, W. J. Quadakkers, U. Reisgen, R. W. Steinbrech, and F. Tietz, "Overview of the Development of Solid Oxide Fuel Cells at Forschungszentrum Juelich," *International Journal of Applied Ceramic Technology*, vol. 3, pp. 470–476, Nov. 2006.

[82] S. H. Jensen, A. Hauch, P. V. Hendriksen, M. Mogensen, N. Bonanos, and T. Jacobsen, "A Method to Separate Process Contributions in Impedance Spectra by Variation of Test Conditions," *Journal of The Electrochemical Society*, vol. 154, no. 12, p. B1325, 2007.

[83] A. Hauch, M. Mogensen, and A. Hagen, "Ni/YSZ electrode degradation studied by impedance spectroscopy - Effect of p(H2O)," *Solid State Ionics*, vol. 192, pp. 547–551, June 2011.

[84] B. A. Boukamp, "A Linear Kronig Kramers Transform Test for Immittance Data Validation," *Journal of The Electrochemical Society*, vol. 142, p. 1885, 1995.

[85] R. Barfod, a. Hagen, S. Ramousse, P. V. Hendriksen, and M. Mogensen, "Break Down of Losses in Thin Electrolyte SOFCs," *Fuel Cells*, vol. 6, pp. 141–145, Apr. 2006.

[86] Z. Jiao and N. Shikazono, "Simulation of Solid Oxide Fuel Cell Anode Microstructure Evolution Using Phase Field Method," *Journal of the Electrochemical Society*, vol. 160, pp. F709–F715, Apr. 2013.

[87] J. Nielsen and J. Hjelm, "Impedance of SOFC electrodes: A review and a comprehensive case study on the impedance of LSM:YSZ cathodes," *Electrochimica Acta*, vol. 115, pp. 31–45, Jan. 2014.

[88] A. Faes, A. Hessler-Wyser, D. Presvytes, C. G. Vayenas, and J. Van herle, "Nickel-Zirconia Anode Degradation and Triple Phase Boundary Quantification from Microstructural Analysis," *Fuel Cells*, vol. 9, pp. 841–851, Dec. 2009.

[89] B. Shaffer and J. Brouwer, "Dynamic Model for Understanding Spatial Temperature and Species Distributions in Internal-Reforming Solid Oxide Fuel Cells," *Journal of Fuel Cell Science and Technology*, vol. 9, no. 4, p. 041012, 2012.

[90] S. Primdahl and M. Mogensen, "Gas Conversion Impedance: A Test Geometry Effect in Characterization of Solid Oxide Fuel Cell Anodes," *J. Electrochem. Soc.*, vol. 145, no. 7, pp. 2431–2438, 1998.

[91] S. Primdahl, *Nickel/yttria-stabilised zirconia cermet anodes for solid oxide fuel cells*. PhD thesis, 1999.

[92] W. G. Bessler and S. Gewies, "Gas Concentration Impedance of Solid Oxide Fuel Cell Anodes," *Journal of The Electrochemical Society*, vol. 154, no. 6, p. B548, 2007.

[93] S. H. Jensen, A. Hauch, P. V. Hendriksen, and M. Mogensen, "Advanced Test Method of Solid Oxide Cells in a Plug-Flow Setup," *Journal of The Electrochemical Society*, vol. 156, no. 6, pp. B757–B764, 2009.

[94] S. Primdahl and M. Mogensen, "Gas Diffusion Impedance in Characterization of Solid Oxide Fuel Cell Anodes," *Journal of The Electrochemical Society*, vol. 146, no. 8, pp. 2827–2833, 1999.

[95] R. Barfod, M. Mogensen, T. Klemensø, A. Hagen, Y.-L. Liu, and P. V. Hendriksen, "Detailed Characterization of Anode-Supported SOFCs by Impedance Spectroscopy," *Journal of The Electrochemical Society*, vol. 154 (4), pp. B371–B378, 2007.

[96] S. H. Jensen, P. V. Hendriksen, M. Mogensen, and T. Jacobsen, "SOFC Ni-electrode Resistance Distribution Investigated by Gas Concentration Impedance in a Plug-Flow Setup," *ECS Transactions*, vol. 13, no. 26, pp. 307–315, 2008.

[97] E. Ramschak, V. Peinecke, P. Prenninger, T. Schaffer, W. Baumgartner, and V. Hacker, "NEW APPROACH FOR DETECTION OF CRITICAL STACK OPERATING CONDITIONS FOR HIGH VOLUME FUEL CELL APPLICATIONS," *ECS Transactions*, vol. 1, no. 8, pp. 367–375, 2006.

[98] E. Ramschak, V. Peinecke, P. Prenninger, T. Schaffer, and V. Hacker, "Detection of fuel cell critical status by stack voltage analysis," *Journal of Power Sources*, vol. 157, pp. 837–840, July 2006.

[99] B. E. Ramschak, V. Peinecke, P. Prenninger, A. V. L. List, T. Schaffer, W. Baumgartner, and V. Hacker, "Online stack monitoring tool for dynamically and stationary operated fuel cell systems," no. October, pp. 12–15, 2006.

[100] Q. Mao and U. Krewer, "Total harmonic distortion analysis of oxygen reduction reaction in proton exchange membrane fuel cells," *Electrochimica Acta*, vol. 103, pp. 188–198, July 2013.

[101] S. Thomas, S. C. Lee, A. K. Sahu, and S. Park, "Online health monitoring of a fuel cell using total harmonic distortion analysis," *International Journal of Hydrogen Energy*, vol. 39, pp. 4558–4565, Mar. 2014.

[102] W. Li, G. W. Liu, and F. H. Yang, "Design of Automatic Measurement System of Lithium Battery Electrochemical Impedance Spectroscopy Based on Microcomputer," *Applied Mechanics and Materials*, vol. 241-244, pp. 259–264, Dec. 2012.

# Nomenclature

**Roman**

| | | |
|---|---|---|
| $A$ | Area | $m^2$ |
| $B$ | Magnetic Field | $\frac{Wb}{m^2}$ |
| $d$ | Diameter | $m$ |
| $E$ | Thermodynamic voltage | V |
| $e$ | Electromotive force generated from external magnetic fields | V |
| $F$ | Faradays constant | $\frac{C}{mol}$ |
| $F$ | Force | $N$ |
| $G$ | Gibbs free energy | $\frac{J}{mol}$ |
| $h$ | Enthalpy | $\frac{J}{mol}$ |
| $I$ | Current | $A$ |
| $J$ | Total area specific reaction rate | $\frac{mol}{m^2\,s}$ |
| $j$ | Current density | $\frac{A}{cm^2}$ |
| $L$ | Inductance | $H$ |
| $l$ | Length | $m$ |
| $M$ | Mutual Inductance | $\frac{Wb}{m^2}$ |
| $N$ | Number of turns for a coil | $-$ |
| $p$ | Partial Pressure | - |
| $R$ | Area Specific Resistance | $\Omega\,cm^2$ |
| $R_g$ | The ideal gas constant | $\frac{J}{mol\,K}$ |
| $T$ | Temperature | $K$ |
| $t$ | Time | $s$ |
| $U$ | Voltage | V |
| $V$ | Volume | $m^3$ |
| $x$ | Mole Fraction | - |
| Z | Impedance | $\Omega$ |

**Greek**

| | | |
|---|---|---|
| $\chi$ | Quality of fit | - |

| | | |
|---|---|---|
| $\delta$ | Skin Depth | $m$ |
| $\epsilon$ | Efficiency | - |
| $\eta$ | Over potential | V |
| $\mu$ | Permeability | $\frac{H}{m}$ |
| $\omega$ | Angular frequency | $\frac{rad}{s}$ |
| $\Phi_B$ | Magnetic Flux | $Wb$ |
| $\rho$ | Resistivity | $\Omega\, m$ |
| $\upsilon$ | Molar flow rate | $\frac{mol}{s}$ |

**Subscripts and Superscripts**

| | |
|---|---|
| $[\,]_c$ | Constant |
| $[\,]_{elec}$ | Electrochemical |
| $[\,]_{FU}$ | Fuel Utilization |
| $[\,]_{GCI}$ | Gas Concentration Impedance |
| $[\,]_{HHV}$ | Higher Heating Value |
| $[\,]_{in}$ | Incoming |
| $[\,]_i$ | Node number |
| $[\,]_{out}$ | Outgoing |
| $[\,]_p$ | Polarization |
| $[\,]_{rev}$ | Reversible |
| $[\,]_{RU}$ | Repeating Unit |
| $[\,]_s$ | Series |
| $[\,]_{thermo}$ | thermodynamic |
| $\dot{[\,]}$ | Flow Rate |
| $\overline{[\,]}$ | Average |
| $\vec{[\,]}$ | Vector |

**Abbreviations**

| | | |
|---|---|---|
| AC | Alternating current | |
| AD | Analog to Digital Converter | |
| AFC | Alkaline Fuel Cell | |
| APU | Auxiliary Power Unit | |
| ASR | Area Specific Resistance | $\Omega\, cm^2$ |

| | |
|---|---|
| CM | Common Mode |
| CMR | Common Mode Rejection |
| CNLS | Complex Nonlinear Least Squares |
| CPE | Constant Phase Element |
| CSTR | Continuously Stirred Tank Reactor |
| DC | Direct Current |
| DLL | Dynamic Link Library. Microsoft shared library files. |
| DR | Degradation Rate $\frac{\%}{kh}$ |
| DSP | Digital Signal Processor |
| DUT | Device Under Test |
| EIS | Electrochemical Impedance Spectroscopy |
| ESR | Equivalent Series Resistance |
| FFT | Fast Fourier Transform |
| FRA | Frequency Response Analyzer |
| FU | Fuel Utilization |
| GmbH & Co. KG | Gesellschaft mit beschränkter Haftung & Compagnie Kommanditgesellschaft. German business abreviaiton for company with limited liability and limitied partnership. |
| GPIB | General Purpose Interface Bus. IEEE-488 standard. |
| HFF | High Fuel Flow |
| LAN | Local Area Network. IEEE 802 standard. |
| LFF | Low Fuel Flow |
| LSCF | Lanthanum strontium cobalt ferrite |
| LSM | Sr-doped $\mathrm{LaMnO_3}$ |
| LTD | Long Term Degradation |
| MCFC | Molten Carbonate Fuel Cell |
| MIEC | Mixed Ionic Electronic Conductor |
| OCV | Open Circuit Voltage |
| PAFC | Phosphoric Acid Fuel Cell |
| PEMFC | Proton Exchange Membrane Fuel Cell |
| PFR | Plug Flow Reactor |
| RMS | Root-Mean-Square |
| RU | Repeating Unit - Interconnect/Seal/Cell/Seal/Interconnect |
| SNR | Signal to Noise Ratio |

| | |
|---|---|
| SOFC | Solid Oxide Fuel Cell |
| THD | Total Harmonic Distortion |
| THDA | Total Harmonic Distortion Analysis |
| UI | Voltage Current Curve |
| USB | Universal Serial Bus |
| YSZ | Yttria-Stabilized Zirconia |

# List of Tables



# List of Figures

Appendix A

# Articles

## A.1 Paper A

B1006

# Detailed electrochemical characterisation of large SOFC stacks

**R. R. Mosbæk (1), J. Hjelm (1), R. Barfod (2), J. Høgh (1), and P. V. Hendriksen (1)**
(1) DTU Energy Conversion, Risø Campus
Frederiksborgvej 399, DK-4000, Denmark
(2) Topsoe Fuel Cell A/S, Nymøllevej 66, DK-2800 Lyngby, Denmark
Tel.: +45-4677-5669
Fax: +45-4677-5858
rasmo@dtu.dk

## Abstract

As solid oxide fuel cell (SOFC) technology is moving closer to a commercial break through, lifetime limiting factors, determination of the limits of safe operation and methods to measure the “state-of-health” of operating cells and stacks are becoming of increasing interest. This requires application of advanced methods for detailed electrochemical characterisation during operation. An operating stack is subject to steep compositional gradients in the gaseous reactant streams, and significant temperature gradients across each cell and across the stack, which makes it a complex system to analyse in detail. Today one is forced to use mathematical modelling to extract information about existing gradients and cell resistances in operating stacks, as mature techniques for local probing are not available. This type of spatially resolved information is essential for model refinement and validation, and helps to further the technological stack development. Further, more detailed information obtained from operating stacks is essential for developing appropriate process monitoring and control protocols for stack and system developers.

An experimental stack with low ohmic resistance from Topsoe Fuel Cell A/S was characterised in detail using electrochemical impedance spectroscopy.
An investigation of the optimal geometrical placement of the current probes and voltage probes was carried out in order to minimise measurement errors caused by stray impedances. Unwanted stray impedances are particularly problematic at high frequencies. Stray impedances may be caused by mutual inductance and stray capacitance in the geometrical set-up and do not describe the fuel cell. Three different stack geometries were investigated by electrochemical impedance spectroscopy.

Impedance measurements were carried out at a range of ac perturbation amplitudes in order to investigate linearity of the response and the signal-to-noise ratio. Separation of the measured impedance into series and polarisation resistances was possible.

# 1. Introduction

The DOE lifetime target for Solid Oxide Fuel Cells (SOFCs) stacks is 60,000 h by 2020 for stationary applications [1]. Understanding and mitigation of the degradation mechanisms in SOFC stacks is therefore crucial in order to improve the durability and increase the stack lifetime [2].

Electrochemical Impedance Spectroscopy (EIS), is a powerful diagnostic technique that can increase understanding of the degradation mechanisms dominating in operating stacks since the technique may provide information on individual losses, including oxygen reduction reaction kinetics, mass-transport processes, and electrolyte resistance loss [3]. EIS has been an increasingly popular diagnostic technique at the SOFC single cell level but has so far only seen limited use on the stack level [4–7].

One of the key challenges in associated with impedance measurements of large area objects, such as the experimental SOFC stack considered here, is that the absolute real impedance for a cell in the experimental stack is in the range of a few mΩ which requires equipment with high precision and minimisation of unwanted stray impedances in the geometrical set-up. Stray impedances are caused by mutual inductance and stray capacitance and do not describe the fuel cell. Three different stack geometries were investigated by electrochemical impedance spectroscopy for stray impedance minimisation. Furthermore active electrical circuits were attached the measurement input in order to ensure the highest measurement resolution of the frequency response analyser.

In the present work, the durability of an experimental 13-cell stack, in which the metallic interconnects were coated with different types of protective layers, has been tested for more than 2500 hours at steady operating conditions. EIS has been used to examine the long-term behaviour and monitor the evolution of series and polarisation resistances for four out of the 13 cells. The losses for the four cells are reported and discussed.

# 2. Experiments

The solid oxide fuel cells (SOFC) used for the 13-cell experimental fuel cell stack were planar anode-supported SOFCs (Ni-YSZ/YSZ/LSM-YSZ) of 12 cm x 12 cm footprint and an active area of approximately 90 cm2. The cell details can be found elsewhere [8]. The interconnects were made of commercial stainless steel. Different coatings was used on the interconnects in the stack (see Table 1) to prevent chromium poisoning on the cathode side [9]. The nickel oxide in the Ni-YSZ electrode was reduced to nickel in hydrogen at start-up and the stack was subsequently tested for performance and durability. The stack testing was performed at DTU Energy Conversion with an experimental stack manufactured by Topsoe Fuel Cell A/S (TOFC).

**Table 1: Cell number and the corresponding interconnect (IC) coating towards the cathode side. Abbreviations: Wet sprayed, ws Standard ceramic coat, st.cer.coat**

| Cell | IC Coating | Cell | IC Coating | Cell | IC Coating |
|---|---|---|---|---|---|
| 1 | st.cer.coat | 6 | Cu | 11 | Cu LSM ws |
| 2 | st.cer.coat | 7 | LSM ws | 12 | Cu |
| 3 | Co | 8 | st.cer.coat | 13 | Co |
| 4 | Co LSM ws | 9 | LSM ws | | |
| 5 | Cu LSM ws | 10 | Co LSM ws | | |

An investigation of the optimal geometrical placement of the current probes and voltage probes was carried out in order to minimise measurement errors caused by stray impedances. Unwanted stray impedances are particularly problematic at high frequencies. The optimal stack geometry was found by performing EIS on three different stacks. The three different stack geometries are shown in Figure 1. For configuration A there was big difference in the high frequency response between the different cells in the stack since the magnetic field from the current conduction was influencing the voltage probes and causing a greater measurement error (greater stray impedance). Configuration B improved the high frequency response, but there was still a large deviation in the high frequency response between different cells in the stack. In configuration C the current conduction (out of the plane) was perpendicular to the voltage probes to minimise stray impedances as much as possible. This gave a consistent high frequency response between the different cells and decreased stray impedances. The experimental stack was therefore assembled with configuration C.

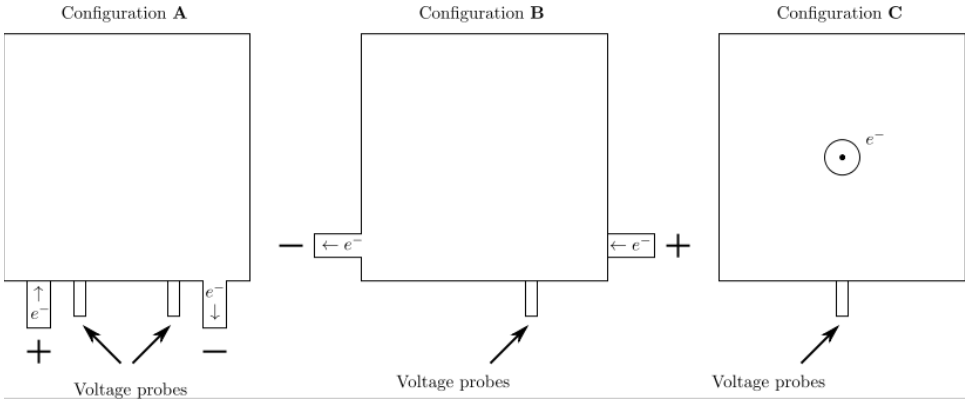


**Figure 1: Three stack configurations shown from above. $e^-$ indicate the current conduction. The current conduction direction for configuration C is out of the plane.**

The stack was sealed along the edges with a glass seal designed by TOFC. The fuel cell stack can be considered to consist of a number of repeating units (RU). Each repeating unit contains interconnects, glass seals and a cell. A schematic representation of the experimental stack is shown in Figure 2.

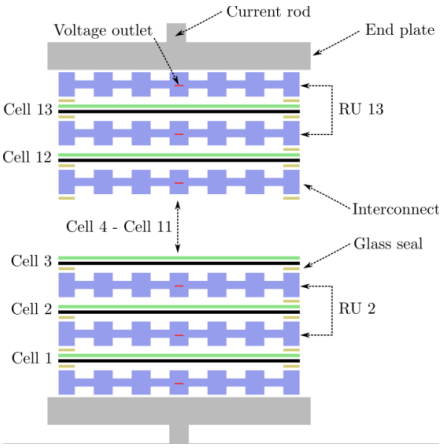


**Figure 2: Schematic representation of the experimental stack.**

The stack was tested using an automated test rig purchased from a commercial supplier. The stack was characterised using Electrochemical Impedance Spectroscopy (EIS). An illustration of the impedance custom test set-up is shown in figure 2. The EIS computer controls the Solartron 1260 Frequency Response Analyzer (FRA), via a GPIB communication bus. The Solartron 1260 sends an AC voltage signal from the generator output to the programmable input (Prg. Input) of a Kepco Bipolar Operational Amplifier 20-20D (Kepco Op-Amp) . The Kepco Op-Amp converts the AC voltage signal to a corresponding AC current signal with a current-to-voltage ratio of 1 A/V. The generated AC current through the SOFC stack is superimposed on the DC current provided by the Electronic load of the test stand. Four terminal measurements were used to measure the (time-dependent) currents and voltages of the RUs. The voltage of a RU was measured by a differential probe connected to the differential input V1 on the Solartron 1260. The current through the stack was measured with an active current transducer (LEM ITN-600) which has a linear response up to 200 kHz. The DC voltage and the common mode voltage was minimised by additional active electrical circuits in order to utilise the highest measurement resolution on the Solartron.

EIS spectra were recorded from 97 kHz to 0.3 Hz with an ac current modulation of 0.8 A at OCV or on top of the nominal dc current of 18.5 A during the galvanostatic long term degradation test. The AC current amplitude was selected by testing four different current amplitudes (0.25A, 0.5A, 1A and 3A). The linear Kramers-Kronig transform test was used for immittance data validation producing residuals within a range of ±2% and a $\chi^2$ in the range of $9.1 \cdot 10^{-5}$ to $10 \cdot 10^{-5}$ [10].

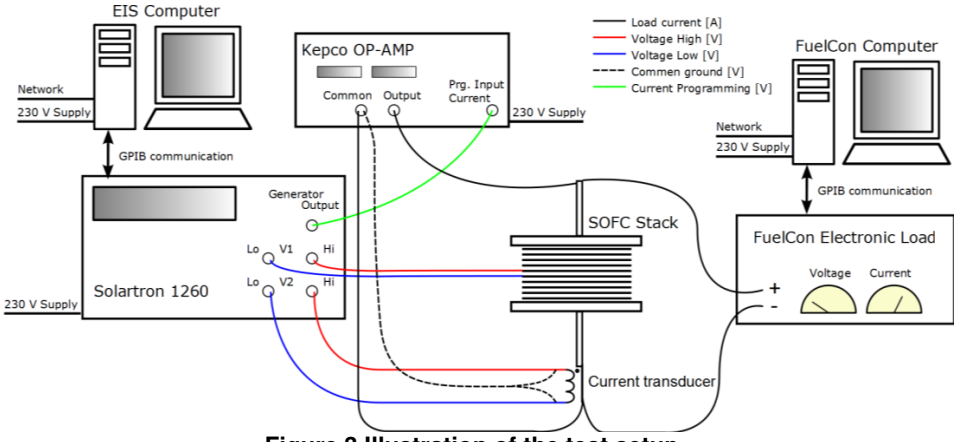


**Figure 3 Illustration of the test setup.**

Before the long term degradation test the stack was characterised with fuel consisting of $H_2$ with 20% $H_2O$ at 700, 750 and 800˚C in order to establish the temperature dependence of the losses in the stack. Temperature monitoring was performed with type S (Pt/Pt-Rh) thermocouples for the fuel and oxidant inlet at the top and bottom end-plates. The long term degradation test was carried out at constant current (galvanostatic) conditions at 0.2 A $cm^{-2}$ (18.5 A) and the stack temperature set to 750˚C. The fuel was $H_2$ with 4% $H_2O$ the oxidant was air. After 200 h, 4% $H_2O$ was added to the air. The fuel and oxygen utilisation was 52% and 19%, respectively.

## 3. Results

### 3.1 Initial performance

Figure 4 shows the initial performance and scattering in resistance of the different cells in the stack measured by EIS. The series resistance, $R_s$ and the polarisation resistance $R_p$ are derived from the EIS data and the cells are grouped in colours which represent the different coatings. The $R_s$ and $R_p$ data presented here were extracted from the real part of the impedance at the highest and lowest frequency. The RUs with the standard ceramic coat has the lowest total resistance, yields the lowest $R_p$ values, and also exhibits among the smallest cell-to-cell variations. The RUs with Cu LSM wet spray coating (cells 5 and 11) has a low $R_s$ value but a high $R_p$ value.

The large scatter in $R_s$ and $R_p$ values for the different cells is likely due to that the stack is an experimental stack optimised for electrochemical impedance spectroscopy, which in this case resulted in a different pressure (compressive force) distribution compared to a standard stack.

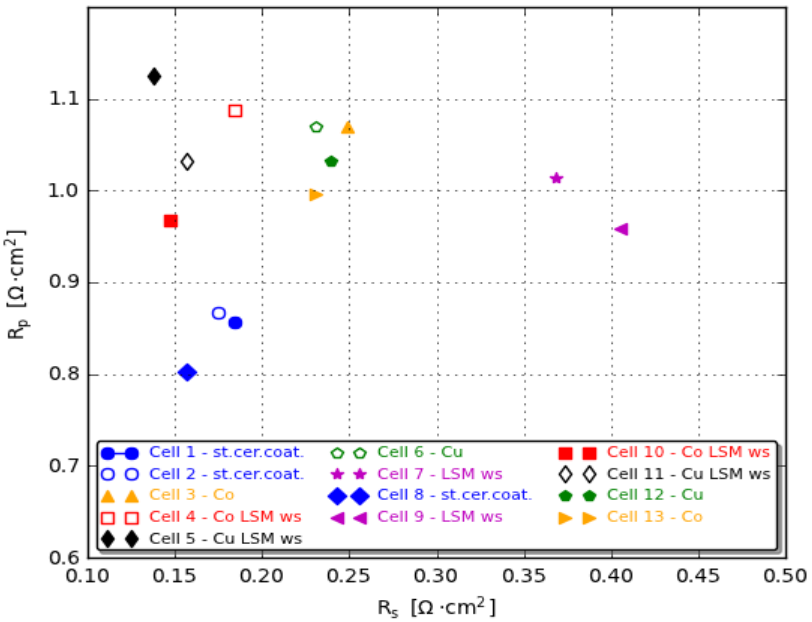


**Figure 4 Initial performance of the cells in the stack measured at OCV with EIS.**

Due to the time-consuming nature of the impedance characterisation carried out, not helped by the largely manual multiplexing between cells, four cells were selected for detailed analysis impedance analysis and degradation mode tracking. The cells (#2,4,6,11) were selected based on physical placement in the stack, and on the interconnect coating material. The temperature dependence in $R_s$ and $R_p$ for the four cells

of interest is shown in Figure 5. The corresponding activation energies for $R_s$ and $R_p$ are shown in Table 2.

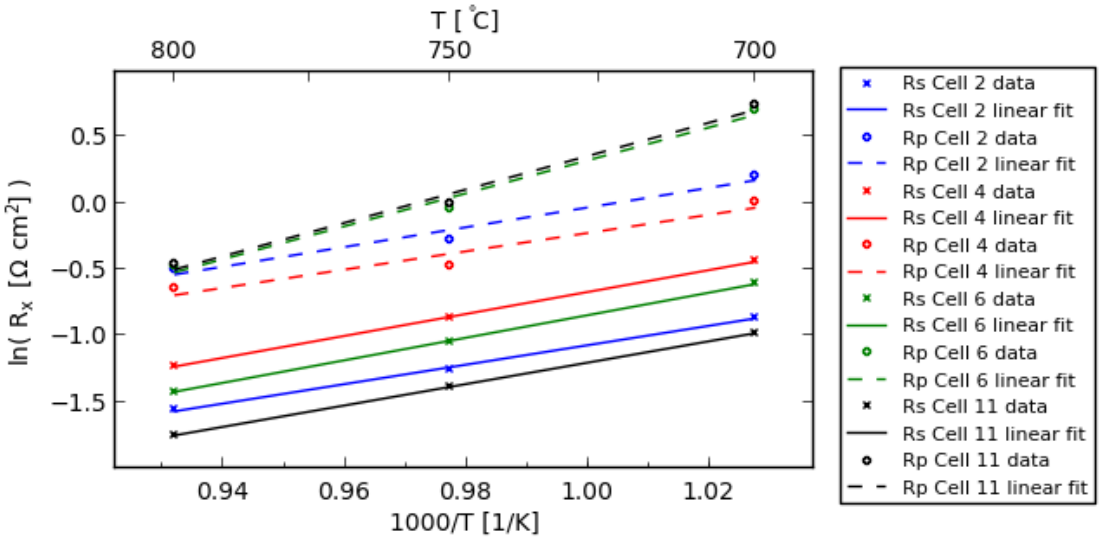


**Figure 5 Arrhenius plot for the four cells of interest. Cell 2 – st.cer.coat, Cell 4 – CO LSM ws, Cell 6 – Cu and Cell 11 – Cu LSM ws**

**Table 2: Activation energies, $E_a$, for $R_s$ and $R_p$ for the different cells.**

| Cell | IC Coating | $E_a$ for $R_s$ | $E_a$ for $R_p$ |
|---|---|---|---|
| 2 | st.cer.coat. | 0.630761 eV | 0.639897 eV |
| 4 | Co LSM ws | 0.711829 eV | 0.592933 eV |
| 6 | Cu | 0.731157 eV | 1.06853 eV |
| 11 | Cu LSM ws | 0.694298 eV | 1.08289 eV |

### 3.2 Long term degradation behaviour

The cell voltage history plot in Figure 6 shows the average cell voltage for the stack RUs. It can be split into four periods divided by shorter periods in which the data-logging system was off-line. In the middle of degradation period 1 the air humidification was initiated. . The galvanostatic test was continuous however, also in periods without data-logging. The average degradation rate is not constant during the test, but is greatest in period 1. When examining individual cell voltages (Figure 7), it is clear that RUs with different coating materials display very different degradation behaviour. In period 2 the degradation rate vary from cell 2 with -4.5 $mV \cdot kh^{-1}$ to cell 6 with -18.4 $mV \cdot kh^{-1}$. In period 4 the degradation rate vary from cell 2 with -1.1 $mV \cdot kh^{-1}$ to cell 11 with -84.2 $mV \cdot kh^{-1}$. Cell 11 displays a progressive degradation trend (accelerating degradation) [11]. This may be due to effects such as spallation of the coating and/or loss of contact between cell and interconnects, leading to hot-spots and increased corrosion, which accelerates the degradation further. The RU with the standard ceramic coat (cell 2) displays a linear degradation in periods 2-4 after the initial nonlinear voltage drop in period 1.

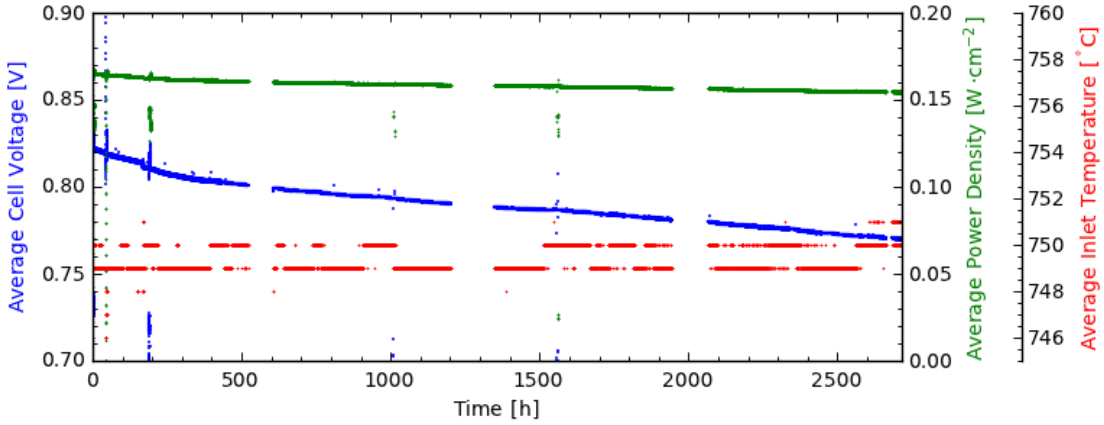


**Figure 6: Overall stack performance during long term degradation.**

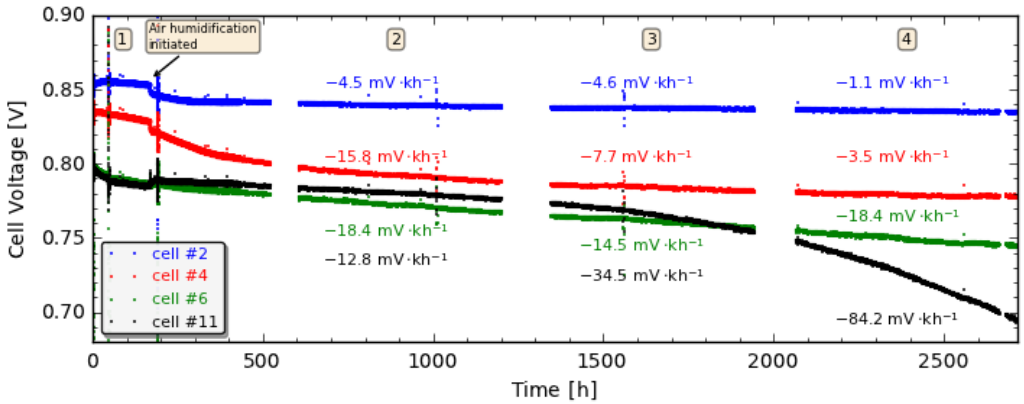


**Figure 7: Cell voltages versus time. Annotation 1-4 corresponds to 4 different degradation periods. Cell 2 – st.cer.coat, Cell 4 – Co LSM ws, Cell 6 – Cu and Cell 11 – Cu LSM ws.**

### 3.2.1 EIS monitoring

EIS spectra were recorded regularly on the four selected cells. **Figure 8** shows EIS spectra of the four cells just after the air humidification was initiated. The absolute value for Rs for the displayed impedance spectra is in the range between 5 to 8 mΩ.

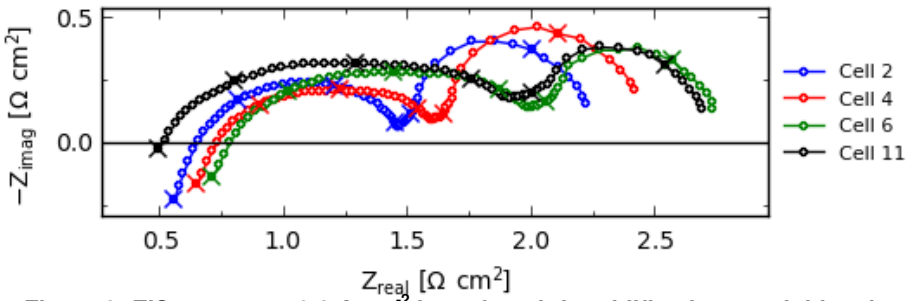


**Figure 8: EIS spectra at 0.2 A cm$^{-2}$ just after air humidification was initiated. Cell 2 – st.cer.coat, Cell 4 – Co LSM ws, Cell 6 – Cu and Cell 11 – Cu LSM ws. X corresponds to the frequencies 97 kHz, 9.7 kHz, 970 Hz, 97 Hz, 9.7 Hz and 0.97 Hz.**

Figure 9 shows the resistance behaviour versus time for the series resistance, $R_s$ and the polarisation resistance, $R_p$, as measured under current.

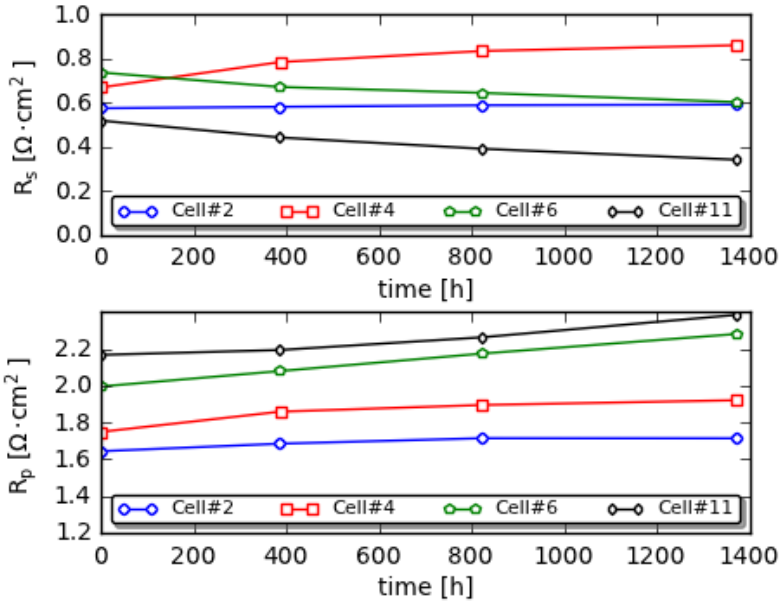


**Figure 9: Resistance behaviour versus time. Cell 2 – st.cer.coat, Cell 4 – Co LSM ws, Cell 6 – Cu and Cell 11 – Cu LSM ws**

### 3.2.2 Degradation mode tracking

Figure 10 shows the normalised polarisation resistance, $R_p^0/R_p$ versus normalised series resistance, $R_s^0/R_s$ where point (1,1) correspond to the initial situation. Plotting the evolution of normalised series and polarisation resistance starting at (1,1) provides useful visual information about the nature and extent of degradation. A degradation mode that mainly affects $R_s$ like oxide layer growth appears as an almost horizontal progressing leftward with increasing extent of degradation [12]. Nickel coarsening (at shorter time-scales) [13], chromium poisoning [14] and/or water induced changes on the cathode side [15], is reflected as a vertical line down from (1,1) since it is mainly affects the $R_p$.

If the normalised resistance trajectory follows the 45 degree line it is an indication that a degradation process that changes the active area of the cell (*e.g.* delamination) may be dominating the degradation [12]. It is important to note that this way of plotting do not identify the degradation specifically, it only aids in identifying main types of degradation, $R_s$ only, $R_p$ only or usually both in various proportions.

Figure 10 illustrates that the degradation of cell 2 with the standard coating is characterised by occurring at the same rate for both $R_s$ and $R_p$ which could indicate a mechanism that changes the active area of the cell. For cell 4 one also observes that both resistances increase, but here Rs increases at a faster rate than $R_p$ – this could indicate a combination of change the active area of the cell and an "$R_s$-only process" like e.g. oxide layer growth. Cell 6 and cell 11 behave differently; for these cells $R_s$ decreases over time, but $R_p$, which dominate the total resistance increases. Figure 10 show the relative changes for $R_s$ and $R_p$. For absolute changes of $R_s$ and $R_p$ see Figure 9.

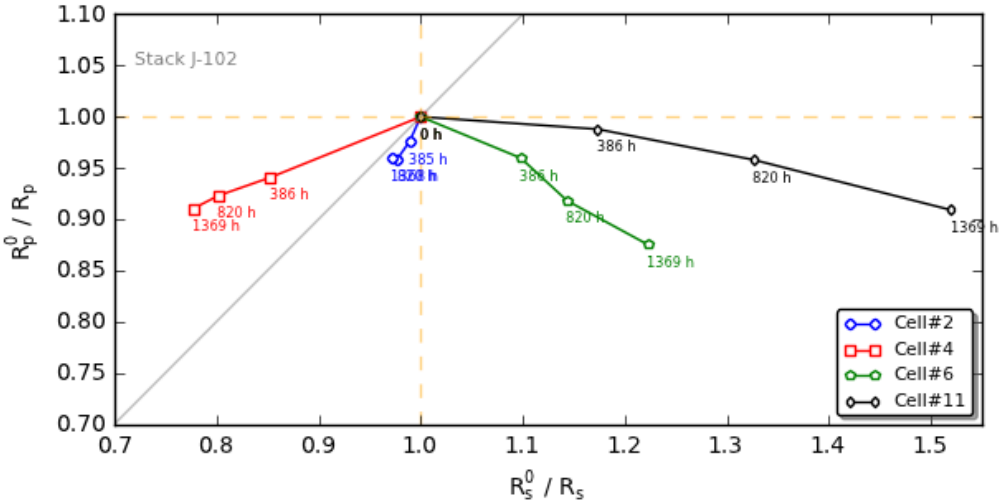


**Figure 10: Degradation mode plot. Cell 2 – st.cer.coat, Cell 4 – Co LSM ws, Cell 6 – Cu and Cell 11 – Cu LSM ws.**

## 4. Conclusions

A 13-cell experimental SOFC stack was tested during 2,500 hours of continuous operation with hydrogen as fuel with 52% fuel utilisation and constant current load (0.2 A cm-2) at 750˚C. Stack interconnects was coated with six different coatings to prevent chromium poisoning on the cathode side.

The stack geometry, in terms of current path and voltage probe placement was optimised for electrochemical impedance spectroscopy (EIS). The results illustrate that detailed EIS is possible on large area stacks and a de-convolution of the total loss into an ohmic and a non-ohmic part can be made.

The linear Kramers-Kronig Transform was used for data validation of the impedance spectra. Four cells were selected for detailed impedance analysis and degradation mode tracking. Cell 2 with the standard ceramic coating displayed the lowest long term degradation. The degradation of cell 4 with Co LSM wet sprayed coating was dominated by an increase of the series resistance with time, which could indicate that oxide layer growth was relatively rapid in the RU. Cell 6 and cell 11 showed increasing Rp values but decreasing Rs values. Analysis of all cell impedances in the stack (carried out at specific times only) show that the difference in behaviour between the four RU's does lie in the different interconnect coatings. Whereas the performance of the experimental coatings is unsatisfactory the experiment is successful in terms of characterisation – the EIS allowed a distinction to be made in terms of the degradation between the four RU types that is not possible from IV-data only.

## Acknowledgements

The authors gratefully acknowledge Copenhagen Cleantech Cluster and EUDP under the project ENS-64010-0052 for financial support, Topsoe Fuel Cell A/S for material supply. Martin Nørby Nielsen from DTU Energy Conversion for improvements to our EIS measurement accuracy. Dr Christopher Graves from DTU Energy Conversion for use of the RAVDAV data analysis software package.

## References


[1] U.S. Department of Energy. Distributed/stationary fuel cell systems 2011.

[2] Yokokawa H, Tu H, Iwanschitz B, Mai A. Fundamental mechanisms limiting solid oxide fuel cell durability. Journal of Power Sources 2008;182(2):400-412.

[3] Huang Q, Hui R, Wang B, Zhang J. A review of ac impedance modeling and validation in sofc diagnosis. Electrochimica Acta 2007;52(28):8144-8164.

[4] Comminges C, Fu QX, Zahid M, Steiner NY, Bucheli O. Monitoring the degradation of a solid oxide fuel cell stack during 10,000h via electrochemical impedance spectroscopy. Electrochimica Acta 2012;59:367-375.

[5] Lang M, Auer C, Eismann a, Szabo P, Wagner N. Investigation of solid oxide fuel cell short stacks for mobile applications by electrochemical impedance spectroscopy. Electrochimica Acta 2008;53(25):7509-7513.

[6] Ebbesen SD, Høgh J, Nielsen KA, Nielsen JU, Mogensen M. Durable soc stacks for production of hydrogen and synthesis gas by high temperature electrolysis. International Journal of Hydrogen Energy 2011;36(13):7363-7373.

[7] Dekker NJJ, van Wees JF, Rietveld G. Determination of the anode flow distribution in a sofc stack at nominal operating conditions by eis. ECS Transactions 2009;25(2):1871-1878.

[8] Hagen A, Barfod R, Hendriksen PV, Liu Y-L, Ramousse S. Degradation of anode supported sofcs as a function of temperature and current load. Journal of The Electrochemical Society 2006;153(6):A1165.

[9] Nielsen KA, Persson A, Beeaff D, Høgh J, Mikkelsen L, Hendriksen PV. Initiation and performance of a coating for countering chromium poisoning in a sofc-stackle. ECS Transactions 2007;7(1):2145-2154.

[10] Boukamp BA. A linear kronig-kramers transform test for immittance data validation. Journal of The Electrochemical Society 1995;142(6):1885.

[11] de Haart LGJ, Mougin J, Posdziech O, Kiviaho J, Menzler NH. Stack degradation in dependence of operation parameters; the real-sofc sensitivity analysis. Fuel Cells 2009;9(6):794-804.

[12] Gazzarri JI, Kesler O. Short stack modeling of degradation in solid oxide fuel cells. Journal of Power Sources 2008;176(1):155-166.

[13] Jiao Z, Shikazono N, Kasagi N. Study on degradation of solid oxide fuel cell anode by using pure nickel electrode. Journal of Power Sources 2011;196(20):8366-8376.

[14] Kornely M, Neumann A, Menzler NH, Leonide A, Weber A, Ivers-Tiffée E. Degradation of anode supported cell (asc) performance by cr-poisoning. Journal of Power Sources 2011;196(17):7203-7208.

[15] Lee D, Ahn S-J, Kim J, Moon J. Influence of water vapor on performance of co-planar single chamber solid oxide fuel cells. Journal of Power Sources 2010;195(19):6504-6509.

## A.2 Paper B

DOI: 10.1002/fuce.201200175

Fuel Cells

ORIGINAL RESEARCH PAPER

# Electrochemical Characterization and Degradation Analysis of Large SOFC Stacks by Impedance Spectroscopy▲

R. R. Mosbæk[1]*, J. Hjelm[1], R. Barfod[2], J. Høgh[1], P. V. Hendriksen[1]

[1] DTU Energy Conversion, Risø Campus, Frederiksborgvej 399, DK-4000 Roskilde, Denmark
[2] Topsoe Fuel Cell A/S, Nymøllevej 66, DK-2800 Lyngby, Denmark

Received September 30, 2012; accepted March 06, 2013; published online March 28, 2013

## Abstract

As solid oxide fuel cell (SOFC) technology is moving closer to a commercial break through, lifetime limiting factors, and methods to measure the "state-of-health" of operating cells and stacks are becoming of increasing interest. This requires application of advanced methods for detailed electrochemical characterization during operation.

An experimental stack with low ohmic resistance from Topsoe Fuel Cell A/S was characterized in detail using electrochemical impedance spectroscopy (EIS). An investigation of the optimal geometrical placement of the current feeds and voltage probes was carried out in order to minimize measurement errors caused by stray impedances. Three different stack geometries were investigated by impedance spectroscopy and the stack geometry with the minimum effect of stray impedances was selected.

A 13-cell experimental SOFC stack was tested during 2,500 h of operation with hydrogen as fuel with 52% fuel utilization and constant current load (0.2 A $cm^{-2}$) at 750 °C. Stack interconnects were coated with six different coatings to prevent chromium poisoning on the cathode side. Four repeating units (RUs) with different coatings were selected for detailed impedance analysis. EIS allowed a distinction to be made in terms of the degradation between the four RU types that is not possible from IV-data only.

**Keywords:** Degradation, Electrochemical Impedance Spectroscopy, Solid Oxide Fuel Cell (SOFC), Stack

## 1 Introduction

As solid oxide fuel cell (SOFC) technology is moving closer to a commercial break through, lifetime limiting factors, determination of the limits of safe operation and methods to measure the "state-of-health" of operating cells and stacks are becoming of increasing interest. This requires application of advanced methods for detailed electrochemical characterization during operation. An operating stack is subject to steep compositional gradients in the gaseous reactant streams, and significant temperature gradients along each cell and across the stack, which makes it a complex system to analyze in detail [1]. Today one is forced to use mathematical modeling to extract information about existing gradients and cell resistances in operating stacks, as mature techniques for local probing are not available. This type of spatially resolved information is essential for model refinement and validation, and helps to further the technological stack development. Further, more detailed information obtained from operating stacks is essential for developing appropriate process monitoring and control protocols for stack and system developers.

The U.S. Department of Energy has set a preliminary lifetime target for SOFCs stacks to be 40,000 h by 2015 for stationary applications [2]. Understanding and mitigation of the degradation mechanisms in SOFC stacks is therefore crucial in order to improve the durability and increase the stack lifetime [3].

Electrochemical impedance spectroscopy (EIS), is a powerful diagnostic technique that can increase understanding of the degradation mechanisms dominating in operating stacks since the technique may provide information on individual losses, including oxygen reduction reaction kinetics, mass-transport processes, and electrolyte resistance loss [4]. EIS has been an increasingly popular diagnostic technique at the

▲ *Paper presented at the 10th European SOFC Forum 2012, June 26–29, 2012 held in Lucerne, Switzerland. Organized by the European Fuel Cell Forum – www.efcf.com*

[*] *Corresponding author, rasmo@dtu.dk*

SOFC single cell level but has so far only seen limited use on the stack level [5–9].

One of the key challenges in associated with impedance measurements of large area objects, such as the experimental SOFC stack considered here, is that the absolute impedance for a cell in the experimental stack is in the range of a few mΩ which requires equipment with high precision and minimization of unwanted stray impedances in the geometrical set-up. Stray impedances are caused by mutual inductance and stray capacitance and do not describe the fuel cells in the stack.

The present work describes the minimization of stray impedance in order to reduce measurement errors when characterizing SOFC stacks. Three different stack geometries were investigated by EIS in order to compare the effect of stray impedances at high frequencies.

An experimental 13-cell stack was assembled with the stack geometry with the lowest effect of stray impedances. Metallic interconnects were coated with different types of protective layers. The stack has been tested for more than 2,500 h at steady operating conditions. EIS has been used to examine the long-term behavior and monitor the evolution of series and polarization resistances for 4 out of the 13 repeating units (RUs). The losses for the four RUs are reported and discussed.

## 2 Experiments

The SOFCs used for the 13-cell experimental fuel cell stack were planar anode-supported SOFCs (Ni-YSZ/YSZ/LSM-YSZ) of 12 cm × 12 cm footprint and an active area of approximately 90 $cm^2$. The cell details can be found elsewhere [10]. Interconnects were made of commercial stainless steel. Different coatings were used on the interconnects in the stack (see Table 1) to prevent chromium poisoning on the cathode side [11]. The nickel oxide in the Ni-YSZ electrode was reduced to nickel in hydrogen at start-up and the stack was subsequently tested for performance and durability. The stack testing was performed at DTU Energy Conversion with an experimental stack manufactured by Topsoe Fuel Cell A/S (TOFC).

An investigation of the optimal geometrical placement of the current probes and voltage probes was carried out in order to minimize measurement errors caused by stray impedances. Unwanted stray impedances are particularly problematic at high frequencies. Stray impedances may be caused by mutual inductance and stray capacitance in the geometrical set-up and do not describe the fuel cell. The optimal stack geometry, with respect to how to place the voltage probes and how to feed current to the end-plates, was found by performing EIS on three different stacks. The placement of the voltage probes and the current leads to the end plates for the three different stack geometries are shown in Figure 1. For configuration A, there were big differences in the high frequency response between the different RUs in the stack since the magnetic field from the current conduction was influencing the voltage probes by mutual inductance and thereby causing a greater measurement error. The operating conditions in the test of Configuration A were: Temperature: 817 °C. Fuel: 70% $H_2$ 30% $H_2O$. Oxidant: Air. EIS recorded at open circuit voltage (OCV).

Table 1 RUs and the corresponding interconnect (IC) coating towards the cathode side.

| RU | IC coating | RU | IC coating | RU | IC coating |
|---|---|---|---|---|---|
| #1 | st.cer.coat | #6 | Cu | #11 | Cu LSM ws |
| #2 | st.cer.coat | #7 | LSM ws | #12 | Cu |
| #3 | Co | #8 | st.cer.coat | #13 | Co |
| #4 | Co LSM ws | #9 | LSM ws | | |
| #5 | Cu LSM ws | #10 | Co LSM ws | | |

ws, wet sprayed; st.cer.coat., standard ceramic coating.

Configuration B improved the high frequency response, but there was still a large deviation in the high frequency response between different cells in the stack. Operating conditions when testing Configuration B were: Temperature: 750 °C. Fuel: 50% $H_2$ 50% $H_2O$. Oxidant: Air. EIS recorded at (OCV).

In configuration C, the current conduction (out of the plane) was perpendicular to the voltage probes (along the plane) to minimize stray impedances as much as possible. This gave a consistent high frequency response between the different cells and decreased the stray impedances. Operating conditions when testing Configuration C were: Temperature: 750 °C. Fuel: 96% $H_2$ 4% $H_2O$. Oxidant: Air. EIS recorded at 0.2 A $cm^{-2}$. The high frequency response towards the real impedance axis from the different RUs needs to be identical of shape, otherwise will the high frequency response of the RUs neither represent the cells nor the interconnects. The experimental stack was therefore assembled with configuration C.

The stack was sealed along the edges with a glass seal designed by TOFC. The fuel cell stack can be considered to consist of a number of RUs. Each RU contains interconnects, glass seals, and a cell. A schematic representation of the experimental stack is shown in Figure 2.

The stack was tested using an automated test rig purchased from a commercial supplier. The stack was characterized using EIS. An illustration of the test set-up is shown in Figure 3. The EIS computer controls the Solartron 1260 frequency response analyzer (FRA), *via* a GPIB communication bus. The FRA sends an AC voltage signal from the generator output to the programmable input (Prg. Input) of a Kepco Bipolar Operational Amplifier 20-20D (Electronic AC Load). The Electronic AC Load converts the AC voltage signal to a corresponding AC current signal with a current-to-voltage ratio of 1 A $V^{-1}$. The generated AC current through the SOFC stack is superimposed on the DC current provided by the Electronic AC Load of the test rig. Four terminal measurements were used to measure the (time-dependent) currents and voltages of the RUs. The voltage of a RU was measured by a differential probe connected to the differential input V1 on the FRA. The current through the stack was measured with an active current transducer (LEM ITN 600-s) which has a linear response up to 200 kHz. The DC voltages were minimized by additional active electrical circuits in order to utilize

  

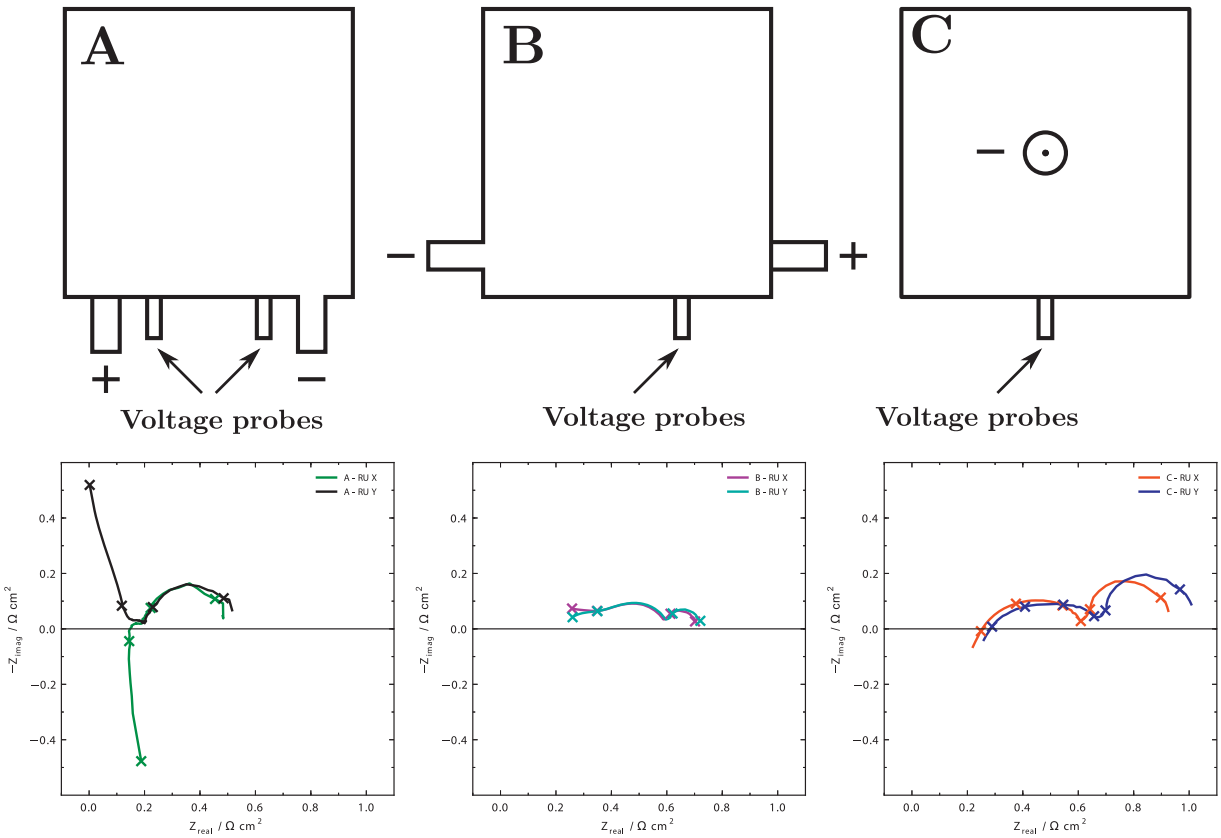


Fig. 1 Placement of voltage probes and current feeds on three different stack configurations (seen from above) and corresponding impedance spectra. The current conduction direction for configuration C is out of the plane. *X* corresponds to 50 kHz, 5 kHz, 500 Hz, 50 Hz, 5 Hz, and 0.5 Hz.

the highest measurement resolution on the FRA. The measurements were not corrected for wire inductances and stray capacitances in the test set-up. It is estimated that this will give a measurement error of <10% for the series resistances and a measurement error of <3% for the polarization resistances.

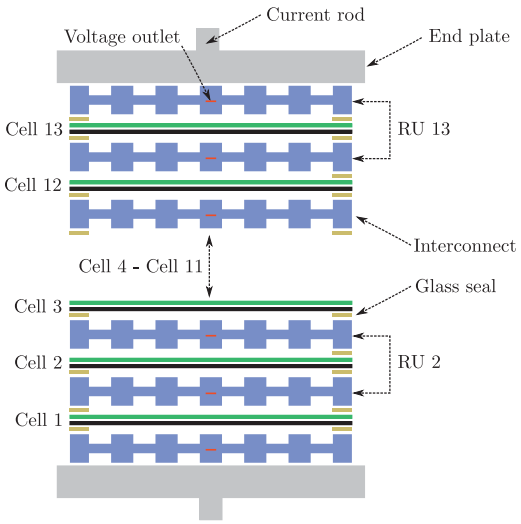


Fig. 2 Schematic representation of the experimental stack.

EIS spectra were recorded from 97 kHz to 0.3 Hz with an AC current modulation of 8.7 mA cm$^{-2}$ at OCV or on top of the nominal DC current of 0.2 A cm$^{-2}$ during the galvanostatic long term degradation test. The AC current amplitude was selected by testing four different current amplitudes (2.7, 5.4, 10.9, and 32.6 mA cm$^{-2}$). The linear Kramers–Kronig transform test was used for immittance data validation producing relative residuals within a range of ±0.5% and a pseudo $\chi^2$ in the range of 6.1 × 10$^{-5}$ to 2.4 × 10$^{-4}$ [12].

Prior to the long term degradation test, the performance of the stack was measured by measuring polarization curves and electrochemical impedance spectra at 700, 750, and 800 °C with 80% $H_2$ + 20% $H_2O$ as fuel and air as the oxidant.

Temperature monitoring was performed with type S (Pt/Pt-Rh) thermocouples for the fuel and oxidant inlet at the top and bottom end-plates. The long term degradation test was carried out at constant current (galvanostatic) conditions at 0.2 A cm$^{-2}$ and the stack temperature set to 750 °C. The fuel was $H_2$ with 4% $H_2O$ the oxidant was air. After 200 h, 4% $H_2O$ was added to the air. The fuel and oxygen utilization was 52 and 19%, respectively.

  

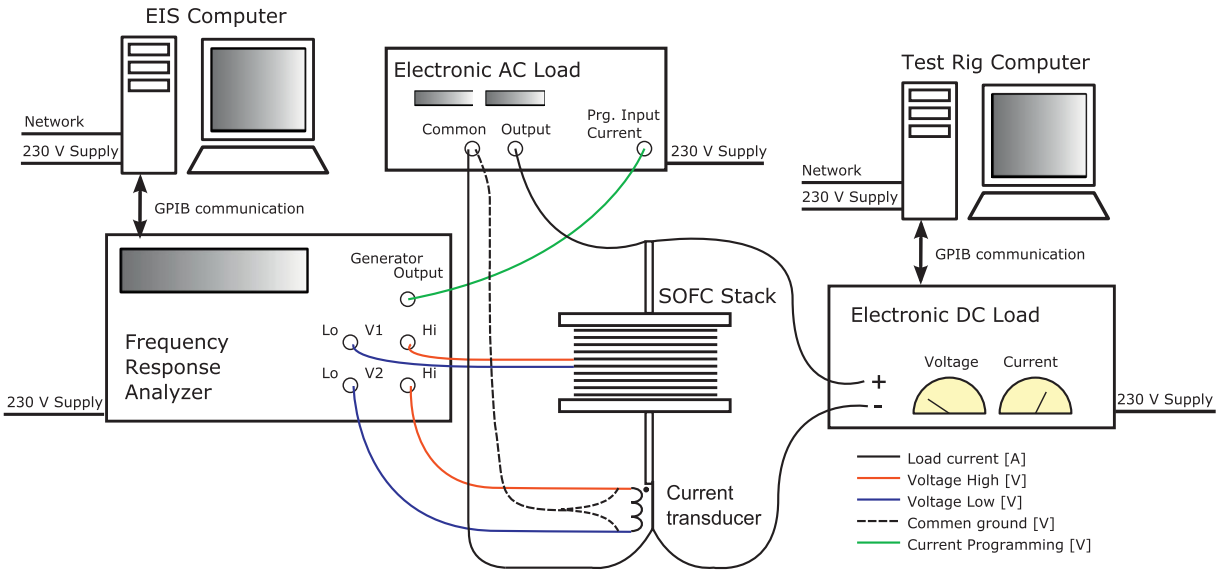


Fig. 3 Illustration of the test set-up.

## 3 Results

### 3.1 Initial Performance

Figure 4 shows the initial performance and scattering in resistance of the different cells in the stack measured by EIS. The series resistance, $R_s$ and the polarization resistance $R_p$ are derived from the EIS data and the RUs are grouped in colors which represent the different coatings. The $R_s$ and $R_p$ data presented here were extracted from the real part of the impedance at the highest and lowest frequency.

RU#5 and RU#11 with Cu LSM wet spray coating have a low $R_s$ value but a high $R_p$ value. RU#1 and RU#2 with standard ceramic coating have the lowest total resistance, yields the lowest $R_p$ values. RU#8, with the same interconnect coating, displays a significantly higher $R_s$ and $R_p$ than RU#1 and RU#2. Most of the increased impedance of RU#8 is in the $R_s$ (increased by more than 60%), while $R_p$ is only moderately increased (by ~20%). This observation is consistent with the predicted behavior when partial contact loss (detachment) occurs at the cathode-interconnect interface in a RU as shown by Gazzarri [13] page 86ff.

Due to the time-consuming nature of the impedance characterization carried out, not helped by the largely manual multiplexing between RUs, four RUs were selected for detailed impedance and degradation analysis. The RU (#2,4,6,11) were selected based on physical placement in the stack, and on the interconnect coating material. The temperature dependence in $R_s$ and $R_p$ for the four RUs of interest is shown in Figure 5. The corresponding activation energies for $R_s$ and $R_p$ are listed in Table 2.

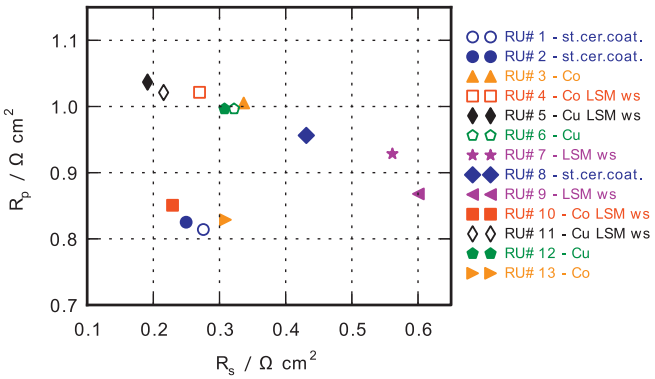


Fig. 4 Initial performance of the cells in the stack measured at OCV with EIS. Temperature: 750 °C Fuel: 80% $H_2$ with 20% $H_2O$. Oxidant: Air.

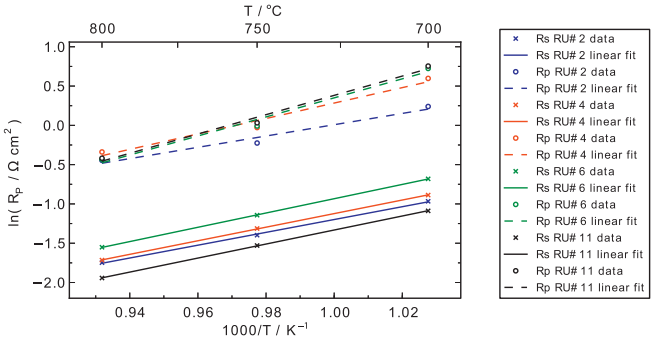


Fig. 5 Arrhenius plot for the four RUs of interest. RU#2 – st.cer.coat, RU#4 – CO LSM ws, RU#6 – Cu and RU#11 – Cu LSM ws. Fuel: 80% $H_2$ with 20% $H_2O$. Oxidant: Air.

  

Table 2 Activation energies, $E_a$, for $R_s$, and $R_p$ for the different RUs.

| RU | IC coating | $E_a$ for $R_s$ | $E_a$ for $R_p$ |
|---|---|---|---|
| #2 | st.cer.coat. | 0.70 eV | 0.62 eV |
| #4 | Co LSM ws | 0.74 eV | 0.85 eV |
| #6 | Cu | 0.78 eV | 1.04 eV |
| #11 | Cu LSM ws | 0.77 eV | 1.06 eV |

### 3.2 Long Term Degradation Behavior

The cell voltage history plot in Figure 6 shows the average cell voltage for the stack RUs. It can be split into four periods divided by shorter periods in which the data-logging system was off-line. In the middle of degradation period 1, the air humidification was initiated. The galvanostatic test was continuous however, also in periods without data-logging. The average degradation rate is not constant during the test, but is greatest in period 1. When examining individual RU voltages (Figure 7), it is clear that RUs with different coating materials display very different degradation behavior. In period 2 the degradation rate vary from RU#2 with –4.5 mV kh$^{-1}$ to RU#6 with –18.4 mV kh$^{-1}$. In period 4, the degradation rate vary from RU#2 with –1.1 mV kh$^{-1}$ to RU#11 with –84.2 mV kh$^{-1}$. RU#11 displays a progressive degradation trend (accelerating degradation) [14]. The origin of the progressive degradation in this experiment is not known to us. The RU with the standard ceramic coating (RU#2) displays a linear degradation in periods 2–4 after the initial nonlinear voltage drop in period 1. The orange dashed lines on Figure 7 indicate where EIS spectra were recorded during the long term test.

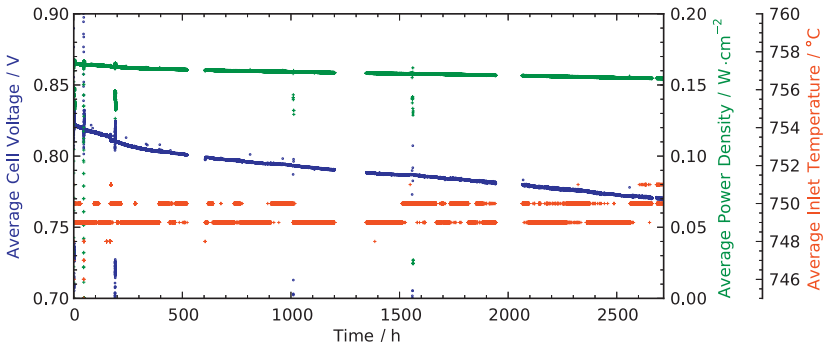


Fig. 6 Overall stack performance during long term degradation.

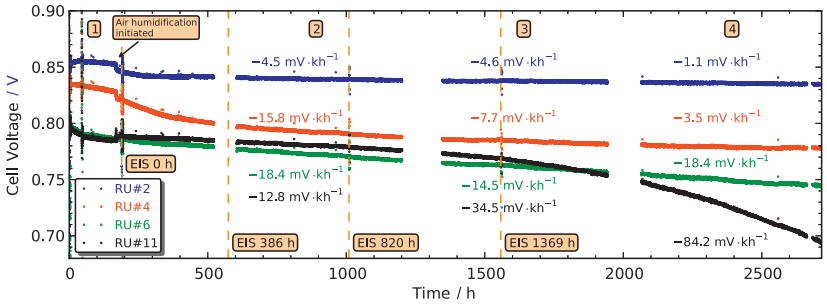


Fig. 7 RU voltages *versus* time. Annotation 1–4 corresponds to four different degradation periods. The orange dashed lines indicate where EIS spectra were recorded. RU#2 – st.cer.coat, RU#4 – Co LSM ws, RU#6 – Cu and RU#11 – Cu LSM ws.

#### 3.2.1 EIS Monitoring

EIS spectra were recorded regularly on the four selected cells. Figure 8 shows EIS spectra of the four RUs just after the air humidification was initiated (0 h) and the last EIS spectra recorded after 1369 h of constant current operation (1369 h). The absolute value for $R_s$ for the displayed impedance spectra is in the range between 2 and 3 mΩ. Significant changes in impedance for RU#4, RU#6, and RU#11 are observed in the frequency range (970 to 9.7 Hz) dominated by the LSM/YSZ cathode [15]. This supports the interpretation that the RUs that display the greatest change in $R_s$ and $R_p$ are subject to a greater degree of chromium poisoning.

Figure 9 shows the resistance behavior *versus* time for the series resistance, $R_s$ and the polarization resistance, $R_p$, measured at 0.2 A cm$^{-2}$.

#### 3.2.2 Degradation Analysis

The degradation analysis proposed by Gazzarri and Kesler [16] called "Degradation mode tracking" was used to plot the evolution of the degradation. Figure 10 shows the normalized polarization resistance, $R_p^0/R_p$ *versus* normalized series resistance, $R_s^0/R_s$ where point (1,1) correspond to the initial situation. Plotting the evolution of normalized series and polarization resistance starting at (1,1) provides useful visual information about the nature and extent of degradation. A degradation mode that mainly affects $R_s$ like oxide layer growth appears as an almost horizontal progressing leftward with increasing extent of degradation [16]. Nickel coarsening (at shorter timescales) [17], chromium poisoning [18] and/or water induced changes on the cathode side [19], is reflected as a vertical line down from (1,1) since it is mainly affects the $R_p$.

If the normalized resistance trajectory follows the 45 degree line, it is an indication that a degradation process that changes the active area of the RU (e.g. delamination) may be dominating the degradation [16]. It is important to note that this way of plotting does not identify the degradation specifically, it only aids in identifying main types of degradation, $R_s$ only, $R_p$ only or usually both in various proportions.

Figure 10 illustrates that the degradation of RU#2 with the standard coating is characterized by occurring at the same rate for both $R_s$ and $R_p$

  

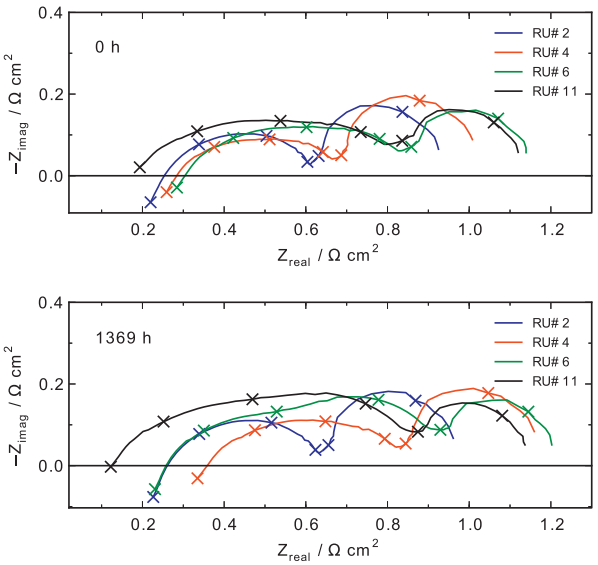


Fig. 8 EIS spectra at 0.2 A cm$^{-2}$ just after air humidification was initiated (0 h) and the last EIS spectra recorded (1369 h). RU#2 – st.cer.coat, RU#4 – Co LSM ws, RU#6 – Cu and RU#11 – Cu LSM ws. Temperature: 750 °C Fuel: 96% $H_2$ with 4% $H_2O$. Oxidant: 96% Air with 4% $H_2O$. *X* corresponds to 97 kHz, 9.7 kHz, 970 Hz, 97 Hz, 9.7 Hz, and 0.97 Hz.

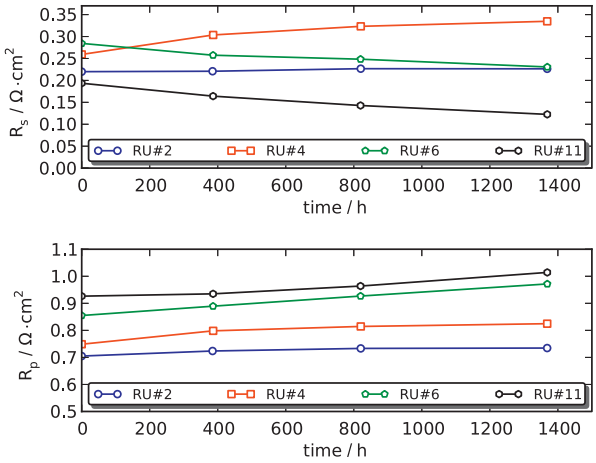


Fig. 9 Resistance behavior *versus* time. RU#2 – st.cer.coat RU#4 – Co LSM ws, RU#6 – Cu and RU#11 – Cu LSM ws. Current: 0.2 A cm$^{-2}$. Temperature: 750 °C. Fuel: 96% $H_2$ with 4% $H_2O$. Oxidant: 96% Air with 4% $H_2O$.

which could indicate a mechanism that changes the active area of the RU. For RU#4 one also observes that both resistances increase, but here $R_s$ increases at a faster rate than $R_P$ – this could indicate a combination of change the active area of the RU and an "$R_s$ – only process" like, e.g. oxide layer growth. RU#6 and RU#11 behave differently; for these RUs $R_s$ decreases over time, but $R_P$, which dominate the total resistance increases. Figure 10 show the relative changes for $R_s$ and $R_P$. For absolute changes of $R_s$ and $R_P$ see Figure 9.

Already at the initial characterization stage of the stack shown in Figure 4, RU#4, RU#6, and RU#11 showed a high $R_P$ compared to RU#2. This indicates that significant chromium poisoning takes place during start-up which has also been reported by Kornely et al. [18]

RU#4 has a slightly lower $R_P$ value compared to RU#6 and RU#11 at 0 h in Figure 9, even though RU#4, RU#6 and RU#11 have the nearly the same relative change in $R_P$ which is significantly higher than RU#2 as shown in Figure 10. This indicates that the coatings on RU#4, RU#6, and RU#11 are not as good chromium barriers, as RU#2 with the standard ceramic coating is.

To arrive at a detailed understanding of the underlying degradation processes in the specific stack the presented electrical analysis has to be supplemented by posttest microscopy and other characterization, which are beyond the scope of the present paper.

## 4 Conclusion

A 13-cell experimental SOFC stack was tested during 2,500 h of continuous operation with hydrogen as fuel with 52% fuel utilization and constant current load (0.2 A cm$^{-2}$) at 750 °C. Stack interconnects were coated with six different coatings to prevent chromium poisoning on the cathode side.

The stack geometry, in terms of current path and voltage probe placement was optimized for EIS. The results illustrate that detailed EIS is possible on large area stacks and a de-convolution of the total loss into an ohmic and a non-ohmic part can be made.

The linear Kramers–Kronig Transform was used for data validation of the impedance spectra. Four RUs were selected

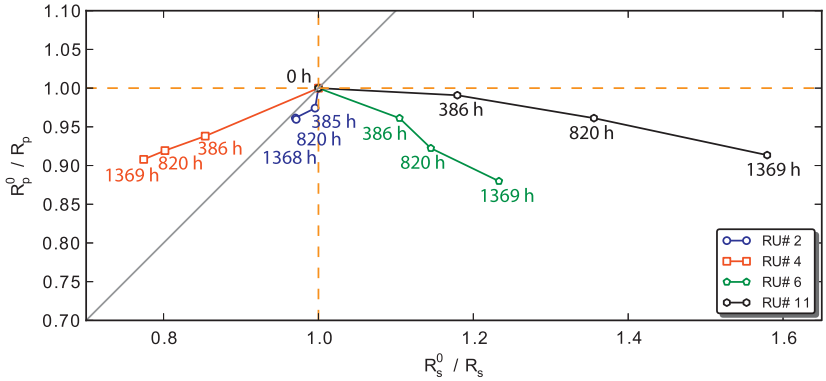


Fig. 10 Resistance normalization plot. RU#2 – st.cer.coat, RU#4 – Co LSM ws, RU#6 – Cu and RU#11 – Cu LSM ws. Current: 0.2 A cm$^{-2}$. Temperature: 750 °C. Fuel: 96% $H_2$ with 4% $H_2O$. Oxidant: 96% Air with 4% $H_2O$.

  

for detailed impedance analysis. RU#2 with the standard ceramic coating displayed the lowest long term degradation. The degradation of RU#4 with Co LSM wet sprayed coating was dominated by an increase of the series resistance with time, which could indicate that oxide layer growth was relatively rapid in the RU. RU#6 and RU#11 showed increasing $R_p$ values but decreasing $R_s$ values. Analysis of all RU impedances in the stack (carried out at specific times only) show that the difference in behavior between the four RUs lies mainly in the different interconnect coatings. Whereas the performance of the experimental coatings is unsatisfactory, the experiment is successful in terms of characterization – the EIS allowed a distinction to be made in terms of the degradation between the four RU types that is not possible from IV-data only.

## Acknowledgements

The authors gratefully acknowledge Copenhagen Cleantech Cluster and EUDP under the project ENS-64010-0052 for financial support, and Topsoe Fuel Cell A/S for supply of materials. Development engineer Martin Nørby Nielsen from DTU Energy Conversion for improvements to our EIS measurement accuracy. Dr. Christopher Graves from DTU Energy Conversion for use of the RAVDAV data analysis software package.

## References

[1] B. Shaffer, J. Brouwer, *J. Fuel Cell Sci. Technol.* **2012**, *9*, 041012.
[2] U.S. Department of Energy, Distributed/Stationary Fuel Cell Systems, can be found under www1.eere.energy.gov, **2011**.
[3] H. Yokokawa, H. Tu, B. Iwanschitz, A. Mai, *J. Power Sources* **2008**, *182*, 400.
[4] Q. Huang, R. Hui, B. Wang, J. Zhang, *Electrochim. Acta* **2007**, *52*, 8144.
[5] C. Comminges, Q. X. Fu, M. Zahid, N. Y. Steiner, O. Bucheli, *Electrochim. Acta* **2012**, *59*, 367.
[6] M. Lang, C. Auer, A. Eismann, P. Szabo, N. Wagner, *Electrochim. Acta* **2008**, *53*, 7509.
[7] S. D. Ebbesen, J. Høgh, K. A. Nielsen, J. U. Nielsen, M. Mogensen, *Int. J. Hydrogen Energy* **2011**, *36*, 7363.
[8] N. J. J. Dekker, J. F. van Wees, G. Rietveld, *ECS Trans.* **2009**, *25*, 1871.
[9] S. Diethelm, J. Van herle, Z. Wuillemin, A. Nakajo, N. Autissier, M. Molinelli, *J. Fuel Cell Sci. Technol.* **2008**, *5*, 031003.
[10] A. Hagen, R. Barfod, P. V. Hendriksen, Y.-L. Liu, S. Ramousse, *J. Electrochem. Soc.* **2006**, *153*, A1165.
[11] K. A. Nielsen, A. Persson, D. Beeaff, J. Høgh, L. Mikkelsen, P. V. Hendriksen, *ECS Trans.* **2007**, *7*, 2145.
[12] B. A. Boukamp, *J. Electrochem. Soc.* **1995**, *142*, 1885.
[13] J. I. Gazzarri, Ph.D. Thesis, University of British Columbia, British Columbia, Canada, **2007**.
[14] L. G. J. de Haart, J. Mougin, O. Posdziech, J. Kiviaho, N. H. Menzler, *Fuel Cells* **2009**, *9*, 794.
[15] R. Barfod, A. Hagen, S. Ramousse, P. V. Hendriksen, M. Mogensen, *Fuel Cells* **2006**, *6*, 141.
[16] J. I. Gazzarri, O. Kesler, *J. Power Sources* **2008**, *176*, 155.
[17] Z. Jiao, N. Shikazono, N. Kasagi, *J. Power Sources* **2011**, *196*, 8366.
[18] M. Kornely, A. Neumann, N. H. Menzler, A. Leonide, A. Weber, E. Ivers-Tiffée, *J. Power Sources* **2011**, *196*, 7203.
[19] D. Lee, S.-J. Ahn, J. Kim, J. Moon, *J. Power Sources* **2010**, *195*, 6504.

  

## A.3 Paper C

A0902

# Fuel flow distribution in SOFC stacks revealed by impedance spectroscopy

**R. R. Mosbæk (1), J. Hjelm (1), R. Barfod (2), and P. V. Hendriksen (1)**
(1) DTU Energy Conversion, Frederiksborgvej 399, DK-4000, Denmark
(2) Topsoe Fuel Cell A/S, Nymøllevej 66, DK-2800 Lyngby, Denmark
Tel.: +45-2365-2319
Fax: +45-4677-5858
rasmo@dtu.dk

## Abstract

As SOFC technology is moving closer to a commercial break through, methods to measure the “state-of-health” of operating stacks are becoming of increasing interest. This requires application of advanced methods for detailed electrical and electrochemical characterization during operation. An operating stack is subject to compositional gradients in the gaseous reactant streams, and temperature gradients across each cell and across the stack, which complicates detailed analysis.

An experimental stack with low ohmic resistance from Topsoe Fuel Cell A/S was characterized using Electrochemical Impedance Spectroscopy (EIS). The stack measurement geometry was optimized for EIS by careful selection of the placement of current feeds and voltage probes in order to minimize measurement errors.

It was demonstrated that with the improved placement of current feeds and voltage probes it is possible to separate the loss contributions in an ohmic and a polarization part and that the low frequency response is useful in detecting mass transfer limitations.

This methodology can be used to detect possible minor changes in the supply of gas to the individual cells, which is important when going to high fuel utilizations. The fuel flow distribution provides important information about the operating limits of the stack when high electrical efficiency is required.

## Introduction

As solid oxide fuel cell (SOFC) technology is moving closer to a commercial break through, lifetime limiting factors, determination of the limits of safe operation and methods to measure the “state-of-health” of operating cells and stacks are becoming of increasing interest. This requires application of advanced methods for detailed electrochemical characterization during operation. An operating stack is subject to steep compositional gradients in the gaseous reactant streams, and significant temperature gradients along each cell and across the stack, which makes it a complex system to analyze in detail[1]. Today one is forced to use mathematical modeling to extract information about existing gradients and cell resistances in operating stacks, as mature techniques for local probing are not available. This type of spatially resolved information is essential for model refinement and validation, and can help in furthering the technological stack development. Further, more detailed information obtained from operating stacks is essential for developing appropriate process monitoring and control protocols for stack and system developers.

The U.S. Department of Energy has set a preliminary lifetime target for SOFC stacks to be 60,000 h by 2020 for stationary applications[2]. Understanding and mitigation of the degradation mechanisms in SOFC stacks are therefore crucial in order to improve the durability and increase the stack lifetime[3].

Electrochemical Impedance Spectroscopy (EIS) is a powerful diagnostic technique that can improve understanding of the degradation mechanisms dominating in operating stacks since the technique may provide information on individual losses, including oxygen reduction reaction kinetics, mass-transport processes, and electrolyte resistance loss[4]. EIS has been an increasingly popular diagnostic technique at the SOFC single cell level but has so far only seen limited use on the stack level[5–11].

One of the key challenges associated with impedance measurements of large area objects, such as the experimental SOFC stack considered here, is that the absolute impedance for a repeating unit (interconnect-seal-cell-seal-interconnect) is in the range of a few mΩ which requires equipment with high precision and minimization of unwanted stray impedances in the set-up. Stray impedances are caused by mutual inductance and stray capacitance and can be a significant source of errors in the measurement data. Three different stack measurement geometries were investigated by electrochemical impedance spectroscopy in order to compare the effect of stray impedances at high frequencies and to reduce measurement errors when characterizing SOFC stacks. Details on optimizing this set-up was reported previously[12].

An experimental 14-cell stack was assembled with the stack measurement geometry with the lowest effect of stray impedances, where the current feed is perpendicular to the voltage probes. Metallic interconnects were coated with protective layers. EIS measurement for 14 repeating units and the stack was recorded simultaneously. This has several advantages such as reduced measurement time and a limited drift in temperature and fuel flow which gives a better comparison between repeating units. The spectra were used to monitor the series, polarization, electrochemical and gas conversion resistances for all the repeating units and the stack simultaneously. The losses for the repeating units are reported and discussed. The gas conversion resistances from the different repeating units are compared in order to investigate the fuel distribution.

## 1. Experiments

The solid oxide fuel cells (SOFC) used were planar anode supported cells with Ni/YSZ anode supports, Ni/YSZ anodes, YSZ electrolytes, CGO barrier layers and LSCF/CGO composite cathodes[13] .

The cells were used in a 14-cell experimental fuel cell stack with an active area of approximately 90 $cm^2$. Interconnects were made of commercial stainless steel. Coatings were used on the interconnects in the stack to prevent chromium poisoning on the cathode side[14]. The nickel oxide in the Ni-YSZ electrodes was reduced to nickel in hydrogen at start-up and the stack was subsequently tested for performance and durability. The stack testing was performed at DTU Energy Conversion using an experimental stack manufactured by Topsoe Fuel Cell A/S (TOFC).

The fuel cell stack can be considered to consist of a number of repeating units (RU). Each repeating unit contains interconnects, glass seals and a cell. A schematic representation of the experimental stack is shown in Figure 1.

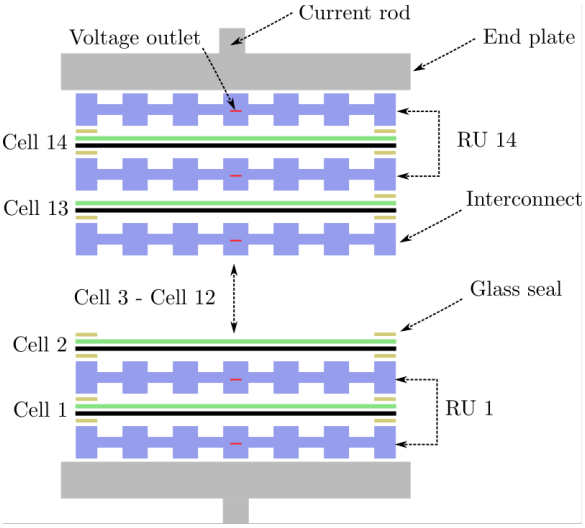


Fig. 1 A schematic representation of the experimental stack.

The stack was tested using an automated test rig purchased from FuelCon AG, and characterized using Electrochemical Impedance Spectroscopy (EIS). An illustration of the EIS test set-up is shown in Figure 2. The test rig computer controls the EIS computer via a network connection. The EIS computer controls the Zahner IM6 Potentiostat via a USB connection. The Zahner IM6 controls the Zahner EL1000 Electronic Load via an EPC connection. In combination the Zahner IM6 and the Zahner EL1000 can record EIS measurements of the stack and 16 RUs simultaneously. The DC current is measured by a current transducer and the data is logged by the test rig control computer via a data logger. A relay is implemented in the set-up in order to disconnect the Zahner IM6 and the Zahner EL1000 if the cell voltages exceed over- or undervoltage limits. The complete test set-up is fully automated. EIS measurements were recorded on 14 RUs and the stack simultaneously.

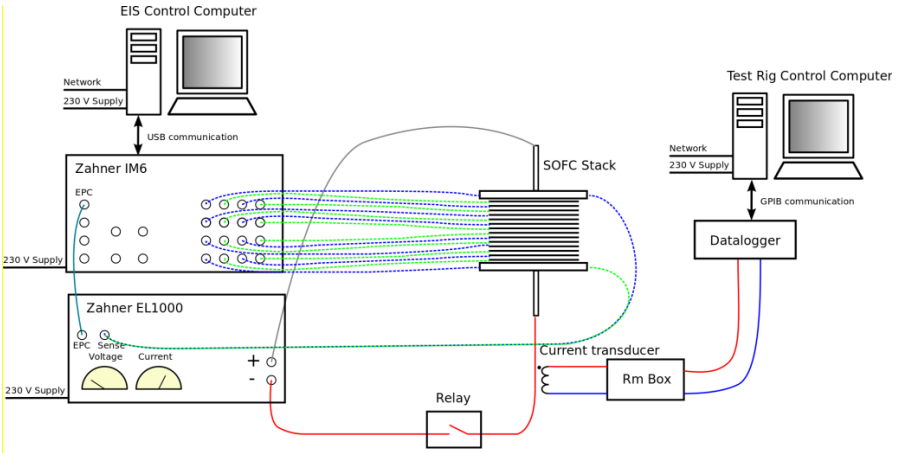


Fig. 2 Illustration of the test set-up for EIS measurements on SOFC stacks.

An investigation of the optimal geometrical placement of the current probes and voltage probes was carried out in order to minimize measurement errors caused by stray impedances. The voltage probes needed to be placed perpendicular to the current feeds to minimize the effect of stray impedances as much as possible. Details on optimizing this set-up was reported previously[12].

## 2. Results

### 2.1 Quality of impedance measurements

EIS spectra were recorded from 18.5 kHz to 0.3 Hz with 12 points per decade with an AC current modulation of 4 A, on top of a DC current of 4 A. The AC current amplitude was selected by testing three different current amplitudes (1A, 2A, 4A). The linear Kramers-Kronig transform test was used for immittance data validation producing relative residuals within a range of ±0.5%[15]. The absolute value for the series resistance, $R_s$, for the displayed impedance spectra was between 5 and 6 mΩ.

Figure 3 A) shows the impedance spectra for the 14 RUs recorded at 700°C with 20% steam and 80% hydrogen as fuel and air as oxidant. Figure 3 B) shows the imaginary impedance vs frequency. Figure 3 C) shows corresponding relative residuals of the linear Kramers-Kronig transform tests[15]. Figure 3 D) shows the distribution of relaxation times - DRT. This preidentification method separates the polarization processes with different time constants directly from the impedance data[16–18]. A first tentative assignment of the various processes observed can be carried out using available data from Leonide et al.[17] who used similar anode supported cells in a single cell set-up although the anode support thickness is different in Leonide et al.[17] and a LSCF/CGO composite cathode was used whereas Leonide et al.[17] used a LSCF cathode and based on previous work on the present anode-supported half-cell as exemplified in Barfod et al.[19]. The DRT spectra can be divided into five processes, P1 to P5. P1 is the gas conversion impedance at ~1Hz, P2 is a gas diffusion impedance ~10Hz, P3 is the activation polarization at the cathode (100Hz to 1kHz), P4 is charge transfer reactions at the triple phase boundary, P5 is the interfacial impedance as well as the ionic transport in the YSZ matrix[17,18].

Prior to calculation of DRT from the impedance spectra the high frequency inductance was removed by subtraction. The inductance was determined by comparison of the imaginary data generated from the experimental real part of the impedance using the Kramers-Kronig transforms[15].

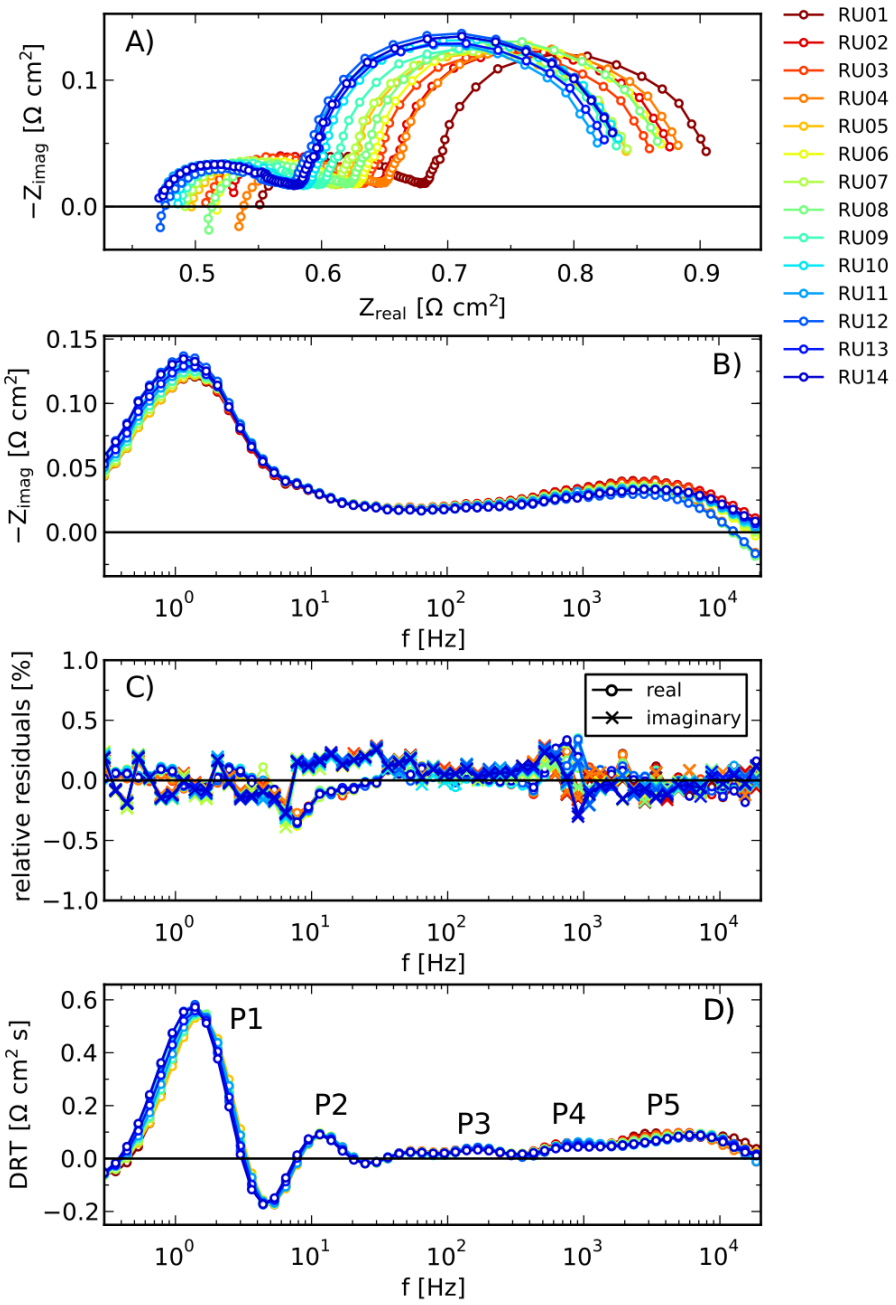


Fig. 3 A) EIS spectra for the 14 RUs in the stack measured at 700°C Fuel: 20% $H_2O$ and 80% $H_2$ Oxidant: Air B) Corresponding imaginary impedance vs frequency C) Corresponding relative residuals from the linear Kramers-Kronig transform test. D) Corresponding DRT spectra with electrochemical processes, P1-P5.

**2.2 A first parameterization of losses**

The loss for each impedance spectrum was divided into a series resistance, $R_s$, polarization resistance, $R_p$, a gas conversion resistance, $R_{GCl}$, and an electrochemical resistance, $R_{elec}$. See Figure 4. The series resistance, $R_s$, is the ohmic resistance and includes the resistance of the YSZ electrolyte[19], and losses associated with in-plane charge transport (current collection losses) and possibly a contribution from constriction at the interconnect/electrode and the electrode/electrolyte interfaces. $R_s$ is determined at the

highest frequency used, 18.5 kHz. The polarization resistance, $R_p$, includes electrochemical polarization losses from the anode and cathode together with the gas diffusion and conversion losses. $R_p$ is determined as the resistance between 18.5 kHz and 0.3 Hz. The gas diffusion and conversion impedance is the low frequency arc on the impedance spectra and has been described in several studies on single cells[20–24], but has so far only few studies describe the low frequency arc in detail on stack level with large area cells[8]. $R_{GCI}$ is the real part of the gas diffusion and conversion impedance. $R_{GCI}$ is determined between 30 Hz and 0.3 Hz. $R_{elec}$ is determined between 18.5 kHz and 30 Hz and describes the electrochemical losses in the anode and cathode.

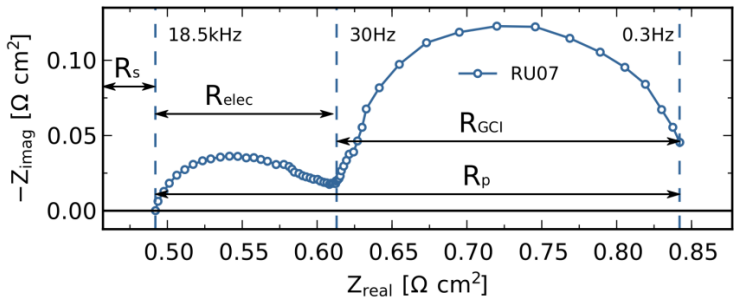


Fig. 4 Impedance spectra for RU07 at 700°C Fuel: 20% $H_2O$ and 80% $H_2$ Oxidant: Air. The series resistance, $R_s$, is extracted at 18.5 kHz, the polarization resistance, $R_p$, is extracted between 18.5 kHz and 0.3 Hz. The gas conversion resistance, $R_{GCI}$, is extracted between 30Hz and 0.3 Hz.

Figure 5 shows $R_s$, $R_p$, and $R_{GCI}$, and $R_{elec}$ as a function of the repeating units. $R_s$ decreases with increasing RU number. $R_s$ is decreasing by 16% from RU01 to RU14. Temperature probes mounted at the top and at the bottom of the stack yield a temperature difference of 12°C between the top and bottom of the stack, with the top being the warmer end. The observed series resistance decreases from bottom (RU01) to top (RU14) by 16%. Estimating the expected temperature difference using a simple Arrhenius expression and the observed activation energy of $R_s$, the difference should be 12%. Thus, the trend in $R_s$ is reflecting the gradient in average RU temperature across the stack. The variations in $R_s$ observed from RU03 to RU09 indicate variations in stray impedances and/or systematic variation in cell/IC contact which will be pursued at a later stage. $R_p$, shows similar electrochemical performance over the stack. $R_{GCI}$ increases with increasing RU number. This is explained in detail in Section 2.3. $R_{elec}$ is decreasing from the bottom to the top of the stack. The $R_{elec}$ is decreasing by 22% from RU01 to RU14.

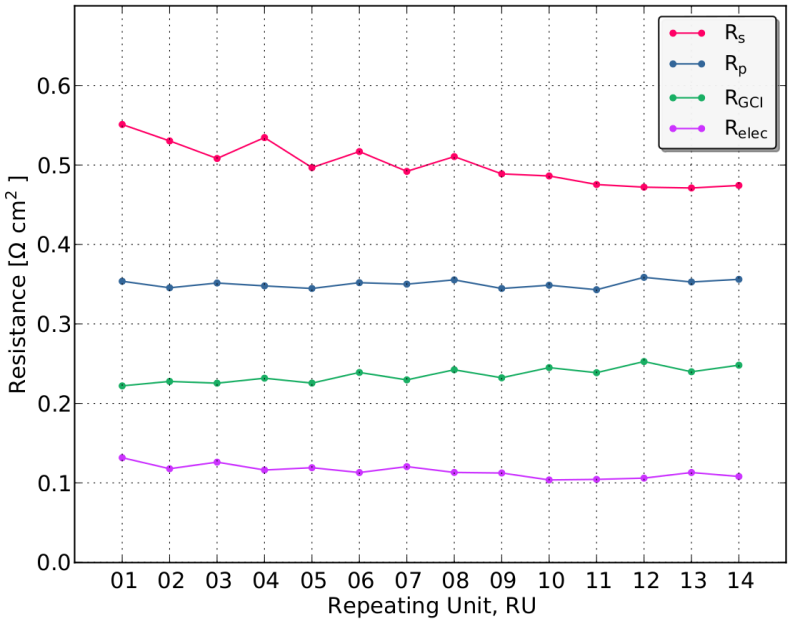


Fig. 5 $R_s$, $R_p$, $R_{GCI}$ and $R_{elec}$ vs repeating unit at 700°C Fuel: 20% $H_2O$ and 80% $H_2$ Oxidant: Air.

Figure 6 shows a comparison between the stack resistance and the sum of the RU resistances. The difference in the series resistance for the stack, $R_s$ Stack, and repeating units, $R_s$ RUs, is 0.8%. The difference in the polarization resistance for the stack, $R_p$ Stack, and repeating units, $R_p$ RUs, is 0.5%. The difference in the gas conversion resistance for the stack, $R_{GCI}$ Stack, and the sum over the repeating units, $R_{GCI}$ RUs, is 0.5%. The difference in electrochemical resistance for the stack, $R_{elec}$ Stack, and the sum over the repeating units, $R_{elec}$, is 2%. This indicates that the measurements are consistent.

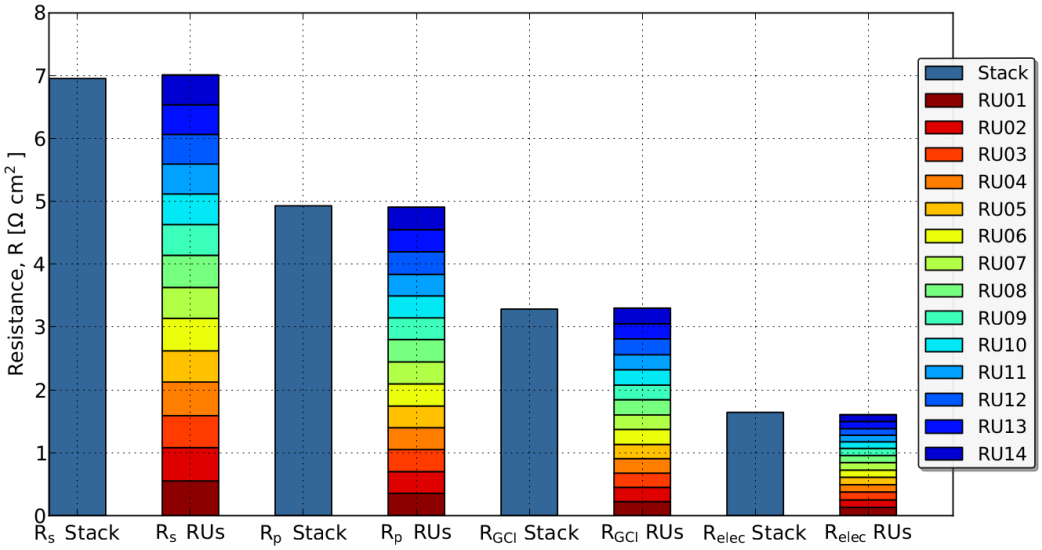


Fig. 6 $R_s$, $R_p$, $R_{GCI}$ and $R_{elec}$ for the stack and the repeating units. Recorded at 700°C Fuel: 20% $H_2O$ and 80% $H_2$ Oxidant: Air.

### 2.3 Gas conversion impedance

In simple models the gas diffusion and conversion impedance can be split into a resistive part and a capacitive part, and is strongly dependent on parameters such as gas composition, temperature, gas flow rate and interconnect geometry[20,24]. Figure 7 shows the gas conversion resistance, $R_{GCI}$, as a function of repeating unit number. The dashed line is the average gas conversion resistance. The difference between the lowest $R_{GCI}$ from RU01 and the highest $R_{GCI}$ from RU12 is ~12%. The general trend is that $R_{GCI}$ increases with increasing RU. An estimate using simple expressions for gas conversion resistances[20,24] with a measured temperature difference on 12°C between top and bottom of the stack shows that the difference should be ~1% if it was a pure temperature effect. This indicates that slightly less fuel is supplied to the top of the stack compared bottom of the stack. In order to understand the fuel flow distribution in more detail gas diffusion and conversion models must be fitted to the observed gas conversion impedance. An accurate estimate of the fuel flow can be obtained from the gas conversion impedance. This has been shown with gas conversion impedance models on single cells[20–24]. In simple gas conversion impedance models the gas conversion resistance, $R_{GCI}$, is inversely proportional to the fuel flow[20,24]. This means that the observed ~12% variation in $R_{GCI}$ corresponds to ~12% variation in fuel flow (if temperature and partial pressures is constant).

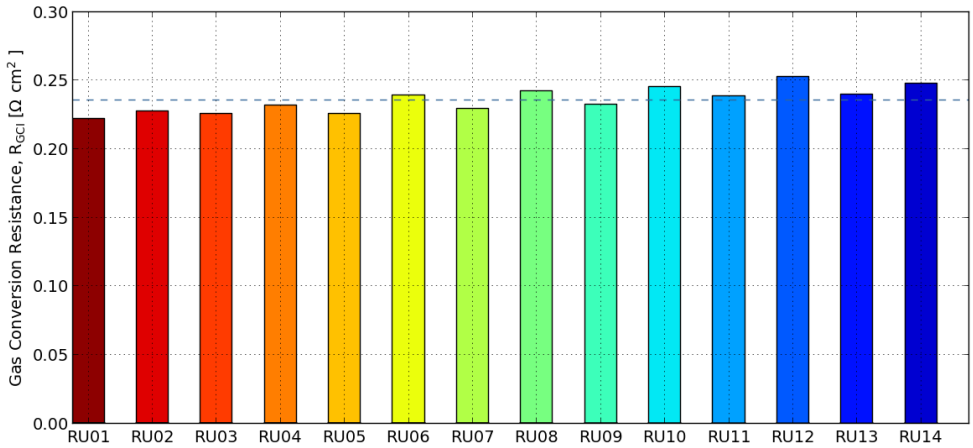


Fig. 7 Gas conversion resistance, $R_{GCI}$, vs Repeating Unit at 700°C Fuel: 20% $H_2O$ and 80% $H_2$ Oxidant: Air. Dashed line is the average gas conversion resistance.

## 3. Conclusion

A 14-cell experimental SOFC stack was tested electrochemical impedance spectroscopy. Stack interconnects were coated to prevent chromium poisoning on the cathode side. The stack measurement geometry, in terms of current path and voltage probe placement was optimized for electrochemical impedance spectroscopy (EIS). The linear Kramers-Kronig transform was used for data validation of the impedance spectra. The results illustrate that detailed EIS is possible on large area stacks and a de-convolution of the total loss into an ohmic, a non-ohmic part, and a part describing the gas conversion and diffusion, is possible. The sum of the RU resistances agreed well with the stack resistances. The experiment was successful in terms of characterization – the EIS allowed a distinction to be made in terms of differences between the RUs that is not possible from IV-data only. The gas conversion resistance increased with increasing RU number (from bottom to top). This indicates that top cells get slightly less fuel than the bottom cells (~12%).

## Acknowledgements

The authors gratefully acknowledge Copenhagen Cleantech Cluster, Energinet.dk under the ForskEL project no 2012-1-10747 and EUDP under the project ENS- 64012-0225 for financial support, and Topsoe Fuel Cell A/S for materials supply. Martin Nørby Nielsen and Anders Petersen from DTU Energy Conversion for technical support. Dr Jens Høgh from DTU Energy Conversion for fruitful discussions. Dr Christopher Graves from DTU Energy Conversion for use of the RAVDAV data analysis software package.

## References

[1] B. Shaffer, J. Brouwer, *J. Fuel Cell Sci. Technol.* **2012**, *9*, 041012.
[2] U.S. Department of Energy, Distributed/Stationary Fuel Cell Systems, can be found under www1.eere.energy.gov, 2009.
[3] H. Yokokawa, H. Tu, B. Iwanschitz, A. Mai, *J. Power Sources* **2008**, *182*, 400–412.
[4] Q. Huang, R. Hui, B. Wang, J. Zhang, *Electrochim. Acta* **2007**, *52*, 8144–8164.
[5] C. Comminges, Q. X. Fu, M. Zahid, N. Y. Steiner, O. Bucheli, *Electrochim. Acta* **2012**, *59*, 367–375.
[6] M. Lang, C. Auer, A. Eismann, P. Szabo, N. Wagner, *Electrochim. Acta* **2008**, *53*, 7509–7513.
[7] S. D. Ebbesen, J. Høgh, K. A. Nielsen, J. U. Nielsen, M. Mogensen, *Int. J. Hydrogen Energy* **2011**, *36*, 7363–7373.
[8] N. J. J. Dekker, J. F. van Wees, G. Rietveld, *Electrochem. Soc.* **2009**, *25*, 1871-1878.
[9] S. Diethelm, J. Van herle, Z. Wuillemin, A. Nakajo, N. Autissier, M. Molinelli, *J. Fuel Cell Sci. Technol.* **2008**, *5*, 031003.
[10] M. Henke, C. Willich, C. Westner, F. Leucht, J. Kallo, W. G. Bessler, K. a. Friedrich, *Fuel Cells* **2013**, *13*, 773–780.
[11] J. Schefold, A. Brisse, M. Zahid, J. P. Ouweltjes, J. U. Nielsen, *ECS Trans.* **2011**, *35*, 2915–2927.
[12] R. R. Mosbæk, J. Hjelm, R. Barfod, J. Høgh, P. V. Hendriksen, *Fuel Cells* **2013**, *13*, 605–611.
[13] N. Christiansen, S. Primdahl, M. Wandel, S. Ramousse, A. Hagen, *ECS Trans.* **2013**, *57*, 43–52.
[14] K. A. Nielsen, A. Persson, D. Beeaff, J. Høgh, L. Mikkelsen, P. V. Hendriksen, *ECS Trans.* **2007**, *7*, 2145–2154.
[15] B. A. Boukamp, *J. Electrochem. Soc.* **1995**, *142*, 1885.
[16] H. Schichlein, A. C. Müller, M. Voigts, A. Krügel, E. Ivers-Tiffée, *J. Appl. Electrochem.* **2002**, *32*, 875–882.
[17] - , *J. Electrochem. Soc.* **2008**, *155*, B36.
[18] - , *J. Electrochem. Soc.* **2008**, *155*, B675.
[19] R. Barfod, A. Hagen, S. Ramousse, P. V. Hendriksen, M. Mogensen, *Fuel Cells* **2006**, *6*, 141–145.
[20] S. Primdahl, M. Mogensen, *J. Electrochem. Soc.* **1998**, *145*, 2431–2438.
[21] S. Primdahl, M. Mogensen, *J. Electrochem. Soc.* **1999**, *146*, 2827–2833.
[22] W. G. Bessler, S. Gewies, *J. Electrochem. Soc.* **2007**, *154*, B548.
[23] T. Jacobsen, P. Hendriksen, S. Koch, *Electrochim. Acta* **2008**, *53*, 7500–7508.
[24] S. H. Jensen, A. Hauch, P. V. Hendriksen, M. Mogensen, *J. Electrochem. Soc.* **2009**, *156*, B757–B764.